REFERENCE ONLY

UNIVERSITY OF LONDON THESIS

Degree	Year	Name of Author
PhD	2005	DEWSHURST, J.P.

UNIVERSITY COLLEGE LONDON

Cluster Investigations of Magnetotail Processes

Jason Peter Dewhurst

Mullard Space Science Laboratory
Department of Space and Climate Physics
University College London

A thesis submitted to the University of London
for the degree of Doctor of Philosophy

ProQuest LLC
789 East Eisenhower Parkway
P.O. Box 1346
Ann Arbor, MI 48106-1346

Abstract

Physical processes in the Earth's magnetotail are investigated using data principally from the Plasma Electron And Current Experiment onboard the European Space Agency's 4 spacecraft Cluster mission.

Three topics are presented: the expansion and thinning of the plasma sheet during the course of a substorm; field-aligned current generation during intervals of flow shears in the plasma sheet; and observations of flux-ropes and travelling compression regions.

Multipoint observations of the boundary between the plasma sheet and the lobe have allowed the determination of the speed and direction of propagation of the boundary. Using the direction of the boundary motion we looked for a trend of Earthward or tailward directed motion that might be indicative of whether near-Earth neutral line formation or current disruption occurred first at substorm onset. Given the time resolution of the observations, we did not find compelling evidence to confirm either initiator of the substorm process.

The occurrence of flow shears in the plasma sheet, associated with phenomena such as bursty bulk flows, may result in the twisting of magnetic field lines. The twisted field should support a field-aligned current and this mechanism has been proposed to be significant at the flow-braking region, where the substorm current wedge is formed. We examine flow shears in the magnetotail and check for the presence of field-aligned currents during these intervals. The variations observed in the field-aligned current can be explained by changes in the position of the greatest flow shear with respect to the spacecraft tetrahedron.

Finally we examine the observations of travelling compression regions in the lobe and flux-ropes within the plasma sheet in order to demonstrate their association with each other. The plasma environments of flux-ropes are examined. Successful identification of flux-ropes fitting a force-free model which are co-incident with travelling compression regions is made.

Dedicated to Margaret Dewhurst, 1944-2002

Acknowledgements

I would like to thank Dr. Christopher Owen for his supervision throughout my research project. As well as his scientific guidance and advice, he has provided support when it was needed and that is much appreciated.

I wish to thank Dr. Andrew Fazakerley (PEACE PI) and the PEACE science and operations teams at MSSL for their support, advice and encouragement throughout my research. I also wish to thank the other staff and students at MSSL for making my time there enjoyable and memorable.

In addition, thanks go to all the other Cluster science and operations teams who have provided data, interpretation and discussion for the material presented in this thesis. I would like to thank the Particle Physics and Astronomy Research Council for providing me with postgraduate funding.

Finally, I wish to thank my family and friends for their encouragement and motivation.

Table of Contents

Table of Figures and Tables

1 Basic Space Plasma Physics

1.1 Introduction

There are many complex physical processes that connect the Sun and the Earth. The interaction between the Sun's magnetic field and the plasma associated with it and those of the Earth forms the essence of the science presented in this thesis. A short description of some basic concepts of space plasma physics is provided here. Topics addressed include the formal definitions of a plasma and the general motions that charged particles exhibit in certain external fields. A description of the magnetohydrodynamic approximation that is used in this work is provided followed by a description of the Earth's local plasma environment and the many components of the magnetosphere. This will lead into a detailed description of the Earth's magnetotail and the dynamic processes that are found there which will form the basis of the original science presented in later chapters.

1.1.1 Definition of a Plasma

A plasma can be defined as a quasineutral gas of ionised particles that exhibit collective behaviour. Quasineutrality allows for short-lived, small-scale charge separations, but over longer time-scales and length-scales the plasma is neutral. There may also be neutral particles co-located with the plasma, but the frequency of collisions between the charged particles and the neutrals must be sufficiently low to allow the plasma to respond to an external perturbation without interference. The charged particles are taken to be 'free' particles which have kinetic energy that is much greater than the potential due to their nearest neighbours.

1.1.2 Debye shielding and Plasma Frequency

To achieve quasineutrality it is necessary to have approximately equal numbers of positively and negatively charged particles in a volume element. For plasma to appear electrically neutral, the electric field of each charge must be cancelled out by the other charges. A charge q has an electric field associated with the potential:

$$\phi_C = \frac{q}{4\pi\varepsilon_0 r} \tag{1.1}$$

where r is the distance from the charge and ε_0 is the permittivity of free space. The constituent charged particles of the plasma respond accordingly to make the plasma electrically neutral. The potential around a charged particle is then:

$$\phi_D = \frac{q}{4\pi\varepsilon_0 r}\exp\left(-\frac{r}{\lambda_D}\right) \tag{1.2}$$

where the characteristic length scale is λ_D, the Debye length, in which a balance between thermal disturbances which effect neutrality and the restoring forces due to charge separation cancel each other.

For the shielding to occur, the Debye length has to be much shorter than the characteristic length scale of the system in question. The Debye length is the scale of the sphere of influence of a charged particle in a plasma and it follows that the number of particles within the Debye sphere must be much greater than one for the shielding effect to take place.

If a quasineutral plasma is disturbed by an external force, the electrons, being much more mobile, respond more to the force and subsequently oscillate about the heavier ions due to the restoring charge separation force. The frequency at which this

occurs is known as the plasma frequency. In order for the plasma to oscillate freely, the time between electron-neutral collisions must be much larger than the reciprocal of the plasma frequency. This forms another condition of an ionised gas being a plasma.

1.2 Single Particle Motion

The motion of a charged particle is largely governed by the presence of electric and magnetic fields that may be external fields or those generated by other moving charged particles. Collisions with other particles will also affect the motion. In this section a brief description is provided of some of the typical motions that a single particle may experience. Throughout this section the particles are distinguished by charge only. In a real plasma, the negative particles are electrons and the positive particles are protons or heavier ions.

1.2.1 Electric and Magnetic Fields

A charged particle of charge q at rest is the source of an electric field, $\mathbf{E}$, which will result in the Coulomb force, $\mathbf{F}_C$, on a unit positive charge:

$$\mathbf{F}_C = q\mathbf{E} \tag{1.3}$$

A charge q moving with velocity $\mathbf{v}$ forms a current that generates a magnetic field $\mathbf{B}$ that produces the Lorentz force, $\mathbf{F}_L$, on a unit positive charge:

$$\mathbf{F}_L = q(\mathbf{v}\times\mathbf{B}) \tag{1.4}$$

The motion of a particle may change the local electric and magnetic fields which may result in a change of the particle's motion. External electromagnetic fields are also important and are governed by the Maxwell equations:

$$\nabla \times \mathbf{B} = \mu_0 \mathbf{j} + \varepsilon_0 \mu_0 \frac{\partial \mathbf{E}}{\partial t} \tag{1.5a}$$

$$\nabla \times \mathbf{E} = -\frac{\partial \mathbf{B}}{\partial t} \tag{1.5b}$$

$$\nabla \cdot \mathbf{B} = 0 \tag{1.5c}$$

$$\nabla \cdot \mathbf{E} = \frac{\rho}{\varepsilon_0} \tag{1.5d}$$

Where the current density, $\mathbf{j}$, and the charge density, ρ, are related to the electron and ion number density and velocity, assuming singly charged ions, by:

$$\rho = e(n_i - n_e) \tag{1.6a}$$

and

$$\mathbf{j} = e(n_i \mathbf{v}_i - n_e \mathbf{v}_e) \tag{1.6b}$$

1.2.2 Gyration

Working from Newton's laws, the equation of motion for a charged particle in electric and magnetic fields is:

$$m\frac{d\mathbf{v}}{dt} = q(\mathbf{E} + \mathbf{v} \times \mathbf{B}) \tag{1.7}$$

If there is no electric field then the particle's speed and kinetic energy do not vary as long as the magnetic field is static, as the Lorentz force acts perpendicular to the field and results in only a change of direction of the particle. The particle will follow gyratory motion about a point, known as the guiding centre, with a characteristic frequency and radius known as the gyrofrequency and gyroradius. Helical motion is produced if the particle has a velocity component along the magnetic field. A useful description of a

particle obeying helical motion is the pitch angle, defined in terms of the angle between the particle velocity vector and the magnetic field line:

$$\alpha = \arctan\left(\frac{v_{\perp}}{v_{\parallel}}\right) \tag{1.8}$$

where the velocity components are taken perpendicular and parallel to the magnetic field.

1.2.3 Drifts

A static electric field has the effect of causing a drift of a gyrating particle's guiding centre, and is know as **E**×**B** drift. The positively and negatively charged particles drift in the same direction. A useful result is derived from this drift. In the frame of the moving particle, the electric field is:

$$\mathbf{E}' = \mathbf{E} + \mathbf{v} \times \mathbf{B} \tag{1.9}$$

Given the particles need to remain free to satisfy the condition of being a plasma, the electric field in the frame of the particle, $\mathbf{E}'$, must be zero. This leads to:

$$\mathbf{E} = -\mathbf{v} \times \mathbf{B} \tag{1.10}$$

Another important drift is formed when the electric field is allowed to vary slowly. In this polarization drift, the mass of the particle and its charge are important to the drift, and so a current is formed which is carried mainly by the ions.

Magnetic field variations do not impart energy to the particle, as the force is always perpendicular to the velocity of the particle. However, a time-varying magnetic field induces an electric field that can alter the particle velocity. Magnetic gradients and curvature also result in particle drifts.

1.2.4 Magnetic Mirrors

An important effect of spatial variations of a magnetic field is the presence of "magnetic bottles" that can trap particles on particular magnetic flux tubes. This magnetic bottle effect is important in the Earth's radiation belts and also is important for the process of thermalization of particle distributions within the magnetotail. To understand magnetic mirrors, characteristic constants of motion of an individual particle in a plasma, the adiabatic invariants, need to be introduced. These qualities are not constants in the true meaning being allowed to vary on time scales longer than the periodicities that the particle exhibits. The three adiabatic invariants are: the magnetic moment, μ, associated with gyration around a field line; J, the longitudinal invariant associated with longitudinal motion and bounce between mirror points; and ϕ, the perpendicular drift invariant.

To explain magnetic mirrors, the magnetic moment and the consequences of its invariance are illustrated. The magnetic moment is defined as:

$$\mu = \frac{mv^2 \sin^2 \alpha}{2B} = \frac{mv_\perp^2}{2B} = \frac{W_\perp}{B} \tag{1.11}$$

where m is the mass of the particle, $v_\perp$ is the particle's velocity perpendicular to the magnetic field, B. $W_\perp$ is the perpendicular component of the particle's kinetic energy and the total energy is represented by:

$$W = W_\parallel + W_\perp \tag{1.12}$$

where $W_\parallel$ is the parallel component. If μ is taken as a conserved quantity, the magnetic field strength at two locations is given by:

$$\frac{\sin^2 \alpha_2}{\sin^2 \alpha_1} = \frac{B_2}{B_1} \tag{1.13}$$

In a converging magnetic field topology, such as on the field lines of the Earth near the magnetic poles, a particle moving into a higher magnetic field strength region will experience an increase in the perpendicular component of the total particle energy. As evident from Equation 1.12, which expresses conservation of the total energy, this increase in $W_{\perp}$ will be at the expense of $W_{\parallel}$, leading to reflection when the pitch angle reaches 90° due to the magnetic gradient force. If two magnetic mirror points exist on a field line, like in a dipolar magnetic field, a particle may become trapped if it has an appropriate value of μ. A trapped particle will exhibit a bounce motion between the mirror points as typically observed in the radiation belts of the Earth [see Section 1.4.5].

1.3 Many-Particle Motion

Deriving the motion of each individual charged particle that makes up real plasma would be computationally difficult. In most plasma related studies an approximation or simplification is made to aid calculation of bulk plasma parameters. Two main methods are used: kinetic theory and magnetohydrodynamics (MHD). In kinetic theory, individual particle motion is taken into account by using statistical distributions in phase-space density i.e. a function of velocity, position and time. Magnetohydrodynamics assumes the plasma can be treated as a fluid. It is possible to work with two or more separate fluids for each particle type within the plasma. A combination of both techniques is frequently used. A short description of kinetic theory and MHD is provided. The complex process of magnetic reconnection is briefly described which builds upon the break-down of ideal MHD.

1.3.1 Kinetic Theory

At a given time, each particle in a system has a position (**x**) and a velocity (**v**) and can be described as occupying a particular part of a six-dimensional (**x**, **v**) space know as phase space. In a multi-particle system the application of statistical averaging gives the concept of phase space density as the number of particles located in the same part of phase space and is represented as:

$$\text{Phase Space Density} = f(\mathbf{x}, \mathbf{v}, t) \tag{1.14}$$

Various theoretical distributions are used to describe plasmas in phase space e.g. Maxwellian and Kappa distributions. Macroscopic plasma parameters, such as density, velocity, pressure and temperature, are calculations of the *i*-th moment of the distribution function:

$$M_i(\mathbf{x},t) = \int f(\mathbf{v},\mathbf{x},t)\mathbf{v}^i d^3v \tag{1.15}$$

For example, the number density and bulk velocity are given by:

$$n = \int f(\mathbf{v}) d^3v \tag{1.16}$$

$$\mathbf{v}_b = \frac{1}{n}\int \mathbf{v} f(\mathbf{v}) d^3v \tag{1.17}$$

1.3.2 Magnetohydrodynamics

Instead of considering the individual particles that make up a plasma, we can consider the plasma as a fluid. As a fluid, the plasma obeys the laws of conservation, as a normal hydrodynamic fluid would, and is also controlled by Maxwell's equations. By considering a two-fluid plasma and assuming small current densities, an equation of conservation, know as the Generalized Ohm's Law, is formed:

$$\mathbf{E}+\mathbf{v}\times\mathbf{B}=\eta\mathbf{j}+\frac{1}{ne}\mathbf{j}\times\mathbf{B}-\frac{1}{ne}\nabla\cdot\mathbf{P}_e+\frac{m_e}{ne^2}\frac{\partial\mathbf{j}}{\partial t} \tag{1.18}$$

where η is the resistivity of the plasma, n is the number density, e is the electronic charge, m_e is the mass of the electron, $\mathbf{j}$ is the current density, and $\mathbf{P_e}$ is the electron pressure. The terms on the right hand side are: the resistive term, the Hall-current term, the anisotropic electron pressure term, and a time dependent term associated with the contribution of electron inertia to the current flow.

1.3.2.1 Diffusion and the Frozen-in Theorem

If variations occur on long times scales and assuming that the electron population can be taken as being isotropic and the Hall term can be neglected then, using σ_0 as the plasma conductivity defined as the reciprocal of the resistivity, Equation 1.18 becomes:

$$\mathbf{E}+\mathbf{v}\times\mathbf{B}=\eta\mathbf{j}=\frac{1}{\sigma_0}\mathbf{j} \tag{1.19}$$

Substitution into Faraday's law and applying Ampere's Law produces:

$$\nabla\times\left(\mathbf{v}\times\mathbf{B}-\frac{\nabla\times\mathbf{B}}{\mu_0\sigma_0}\right)=\frac{\partial\mathbf{B}}{\partial t} \tag{1.20}$$

The vector identity $\nabla^2\mathbf{A}=\nabla(\nabla\cdot\mathbf{A})-\nabla\times(\nabla\times\mathbf{A})$ reduces this to:

$$\nabla\times(\mathbf{v}\times\mathbf{B})+\frac{\nabla^2\mathbf{B}}{\mu_0\sigma_0}=\frac{\partial\mathbf{B}}{\partial t} \tag{1.21}$$

which illustrates that the magnetic field can be changed by convection with the plasma and also by diffusion process of the magnetic field through the plasma. If the conductivity and the length scales of the plasma are large, as is usually the case for a collisionless space plasma, then the above reduces to the ideal MHD case of:

$$\mathbf{E}+\mathbf{v}\times\mathbf{B}=0 \tag{1.22a}$$

$$\nabla\times(\mathbf{v}\times\mathbf{B})>>\frac{\nabla^2\mathbf{B}}{\mu_0\sigma_0} \tag{1.22b}$$

which is often used as a statement of the plasma being frozen-in to the magnetic field. If the magnetic field is frozen-in to the plasma then the two will move with each other and the plasma will remain on that field-line. If diffusion is allowed to occur, by a break down in the assumption that the conductivity is infinite for example, then the plasma need no longer be associated with a given magnetic field line. This has important consequences the process of magnetic merging or reconnection that is discussed later.

1.3.2.2 Magnetic Tension and Plasma Beta

Assuming temporal variations of the electric field are small, Ampére's Law crossed with the magnetic field gives:

$$\mathbf{j}\times\mathbf{B}=-\frac{1}{\mu_0}\mathbf{B}\times(\nabla\times\mathbf{B}) \tag{1.23}$$

which can be rewritten as:

$$\mathbf{j}\times\mathbf{B}=-\nabla\left(\frac{B^2}{2\mu_0}\right)+\frac{1}{\mu_0}\nabla\cdot(\mathbf{BB}) \tag{1.24}$$

The $B^2/2\mu_0$ on the right hand side is equivalent to a magnetic pressure. The ratio of gas pressure to magnetic pressure defines the plasma-β parameter which indicates if the magnetic field pressure or the plasma pressure dominates a given system. The $\boldsymbol{BB}/\mu_0$ term is the magnetic stress tensor which leads to the concept of magnetic tension. This is important in the dynamics of plasma on field lines that are curved, and will be illustrated in the next section.

1.3.3 Magnetic Reconnection

The process of magnetic reconnection or merging allows magnetic fields to be reconfigured and plasma populations to mix and accelerate. The reader is directed to the wealth of literature on magnetic reconnection models and concepts [e.g. Parker, 1963; Vasyliunas, 1975; Treumann and Baumjohann, 1997]. Two anti-parallel fields must be separated by a current sheet, as shown in Figure 1-1a, provide a candidate location for magnetic reconnection to occur. If a perturbation of a sufficient size to the current sheet occurs, a change in plasma conductivity for example, then a diffusion region is formed, as in Figure 1-1b. In this region the frozen-in flow condition is no longer satisfied and the particles are no longer constrained to the magnetic field. The magnetic fields are then able to merge vectorially and an x-line is formed, see Figure 1-1c. At this point the magnetic field configuration changes and these reconnected field lines contract under the influence of magnetic tension forces as in Figure 1-1d. The acceleration of the particles on the field lines that have been reconnected, at the expense of free magnetic energy, heat the plasma.

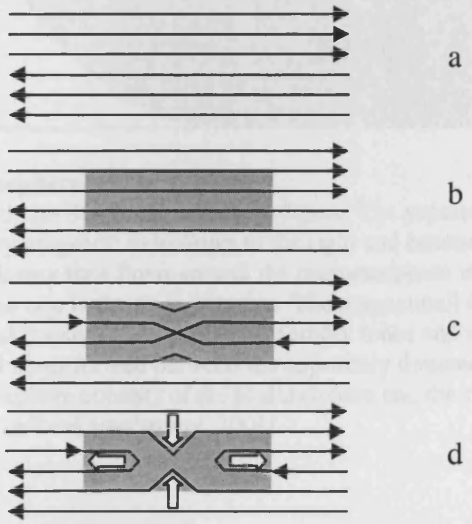

Figure 1-1 Magnetic reconnection
The two anti-parallel magnetic field lines (a) experience a instability which creates a diffusion region (b) shaded here in grey. At this diffusion region the magnetic field is allowed to merge (c). These reconnected field lines then retract (d) to reduce their magnetic tension.

1.4 Geophysical Plasmas

A brief description of the plasma environment appropriate to the study of the solar-terrestrial interaction is provided in this section. More detail is provided to aid the setting of the science presented in this thesis. Figure 1-2 illustrates the various regions of the magnetosphere shown side on with the Sun to the left of the page and the solar wind flowing to the right.

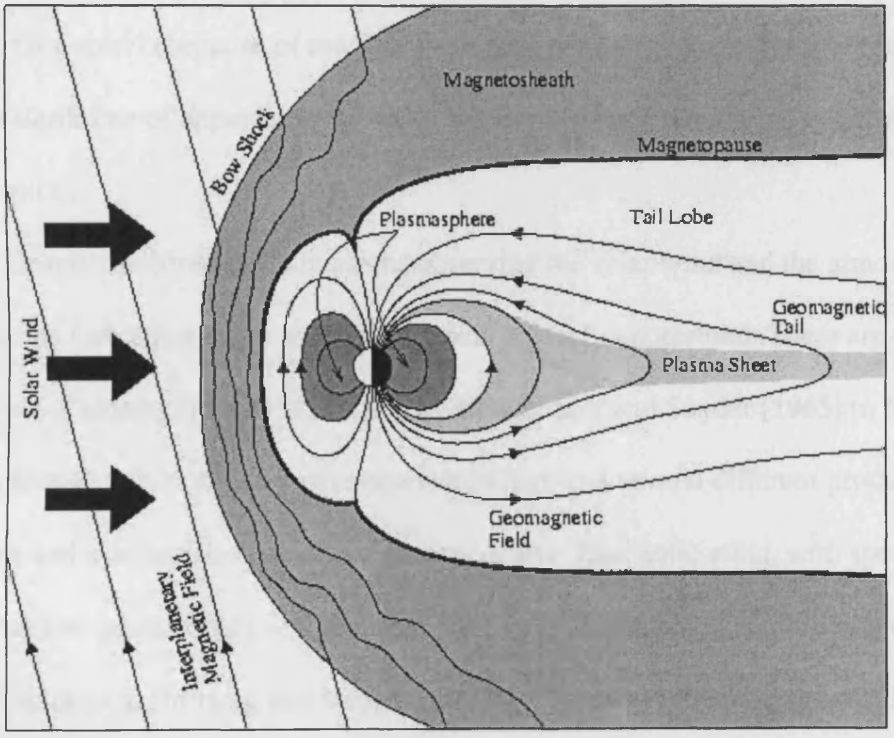

Figure 1-2 The magnetosphere and its regions
This is a side on view with the Sun to the left of the figure. The supersonic solar wind carrying the interplanetary magnetic field flows to the right and encounters the bow shock. The subsonic, shocked plasma then flows around the magnetosphere in the magnetosheath. The boundary between the two is the magnetopause. The magnetotail is stretched on the night side of the Earth and consists of two relatively empty lobes and a denser plasma sheet encompassing the neutral sheet formed between the oppositely directed magnetic fields in the lobes. The inner magnetosphere consists of the plasmasphere and the radiation belts. [Taken from http://www.tp.umu.se/forskning/space/, 2004]

1.4.1 Solar wind

Comet tail observations [Biermann, 1951] led to the concept of some form of continuous flow from the Sun and this concept was developed by the idea of the solar corona expanding into interplanetary space and termed the 'solar wind' [Parker, 1959]. The high conductivity of the solar wind results in the solar magnetic field being carried by the plasma. The plasma moves nearly parallel to the Sun-Earth line, and the frozen-in field forms a spiral (because of the Sun's rotation) with an average angle of incidence to the Sun-Earth line of approximately 45° at the Earth's orbit. This spiral is known as the Parker spiral.

Despite multiple space missions observing the solar wind and the atmosphere of the Sun, the formation of the solar wind remains poorly understood. There are two main categories of solar wind (first identified by Neugebauer and Snyder [1965] in Marina 2 data), although sub-categories have been identified, and several different production locations and mechanisms have been proposed. The 'fast' solar wind, with speeds ~ 750 kms^{-1}, has two contributory sources: solar plumes [e.g. Gabriel et al., 2003] and solar coronal holes [e.g. Hollweg and Isenberg, 2002]. The 'slow' solar wind, ~400 kms^{-1}, is likely to emerge from the near the equator [e.g. Ohmi et al., 2004]. The solar wind has a particle number density of 3-20 cm^{-3} at the Earth's orbit and consists mainly of electrons and protons. The magnetic field is on average ~6 nT, but is variable in magnitude and direction due to solar activity. The solar cycle influences the structure of the solar wind, which has most recently been quantified by the Ulysses spacecraft [e.g. Salem et al., 2003].

The scale sizes of variations in the solar wind are important to global magnetospheric changes and are discussed by e.g. Russell et al. [1980] and Crooker et al. [1982]. Variations in the magnetic field direction and in the plasma density are fundamental to driving magnetospheric dynamics.

1.4.2 Bow shock

The solar wind, because of its high conductivity, has its associated magnetic field 'frozen-in'. It is therefore required to flow around the Earth's magnetic field as diffusion processes are not strong enough to allow the solar wind field to flow through the magnetosphere [Axford, 1962; Kellogg, 1962]. The supersonic flow has to be slowed down to subsonic speeds for this deflection to occur. The size and shape of the bow shock have been studied [e.g. Formisano, 1979] and was found to be 100-1000 km thick and located 10-15 R_E away from the Earth at the sub-solar point, increasing to 15-20 R_E towards the flanks. However, this does depend on the solar wind conditions upstream of the shock [e.g. Cains and Lyons, 1995]. As it crosses the bow shock heading Earthwards, the solar wind density, temperature and magnetic field strength increases and the plasma velocity decreases. Using Cluster results, Horbury et al. [2001] provide details of the orientation, motion and structure of the bow shock and identify that even with rapid motion of the bow shock over the spacecraft quartet, the normal of the bow shock remains constant.

1.4.3 Magnetosheath

The shocked solar wind flows with velocities of the order 100-200 kms^{-1} around the Earth's magnetic obstacle, the magnetosphere, in what is known as the

magnetosheath. The separatrix between these two regions is known as the magnetopause. The plasma is denser than in the solar wind, 3-30 cm^{-3}, and is turbulent. Ions have typical energies of 1 keV with electrons having energies around 100 eV. Wave activity is very common in the magnetosheath [e.g. Smith et al., 1969]. Fluctuations in the magnetosheath result in variations in the location of the magnetopause [e.g. Sibeck and Gosling, 1996].

1.4.4 Magnetopause and Magnetosphere

The separatrix between the magnetosheath and the magnetosphere carries the magnetopause current that is created due to the different penetration depths of the ions and electrons that encounter the boundary and supports the shear in the magnetic fields. To first approximation the location of the magnetopause can be estimated from a balance between the solar wind dynamic pressure and the Earth's magnetic field pressure just inside the boundary and is found generally between 8 and 13 R_E in front of the Earth. The nature of the flowing magnetosheath plasma results in a compressed dayside and an extended night side magnetosphere when compared to an undisturbed dipole field. Sibeck et al. [1991] provides a description of the magnetopause shape.

The magnetosphere is the magnetic cavity in the solar wind in which the Earth's magnetic field dominates. The magnetosphere contains many distinct regions and plasma populations.

1.4.5 Ionosphere, Plasmasphere, and Radiation Belts

The ionosphere is created by ionisation of the upper atmosphere by solar radiation. The magnetic field lines passing through the ionosphere control ionospheric

convection, as discussed later in Section 1.5.2. The upper part of the ionosphere forms the plasmasphere as some of the ionospheric particles have a temperature which is not sufficiently low enough to keep them bound by gravity. The plasmasphere extends to 2-5 R_E and contains cold plasma (~1 eV) with a density of ~10^3 cm^{-3} and co-rotates with the Earth. Co-existing with the plasmasphere are the radiation belts. There are two main radiation belt regions, which overlap to some extent, discovered by Van Allen et al. [1958]. The inner belt consists primarily of protons (with energies exceeding 10 MeV) and the outer belt primarily of electrons (of up to 10 MeV) [Van Allen and Frank, 1959]. The particles in these radiation belts follow bounce, drift and gyratory motion along the near dipolar magnetic field found there.

1.4.6 Magnetotail

The magnetotail is the region of primary interest for the studies presented in this thesis. The magnetotail consists of two magnetic lobes separated by a neutral sheet that is embedded in a thicker plasma sheet. The magnetotail is drawn out in the anti-solar direction due to interactions between the solar wind and the magnetosphere. The tail structure was debated in many early works [e.g. Heppner et al, 1963; Ness, 1965] and early observations by spacecraft [e.g. Bame et al., 1967; Fairfield and Ness, 1967] confirmed the shape of the magnetotail. The magnetotail changes during the course of geomagnetic activity and this is discussed in Section 1.5. However, a 'quiet' time description of these various regions follows here.

The lobes are made up of open magnetic field lines with one end located within the polar cap ionosphere, the region bound by the auroral oval, and the other embedded in the solar wind. The lobes are relatively void of plasma, with a number density of ~0.01

cm^{-3} near the Earth, with the plasma density increasing down the tail [Zwickl et al., 1984] to approximately 0.1 cm^{-3} from 0.01 cm^{-3}. The plasma that is present is anisotropic, field aligned and contains electrons with energies of 100 eV which is consistent with solar wind electrons and suggests that these field lines are indeed open and connected to the solar wind [Fairfield and Scudder, 1987]. The magnetic field strength decreases away from the Earth [e.g. Yamomoto et al., 1994].

The plasma sheet boundary layer is situated between the lobes and the plasma sheet [e.g. Parks, 1979] and is identified by large parallel pitch-angle particle fluxes [e.g. Eastman et al., 1984]. The origin of these particles is understood to be magnetic reconnection in the tail that completes the Dungey cycle in the open magnetosphere [Williams, 1981; Lyons and Speiser, 1982] which is described in more detail in Section 1.5. The field-aligned nature of the particle distributions soon thermalizes with increasing distance from the lobe and become more isotropic with repeated reflections in the magnetic bottle formed by the more dipolar field near the Earth [Eastman et al., 1984]. These authors also identify the boundary layer as being 0.3 to 3 R_E wide.

The plasma sheet is dense compared to the lobes [e.g. Baumjohann et al., 1989] with densities of 0.4 – 2 cm^{-3} and is hot with energies up to a few keV. The plasma sheet is populated in part by hydrogen and oxygen ions that indicate some connection both with the solar wind and with the ionosphere [e.g. Daglis et al., 1994].

The neutral sheet is embedded within the plasma sheet. The two lobes have oppositely direct magnetic fields and therefore there is a neutral sheet between the two. The neutral sheet has been observed to exhibit oscillations due to diurnal and annual movement of the neutral sheet location due to the angular difference between the

magnetic and spin axes of the Earth [Lopez, 1990]. Due to motion of the neutral sheet, the plasma sheet also moves with diurnal and annual periodicities. As a consequence of the oppositely directed field of the lobe and by Ampere's law, a current flows across the tail parallel to the neutral sheet in the dawn to dusk direction, known as the cross-tail current.

There have been many recent works on magnetotail topics using the Cluster spacecraft. These will be described as appropriate in Chapters 3, 4 and 5.

1.5 Convection and Substorms

The motion of ionospheric plasma within and around the polar cap indicates convection of magnetic field lines within the magnetosphere by viscous interaction [Axford and Hines, 1961] or by magnetic reconnection processes which are dependent on IMF orientations [e.g. Heelis, 1984]. Flow towards midnight at high latitude returns to the dayside at lower latitudes setting up a twin convection cell that is typically observed for south interplanetary magnetic field [e.g. Clauer and Kamide, 1985]. Two contrasting models of steady state convection were originally conceived [Chapman and Ferraro, 1932; Dungey, 1961] and these are discussed in Section 1.5.1 followed by a brief description in Section 1.5.2 of the events when steady state convection breaks down and results in a geomagnetic substorm.

1.5.1 Steady State Convection

Initially, the magnetosphere was understood to be 'closed', meaning that the interplanetary magnetic field could not propagate through the magnetosphere [Chapman and Ferraro, 1931, 1932]. Convection of the terrestrial magnetic field was thought to be

driven by viscous interaction between the solar wind and the closed field lines of the Earth's magnetic field [Axford and Hines, 1961]. The 'closed' magnetosphere is shown in Figure 1-3a showing the interplanetary magnetic field moving around the magnetosphere with the terrestrial magnetic field remaining completely isolated. More modern models assume a fundamental interaction occurs between magnetic field lines: magnetic reconnection. With reconnection of solar wind and magnetospheric magnetic field lines, plasma populations could be exchanged and the global dynamics of the magnetosphere are more easily explained.

The 'open' magnetosphere [Dungey, 1961] and the magnetospheric convection cycle are shown in Figure 1-3b. The figure shows the solar wind magnetic field encountering the Earth's magnetic field and reconnection occurring near the sub-solar point. The open field line is then pulled anti-sunward as one end of the field is still frozen-in to the solar wind. On the Earth, the movement of the field lines in the anti-sunward direction drives ionospheric convection in the polar cap. Reconnection in the distant magnetotail closes the open field lines and the newly closed field line returns to the dayside under magnetic tension.

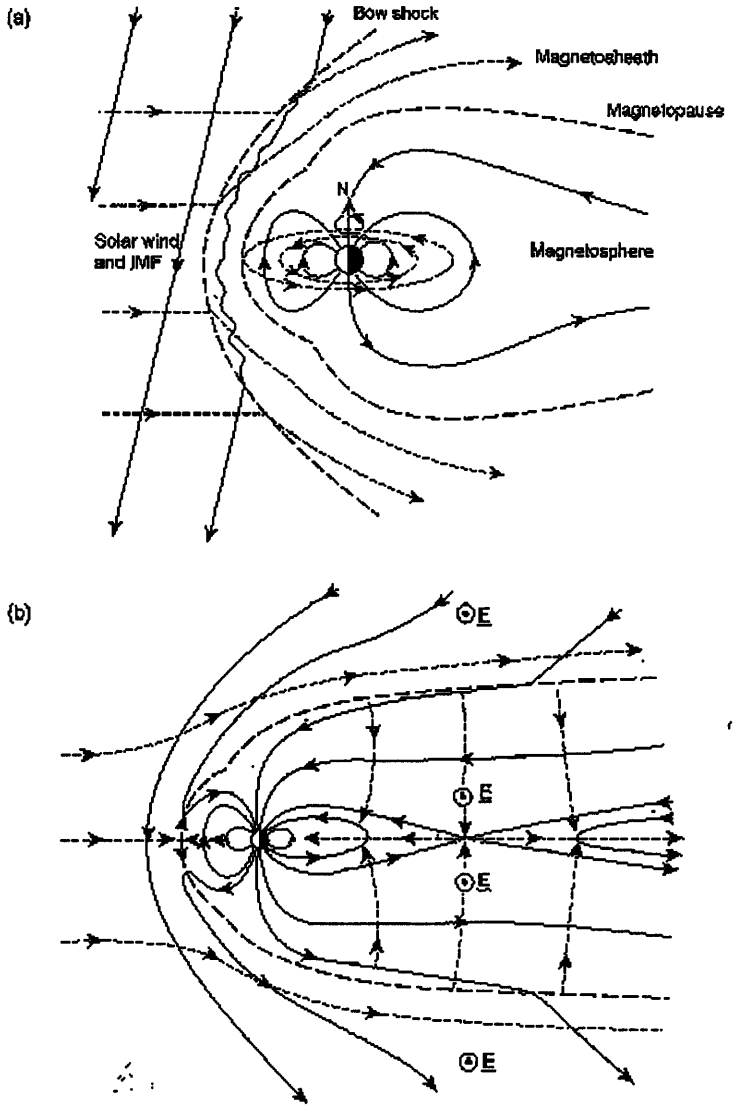

Figure 1-3 The 'open' and 'closed' magnetospheres
A) The 'closed' magnetosphere where the magnetic fields of the solar wind and the Earth are not allowed to merge. Viscous interaction of the flowing solar wind plasma initiates convection of the terrestrial magnetic field. B) The 'open' magnetosphere where reconnection of solar wind and terrestrial field lines at the dayside of the magnetosphere results in the open field lines existing within the magnetosphere. These field lines propagate towards the magnetotail due to the propagation of the solar wind. In the magnetotail, reconnection occurs again and closed magnetic field lines are formed which then propagate Earthward. [Taken from www.agu.org/sci_soc/cowley.html, 2005]

1.5.2 Substorm Processes

The steady state picture described above is rarely achieved for long periods of time. Varying solar wind conditions can result in two main forms of geomagnetic activity: storms and substorms. Chapman and Ferraro [1932] postulated that a burst of solar activity caused geomagnetic storms. Storms are large scale global geomagnetic disturbances caused by the compression of the magnetosphere as a whole and the inward displacement of the magnetopause and last on the order of days. An increase in the ring current caused by the drift of particles in the inner-magnetosphere results in a depression of the horizontal magnetic field at the of the Earth's surface. Substorms, not necessarily associated with storm-time intervals, are associated with shorter lived disturbances of the terrestrial magnetic field associated with the polar regions of the Earth. These transient events are important in the energy transfer from the solar wind through the magnetosphere and into the ionosphere [Rostoker et al., 1980]. The dynamics associated with substorm activity are the principle topic for this thesis and the substorm process is detailed here.

A substorm is defined in terms of three phases: growth, onset of expansion and recovery, although substorm activity is usually more complex than the three terms suggest, with multiple onsets often occurring in short succession.

During the growth phase [Akasofu, 1968] enhanced solar wind – magnetosphere coupling results in net magnetic flux being added to the magnetotail. The reconnection rate at the dayside magnetopause and the distant neutral line do not match and there is an imbalance. When reconnection at the dayside is enhanced, usually during periods of southward interplanetary magnetic field, the dayside magnetosphere is eroded [Maezawa,

1975; Baker et al., 1984] and more open flux is added into the magnetotail than can be removed by reconnection at the distant neutral line. This results in the magnetotail being stretched into a more extended structure becoming thicker and having a greater flaring angle. The cross-tail current also increases in the near-Earth plasma sheet as pressure balance results in a compressed plasma sheet and current sheet.

Upon substorm onset a multitude of events occur. The term 'substorm onset' is often ambiguously used. The origin of the term came from the observation of the auroral substorm [Akasofu, 1964]. At that time, only ground observations were available, and the 'auroral substorm onset' was taken as the point at which the auroral bulge towards the pre-midnight sector suddenly brightened. Other ground based data introduced 'onsets' – Pi2 activity in ground magnetometer data associated with auroral activity for example. With the addition of spacecraft observations, other 'onset' signatures were noted – the 'onset' of fast flows, the 'onset' of reconnection and the 'onset' of disruption of the cross-tail current into the ionosphere. Ambiguity in the timing of these processes has so far failed to completely reveal the event precedence during a substorm [Liou et al., 1999]. Ultimately, at or near substorm onset a release of stored magnetic energy in the magnetotail occurs and some of this is transported into the ionosphere by the diversion of the enhanced cross-tail current from the near-Earth magnetotail and results in auroral precipitation.

Within the magnetotail, a series of complex events occurs around the onset of expansion phase [Hones, 1967]. At some critical threshold or trigger point, another neutral line is formed, Earthward of the distant neutral line, known as the Near-Earth Neutral Line (NENL). The mechanism for the triggering of the NENL formation is still

unresolved but is associated with an instability occurring in the thinning current sheet resulting from the extra magnetic flux in the lobes. Reconnection at the NENL, initially produces closed field lines, one attached to the Earth, and the other attached to the distant neutral line. The closed field-lines of the Earth contract towards the Earth, while the closed field lines forming a magnetic loop or plasmoid are ultimately ejected from the magnetosphere and into the downstream solar wind. The open magnetosphere with the formation of the NENL is shown in Figure 1-4.

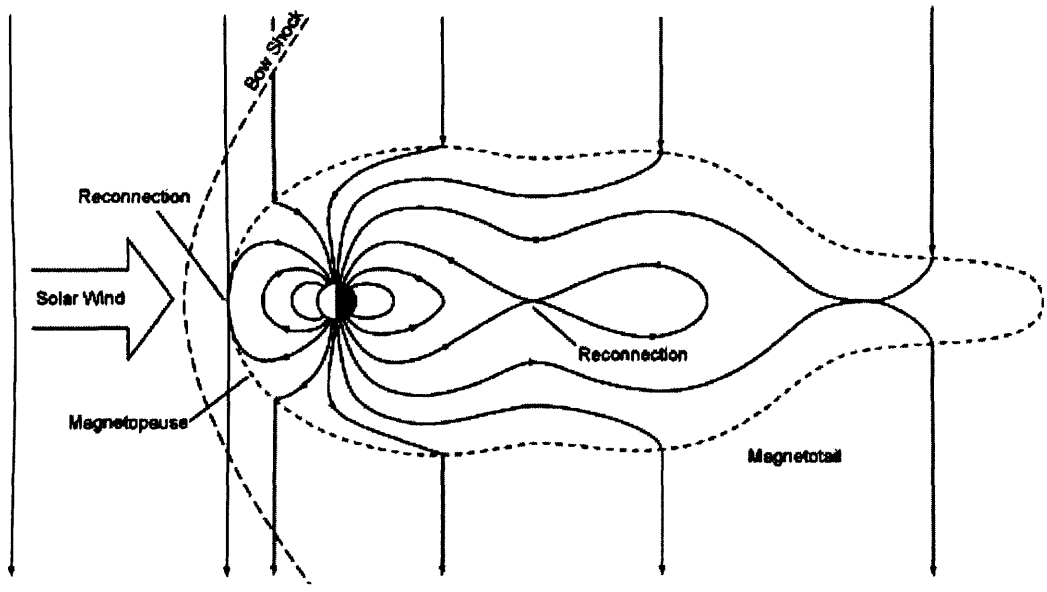

Figure 1-4 The 'open' magnetosphere near substorm initiation
A build-up of magnetic flux has occurred and reconnection Earthward of the distant neutral line has been initiated where shown. [Taken from http://geomag.usgs.gov/intro.html, 2004]

What causes the formation of the NENL and what role the NENL has in the substorm onset and the substorm as a whole is unresolved. Two main proposed mechanisms, either current disruption or magnetic reconnection at the NENL [see review by Lui et al., 1996, and Baker et al., 1996], are candidates to start the substorm onset process. However, in both models once the substorm has been initiated by the 'onset' mechanism the other phenomenon and associated signatures follow. Current disruption is

the phenomena where the cross-tail current is diverted into and then back out of the ionosphere – forming the substorm electrojet current signatures observed on the ground. There is a wealth of event studies that conclude that one of the models correlates with the observed data, but neither model appears to be suitable for every event. Lack of high-resolution auroral imaging data, and the scarcity of spacecraft data from the appropriate regions of space, will keep this discussion open at least for the near future. These topics are discussed in more detail later in this thesis.

Once the stored energy has been dissipated the magnetosphere recovers to its pre-growth phase state during the recovery phase.

1.5.2.1 Plasma sheet dynamics

As described above, the plasma sheet is dynamic with both oscillatory motion and substorm related activity. Prior to the Cluster mission, only single or dual spacecraft observations of the plasma sheet expansion and thinning during a substorm had been made. These observations, described below, provide evidence for the location of the NENL.

Plasma sheet observations made by the VELA spacecraft in an 18 R_E circular orbit [Hones et al., 1984], provided insight into the plasma sheet during a substorm. Rapid expansion of the plasma sheet was seen Earthward of 10-15 R_E with the tailward plasma sheet remaining thin. This is consistent with a neutral line forming between 10 and 15 R_E extending substantially in the cross tail direction. The newly reconnected field lines collapsing Earthward explain the expansion of the plasma sheet. The section of the plasma sheet tailward of the neutral line is severed and removed, hence the prolonged thinness of the plasma sheet near VELA apogee. Analysis of 461 plasma sheet drop outs

observed by ISEE 1 and 2 [Dandouras et al., 1986] indicates that drop outs occur uniformly between 12 and 23 R_E in geocentric distance and also across the entire night side plasma sheet. This is taken to be consistent with the NENL model where the neutral line is formed at different distances, sometimes within X = 12 R_E near-Earth and at other times beyond 23 R_E. Substorms with no associated plasma sheet flux drop out events were noted within 11 R_E.

The speed of plasma sheet expansion, i.e. the rate at which the boundary between the plasma sheet and lobe moves, measured by VELA 4A, VELA 5A and OGO 5, was found to be approximately 40 kms^{-1} up to 6 R_E away from the neutral sheet [Pytte et al., 1978].

A further AMPTE/IRM study, Baumjohann et al. [1992], analysed 39 major substorm onsets, as defined by the AE index, during substorms. As AMPTE/IRM had an apogee of 19 R_E, the study region was the relatively near-Earth plasma sheet. Plasma sheet thinning was observed to begin 30-45 minutes before substorm onset in the region 10-19 R_E. The plasma sheet began to expand after onset, regaining pre-substorm thickness about 45 minutes later. This expansion coincides with the start of the recovery phase as seen in the AE index. This study placed the NENL beyond 20 R_E consistent with Dandouras et al. [1986]. Nagai and Machida [1998] used data taken by the Geotail spacecraft during 138 well-defined substorms to obtain limits on the location of the magnetic reconnection region. Their study of the location of Earthward and tailward flows placed an inner limit of the reconnection region position at 22 R_E down the X_{GSM} axis, and an outer limit at 30 R_E down tail and within the pre-midnight region. Analysis

of Geotail data by Miyashita et al. [2000] placed the average NENL formation region at (X, Y) ~ (-19, 6)R_E.

Using Cluster, an in depth study of the plasma sheet expansion and thinning has been made and is presented in Chapter 3. Information on the expansion and thinning direction and the associated velocity distribution are provided and an attempt to qualify the dominant substorm trigger of NENL vs. CD is made.

1.5.2.2 Plasma Flows

Magnetic reconnection in the magnetotail produces high-speed field-aligned flows on the plasma sheet boundary layer and more convective flows in the central plasma sheet. These convective flows are often termed bursty bulk flows (BBFs) [e.g Baumjohann et al., 1999].

Observations in Geotail data [e.g. Baumjohann et al., 1999; Machida et al., 1999; Nagai and Machida, 1998] of fast Earthward plasma flows when Geotail was located at X > -20 R_E and fast tailward plasma flows when located at X < -25 R_E place the usual location of the NENL between 20 and 25 R_E down tail. Other Geotail studies have observed fast tailward ion flows, tailward of the NENL location, sometimes accompanied by fast keV tailward electrons [Nagai et al., 1998]. These authors report that in the high plasma beta region close to the neutral sheet ($|\mathbf{B}| < 5$nT), the ions show strong convection and the electrons are highly isotropic. In the plasma sheet – lobe boundary region there are two distinct ion components: those convecting inwards to the neutral sheet at lower energies and those streaming parallel to the magnetic field leaving the reconnection site after being accelerated and heated at higher energies. These ion components are observed

together with high-energy electrons streaming away from the reconnection site, whilst medium-energy (3 keV) electrons stream towards it. In the off-equatorial plasma sheet – tail lobe boundary, the convective and parallel ion components are accompanied by isotropic low energy electrons and highly streaming field-aligned electrons of energies greater than 10 keV propagating from the reconnection site.

Plasma flow shears have been observed, but the full extent of the plasma vorticity has not been quantified prior to Cluster. Flow vorticity is associated with the curl of the magnetic field and hence currents should form. In Chapter 4, three case studies are presented showing the effect of vorticity on field-aligned electron flows within the central plasma sheet.

1.5.2.3 Plasmoid / Flux Rope generation

The closed magnetic structures formed by magnetic reconnection at the NENL with reconnected lines at the distant neutral line are best described as a magnetic flux rope [e.g. Slavin et al., 2003a]. As well as tailward directed plasmoids, flux ropes are formed that travel Earthward.

These structures have also been identified as a result of the motion of an overlaying bulge in the plasma sheet – this creates a lobe magnetic field enhancement as the object passes by [Moldwin et al., 2001]. These enhancements are known as travelling compression regions (TCRs). As viewed by a spacecraft in the lobe, the magnetic field strength would increase as a TCR passed. A bipolar signature in the B_Z component from which the direction of motion of the TCR can be identified: north-then-south for tailward propagation and south-then-north implying Earthward propagation.

Observations of TCRs were reported by Slavin et al. [1993]. This survey was made in the distant tail and identified singular, paired and multiple TCR signatures. The magnitude of the magnetic field compression ($\Delta B/B$) was found to be greatest for the single events and decreased with the number of TCRs within the event. This was also shown in the duration of the events. When the timings of these events were compared to AL, Pi 2 and energetic particle data they usually occurred just after substorm onset or intensification. As these plasmoids leave the magnetosphere, they provide important information for the substorm energy budget calculation of the magnetosphere.

South-then-north propagating TCR signatures, together with the associated solar wind conditions, were studied to identify if these were actually caused by solar wind / sheath pressure pulses and not by a flux-rope in the plasma sheet [Moldwin et al., 2001]. In this work, most, but not all, TCR signatures could be explained by a pressure pulse, which requires both explanations to be tested where possible. Their selection of events, however, was taken mainly during northward IMF conditions and there is the possibility that the magnetotail may respond differently to a pressure pulse in the magnetosheath when under southward IMF.

Using Cluster's multipoint measurements which allow different plasma regions to be observed simultaneously may allow determination of TCR signatures being directly generated by flux-ropes within the plasma sheet. In Chapter 5, the observations of magnetic field and plasma within the plasma sheet during TCRs identified in magnetic field data are made. The magnetic field data from a spacecraft within the plasma sheet whilst another observes a TCR will be compared to a force-free flux rope model. If a

simple successful fit exists then this is direct evidence of TCR signatures generated by flux-ropes.

2 The Cluster Mission and PEACE

In this chapter we present a description of the Cluster mission which will be followed by an outline of the Plasma Electron And Current Experiment (PEACE). This instrument is the main source of the data used in the analysis presented in subsequent chapters. A short summary of the other Cluster instruments which provide supporting data for our analyses is also presented for reference.

2.1 The Cluster Mission

The aim of the Cluster mission is to enable the study of small scale plasma structures of the solar wind, bow shock, magnetopause, polar cusps, magnetotail and the auroral zones in three dimensions. Measurements of static and high frequency magnetic and electric fields and electron and ion distribution functions are made. Four point spacecraft measurement allows the resolution of spatial and temporal phenomena including gradients of plasma properties and boundary waves passing over the spacecraft tetrahedron.

The spacecraft are located in a 4×19.6 R_E orbit whose plane is fixed in inertial space. Throughout the year, the position of the Earth with respect to the Sun changes resulting in a full 360° revolution of the magnetosphere with respect to the Cluster orbit. This revolution of the whole magnetosphere with respect to the orbit results in different plasma regimes being preferentially surveyed throughout the year, for example the magnetotail is observed between the months of July through to November with the orbit apogee being located at midnight magnetic local time around the beginning of September.

The scale size of the constellation of the spacecraft is varied throughout the mission to address many different scientific goals. Only data from the 2001 and 2002 tail seasons is presented in this thesis where the separation scale length was ~1000 km and ~2000 km respectively.

Orbital mechanics also determines the formation of the Cluster constellation from a regular tetrahedron to a 'string of pearls' structure and this affects the type of analysis that is available. During the tail seasons studied for this thesis, the spacecraft were in a tetrahedron formation for the crossing of the magnetotail neutral sheet with a near-regular tetrahedron being formed in the midnight sector of the tail. Toward the flanks of the magnetotail the formation becomes less regular at the neutral sheet. Illustrations of the spacecraft configuration are shown in this thesis when appropriate.

2.1.1 A Multi-Spacecraft Mission

Single-point observations of magnetospheric plasma provide information of the plasma and magnetic and electric fields in the immediate vicinity of the spacecraft at a particular instant in time. There have been several conjunctions, in favourable locations within geospace, of two or more independent spacecraft e.g. FAST and Geotail [e.g. Sigsbee et al., 1998] and between Wind and Geotail [e.g. Berdichevsky, 1999]. There have also been multiple spacecraft missions resulting in new scientific results e.g. AMPTE [Krimigis, 1982] and ISEE [e.g. Elphic, 1988; Song et al., 1988]. To minimize the high cost associated with spacecraft launch, missions comprising of two segments that separate in orbit have been launched, e.g. Interball [Zelenyi et al., 1997].

Whilst there have been some multi-spacecraft missions, none have been able to fully explore the plasma environment of the Earth in three dimensions. This can only be

achieved by having at least four spacecraft. The ability that four spacecraft have to resolve spatial and temporal phenomena over the scale of the tetrahedron that they form was the initial concept for the Cluster mission.

2.1.2 Experiments

Onboard each of the four Cluster spacecraft there are 11 instruments designed to make measurements of the local plasma population, the direct current magnetic and electric fields and the variations of these fields. The instruments are named in Table 2-1 with a short description of what they measure.

Instrument Acronym	Instrument Name	Description
PEACE	Plasma Electron and Current Experiment	Spectrometry of electrons with energies between 0.59 eV and 26.4 keV
CIS	Cluster Ion Spectrometry	Spectrometry with mass determination of ions with energy between 0 and ~40 keV, with energy information provided for hotter ions without mass determination
RAPID	Research with Adaptive Particle Imaging Detectors	Detection of suprathermal electrons (20 keV to 400 keV) and ions (40 keV to 4000 keV)
EDI	Electric Drift Instrument	Calculation of plasma properties by detecting controlled emission
ASPOC	Active Spacecraft Potential Control	Spacecraft potential control by ion emission
FGM	FluxGate Magnetometer	Measures the local magnetic field (3D)
EFW	Electric Field and Wave experiment	Measures the local electric field (3D)
WHISPER	Wave of HIgh frequency and Sounder for Probing of Electrons by Relaxation.	Study of 2 - 80 kHz range waves including an active sounder to measure the absolute electron density in the vicinity of the spacecraft
WBD	Wide Band Data	Electric and magnetic waves in the frequency range 25 Hz to 577 kHz
DWP	Digital Wave Processing experiment	Provides digital processing of the wave instruments' data
STAFF	Spatio-Temporal Analysis of Field Fluctuation experiment	Magnetic field waves up to 4kHz in frequency

Table 2-1 The instruments onboard Cluster.

2.2 The Plasma Electron and Current Experiment (PEACE)

The primary source of data for the studies presented in this thesis is the University College London's Mullard Space Science Laboratory built Plasma Electron And Current Experiment (PEACE). A. N. Fazakerley is the Principal Investigator of PEACE. This instrument makes measurements of the local population of electrons with energies between 0.59 eV and 26.4 keV [Johnstone et al., 1997]. The PEACE instrument consists of two detectors mounted diametrically opposite each other on each of the four Cluster spacecraft. These detectors use differential electrostatic analysers with electron multipliers to make their measurements. The design and operation of PEACE is described below (see Johnstone et al. [1997] for further details).

Electrostatic analysers allow differential energy measurements at a high angular resolution and when mounted on a spinning spacecraft or platform can survey the complete sky within a spin or scan period. This type of detector has been used successfully onboard many missions, e.g. Geotail [Mukai et al., 1994] and AMPTE UKS [Coates et al., 1985], and with each one the technology has improved allowing better resolution and precision. For Cluster, the detector construction was needed to meet a requirement for greater precision to allow gradients in the plasma to be examined in more detail. In addition, the instrument had to provide good 3D distribution data products with a lower minimum energy level of the detector than previously flown. The differing plasma environments that are surveyed by Cluster require an instrument with a large energy range and appropriate sensitivities to the widely varying number densities.

Each PEACE instrument is comprised of two sensors based on the 'Top Hat' design of electrostatic analysers [Carlson et al., 1983; Sablik et al., 1990] with double-

thickness chevron-pair micro-channel plates (MCPs) as an electron multiplier with an associated gain of 2×10^6. The amplified electron charge cloud then reaches a detecting anode, the signal from which is extracted for amplification and processed by the onboard electronics.

A simplified schematic of one of the analyser systems is shown in Figure 2-1. The two analysers, known as the High Energy Electrostatic Analyser (HEEA) and the Low Energy Electrostatic Analyser (LEEA) differ primarily in the width of the entrance aperture. For the LEEA detector (which is typically operated to detect low energy electrons which occur with a greater number density) this is reduced to preserve the MCPs which would otherwise quickly degrade.

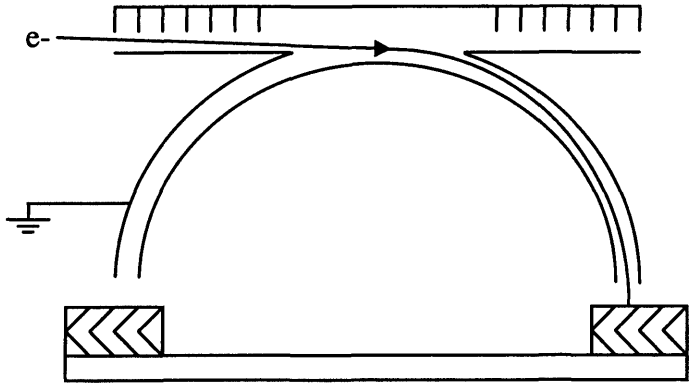

Figure 2-1 The 'Top Hat' analyser
A simple schematic of a 'Top Hat' electrostatic plate analyser that forms one sensor of the PEACE instrument.

The detector is able to measure a range of electron energies by varying the potential of the inner hemispherical plate. This energy selector causes electrons of the incorrect energy to hit the sides of the hemispherical plate and thus be removed from the system. The full energy range from 0.59 eV to 26.4 keV is split into 88 energy levels. The first 16 are linearly spaced between 0.59 eV and 9.45 eV. The remainder are

logarithmically spaced by a factor of 1.165. Each sensor operates over a subset of these energies due to telemetry constraints and is configured by uploaded commands. The energy sweep to cover the energy levels selected by the instrument commands begins at the higher energy level (after the fly back period when the voltage is being ramped up on the inner hemisphere) and is swept downwards. The time for a full sweep and the spin rate defines the azimuthal angular resolution, ϕ, of the sensor and this is shown for different operating modes in Table 2-2. An illustration of part of an energy sweep is shown in Figure 2-2[Wilson, 2004]. Note that the two sensors can operate in different modes and can be commanded separately.

Mode	Energy Bins	Energy Step	Sweeps per Spin	Azimuthal Resolution ϕ
Low Angular Resolution (LAR)	60	1	16	22.5°
Medium Angular Resolution (MAR)	30	2	32	11.25°
High Angular Resolution (HAR)	15	2	64	5.625°

Table 2-2 Sweep modes
The method of sweeping the energy range of the sensor affects the azimuthal resolution of the sensor. Most data presented in this thesis is obtained in Medium Angular Resolution mode

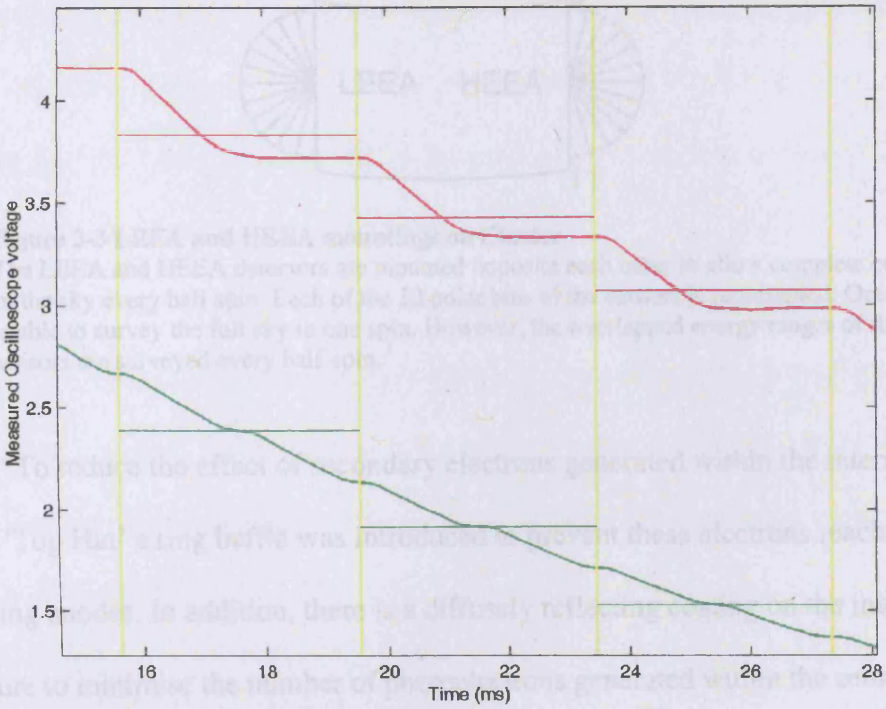

Figure 2-2 Voltage sweep
An example of the voltage variations of the inner hemisphere that change energy selected for detection. A trace for LAR (Red) and MAR (Green) is shown with vertical lines indicating the data bins that are formed and the representative energy associated for that bin is marked by the horizontal bar.

Although the general Top Hat design allows for a 360° field-of-view, the PEACE sensors are placed opposite each other on the spacecraft with the central anodes of each sensor viewing perpendicular to the spin axis of the spacecraft. Each sensor has a field of view of 180°, but the combined sensor system allows the complete sky to be viewed every half spacecraft rotation. Each of the sensors has 12 anodes providing polar bins of 15°. The position on the Cluster spacecraft and the field-of-view of the HEEA and LEEA sensors are illustrated in Figure 2-3.

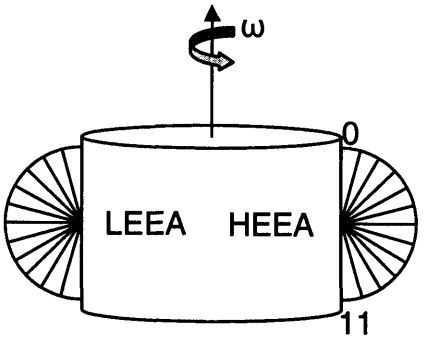

Figure 2-3 LEEA and HEEA mountings on Cluster
The LEEA and HEEA detectors are mounted opposite each other to allow complete coverage of the sky every half spin. Each of the 12 polar bins of the sensors is represented. One sensor is able to survey the full sky in one spin. However, the overlapped energy ranges of the two sensors are surveyed every half-spin.

To reduce the effect of secondary electrons generated within the internal structure of the 'Top Hat' a ring baffle was introduced to prevent these electrons reaching the detecting anodes. In addition, there is a diffusely reflecting coating on the internal structure to minimise the number of photoelectrons generated within the sensor.

2.2.1 Modes, Commanding and Data Products

Each sensor operates independently of the other and is commanded separately. Each command to the PEACE instrument configures the operation of HEEA and LEEA and also the return order and priority of the data products in the telemetry stream. The telemetry bandwidth available per spin varies between spacecraft as telemetry from non-functioning experiments on the same spacecraft is utilized allowing higher resolution data products to be recorded more frequently. Periods of Burst Mode (BM) exist where the entire spacecraft is given greater telemetry rates than in Normal Mode (NM). During BM periods greater resolution 3D distributions are usually obtained every spin from PEACE.

The operation of the HEEA and LEEA detectors varies over the orbit and throughout the year as different plasma regimes are sampled. The operational energy ranges of both sensors are altered to maximise the collection rate of useful data. A

command to a sensor states the upper and lower energy level to be operated at and also how the energy range shall be swept. An example would be the command '88m28' setting the sensor to operate from energy level 88 to 28 (26.4 keV to 34 eV), using the Medium Angular Resolution (MAR) sweep mode where data is collected at 30 alternate energy levels 32 times in the 4 second spin.

The onboard moment calculations, pitch-angle distributions (PAD) and specific information from other experiments are routinely obtained in both Normal and Burst Mode telemetry rates. Several sets of onboard moments are calculated from several electron energy ranges obtained by having two overlapping instrument energy ranges from combining HEEA and LEEA. This is illustrated in Figure 2-4.

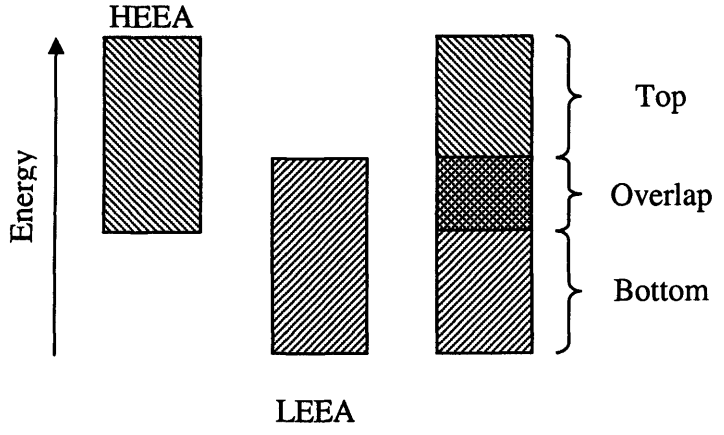

Figure 2-4 The 'Top', 'Overlap' and 'Bottom' energy regions
The two separate sensors can be combined to produce several different data sets. This is most frequently found in the onboard moments calculations. There exists an overlap in the energy ranges that HEEA and LEEA operate at and with this two associated regions above and below this overlap.

The PAD data is a 2D subset of the full 3D distribution extracted from the collected data by knowledge of the previous spins' magnetic field direction, provided by the FGM experiment. The selected data is that from the azimuthal bins containing the magnetic field vector which occur twice per spacecraft spin. Figure 2-5 illustrates which

data is collected for the PAD distribution from the two intervals where the magnetic field is in the plane of the sensor aperture (separated in time by half a spin). The data taken from the polar sector 9 containing the magnetic field through to the polar bin numbered 11 in this figure forms part of the PAD distribution. The other part of the distribution is obtained from data bins 2 to 11 from the second half of the spin. In total 13 data bins are collected for the PAD distribution. The PAD data product is re-ordered on the ground to produce a workable pitch angle distribution (SpinPAD) that has the data ordered from field-aligned, through to perpendicular and anti-field-aligned polar bins.

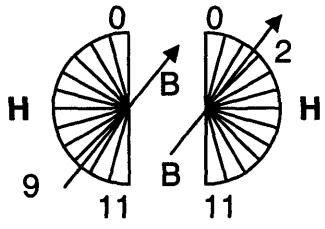

Figure 2-5 The construction of PAD data
Taking the PAD data from the HEEA sensor (for example) for the two azimuthal bins containing an estimate of the location of the magnetic field a full distribution can be created ranging from field-aligned, through to perpendicular pitch-angled electrons, to oppositely directed field-aligned electrons. In this example polar bins number 2 to 11 from one half of the spin and bins 9 to 11 will be used to create SpinPAD.

With high resolution magnetic field data it is possible to recalculate this pitch-angle plot on the ground to check the validity of using the previous spins magnetic field direction. This clearly indicates which pitch angles were not detected due to movement of the magnetic field. An example of the re-binning process is shown in Figure 2-6.

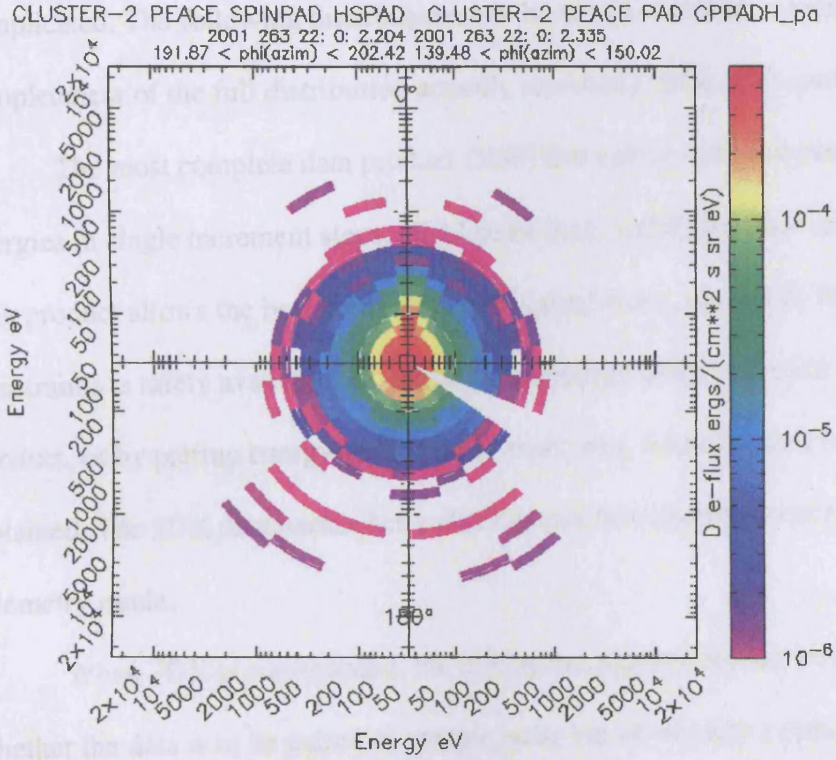

Figure 2-6 SpinPAD and re-ordered SpinPAD
When the high resolution magnetic field data is incorporated with the original PAD data it is possible to calculate the pitch angle for each individual component and then construct an improved SpinPAD distribution. On the left is the original SpinPAD distribution with the magnetic field direction up the plane, energy radially outwards and shown with a differential energy flux scale. On the right, the re-ordered PAD data shows clearly that one set of pitch-angles was not actually collected by the instrument.

Usually the Low Energy Reduced (LER) data product is also transmitted during Normal Mode. This data product provides full coverage of the low energy linear part of the energy range, but at a low angular resolution. It facilitates determination of the spacecraft potential when it is below 10 V.

When there is more telemetry for fuller distributions the commanding is more complicated. The following distributions can be obtained (listed in increasing completeness of the full distribution actually recorded): 3DR, 3DX and 3DF.

The most complete data product (3DF) that can be obtained consists of all the energies in single increment steps, all 12 polar bins, and all possible azimuthal bins. This data product allows the best ground moment calculations, but due to the telemetry constraints is rarely available. By reducing the energy range collected for a 3D data product, or by pairing energy bins or polar angle bins, a smaller data product can be obtained. The 3DX data packet has a size that can be transmitted once per spin in burst telemetry mode.

When 3DX is commanded, the instrument requires further information, namely whether the data is to be paired in energy, polar bin or whether a reduced energy 'window' is to be used. Commanding varies for each spacecraft as PEACE cannibalises telemetry from defunct instruments, and therefore allows fuller distributions to be collected on certain spacecraft more frequently.

Suitable for frequent transmission in normal telemetry modes, 3DR provides a 3D distribution but with reduced energy resolution only collecting 15 energy levels over 6 polar zones and 16 azimuthal angular bins.

2.2.2 Micro-Channel Plate (MCP) Degradation

For each incoming electron into the analyser there is a certain charge extraction from the MCP to allow a count to be registered by the detecting anode. As the number of valence electrons within the walls of the MCPs is depleted, the potential difference over the MCP has to be increased in order to maintain the correct gain levels. Instrument life time is thus limited as the extraction voltage cannot be incremented indefinitely. Once the highest level is achieved the charge extraction will diminish until there is no longer enough charge to register a count.

To prolong the life of the detector a few simple procedures are implemented by the operations team. Where possible the most appropriate energy range of the detectors is chosen to reduce effect of photoelectrons on the MCP. The gain used for the charge extraction is incremented slowly and monitored to allow for more future changes to occur.

In addition, penetrating radiation in particularly energetic regions can be dangerous to the instrument. An extreme situation, where the spacecraft enters perigee and passes through the Earth's radiation belts, results in the risk of damage to the instrument being so severe that the instrument is not operated. The instrument is also turned off during some magnetosheath passages due to high count rates.

2.2.3 ASPOC Operations and PEACE

The spacecraft potential plays an important part in the design, operation and subsequent analysis of the data of a particle instrument, particular electron instruments. Ignoring the natural plasma environment of space, a spacecraft will charge and discharge

with its exposure to sunlight through the photoelectric effect: charging when in sunlight and discharging when in eclipse by another body. Photoelectrons themselves can be energetic enough to release secondary electrons by collision with the spacecraft. Naturally, the local plasma population support currents that can affect the charging of the spacecraft. When no net current flows at the spacecraft, the spacecraft potential has been reached. The ability of the local plasma to react to the charging of the spacecraft by photo- and secondary- electron emission by shielding the spacecraft results in a lowering of the spacecraft potential. As the density of the plasma environment changes drastically throughout the magnetosphere so does the spacecraft potential with highest values associated with the rarest plasma populations such as in the lobes.

Active ion emitters can be used to reduce the spacecraft potential. By emitting a beam of ions, at a known energy and species to prevent erroneous local ion population measurements, at a rate proportional to the charging due to electron escape, the spacecraft potential can be controlled. The Cluster spacecraft have an active spacecraft potential controller onboard and this is discussed in details in Section 2.3.1.

A local plasma electron will be accelerated as it approaches a positively charged spacecraft. This acceleration, relatively more significant at lower energies, will result in an electron detector measuring a modified electron velocity distribution. As well as energization of particles, the spacecraft potential also changes the trajectory of the particle: again affecting lower energy particles to a larger extent. This can result in a modification to the effective viewing angle of the instrument and may result in an incorrect determination of moments of the plasma distribution. In effect, the plasma

detector's geometric factor is also a function of spacecraft potential and therefore solar UV incidence and plasma density [Scime, 1998].

The PEACE instrument was designed to reduce the electron count rate from electrons released by collision near the aperture and by photoelectron emission when each detector is aligned to the sun by the inclusion of a baffle and a diffuse material coating. To prevent differential charging the exterior of the spacecraft was coated in a conductive material [Credland et al., 1997] with a few unavoidable exceptions.

The design of the onboard software of PEACE also allowed for spacecraft photoelectrons. The software calculates electron moments onboard to avoid the need for a full 3D distribution to be transmitted every spacecraft spin, which is impossible in normal mode telemetry. Several energy ranges are used for the onboard moment calculation and these are determined by the operational mode of each of the detectors. However, the accurate onboard moment calculation over the full energy range of the PEACE instrument is often impossible due to photoelectron contamination. It was expected that the active spacecraft control experiment (ASPOC, see Section 2.3.1) would reduce the spacecraft potential to 10 V or less, providing a lower cut-off for the moment calculation at 10 eV. Due to the failure of ASPOC on spacecraft 1 and a reduced operation on the other spacecraft, the spacecraft potential often rises above 10 V. Thus the suitability of the onboard moments needs to be assessed for each case study. When 3D data is available ground moments may be calculated and correction factors applied appropriately.

2.2.4 Data Quality

As well as photoelectron contamination and spacecraft potential effects there are several instrument related phenomena that can cause questions regarding the quality of

the data. These include: incorrect determination of the geometric factor of the instrument which is related to the dimensions of the aperture; incorrect measurement of the detector efficiencies effecting data calibration; and, exposure dependent degradation of the MCPs.

There is a common problem associated with this type of instrument where detector sensors aligned with the spin axis are associated with an offset as there is no spin averaging to nullify the offset. This manifests itself as a V_Z offset in the PEACE dataset. If the calibrations of the two spin-aligned detector sectors are perfect then the offset is corrected for. However, one data artefact which is of significant importance to the work presented in Chapter 4 of this thesis is associated with differing MCP and anode efficiency across the detector array. There is potentially energy dependence to this as well making the calibration and data correction very complex. As a result, a V_Z offset remains in the data. This offset varies over the dataset and may have energy and time dependencies and is the subject of on-going research and calibration. A simple method of handling this offset is presented in Chapter 4.

2.3 Description of Selected Cluster Instruments

Data from several other instruments onboard Cluster are used in the research presented in this thesis. A short summary of the instruments used to obtain this data is included here for reference. Other instruments also affect the operation and the observations of PEACE and are mentioned here.

2.3.1 ASPOC – Active Spacecraft POtential Control

Due to the high plasma densities of the plasmasphere- and ionosphere, spacecraft charge to negative potentials of a few volts. This occurs because of the lower mass and

consequently the higher thermal velocities of the electrons that make up the plasma when compared to the ions. When located in the near-Earth plasma sheet, auroral zones and the ring current, spacecraft exhibit moderate negative charges as the plasma electron temperature is high during generally disturbed times. Where the natural plasma electron temperature is less than a few keV, current balance between the spacecraft and the plasma is between photoelectrons and the plasma electrons, and the spacecraft potential is a few volts positive. When located in sparse plasma regions such as the magnetotail lobes (<0.1 cm^{-3}) potentials can be of the order 100 V.

Due to the Cluster spacecraft sampling many different plasma regions during their mission, the spacecraft will exhibit varying potentials. In addition, lunar and terrestrial eclipses will drastically affect the spacecraft potential by reducing the amount of photoelectron emission.

The important consequence for a science mission measuring space plasmas is the effect the spacecraft charging will have on the ambient plasma environment. By installing an active spacecraft potential controller onboard Cluster both the PEACE and CIS instruments gain from a reduced spacecraft potential, as do EFW and EDI. Many studies have shown that spacecraft potentials can hide many ion and electron populations from observations [e.g. Olsen, 1982]. The reduction of the spacecraft sheath generated electric field will reduce the error on the ambient electric field measurements by EFW and on the small scale variations measured by EDI.

The principle of ASPOC is to emit charge from the spacecraft that is sufficient to balance the excess of charge accumulating on the spacecraft from the local plasma

environment. By design, the experiment only emits positive ions and therefore cannot control the spacecraft potential when the potential is negative.

The ASPOC unit on each of the Cluster spacecraft consists of 8 emitters each constructed of a needle held at a high potential to an extracting anode, located in a liquid metal ion source of indium as the charge material. Increasing the potential between the needle and the extracting anode results in an ion current evaporating off the needle. EFW or PEACE can be used to provide information to ASPOC of the spacecraft potential in a feedback mode, although EFW data is preferred due to the higher time resolution and the simpler technique associated with fewer errors. A fixed emission current mode exists as a backup and can be set at a level appropriate for the ambient plasma.

2.3.2 CIS – Cluster Ion Spectrometry Experiment

Due to the variety of ion populations to be observed by the Cluster spacecraft it was necessary to incorporate two different ion sensors on each of the spacecraft forming the Cluster Ion Spectrometer experiment (CIS) [Remé et al., 1997]. The Hot Ion Analyser (HIA) detecting ions of energy 5 eV to 32 keV and the Ion COmposition and DIstribution Function analyser (CODIF) measure ions of 1 to 32 atomic mass units with energies of 0.02 to 40 keV. The two detectors are located opposite each other on the spacecraft.

HIA is a Top-Hat quadrispherical electrostatic plate analyser split into two 180° field-of-views to allow for differing sensitivities at the detecting anode. A chevron MCP is used to multiply the charge as in the PEACE instrument.

CODIF is a mass-resolving spectrometer aimed at resolving H^+, He^+, He^{++} and O^+. An extra device is included on CODIF to pre-accelerate low energy ions so that they

can be detected should science require it. The instrument consists of a toroidal electrostatic plate analyser with a time-of-flight chamber allowing the mass resolution.

2.3.3 EFW – Electric Field and Waves Experiment

The Electric Field and Wave experiment (EFW) [Gustafsson et al, 1997] measures the electric field fluctuations with a sample rate of up to 36000 samples per second. EFW is able to measure the quasi-static field of up to 700 mVm^{-1} and monitor variations of the electric and magnetic fields. Combined with the ability to remote sense the plasma density by monitoring the spacecraft potential, EFW data is useful as a comparison to PEACE data.

The electric field is measured within the spin plane providing E_{Sun} and E_{Dusk} vectors. The electric field parallel to the spin axis, E_Z, can be computed under the assumption that $E \cdot B$ is zero. This frame is then convertible to GSE or GSM coordinates as appropriate. The assumption that $E \cdot B = 0$ may not be valid. Data provided by the Principle Investigating team has had all data removed where the fitting assumption for E_Z may not be strongly held.

2.3.4 FGM – Flux Gate Magnetometer

The Flux Gate Magnetometer (FGM) [Balogh et al., 1997] measures the magnetic field. Consisting of two tri-axial fluxgate magnetometers per spacecraft, FGM is able to measure the magnetic field in the large variety of magnetic field conditions in the magnetosphere and can switch between modes automatically or by command. These modes are summarised in Table 2-3. The instrument can telemeter either ~16 or ~67 vectors per second depending on the telemetry mode used.

Range (nT)	Digital Resolution
-64 to +63.992	7.813×10^{-3}
-265 to +255.97	3.125×10^{-2}
-1024 to +1023.9	0.125
-4096 to +4095.5	0.5
-65536 to +65528	8

Table 2-3 FGM operational modes

3 Thinning and Expansion of the Substorm Plasma Sheet: Cluster PEACE Timing Analysis

3.1 Introduction

Geomagnetic activity is driven, at least in part, by variations in speed, density and pressure of the solar wind and the magnitude and direction of the interplanetary magnetic field (IMF). In particular, the magnetospheric substorm [Akasofu, 1968] links the disturbances in the magnetosphere and ionosphere that result from enhanced coupling with the solar wind and are observed as fluctuations of the terrestrial magnetic field measured at high-latitudes on the ground [Akasofu and Chapman, 1961] and are associated with auroral signatures [Akasofu, 1964]. It was found that during substorm activity the magnetotail plasma sheet exhibits expansions and contractions associated with the addition and removal of magnetic flux to and from the magnetotail [Bame et al., 1967].

Two leading explanations for geomagnetic substorm activity were proposed in 1961. Firstly, Dungey [1961] suggested that magnetic reconnection occurring at the magnetopause subsolar point allows the interplanetary magnetic field to directly connect to the Earth's magnetic field. The 'open' flux tubes formed by this process, with only one end of the flux tube connected to the Earth, are transported over the poles and into the magnetotail. Subsequent reconnection in the tail, at a distant neutral line, creates closed flux tubes, which return to the near-Earth region and ultimately back to the dayside. This process thus couples the momentum of the solar wind flow into the magnetosphere and drives the magnetospheric convection system. The second suggested cause of activity depends on a viscous interaction between the solar wind and the magnetosphere [Axford

and Hines, 1961]. These authors suggested such processes drag closed magnetic field lines just inside the flank magnetopause in the antisunward direction and that a return flow is set up along the tail centre, thus also setting up a magnetospheric convection cycle. Although both processes are now thought to play a role in driving the dynamics of the magnetosphere, the magnetic reconnection processes provide enhanced coupling under southward IMF conditions and are thus more relevant to substorm activity, which is known to occur preferentially under these conditions [Cowley, 1982].

Auroral substorms were shown to develop in the following order: the growth phase; the onset of the substorm; expansion poleward and in local time; and finally, recovery to the pre-substorm state [Akasofu, 1964]. Magnetosphere-ionosphere changes occur corresponding to each auroral substorm phase, particularly in the magnetotail [e.g. McPherron, 1970; Aubry and McPherron, 1971; Russell and McPherron, 1973].

The growth phase of a substorm begins when the IMF turns southward forming the dayside magnetopause neutral line and enhanced magnetic reconnection occurs leading to the rapid erosion of dayside magnetic flux [Maezawa, 1975; Baker et al., 1984]. Reconnected magnetic flux is transported over the poles and stored in the magnetotail. The addition of large amounts of open flux to the magnetotail is associated with enhanced ionospheric plasma convection and an increase in the size of the polar cap [Akasofu, 1968]. The flux added to the magnetotail during the growth phase causes an increase in the tail radius and an increase in the magnetopause flaring angle [Coroniti and Kennel, 1972; Fairfield, 1984]. This, in turn, allows the solar wind to exert a greater pressure on the magnetopause. To maintain overall pressure balance, the magnetic pressure of the lobes increases [e.g. Fairfield and Ness, 1970] and the plasma sheet tends

to thin with an increase in plasma pressure [e.g. Axford et al., 1965]. This process is dynamic and continually adjusts to maintain pressure balance. This compression of the plasma sheet during the growth phase of a substorm was first observed by the VELA 2A and 2B satellites [Hones et al., 1967]. Subsequently, observational evidence of thinning of the central plasma sheet associated with a southward turning of the IMF was reported by Hones et al. [1971a] and Aubry and McPherron [1971]. Thinning in the dawn and dusk flanks of the tail is generally not as pronounced as it is in the midnight sector suggesting that plasma sheet plasma and magnetic flux may be forced towards the flanks in the process [Hones et al., 1971a]. The cross-tail current density intensifies prior to substorm onset and supports the stretched magnetic field lines of the magnetotail [McPherron et al., 1973]. Even at geosynchronous orbit the magnetic field becomes very stressed and tail-like [e.g. Fairfield and Ness, 1970; Nagai, 1982; Kaufmann, 1987; and Lopez et al., 1998]. The addition of this open flux into the magnetotail increases the energy content of the tail.

The growth phase ends with the onset of a substorm, representing a rapid release of the stored energy and characterized by the sudden brightening of the most equatorward auroral arc [Akasofu, 1964; Rostoker et al., 1980]. The auroral brightening is associated with the diversion of the growth phase cross-tail current along magnetic field lines and into the ionosphere, forming the substorm current wedge [Bonnevier and Rostoker, 1970, McPherron et al., 1973; Rostoker, 1974]. The associated dipolarization of the magnetic field that occurs at substorm onset has been well documented [e.g. Cummings et al., 1968, Kokubun and McPherron, 1981].

The two most developed models of substorm activity at and after auroral onset are suggesting onset occurs either by upon the formation of a near-Earth neutral line (NENL) [see review by Baker et al., 1996] or by current disruption (CD) nearer Earth [see review by Lui et al., 1996]. However, other models exist and are summarized by Rostoker et al. [1996]: magnetosphere-ionosphere coupling [Kan et al., 1988] stresses the importance of the ionosphere conductivity to substorm development; thermal catastrophe in which the high latitude plasma sheet is heated by waves that are initiated by the solar wind that propagate through the lobes and are absorbed by the plasma sheet [Goertz and Smith, 1989]; ballooning instabilities in the plasma sheet [Roux et al., 1991]; and, the reduction of the convection electric field [Lyons, 1995].

In the NENL model, the late growth and early expansion phases are characterised by the reconnection of magnetic field lines at an X-line newly formed in the thinned plasma sheet [Hones, 1973; McPherron et al., 1973; Russell and McPherron, 1973]. Closed plasma sheet field lines are reconnected first, followed by the open field lines in the lobes. Earthward of the new neutral line the newly closed field lines contract Earthward due to their magnetic tension. These returning field lines become more dipolar as they propagate towards the Earth. This newly reconnected flux returns to the dayside and thus replaces the magnetic flux lost through reconnection at the dayside magnetopause during the growth phase. Tailward of the new neutral line, reconnected closed plasma sheet field lines are pinched off and form a plasmoid: a closed loop or tightly wound helical structure around an O-line in which the magnetic field is neither connected to the Earth nor the solar wind [Hones et al., 1984]. As the last closed field line is reconnected, the NENL is momentarily connected to the DNL. Subsequent

reconnection of open lobe flux leads to sharply bent field lines draped around the plasmoid and connected to the solar wind far downstream. A combination of magnetic forces and a particle pressure gradient in the near tail acts to expel the plasmoid tailward into the downstream solar wind, removing stored magnetic field and plasma energy from the system [e.g. Schindler, 1974]. Many observations of plasmoids moving downtail have been reported [e.g. Slavin et al., 2002; Ieda et al., 2001; Moldwin and Hughes, 1994].

Moreover, observations of bursty bulk flows and associated magnetic dipolarizations [e.g. Angelopoulos et al., 1996; Baumjohann et al., 1991, 1999; Machida et al., 1999; Nagai and Machida, 1998] have also been interpreted as evidence for the near-Earth neutral line. The location of the NENL has been placed to be between 21 and 26 R_E [e.g. Baumjohann et al., 1999].

Plasma sheet observations made by the VELA spacecraft in an 18 R_E circular orbit [Hones et al., 1984], provided further insight into the plasma sheet during a substorm. Thinning of the near-Earth plasma sheet was seen at many points on the VELA orbit. Rapid expansion of the plasma sheet was seen Earthward of 10-15 R_E with the tailward plasma sheet remaining thin. This is consistent with a neutral line forming between 10 and 15 R_E extending substantially in the cross tail direction. The newly reconnected field lines collapsing Earthward explain the expansion of the plasma sheet Earthward. The section of the plasma sheet tailward of the neutral line is severed and removed, hence the prolonged thinness of the plasma sheet near VELA apogee. Analysis of 461 plasma sheet dropouts observed by ISEE 1 and 2 [Dandouras et al., 1986] indicates that drop outs occur uniformly distributed between 12 and 23 R_E in geocentric distance and also across the entire night side plasma sheet deviating from this towards the

flanks and is consistent with the NENL model where the neutral line is formed at different distances, sometimes within X = 12 R_E near-Earth and at other times beyond 23 R_E, but with limited cross tail extent. Substorms with no associated plasma sheet flux drop out events were noted within 11 R_E.

The speed of plasma sheet expansion, i.e. the rate at which the boundary between the plasma sheet and lobe moves, measured by VELA 4A, VELA 5A and OGO 5, was found to be approximately 40 km s^{-1} up to 6 R_E away from the neutral sheet [Pytte et al., 1978]. These authors also suggest that expansions associated with quasi-isolated substorms proceed rapidly, and others associated with multiple onsets proceed more slowly. The possibility of large-scale motion of the plasma sheet being incorrectly recorded as an expansion in such work was noted by Dandouras et al. [1986].

A further AMPTE/IRM study, Baumjohann et al. [1992], analysed 39 major substorm onsets (as defined by the AE index) during substorms. As AMPTE/IRM had an apogee of 19 R_E the study region was relatively near-Earth plasma sheet. Plasma sheet thinning was observed to begin 30-45 minutes before substorm onset in the region 10-19 R_E, the plasma sheet began to expand after onset, regaining pre-substorm thickness about 45 minutes later. This expansion coincides with the start of the recovery phase as seen in the AE index. This study placed the NENL beyond 20 R_E consistent with Dandouras et al. [1986]. Nagai and Machida [1998] used data taken by the Geotail spacecraft during 138 well-defined substorms to obtain limits on the location of the magnetic reconnection region. Their study of the location of Earthward and tailward flows placed an inner limit of the reconnection region position at 22 R_E down the X_{GSM} axis, and an outer limit at 30

R_E down tail and within the pre-midnight region. Analysis of Geotail data by Miyashita et al. [2000] placed the NENL formation region at (X, Y) ~ (-19, 6)R_E.

By performing timing analysis on data from PEACE taken from the first two tail seasons, July through to November of 2001 and 2002, we determine the directions and normal component velocities of the plasma sheet – lobe boundary as it expands or contracts over the spacecraft quartet during the course of substorms. This allows us to determine any bias of the plasma sheet thinning and/or expansion direction vector and to consider whether these provide supporting evidence for either the NENL or CD models of substorms. This work is also published by Dewhurst et al. [2004].

In Section 3.2 the timing analysis method used is explained. A case study of a plasma sheet thinning and expansion is discussed in Section 3.3.1 and it is followed by an example of multiple thinning-expansion events occurring during a complex substorm. Survey statistics are provided in Section 3.3.3. Observations of pairs of thinnings and expansions are detailed in Section 3.3.4. Finally, these results are discussed and the complex nature of the plasma sheet is illustrated.

3.2 Methodology

There are several methods for the analysis of boundaries between different fields and plasma populations using multi-spacecraft data [Dunlop and Woodward, 1999; Harvey, 2000; Haaland, 2003]. Dunlop and Woodward [1999] make use of four-point magnetic field minimum variance analysis vectors to obtain a description of non-planar, accelerating boundaries. The local normal vector of the boundary can be calculated at each point and the variation of this normal through space and with time can be assessed. However, the signature of the spacecraft transition between the lobe and the plasma sheet,

which are the prime interest in this study, are generally observed as a change of plasma properties rather than magnetic field direction. Therefore the Dunlop and Woodward [1999] method is not adopted in this study.

Boundary analysis which considers the properties of the transition boundary layer between two plasma regions in detail is described by Haaland [2003]. This method assumes the interface maintains a constant thickness during passage across the four spacecraft, and thus variations in its profile can be de-convolved into accelerations of the boundary.

As there is a major contrast in density of the plasma sheet and the lobes and given that the PEACE data set used in this study has a temporal resolution of 4 seconds, suggesting a timing error of ±2 seconds compared to a typical time lag of ~10 time stamps (40 seconds), we believe that a simpler method can be used with a basic correlation technique to provide required boundary parameters. Assuming that the boundary between the plasma sheet and the lobe can be represented as a plane moving at constant velocity, its characteristic unit normal $\hat{n}$ and velocity V along that normal can be calculated [Harvey 2000]. An unambiguous boundary is represented by a repeatable and observable change in a given plasma parameter observed to pass over each of the four spacecraft at a time t_α with no possibility of inconsistency as illustrated in Figure 3-1. In this figure the Cluster spacecraft are represented by C1, C2, C3 and C4 and are shown in a typical orientation for the mid-season tail apogee pass with respect to the GSM co-ordinate system. For each spacecraft, a generic plasma parameter trace is shown at the bottom of the figure and corresponds to the changes observed as a boundary between two plasma population passes over the spacecraft in the direction indicated by the progression

of time, t. During the time $t_\alpha - t_3$, the time lag of the event seen at spacecraft α to that seen at the reference spacecraft (C3), the plane moves along the boundary normal a distance equal to the projection of the separation distance of the two spacecraft on to the plane normal:

$$(\vec{r}_\alpha - \vec{r}_3)\cdot\hat{n} = V(t_\alpha - t_3) \qquad (3.1)$$

where $\vec{r}$ is the position vector of the spacecraft from some origin. When all spacecraft are considered, the above is generalized to:

$$D\frac{\hat{n}}{V} = T \qquad (3.2)$$

where the matrix D and linear array T are:

$$D = (\vec{r}_1 - \vec{r}_3, \vec{r}_2 - \vec{r}_3, \vec{r}_4 - \vec{r}_3) \text{ and } T = \begin{pmatrix} t_1 - t_3 \\ t_2 - t_3 \\ t_4 - t_3 \end{pmatrix}.$$

If the spacecraft are not co-planar then D^{-1}, the inverse of D, exists and the unit normal and the boundary velocity can be calculated:

$$\frac{\hat{n}}{V} = D^{-1}T \qquad (3.3)$$

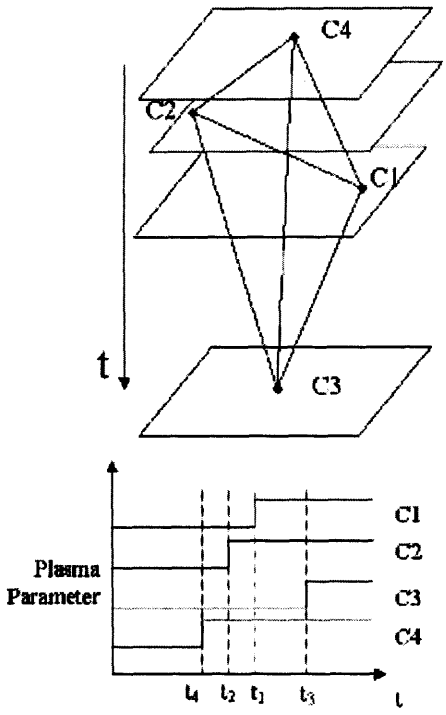

Figure 3-1 Boundary detection by Cluster
A boundary between two distinct plasma regions passes over the Cluster quartet, marked by C1 to C4, and can be observed to cross spacecraft α at a time t_α. The plasma boundary is marked by a plane moving in the negative GSM-Z direction with time, t. As the boundary passes each spacecraft the different plasma population are seen as a change in the parameter time-series; shown here for all four spacecraft. The boundary is assumed to be planar on the scale of the tetrahedron.

In order to practically implement this method, we need to identify a plasma parameter that shows a gradient at the boundary of interest. For the lobe – plasma sheet interface there is usually a significant change in the plasma density. However, even the HEEA sensor, which for tail pass operations is usually set to detect electrons in the range 34 eV to ~ 26.5 keV, may at times be contaminated with photoelectrons from the spacecraft. This prevents the routine use of the onboard moments for our study. Hence we construct, on the ground, a pseudo-density moment using the PAD data that are routinely returned from the PEACE instrument at four-second resolution for the interval surrounding the spacecraft traversal of a lobe – plasma sheet interface. We first identified

for each period of interest the highest energy level bin that was contaminated with photoelectrons at some point within the period. We then perform a pseudo-density moment calculation from the pitch-angle distribution, assuming gyrotropy of the original distribution, and integrating only across those energy bins above this contaminated level. We thus form a rough proxy to the electron density in that energy range. This parameter can be used to make a clear determination of the time of the transition between plasma sheet and the lobe by each spacecraft.

We apply a cross-correlation technique to the resulting four pseudo-density data sets in order to determine the relative time lags of the boundary crossing at each spacecraft. Given knowledge of the relative position of each spacecraft, Equation 3.3 can then be used to calculate the normal and speed for an assumed planar boundary. As the pitch-angle distributions used in this method are obtained once per spacecraft spin, approximately 4 seconds, there is up to ±2 second error on the timing of the crossing. This is the largest source of error on the calculation of the boundary characteristics as the error on spacecraft location is small compared to the spatial scales involved.

Note that the method here assumes that the plasma sheet boundary is locally planar on the scale of the spacecraft separations. Thus only the normal velocity, which is provided by this method, has any meaningful information. More global dynamics, such as large scale transverse waves, cannot be inferred directly from any one velocity determination. We attempt in this chapter to illuminate such dynamics by examining statistically the average motion of the edge of the plasma sheet as a function of position within the tail.

3.3 Results

To illustrate the various observations of plasma sheet thinning and expansion by the Cluster quartet, two case studies are presented. The first shows one isolated thinning and expansion cycle. The second example shows two cycles of plasma sheet thinning and expansion and occurs during a comparatively more complicated substorm. Following the case studies are various statistics from a survey of two years of magnetotail data.

3.3.1 Case Study – Single Thinning and Expansion

An example of thinning and expansion of the plasma sheet over the Cluster quartet located at ~ $(-17.4, -5.5, -2.6)_{GSM}$ is now presented. Ancillary data that indicates the occurrence of a substorm on 13th August 2001 is provided first as a context for the Cluster data.

The AE trace shown in Figure 3-2 shows that prior to ~ 01:30 UT the system was in a recovery phase. A slow build up of the AE index follows and is then punctuated by a rise of ~200 nT at approximately 02:50 UT lasting ~8 minutes. This onset is followed by several others associated with much larger AE index values from ~03:30 UT onwards.

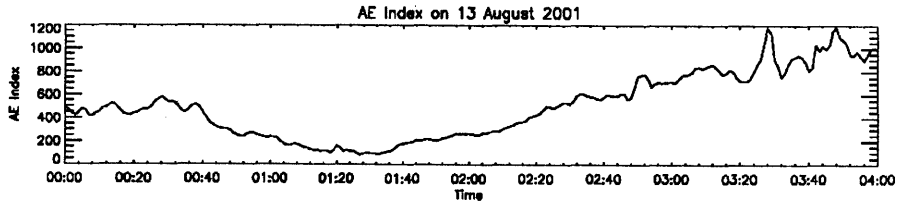

Figure 3-2 The AE index for 13th August 2001
The AE index (nT) for the period 00:00 UT to 04:00 UT on 13th August 2001. Of note is the intensification around 02:50 UT of ~200 nT which is associated with dynamics in the plasma sheet.

A possible substorm onset time is given as 02:40 UT as defined by the presence of at least 2 minutes of continuous Pi2 activity after at least a 10 minute period of inactivity in the SAMNET magnetometer chain magnetic field H-component data (not shown). The onset of a negative bay in Canopus ground magnetometer data occurs at ~ 02:50 UT. An electron injection is seen on mid-energy channels of 1994-084's low energy electron detector (LoE) at ~02:35 UT and at LANL-01A at ~ 03:00 UT. In Figure 3-3 a frequency (kHz) against time plot from the Wind spacecraft's Waves instrument (RAD1 detector with the intensity (dB) on the colour scale) shows a Type III radio burst, with frequencies higher than 100 kHz, with auroral kilometric radiation superimposed from ~ 02:55 UT indicating substorm activity. Geotail was not located in the magnetotail during this interval.

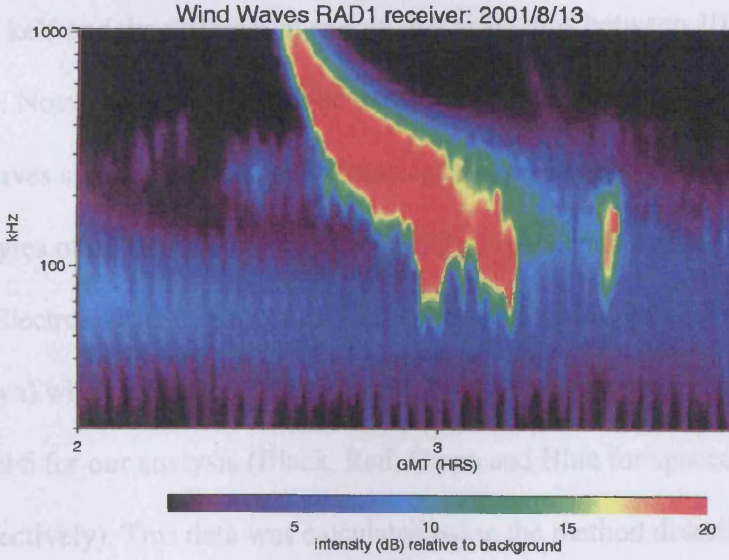

Figure 3-3 Wind WAVES data for 02:00 – 04:00 UT 13th August 2001
A frequency spectrogram of the RAD1 receiver on the Waves experiment onboard the Wind spacecraft for the period 02:00 UT to 04:00 UT on 13th August 2001. Onset of auroral kilometric radiation occurs at ~ 02:55 UT with an enhancement of the intensity of the wave activity at ~ 60 to 100 kHz.

An example of plasma sheet thinning and expansion observed by Cluster located at ~ $(-17.4, -5.5, -2.6)_{GSM}$ R_E is presented. The spacecraft configuration, showing the separation of the spacecraft from the reference position, is shown in Figure 3-4 with C1 to 4 marked in Black, Red, Green and Blue respectively. It should be noted that C3 is the furthest south of the four spacecraft followed by C1, which is displaced in X from the other spacecraft, and then C4 and C2. This order should be thus similar to that of the detection by each spacecraft of a boundary that lay in the GSM-XY plane and travelled purely in the GSM-Z direction during the thinning and expansion phases. Data from the PEACE instrument with ancillary magnetic field data is shown in Figure 3-5. Panels 1 to 4 show omni-directional energy spectrograms in differential energy flux of the electrons detected by the HEEA detector for each spacecraft, C1 down to C4, for a 50 minute interval 02:10 to 03:00 UT. Electron energy is split into 30 bins between 34 eV and ~ 26.5 keV and the differential energy flux scale runs between 10^{-6} and 10^{-4} ergs $(cm^2\ s\ str\ ev)^{-1}$. Note that in the south lobe (between ~02:23 UT and ~02:50 UT) each spacecraft observes significant fluxes of photoelectrons within the HEEA energy range which reach energies of up to ~100 eV (at ~02:46 UT on spacecraft 2 associated with the operation of the Electron Drift Instrument). These photoelectrons dominate the onboard moments (not shown) when the spacecraft are in the lobe, and thus we use the pseudo-moment shown in panel 5 for our analysis (Black, Red, Green and Blue for spacecraft number 1, 2, 3 and 4 respectively). This data was calculated using the method described above taking all energy bins above 135 eV on all spacecraft to ensure the comparison of similar data products. The magnetic field B_x and B_z components in GSM co-ordinates are then shown

in panels 6 and 7. Data from each of the four spacecraft is shown, with C1 data represented by the black trace, C2 by red, C3 by green and C4 by blue.

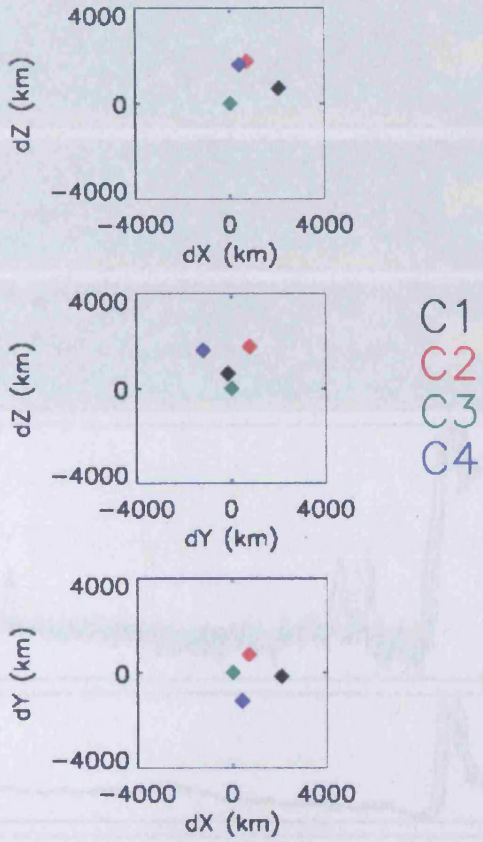

Figure 3-4 Cluster configuration on 13th August 2001
The separations of each of the Cluster spacecraft (C1, C2 and C4) from reference spacecraft (C3) position are shown in the GSM-XY, -XZ and –YZ planes. C1, C2, C3 and C4 are marked in black, red, green and blue respectively. The order of the spacecraft in the GSM-Z direction is the expected order in which the plasma sheet – lobe boundary should traverse the spacecraft quartet if the motion is purely in the GSM-Z direction.

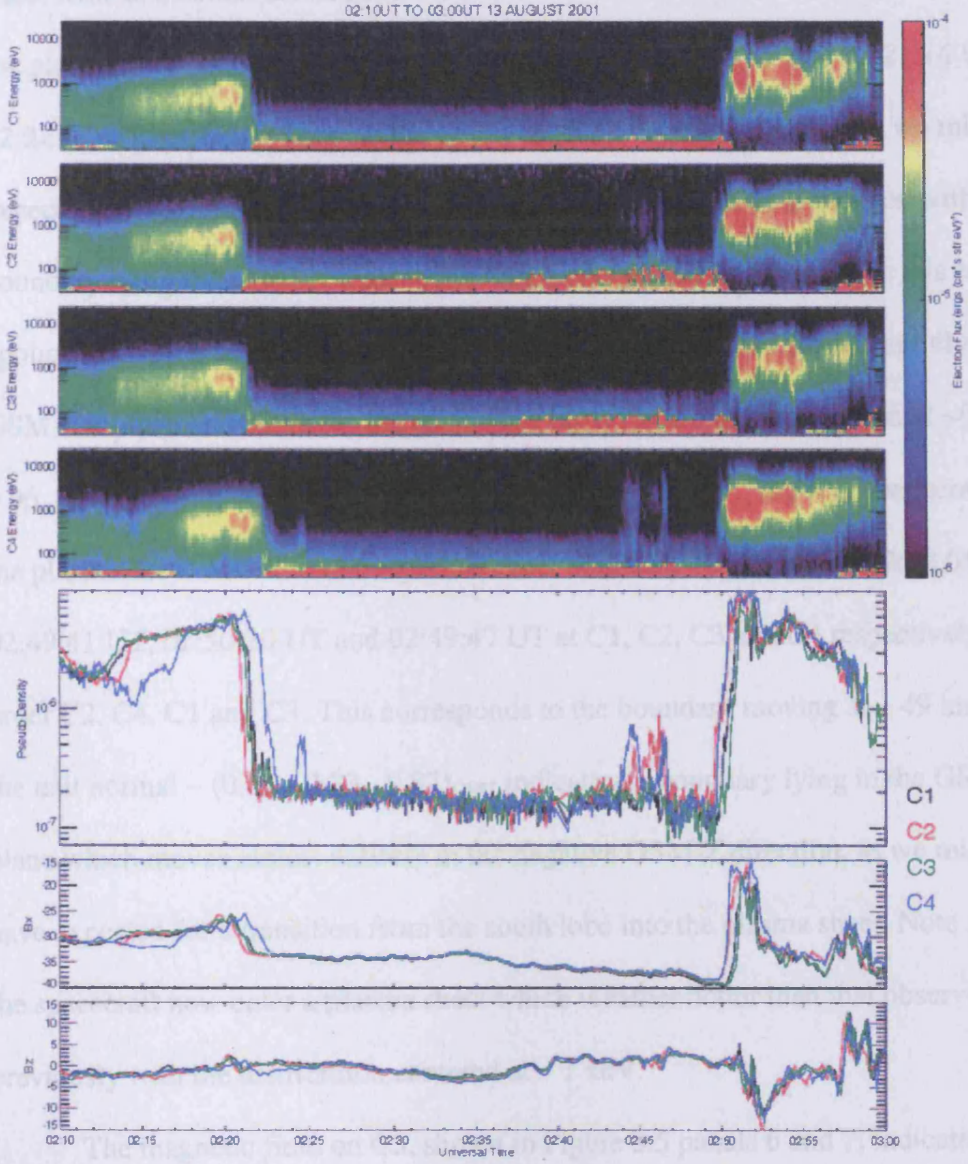

Figure 3-5 PEACE and FGM data for 13th August 2001
Electron energy - differential flux spectrogram for C1 to C4 in the first four panels showing data summed over all pitch angles for the interval 02:10 UT to 03:00 UT on 13th August 2001. Plasma sheet plasma is punctuated by a period in the lobe. A density proxy (summed of all electrons above 135 eV) is plotted in panel 5 using Black, Red, Green and Blue for C1 to C4 respectively. The B_X and B_Z components of the magnetic field measured at the spacecraft are shown in panels 6 and 7. A clear magnetic field rearrangement is seen at the space around the time of the plasma sheet passing over the spacecraft quartet.

At the beginning of the period shown, each spacecraft is in a low-energy plasma sheet with an electron distribution centred on ~ 250 eV. C1, C2, C3 and C4 moved out of the plasma sheet into the south lobe at ~ 02:21:23 UT, 02:20:53 UT, 02:21:14 UT and 02:22:03 UT respectively i.e. in the order, C2, C3, C1 and C4. Although we might have expected a transition from the plasma sheet to the south lobe be associated with a boundary lying the GSM-XY plane moving predominately northward, in this case application of the timing analysis reveals that the boundary lies almost entirely in the GSM-XZ plane and moves in the dawnward direction along the unit normal ~$(0.06, -0.96, 0.27)_{GSM}$ with a speed along that normal of ~23 km s^{-1}. The four spacecraft re-enter the plasma sheet with the lobe – plasma sheet boundary observed at ~ 02:50:05 UT, 02:49:41 UT, 02:50:30 UT and 02:49:47 UT at C1, C2, C3 and C4 respectively i.e. in the order C2, C4, C1 and C3. This corresponds to the boundary moving at ~ 49 km s^{-1} along the unit normal ~ $(0.02, -0.23, -0.97)_{GSM}$ indicating a boundary lying in the GSM-XY plane which moves almost entirely in the negative GSM-Z direction, as we might naïvely have expected for a transition from the south lobe into the plasma sheet. Note also that the spacecraft now enter a plasma sheet which is rather hotter than that observed previously with the distribution centered at ~ 1 keV.

The magnetic field on C3, shown in Figure 3.5 panels 6 and 7, indicates a clear example of a major reorganisation of the magnetic field during this interval. At ~ 02:51 UT the magnetic field in the GSM-X direction is reduced by approximately 20 nT and is accompanied by a strengthening of the GSM-Z component of the magnetic field by approximately 10 nT. This indicates a magnetic field dipolarization.

The thinning of the plasma sheet at Cluster is seen at ~ 02:21 UT. Pi2 pulsations observed at SAMNET at ~ 02:40 UT preceded events in both the AE index and Canopus magnetometer data which place the onset of the substorm at ~ 02:50 UT which may by explained by the differences in local time of the various observations. At this time the plasma sheet is seen to expand over the Cluster quartet and the onset of auroral kilometric radiation is seen shortly after at ~ 02:55 UT. At 03:00 UT an injection is seen at geosynchronous orbit.

3.3.2 Case Study – Multiple Thinning and Expansion

There are two instances of multiple plasma sheet thinning and expansion associated with complex geomagnetic activity within our dataset. Analysis may provide a measure of how much the plasma sheet changes throughout the course of a complex substorm. For example, changes in the orientation of the neutral sheet may occur and therefore affect the direction of future thinnings and expansions.

To illustrate this, we take the repeated thinnings and expansions of the plasma sheet that were observed by Cluster on 11th August 2002 between 16:40 UT and 16:54 UT when Cluster was located at $(-17.6, -7.1, 2.0)_{GSM}$ R_E.

The AE index is not available in digital form for this period so a description of this data follows. Prior to this interval, the AE index indicates two large substorm onsets at ~14:15 UT and ~14:35 UT with AE index values of ~750 nT and ~1200 nT respectively. The AE at the beginning of this study interval had reached ~700 nT, after rising steadily from ~550 nT at ~16:25 UT. At ~ 16:50 UT there is an enhancement of the AE index to ~800 nT returning to ~700 nT before an enhancement to ~750 nT at 17:00 UT. A chain of intensifications to near 500 nT follow 18:00 UT. A slight enhancement of

proton differential flux as detected by LoP (not shown) on LANL-02A and at LANL-97A at geosynchronous orbit at ~16:35 UT with similar signatures seen in the LoE electron data (not shown). Geotail was not located in the magnetotail during this interval.

The position of each of the spacecraft is shown in Figure 3-6 using the same format as Figure 3-4. Note that Cluster 1 is separated in GSM-X from the other spacecraft. Data from Cluster PEACE and the magnetometer for the interval 16:40 to 16:54 UT is shown in Figure 3-7 with the same structure as that of Figure 3-5. Prior to 16:40 UT a thinning of the plasma sheet was seen at Cluster at ~ 14:26 UT and the plasma sheet expanded over Cluster at ~ 14:47 UT. The plasma sheet, now heated by ~500 eV, has a varying electron distribution centred between 2 to 6 keV until the interval of Figure 3.7 starts.

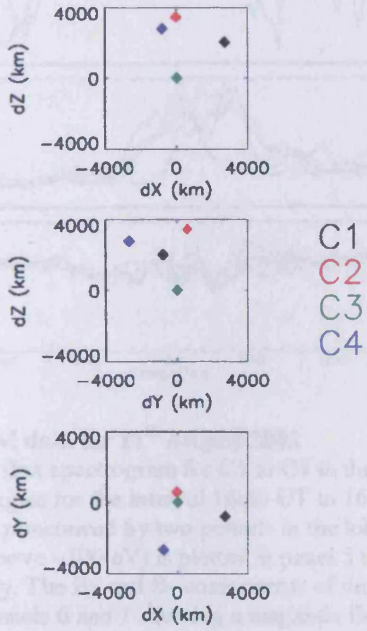

Figure 3-6 Cluster configuration on 11th August 2002
The separations of each of the Cluster spacecraft from the reference position are shown in the GSM X-Y, -XZ and –YZ planes. C1 to C4 are marked in black, red, green and blue respectively. The order of the spacecraft in the GSM-Z direction is the expected order in which the plasma sheet – lobe boundary should traverse the spacecraft quartet.

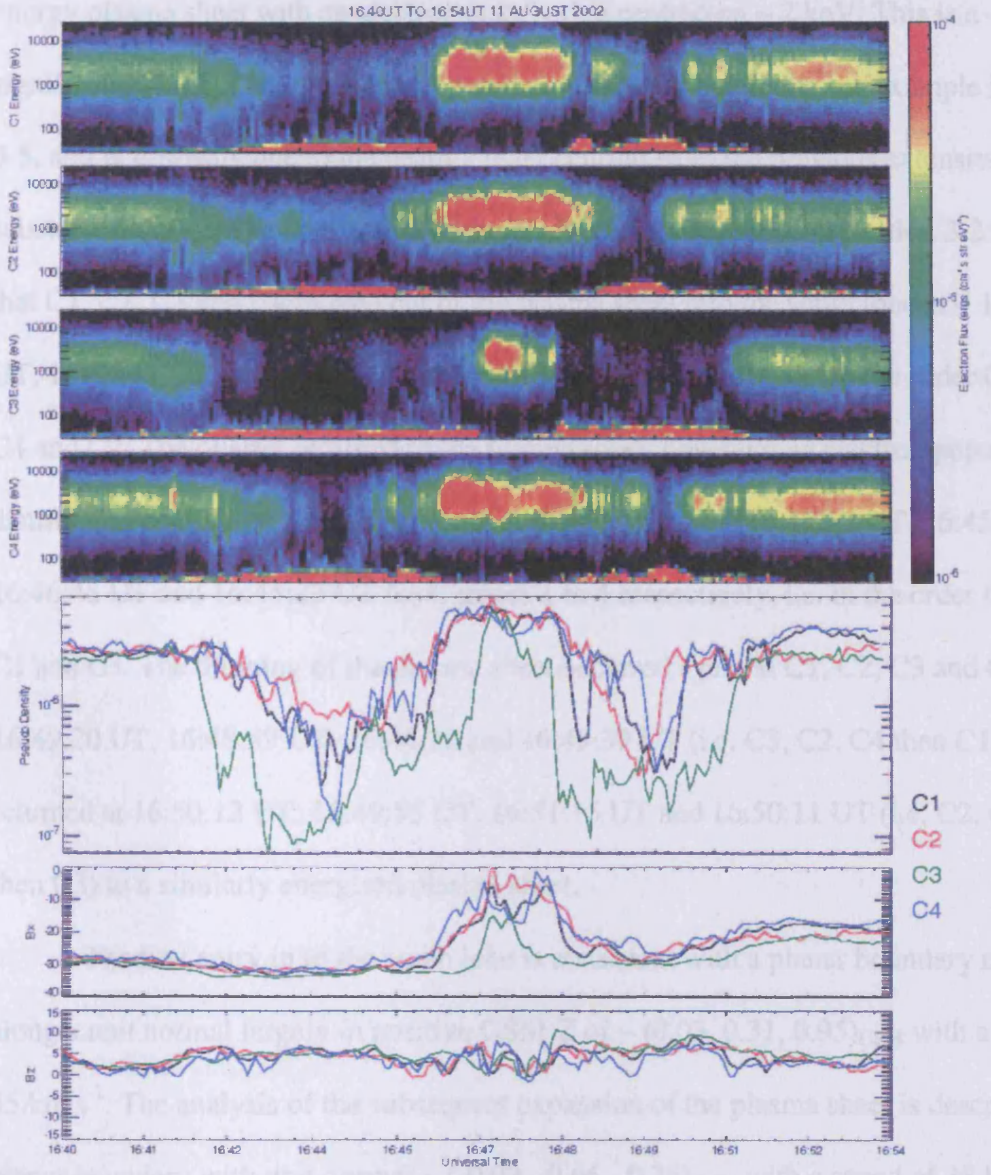

Figure 3-7 PEACE and FGM data for 11th August 2002
Electron energy - differential flux spectrogram for C1 to C4 in the first four panels showing data summed over all pitch angles for the interval 16:40 UT to 16:54 UT on 11th August 2002. Plasma sheet plasma is punctuated by two periods in the lobe. The density proxy (summed over all electrons above ~100 eV) is plotted in panel 5 using Black, Red, Green and Blue for C1 to C4 respectively. The B_X and B_Z components of the magnetic field measured at the spacecraft are shown in panels 6 and 7 showing a magnetic field re-arrangement at ~16:47 UT.

At the beginning of the period shown in Figure 3-7, each spacecraft is in a high-energy plasma sheet with an electron distribution centred on ~ 2 keV. This is a significantly higher energy electron population when compared to the example in Figure 3-5, and is probably due to the heating that occurred from the previous extensive substorm activity. The application of the methodology described in Section 3.2 indicated that C1, C2, C3 and C4 moved out of the plasma sheet into the south lobe at ~ 16:43:20 UT, 16:43:47 UT, 16:42:45 UT and 16:43:38 UT respectively, i.e. in the order C3, C1, C4 and C2. The quartet returned to the plasma sheet, now with an electron population distribution centred on 3 keV and a higher energy flux, at ~ 16:46:12 UT, 16:45:39 UT, 16:46:46 UT and 16:45:22 UT for Clusters 1 to 4 respectively, i.e. in the order C4, C2, C1 and C3. The thinning of the plasma sheet occurred again at C1, C2, C3 and C4 at ~ 16:49:20 UT, 16:48:59 UT, 16:48:18 and 16:49:39 UT (i.e. C3, C2, C4 then C1) and returned at 16:50:12 UT, 16:49:55 UT, 16:51:15 UT and 16:50:11 UT (i.e. C2, C4, C1 then C3) to a similarly energised plasma sheet.

The first entry in to the south lobe is consistent with a planar boundary moving along a unit normal largely in positive GSM-Z of ~ $(0.03, 0.31, 0.95)_{GSM}$ with a speed of 35 km s^{-1}. The analysis of the subsequent expansion of the plasma sheet is described by a planar boundary with unit normal ~ $(-0.02, -0.66, -0.75)_{GSM}$ with a speed of 38 km s^{-1} along that normal. The second thinning has a plane of unit normal in GSM-X and GSM-Z ~ $(0.84, 0.19, 0.51)_{GSM}$ with a speed of 48 km s^{-1} with a subsequently associated expansion with a plane unit normal again in negative GSM-Z ~ $(-0.21, -0.45, -0.87)_{GSM}$ and a speed of 45 km s^{-1} along that normal. The GSM-Z components provide further evidence that the expansion vectors follow the expected direction while the thinning

vectors are more varied in this case. In these two thinnings the prominent direction for the thinning has changed from the GSM-Z direction to the GSM-X direction. It may have been expected that the second event had less energy for a vigorous expansion, but the speeds of thinning and expansion were greater and in approximately the same ratio as the first paired event. However, the complexity of substorms with multiple onsets and the lack of observations of thinnings and expansions associated with each onset of a complex substorm provide interpretational difficulties.

The magnetic field from all spacecraft using the same colour code as above is shown in Figure 3-6 panels 6 and 7, indicates a reorganisation of the magnetic field during this interval at ~ 16:47:10 UT and possibly one at ~ 16:51 UT. Whilst there is a reduction of approximately 15 nT in B_X only slight variation occurs in B_Z. These field changes may be due to pressure balances from low to high β plasma.

Two tail seasons of Cluster data were available for this study. In the following section survey statistics of the observed substorm-associated plasma sheet thinnings and expansions will be described.

3.3.3 Statistical Survey

We surveyed two tail seasons to identify all substorm related expansions and contractions of the plasma sheet observed at the Cluster spacecraft. To distinguish between substorm-related activity (both growth phase thinning and onset related expansion) and the passage of the plasma sheet over the spacecraft related to diurnal motion and boundary waves, only crossings that are located within 15 minutes of an AE intensification or onset where the background AE is $AE \geq 100$ nT were selected. In addition boundaries with normal velocities on the order of that of the spacecraft orbital

motion (~3 km s^{-1}) are not included in our database. These are probably not substorm-related and are subject to significant errors as it is unlikely the boundary has remained both planar and moved at constant velocity throughout the associated extended time-lag between spacecraft. A total of 44 passages from the north lobe to the plasma sheet were observed and 33 transitions were observed from the south lobe to the plasma sheet corresponding to plasma sheet expansion. In addition there were 31 passages from the plasma sheet to the north lobe and 35 to the south lobe corresponding to plasma sheet thinnings.

The distribution of events satisfying the above criteria is shown in Figure 3-8 in the GSM co-ordinate system. The GSM-XZ plane is shown in the top panel with the GSM-X axis shown from -5 R_E to -25 R_E and the GSM-Z axis shown from -10 to 10 R_E. The GSM-YZ plane is shown in the bottom panel with the GSM-Y axis plotted from -20 to 20 R_E and with the GSM-Z axis again shown from -10 to 10 R_E. The positions of the 44 passages from the north lobe to the plasma sheet and 33 transitions from the south lobe to the plasma sheet are represented by green squares (□) and black plus signs (+) respectively in the plots. The positions of the 31 passages from the plasma sheet to the north lobe and 35 to the south lobe are represented by blue crosses (×) and red diamonds ( ) respectively. The GSM-YZ plane clearly shows that substorm associated lobe – plasma sheet boundary motions were detected across the entire magnetotail from dawn to dusk. Groups of events, e.g. that at ~$(-12.5, 5)_{GSM}$ R_E in the GSM-YZ plane, occur during very complex substorm activity where there are repeated plasma sheet thinnings and expansions within only a few hours and thus only a small change of position had occurred. There are 29 pairs of events (c.f. case 1 above) where the spacecraft goes from

the plasma sheet into the lobe and then back again. However, it should be also noted that there are often missing 'partner' events where the data is too complex (e.g. on one or more spacecraft there are several possible points that could be taken as the plasma sheet – lobe boundary that corresponds to the boundary observed on other spacecraft or one or more spacecraft did not cross the boundary) for boundary analysis or instrument operation ceases on one or more spacecraft prior to the partner event.

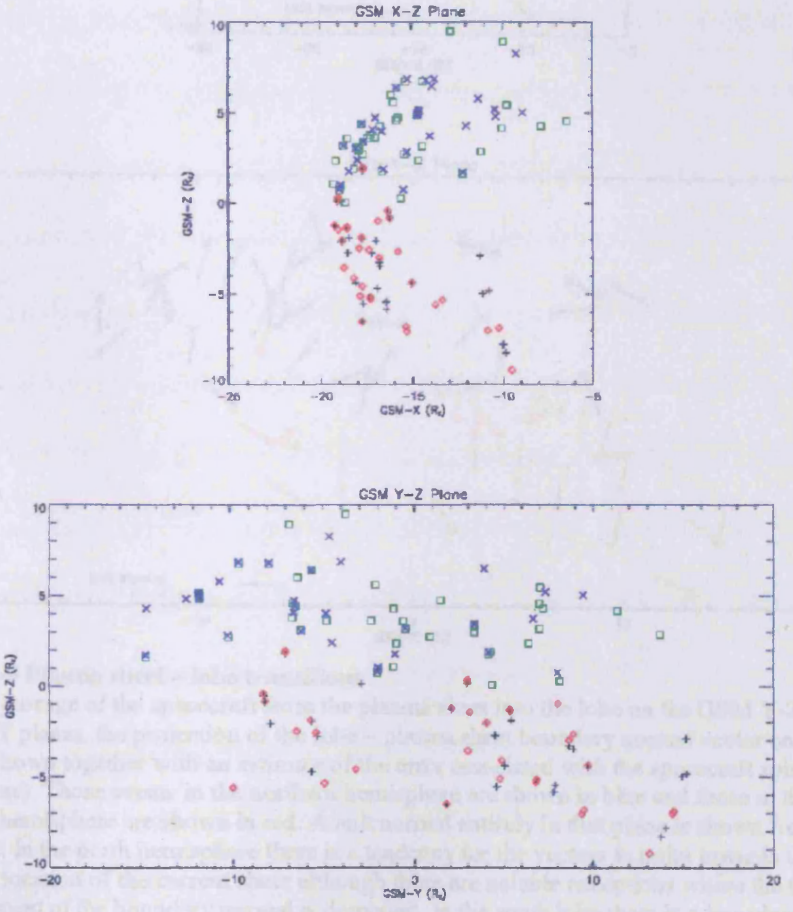

Figure 3-8 The distribution of plasma sheet – lobe and vice versa transitions
The distribution of all the passages of the spacecraft from the lobe into the plasma sheet and vice-versa in the GSM Y-Z and GSM X-Y planes. Expansion crossing are marked by green squares and black plus signs for the north and south lobes respectively. Thinning crossings are indicated by blue crosses and red diamonds in the north and south lobes respectively. The data points are evenly distributed over the GSM Y-Z plane.

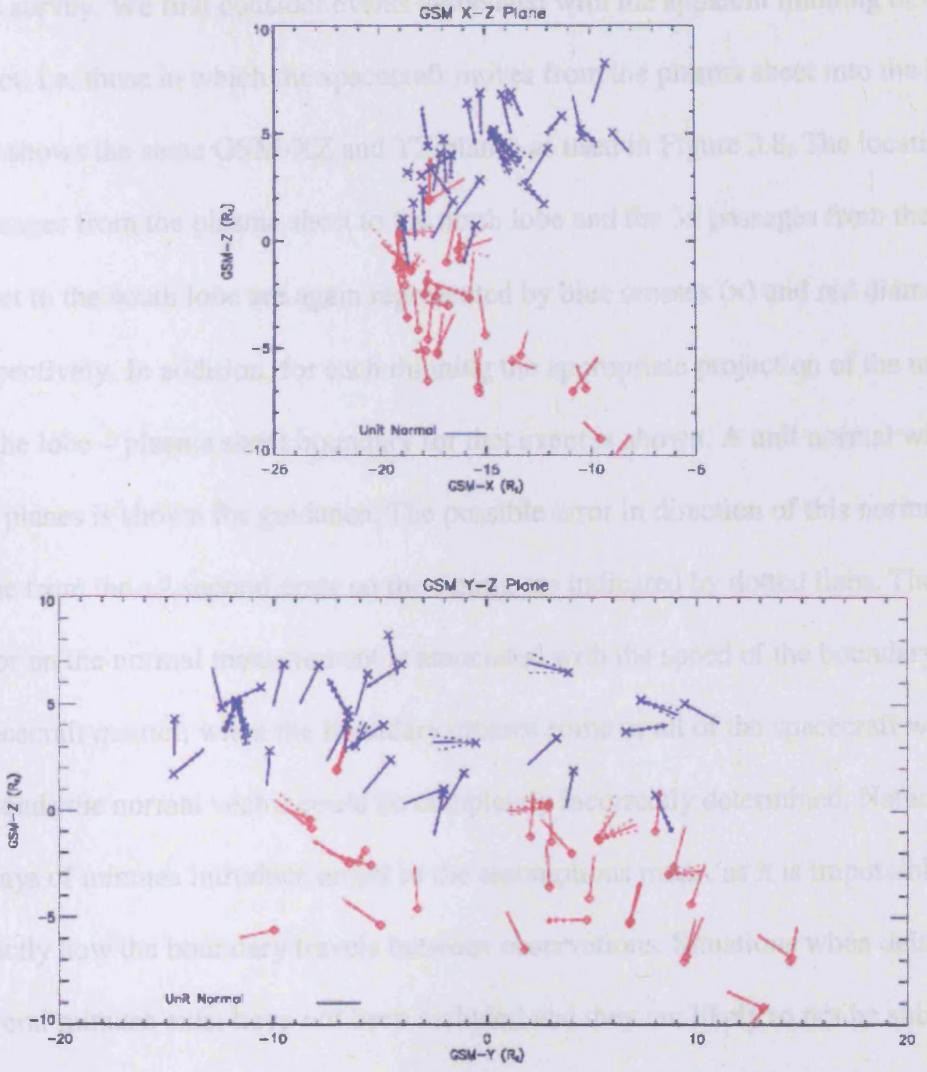

Figure 3-9 Plasma sheet – lobe transitions
For each passage of the spacecraft from the plasma sheet into the lobe on the GSM Y-Z and GSM X-Y planes, the projection of the lobe – plasma sheet boundary normal vector on that plane is shown together with an estimate of the error associated with the spacecraft spin (dotted line). Those events in the northern hemisphere are shown in blue and those in the southern hemisphere are shown in red. A unit normal entirely in that plane is shown for reference. In the north hemisphere there is a tendency for the vectors to point towards the expected location of the current sheet although there are notable exceptions where the GSM-Y component of the boundary normal is dominant. In the south lobe there is a less clear trend for the vectors to point to the current sheet, instead the vectors contain a mainly negative GSM-Y component.

We now move on to consider the results of the timing analysis of the events in this survey. We first consider events associated with the apparent thinning of the plasma sheet, i.e. those in which the spacecraft moves from the plasma sheet into the lobe. Figure 3-9 shows the same GSM-XZ and YZ planes as used in Figure 3.8. The location of the 31 passages from the plasma sheet to the north lobe and the 35 passages from the plasma sheet to the south lobe are again represented by blue crosses (×) and red diamonds ( ) respectively. In addition, for each thinning the appropriate projection of the unit normal of the lobe – plasma sheet boundary for that event is shown. A unit normal within each of the planes is shown for guidance. The possible error in direction of this normal vector arise from the ±2 second error on the timing are indicated by dotted lines. The size of the error on the normal measurement is associated with the speed of the boundary over the spacecraft quartet: when the boundary crosses some or all of the spacecraft within ~ 4 seconds the normal vector could be completely incorrectly determined. Naturally, large delays of minutes introduce errors in the assumptions made, as it is impossible to say exactly how the boundary travels between observations. Situations when delays of several minutes exist have not been included and they are likely to not be substorm-associated. In the northern hemisphere the normal vector (Blue vectors) in the GSM-YZ plane usually points towards the expected location of the current sheet although there are notable exceptions towards high GSM-Z values where they tend to have mostly a GSM-Y component. In the southern hemisphere (Red vectors) this trend is replaced by a mainly negative GSM-Y component of the normal. In the GSM-XZ plane there is no clear overall trend in the GSM-X component of the unit normal. We now bin the data into smaller distance ranges to allow further clarity.

The data were binned into four 4 R_E bins along the GSM-X axis, six 6 R_E bins along the GSM-Y axis and into four $5R_E$ bins in the GSM-Z axis. The size of each bin was chosen to reflect the spatial extent of the sampled data and to maintain a suitably fine mesh size for further analysis. Within each bin, the average normal direction for the thinnings in each hemisphere were calculated. There are data bins that suffer from low-frequency statistical errors, but binning into variable bin sizes would mask the detail of the overview.

Figure 3-10 shows the GSM Y-Z projection of the binned normal vector averages for two of the four bins along the GSM-X axis ($-20 \leq X_{GSM} \leq -16$ R_E and $-16 \leq X_{GSM} \leq -12$ R_E) for those boundaries associated with the spacecraft passing from the plasma sheet into the lobe. Each panel, labelled by GSM-X bin, has the GSM-Z bin along the ordinate axis against the GSM-Y bin along the abscissa. At each mesh point the projection of the average normal vector in the GSM-ZY plane of the plasma sheet – lobe boundary associated with plasma sheet thinning is shown for that bin. Events located in the north lobe are marked in blue and those in the south lobe marked in red. At each mesh-point the projection of the average normal vector created by taking the extreme timing error on the component normals is also shown to provide an assessment of the error. Due to the natural orbit procession and the inclination of the orbit, we expect there to be more data points in the central parts of the GSM-YZ plane for the $-20 \leq X_{GSM} \leq -16$ R_E bin for apogee and more points on the flanks for the $-16 \leq X_{GSM} \leq -12$ R_E bin.

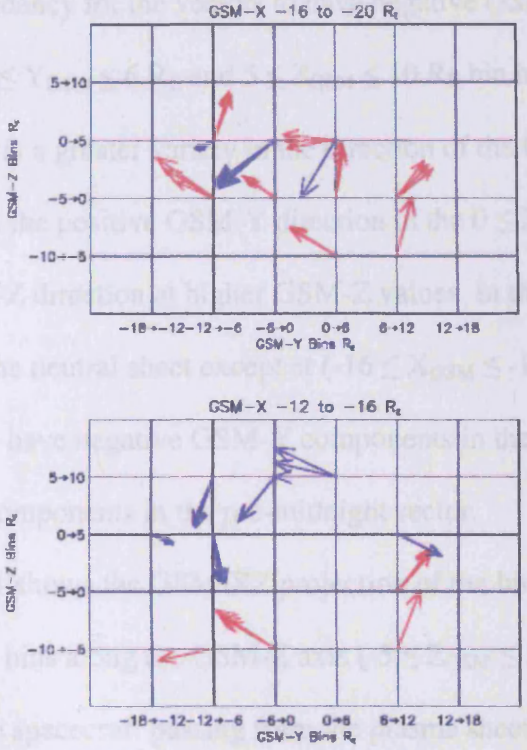

Figure 3-10 Binned plasma sheet – lobe transitions (GSM-ZY plane)
The projection of the average unit normal of the boundary between the thinning plasma sheet and the lobe in the GSM-ZY direction is shown as a function of position in the GSM-ZY plane for two GSM-X bins/ Plasma sheet to lobe crossing are marked in blue and red vectors for the north and south lobes respectively. Error bars, calculated from the extreme errors on the individual vectors, are plotted when more than one normal vector was used for the averaging. The top panel shows that thinning in the north and south lobes tend to have a negative GSM-Y component with a variety of GSM-Z dominance. The bottom plot suggests that there are a greater variety of GSM-Y components closer to the Earth.

The $-20 \leq X_{GSM} \leq -16$ R_E bin shows that the thinnings in the north and south lobes tend to have a negative GSM-Y component at all cross tail distances. All vectors (except $0 \leq Y_{GSM} \leq 6$ R_E and $0 \leq Z_{GSM} \leq 5$ R_E) in this X_{GSM} bin point towards the expected location of the neutral sheet. It is noted that the dominance of the GSM-Z component varies over the binned data, with the most predominantly GSM-Z thinning vectors being located in the positive GSM-Y part of the data set, except for the $0 \leq Z_{GSM} \leq 5$ R_E and $0 \leq Y_{GSM} \leq 6$ R_E bin. All the thinnings that occur in the north lobe (blue vectors) have a negative GSM-Z component, all having a negative GSM-Y component.

The thinning averages for north lobe (blue vectors) in the $-16 \leq X_{GSM} \leq -12\ R_E$ bin show there is a tendency for the vectors to have negative GSM-Z component, although the exception at $0 \leq Y_{GSM} \leq 6\ R_E$ and $5 \leq Z_{GSM} \leq 10\ R_E$ bin has a positive GSM-Z component. There is a greater variety in the direction of the GSM-Y component with the vectors pointing in the positive GSM-Y direction in the $0 \leq Z_{GSM} \leq 5\ R_E$ bin and then in the negative GSM-Z direction at higher GSM-Z values. In the south lobe there is thinning strongly towards the neutral sheet except at ($-16 \leq X_{GSM} \leq -12\ R_E$ and $-10 \leq Z_{GSM} \leq -5\ R_E$). The thinnings have negative GSM-Y components in the post-midnight sector and positive GSM-Y components in the pre-midnight sector.

Figure 3-11 shows the GSM-XZ projection of the binned normal vector averages for the central two bins along the GSM-Z axis ($-5 \leq Z_{GSM} \leq 5\ R_E$) for those boundaries associated with the spacecraft passing from the plasma sheet into the lobe. The panel has the GSM-Y bin along the ordinate axis against the GSM-X bin along the abscissa. At each mesh point the projection of the average normal vector in the GSM-XZ plane of the plasma sheet – lobe boundary associated with plasma sheet thinning is shown for that bin. Events located in the north lobe are marked in blue and those in the south lobe marked in red. At each mesh-point the projection of the average normal vector created by taking the extreme timing error on the component normals is again shown to provide an assessment of the error.

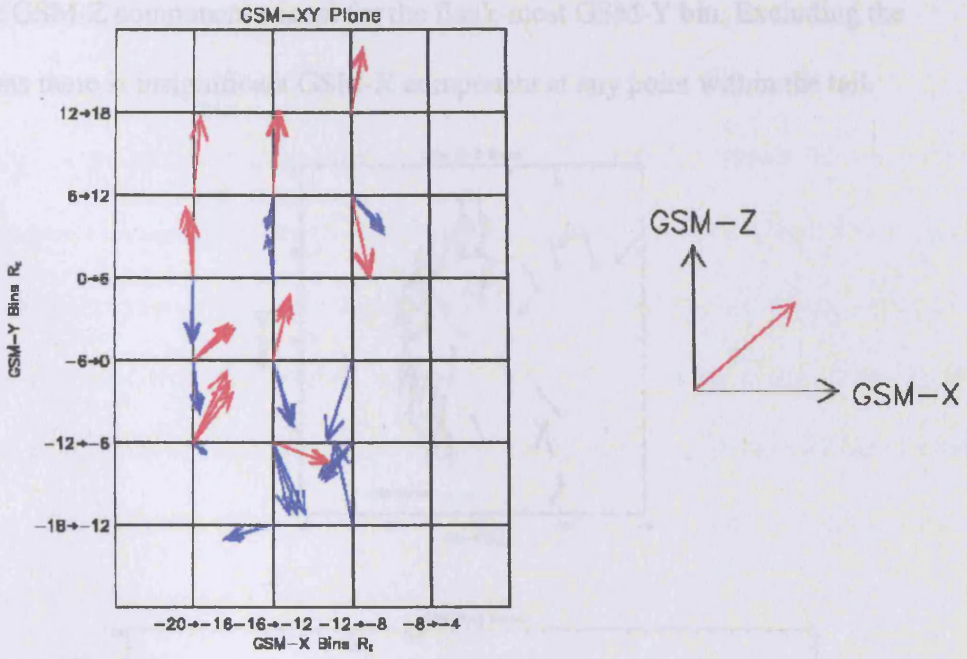

Figure 3-11 Binned plasma sheet – lobe transitions (GSM-YZ plane)
The projection of the average unit normal of the boundary between the thinning plasma sheet and the lobe in the GSM-ZX direction is shown as a function of position in the GSM-YX plane for two GSM-Z bins. Plasma sheet to lobe crossing are marked in blue and red vectors for the north and south lobes respectively. Error bars, calculated from the extreme errors on the individual vectors, are plotted when more than one normal vector was used for the averaging. The plot shows that the thinning vectors in the north lobe have a positive GSM-Z component and a slightly negative GSM-X component for those thinnings observed in the pre-midnight region. Thinnings occurring in the post-midnight sector in the south lobe have a strong GSM-Z component with a GSM-X component varying from minimal to strongly positive.

All but two of the thinning vectors in the south lobe (red vectors) have a positive GSM-Z component with the exceptions having no GSM-Z component ($0 \leq Y_{GSM} \leq 6\ R_E$ and $-20 \leq X_{GSM} \leq -16\ R_E$) and a strongly negative one ($6 \leq Y_{GSM} \leq 12\ R_E$ and $-12 \leq X_{GSM} \leq -8\ R_E$). Considering the $-20 \leq X_{GSM} \leq -16\ R_E$ bin (ignoring the exception) the thinning vectors in the dusk sector have a slight negative GSM-X component and those in the dawn sector have a slight positive GSM-X component.

In the north lobe, the thinning vectors (blue vectors) all have a strongly to weakly negative GSM-Z component except for the flank-most GSM-Y bin. Excluding the exceptions there is insignificant GSM-X component at any point within the tail.

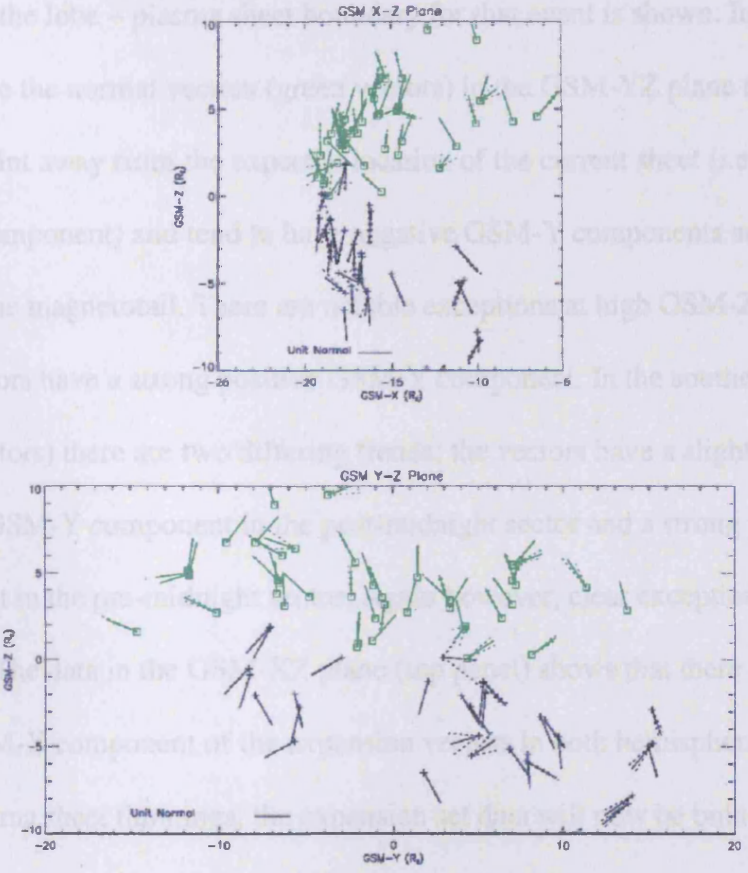

Figure 3-12 Lobe – plasma sheet transitions
For each passage of the spacecraft from the lobe into the plasma sheet on the GSM Y-Z and GSM X-Y planes, the projection of the lobe – plasma sheet boundary normal vector on that plane is shown together with an estimate of the error associated with the spacecraft spin (dotted line). A unit normal entirely in that plane is shown for reference. In the north lobe the trend is for expansion normals to point away from neutral sheet and have a negative GSM-Y component. In the south lobe there are two trends: in the pre-midnight region the vectors have a positive GSM-Y component and in the post-midnight region the have a negative GSM-Y component.

We now go on to consider events that are associated with the expansion of the plasma sheet, i.e. those in which the spacecraft moves from the lobe into the plasma sheet. Figure 3-12 shows the projection of the unit normal of the lobe – plasma sheet

boundary for these events in the GSM X-Z and Y-Z planes and has the same format as Figure 3-9. The location of the 44 passages from the north lobe to the plasma sheet and the 33 passages from the south lobe to the plasma sheet are represented by green squares (□) and black plus signs (+) respectively with the appropriate projection of the unit normal of the lobe – plasma sheet boundary for that event is shown. In the northern hemisphere the normal vectors (green vectors) in the GSM-YZ plane (lower panel) usually point away from the expected location of the current sheet (i.e. have a positive GSM-Z component) and tend to have negative GSM-Y components across the whole width of the magnetotail. There are notable exceptions at high GSM-Z values where some vectors have a strong positive GSM-Y component. In the southern hemisphere (black vectors) there are two differing trends: the vectors have a slight tendency to a negative GSM-Y component in the post-midnight sector and a strong positive GSM-Y component in the pre-midnight sector. Again however, clear exceptions exist at all GSM-Z values. The data in the GSM-XZ plane (top panel) shows that there is strong variation in the GSM-X component of the expansion vectors in both hemispheres. As for the case of the plasma sheet thinnings, the expansion set data will now be binned to provide further clarity.

Figure 3-13 shows the GSM Z-Y projection of the binned normal vector averages for two of the four bins along the GSM-X axis ($-20 \leq X_{GSM} \leq -16$ R_E and $-16 \leq X_{GSM} \leq -12$ R_E) for those boundaries associated with the spacecraft passing from the lobe into the plasma. The format and binning used is the same as for Figure 3-10.

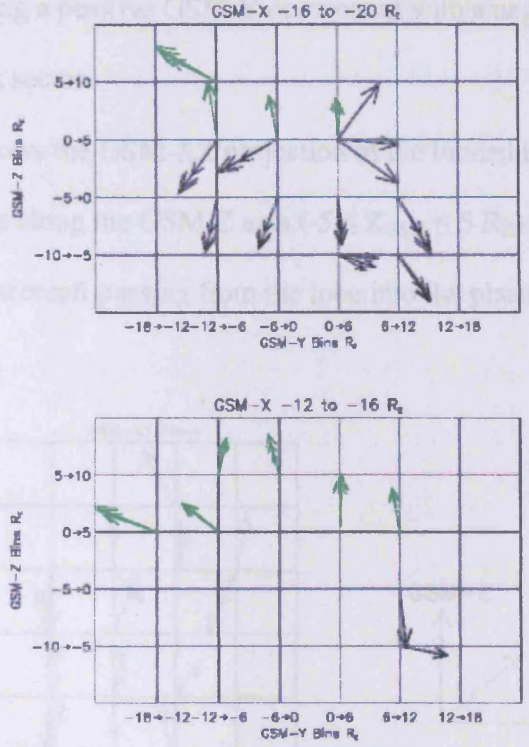

Figure 3-13 Binned lobe – plasma sheet transitions (GSM-ZY)
The projection of the average unit normal of the boundary between the expanding plasma sheet and the lobe in the GSM-ZY direction is shown as a function of position in the GSM-ZY plane for two GSM-X bins. Plasma sheet to lobe crossing are marked in green and black vectors for the north and south lobes respectively. Error bars, calculated from the extreme errors on the individual vectors, are plotted when more than one normal vector was used for the averaging. The tendency for expansion to have a negative GSM-Y component is clarified in the northern hemisphere. The south lobe exhibits the two-trend structure to have a positive GSM-Y component in the pre-midnight sector and a negative one in the post-midnight sector.

In both GSM-X bins the expansion vectors in the northern hemisphere (green vectors) typically have a negative GSM-Y component increasing in significance towards the dawn flank usually with a positive GSM-Z component. For expansions in the south lobe (black vectors) there are two significant trends in the $-20 \leq X_{GSM} \leq -16$ R_E bin where the vectors in the pre-midnight sector have a positive GSM-Y component whereas in the post-midnight sector they have a negative GSM-Y component. There are only two data bins in the $-16 \leq X_{GSM} \leq -12$ R_E range that contain expansion vectors, and these exhibit

the same trend of having a positive GSM-Y component with a negative GSM-Z component in the dusk sector.

Figure 3-14 shows the GSM-XZ projection of the binned normal vector averages for the central two bins along the GSM-Z axis ($-5 \leq Z_{GSM} \leq 5\ R_E$) for those boundaries associated with the spacecraft passing from the lobe into the plasma sheet using the same format as Figure 3-11.

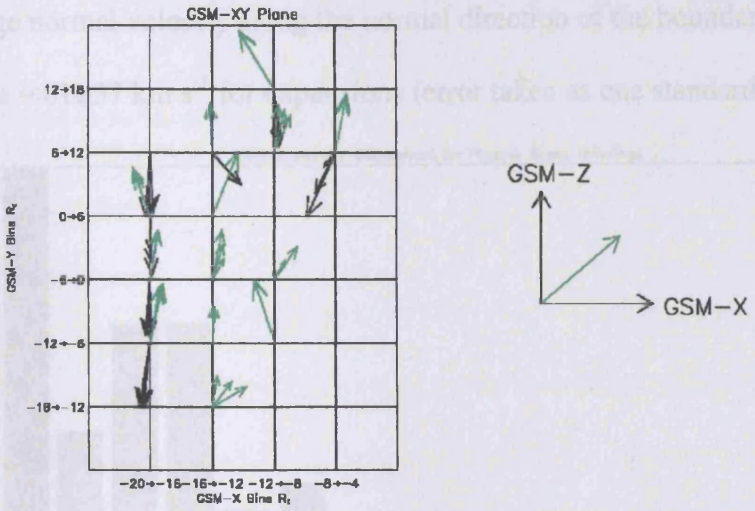

Figure 3-14 Binned lobe – plasma sheet transitions (GSM-YZ plane)
The projection of the average unit normal of the boundary between the expanding plasma sheet and the lobe in the GSM-ZX direction is shown as a function of position in the GSM-YX plane for two GSM-Z bins. Plasma sheet to lobe crossing are marked in green and black vectors for the north and south lobes respectively. In the pre-midnight sector of the northern hemisphere the expansions, on average, have a negative GSM-X component that is reversed on the post-midnight sector. Bar a couple of exceptions, the expansion vectors in the south lobe have a GSM-X component ranging from minimal to strongly positive.

In the northern hemisphere, the expansion vectors (green) exhibit a slight positive GSM-X component in the post-midnight sector compared to a variety of directions in the pre-midnight sector. In the southern hemisphere the post-midnight sector shows a slight negative GSM-X component with the pre-midnight sector exhibiting a slight positive GSM-X component.

The distribution of normal velocity magnitudes is shown in Figure 3-15 for the 66 cases of plasma sheet thinnings. The data was binned into 10 km s^{-1} bins. The absence of a 0 to 10 km s^{-1} bin is due to the event selection criteria eliminating those events subject to large timing errors and for where the assumptions may not be valid. Outliers beyond the 180 to 190 km s^{-1} bin have also been excluded. The average normal velocity of thinnings is ~ 44±32 km s^{-1} errors from one standard deviation). Similarly, the expansion normal velocities magnitudes are shown in Figure 3-16 and are binned in the same way. The average normal velocity along the normal direction of the boundary motion was found to be ~ 61±37 km s^{-1} for expansions (error taken as one standard deviation).

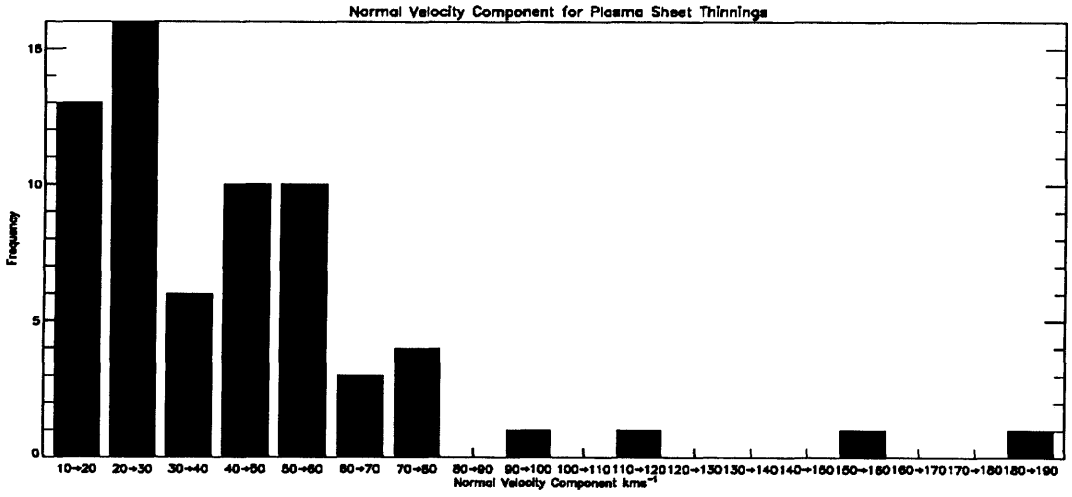

Figure 3-15 Thinning velocities
A bar chart of the normal velocity component of all plasma sheet – lobe boundaries passing over the spacecraft associated with plasma sheet thinning. The speeds are binned into 10 km s^{-1} bins. The average is 44±32 km s^{-1}.

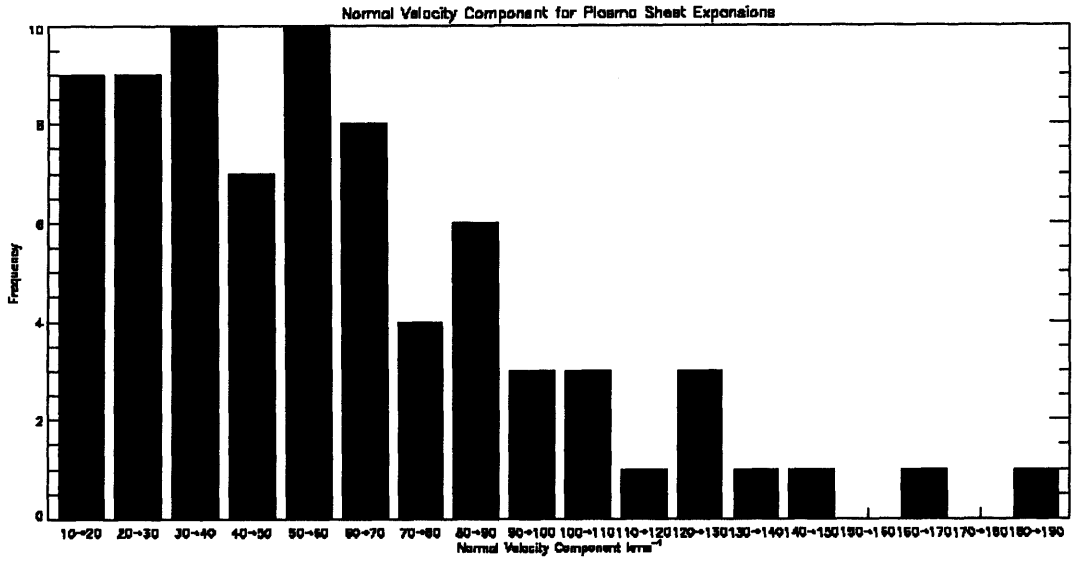

Figure 3-16 Expansion velocities
A bar chart of the normal velocity component of all plasma sheet – lobe boundaries passing over the spacecraft associated with plasma sheet expansion. The speeds are binned in to 10 km s^{-1} bins. The average is 61±37 km s^{-1}.

An assessment of whether the expansion speed of the plasma sheet over the Cluster quartet scales with the magnitude of the associated substorm auroral electrojet (AE) index was made. The AE index was averaged over a period of 30 minutes, centered on the time of each boundary crossing, and then rounded to the nearest 50nT to provide an indicator of the intensity of the associated substorm. At the time of publication only numerical data for the 2001 provisional AE index was available from the World Data Centre (WDC-C2, Kyoto), accordingly the averages for the 2002 events was assessed by visual inspection of the AE Quick Look data plots available from the World Data Centre.

The average AE (in nT) and the plasma sheet expansion velocity magnitude (in km s^{-1}) along the normal direction of the plasma sheet – lobe boundary is shown in Figure 3-17. The Pearson's product moment correlation coefficient for the plotted data is -0.06, indicating little association between the normal velocity component and the AE index. It

should be noted that the occurrence of strong substorms (i.e. AE greater than 450nT) are relatively uncommon in this data set with an average AE nearer 350nT. Limited observations of high AE substorms may skew the distribution.

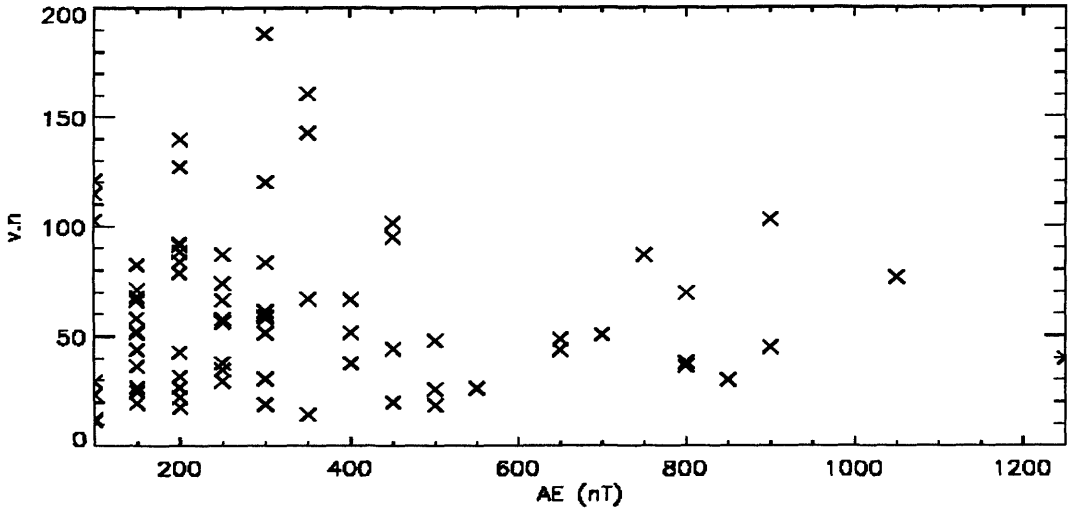

Figure 3-17 Normal velocity as a function of AE
The normal velocity component of the plasma sheet expansions plotted against average AE conditions to test for substorm size dependence on the expansion normal velocity. The average substorm condition in this data set has an AE of ~350 nT. There exists no correlation with a Pearson's product moment correlation coefficient of –0.06.

To assess the effect of the variation in IMF direction on the data set the relation between IMF B_Y (in nT) and the GSM-Y, n_Y, component of the expansion normal unit vector is shown in Figure 3-18. Where possible the IMF data was obtained by averaging the solar wind velocity as measured by the ACE/SWE experiment over the period 50 to 70 minutes before the expansion event observed at Cluster. The average velocity was used to obtain an average lag time with reference to the ACE-Earth distance. The values for the IMF were then found by lagging the magnetic field data from MFI by this averaged time lag. When data gaps were present the data was visually inspected to obtain the appropriate magnetic field components. A positive n_Y indicates expansion in the positive GSM-Y direction, i.e. towards dawn. There are more events with a positive IMF

B_Y component, but these occur with a wide spread in the normal direction. Consequently, there is no simple relationship between the IMF B_Y component and the normal GSM-Y component.

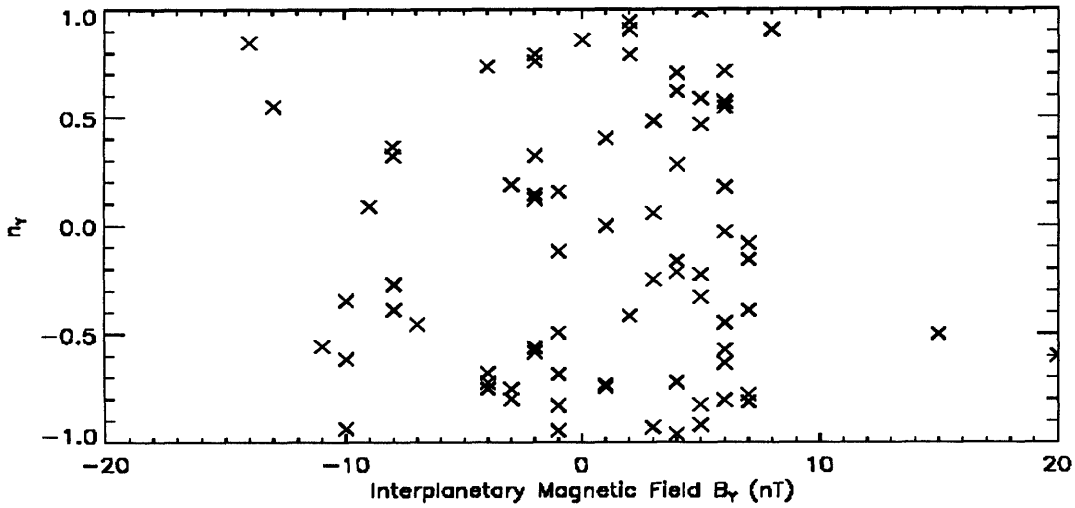

Figure 3-18 Boundary normal direction as a function of IMF B_Y
The GSM-Y component of the normal unit vector is compared to the IMF-Y (GSM) component to test for correlation. Lagged magnetic field data from ACE was used to obtain the IMF-Y input. No simple relationship exists between the IMF-B_Y and the normal vector of the expansion.

An attempt to determine if the plasma sheet – lobe boundary decelerates with distance from the expected neutral sheet location was also made. The average neutral sheet location was taken to be that modeled by Dandouras [1988] and the normal component of the velocity (km s^{-1}) against the distance of the spacecraft quartet from the neutral sheet, dZ (R_E), is plotted in Figure 3-19. A decelerating boundary would result in those observations made further away from the neutral sheet being associated with slower boundaries. However, there appears to be a significant variability of the normal velocity component with distance up to 8 R_E away from the neutral sheet implying that the plasma sheet can expand with large velocities and that these can be maintained over a large distance.

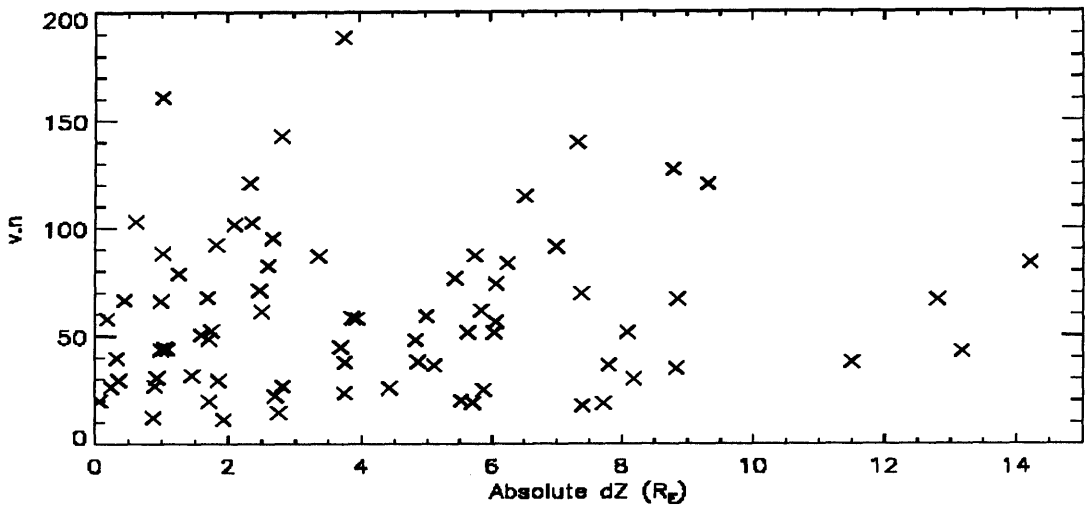

Figure 3-19 Normal velocity with distance from the neutral sheet
The normal velocity component plotted against distance from the neutral sheet modelled by Dandouras [1988] for plasma sheet expansions. The variability of the normal velocity component with dZ suggests that the velocity at which the boundary moves is sustained, or is not decelerated, after its initial acceleration.

3.3.4 Paired and Multiple Events

As the magnetospheric substorm goes through its cycle, the plasma sheet is expected to first thin, and then expand over the spacecraft. As a result of this cyclic nature we would expect that in the available data set all thinnings are followed by an expansion. Naturally, due to the variable extents of plasma sheet expansion in the north-south direction and with extra complications due to spacecraft and instrument operations, we do not have a complete data set of paired events. For those events that have both the thinning – expansion components, as in the example shown in Figure 3-5, we are able to compute the ratio of the thinning to expansion normal velocities to examine, for example, whether or not a rapid thinning is followed by a rapid expansion.

In total there are 29 paired plasma sheet thinning and expansion events defined as a growth phase type thinning followed by an onset type expansion located within 15 minutes of an AE intensification or onset that are clearly defined in the data set allowing the timing analysis to be used. Of these there are 16 events where the expansion velocity is greater than the thinning velocity. There are two outlying events with a thinning to expansion normal velocity ratio of ~4.8 and ~16.5. The average thinning over expansion ratio of the normal velocity components, including the outliers is 1.58, implying that, on average, the expansion velocity is slower than the thinning velocity. Excluding the outliers this ratio drops to 0.91 suggesting that on average the expansion velocity is similar to the thinning velocity. With reference to the averages presented for the expansion and thinning normal velocity component, we would place this average ratio to be approximately 0.8.

3.4 Summary and Discussion

The observed expansions of the plasma sheet over the Cluster spacecraft for the first time provide information on the direction of the propagation of expansion and thus may indicate the relative location of the onset region. Our expectations were that in the GSM-ZY plane, expansions solely in the Z direction indicate that the plasma sheet expands uniformly along the whole tail (Figure 3-20a). Alternatively a negative X component showing that the plasma sheet expands from the dipolar magnetic field region as the excess open flux is removed and the pressure is released (Figure 3-20b). Finally a positive X component of the expansion normal vector perhaps implies that the onset of expansion is initiated tailward of the spacecraft and therefore allowing expansion to begin and propagate Earthward (Figure 3-20c).

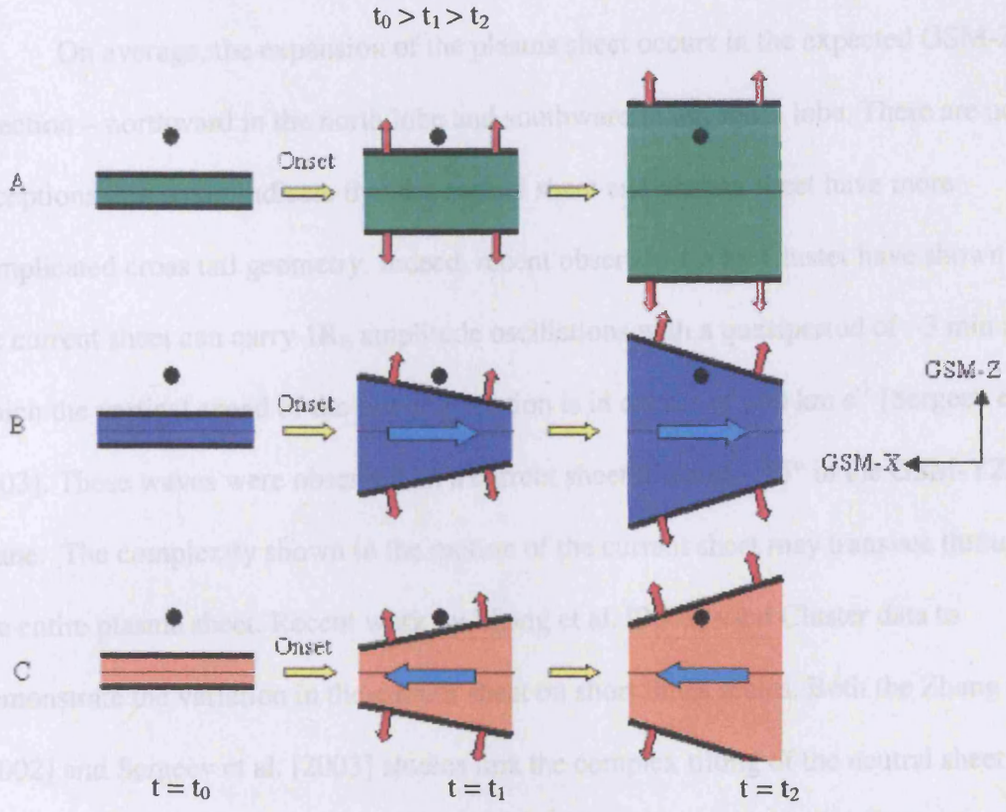

Figure 3-20 Plasma sheet expansion models
The normal vectors (red) of the lobe – plasma sheet boundary as the plasma sheet expands: A) uniformly down the X axis; B) tailwards from near the Earth; C) and, Earthwards from tailward of the spacecraft. For each case, the plasma sheet prior to onset and its subsequent expansion is shown. Any propagation direction of the expansion is also shown (cyan). The spacecraft quartet is shown as a black circle.

In the GSM-ZY plane, as shown in Figure 3-13, the projection of the expansion vectors should trace back to the average location of onset if the open flux is evenly distributed throughout the tail lobes and the expansion that occurs at the onset region is allowed to propagate radially away from the onset region in the GSM-YZ plane. The plasma sheet can also be tilted due to interplanetary magnetic field conditions [e.g.

Akasofu, 1986; Owen et al., 1995]. The complexity of the tail dynamics superposed upon the variable location and orientation of the plasma sheet adds to the difficulty in drawing definitive conclusions.

On average, the expansion of the plasma sheet occurs in the expected GSM-Z direction – northward in the north lobe and southward in the south lobe. There are notable exceptions that could indicate that the neutral sheet and plasma sheet have more complicated cross tail geometry. Indeed, recent observations by Cluster have shown that the current sheet can carry $1R_E$ amplitude oscillations with a quasiperiod of ~3 min in which the vertical speed of the flapping motion is in excess of 100 km s^{-1} [Sergeev et al., 2003]. These waves were observed on a current sheet tilted at ~ 45° in the GSM-YZ plane. The complexity shown in the motion of the current sheet may translate through to the entire plasma sheet. Recent work by Zhang et al. [2002] used Cluster data to demonstrate the variation in the current sheet on short times scales. Both the Zhang et al. [2002] and Sergeev et al. [2003] studies link the complex tilting of the neutral sheet to dawn-to-dusk wave propagation super-imposed onto the already tilted neutral sheet.

In the dusk sector of the south lobe there is predominately an expansion in the positive GSM-Y direction and, complementarily, a negative GSM-Y component in the dawn sector. This is consistent with the site of onset occuring mid-tail with expansion occurring dawnward and duskward. Figure 3-21 illustrates this mode of expansion in the GSM-YZ plan as viewed from the Earth looking tailward.

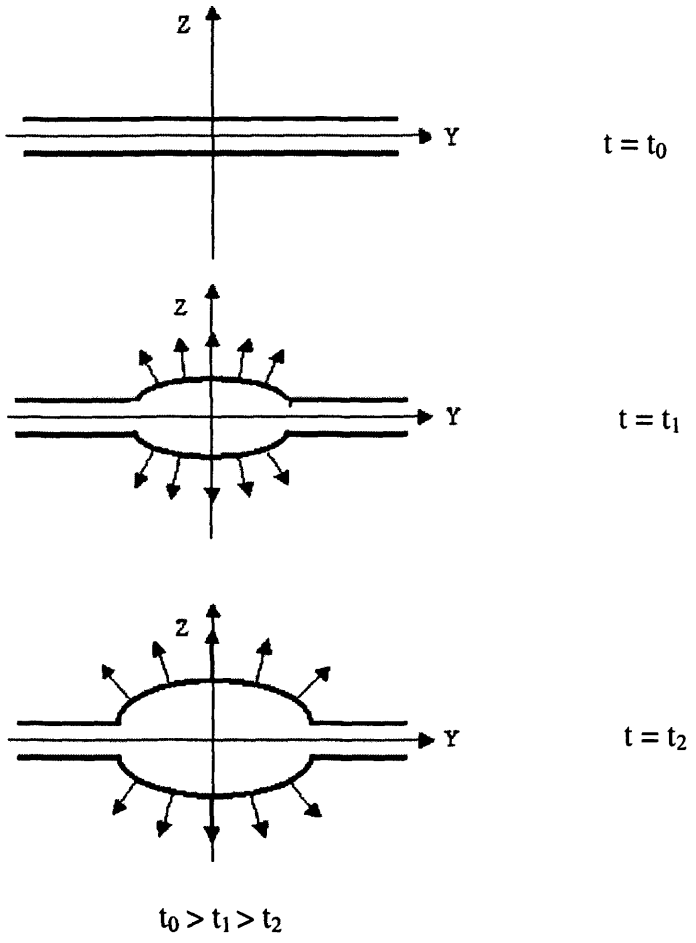

Figure 3-21 Plasma sheet expansion model (GSM-YZ plane)
An illustration of a model expansion of the plasma sheet in the GSM Y-Z plane as viewed from the Earth looking tailward. The onset region for the expansion is in the central GSM-Y region.

There is a negative GSM-Y component in most north lobe to plasma sheet expansions increasing in significance towards the dawn flank. Towards dawn, this would be consistent with expansion propagating from the central GSM-Y region of the plasma sheet. The negative GSM-Y component in the dusk sector would suggest that there is expansion of the plasma sheet that originates from a more positive GSM-Y location, possibly beyond GSM-Y =18 R_E, but it is likely that the lack of observations in this region has biased the results. If the expansion occurs principally in the normal of this

plane an extreme tilt of the current and plasma sheet [e.g. Akasofu, 1986] may cause the expansion to have a stronger GSM-Y component which otherwise looks like an anomalous boundary. The events that have a large component along the GSM-Y axis during entry into the plasma sheet are possibly attributed to dramatic tilting of the neutral sheet and plasma sheet structure [Sergeev et al., 2003].

Periods of repeated boundary crossings with varying normal directions indicate that the plasma sheet dynamics are highly complicated. These variations could be triggered by changes in the structure of the magnetosphere by variation in the IMF [Akasofu, 1986] or inherent plasma sheet inhomogenities, foe example.

In most of the data bins there is no major GSM-X component of the expansion normal as expansion in the GSM-YZ plane is dominant. No strong evidence has been obtained to favour either direction sense of the propagation of the plasma sheet expansion in the GSM-X direction, therefore neither mode of onset (current-disruption or near-Earth reconnection) can be said to predominate from this study. Simultaneous measurements from close to Cluster apogee and from the near-Earth are probably required to examine the propagation of the expansion. The possibility of X-line observations by Cluster at ~ -20 R_E also complicates the observation of plasma sheet thinning and expansion and require careful analysis to handle any complex topography near the expected neutral line region.

The explosive nature of the expansion phase is shown with velocities averaging ~61±37 km s^{-1}. This is approximately 20 km s^{-1} faster than that presented by Pytte et al. [1978]. Although our estimate is averaged over all distances away from the neutral sheet, the scatter of normal velocity component against distance calculated from the model

neutral sheet by Dandouras [1988], shown in Figure 3-19, provides no evidence of acceleration or deceleration of the plasma sheet – lobe boundary. Of note is the large standard deviation from the mean velocities: plasma sheet thinnings can be greater than the velocities associated with the subsequent plasma sheet expansion.

The observed thinnings of the plasma sheet show the expected GSM-Z direction, although there is significant variety in the GSM-Y components across the tail. This implies that there is a lot of variation in the tail during the growth phase and the variation in the thinning normal may be because of twisting of the tail or magnetic flux being added non-uniformly across the tail for example. The possibility of post-flow associated thinning of the plasma sheet being included in this study exists, but is believed to be minimised by the AE selection criteria.

The difference in the speeds of the thinnings to expansions is understandable in terms of the explosive nature of substorm onset, although the details of the individual pairs of thinning to expansion speeds shows that thinnings speeds can comparable to expansion speeds.

3.5 Conclusions

In the 2001 and 2002 magnetotail passes, 77 expansions of the plasma sheet over the Cluster quartet were clearly observed. The direction and normal velocity were calculated for these events and the principle observation was the main direction of the expanding plasma sheet was in the GSM-YZ plane. There is insufficient evidence in this dataset to determine whether the expansion of the plasma sheet begins at the region associated with current disruption and propagates tailward or in the vicinity of the near-Earth neutral line and propagates tailward. Higher temporal resolution or multiple

observation sites along the axis of the magnetotail are required. The presented data confirms the expected complexity of the plasma sheet and its dynamics and high degrees of tilting or undulations of the plasma sheet in the GSM Y-Z plane may explain the range of directions of the expansion normal. The more variable nature of the thinning normal may be explained by tilting of the magnetotail during the growth phase or by the non-uniform addition of magnetic flux along the cross-section of the tail.

4 Flow Shears and Field-Aligned Current Generation

4.1 Introduction

Field-aligned currents (FACs) form a fundamental link between the magnetosphere and the ionosphere. For example, during geomagnetic substorms, field-aligned currents are formed during the disruption of the cross-tail current and direct this current into and then out of the ionosphere forming the substorm current wedge [Atkinson, 1967; McPherron et al., 1973]. Many studies of the large-scale substorm current wedge system have been made from ground measurements and from spacecraft at or near geostationary orbit [e.g. Shiokawa et al., 1998]. Previous studies have observed the large-scale phenomena that occur during dynamic intervals, but have not studied the short time and spatial scales.

An important example of field-aligned current generation is shown in MHD simulations of the magnetotail [Birn et al., 1996]. During dipolarizations of magnetic field lines, the equatorial flux tubes are deflected away from the midnight sector as they move closer to the Earth. Moreover, they experience greater deflection than those field lines at higher latitudes. The associated magnetic shear or twist gives a rotation of the field direction which drives a current in the same sense as ionospheric current systems associated with dipolarizations. This FAC generation mechanism is illustrated in Figure 4-1.

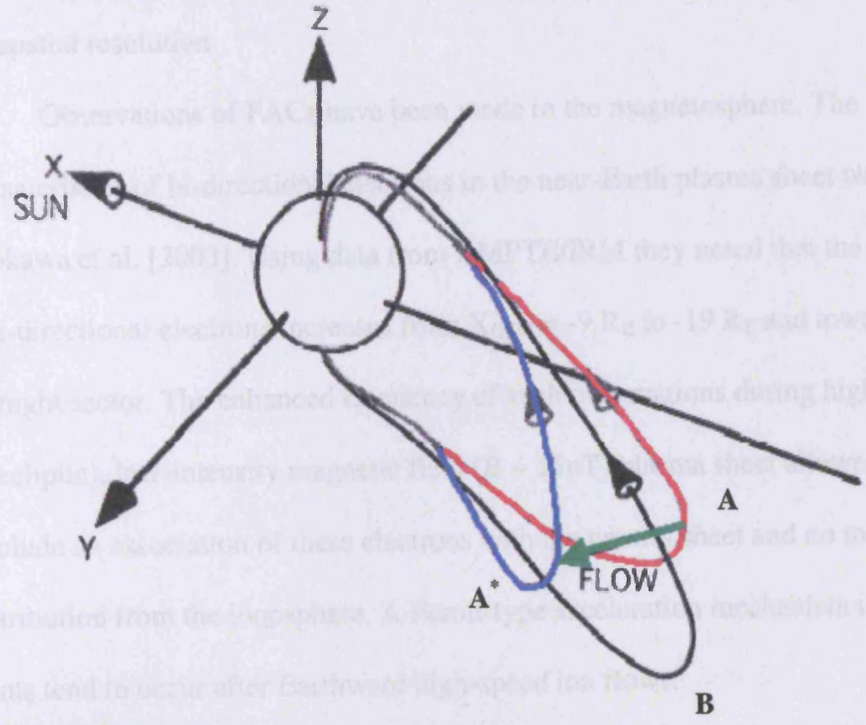

Figure 4-1 Scenario for FAC generation by sheared magnetic fields
Field line A is forced to move to location A* when it encounters the dipolar field region of the Earth as it propagates Earthward after reconnection. There is a shear between this field line and those of higher latitude (e.g. field line B) and hence a parallel current shall flow. This is a proposed mechanism for field-aligned current generation in the braking region [Birn, 1996].

MHD simulations using data from the Geotail, Interball and IMP8 data have also verified the creation of the field-aligned currents that form the substorm current wedge [El-Alaoui, 2001]. In a simulation of a substorm event, the cross-tail current density decreased in a region in the near-Earth plasma sheet and currents were deflected into the ionosphere. This simulation showed that the field-aligned currents were associated with velocity shears and flow vortices. The coupling effect of shear flows and pressure gradients and other instabilities at the inner edge of the plasma sheet have also been proposed as being important in the vortex generation and auroral arc intensification [Voronkov et al., 1997]. Troshichev [2004] examines plasma pressure gradients as a

viable field-aligned current generation mechanism. This author also comments on the lack of knowledge of the plasma pressure within the plasma sheet at a suitable temporal and spatial resolution.

Observations of FACs have been made in the magnetosphere. The occurrence characteristics of bi-directional electrons in the near-Earth plasma sheet were studied by Shiokawa et al. [2003]. Using data from AMPTE/IRM they noted that the occurrence rate of bi-directional electrons increases from X_{GSM} = -9 R_E to -19 R_E and towards the midnight sector. The enhanced frequency of such observations during high-elevation (to the ecliptic), low-intensity magnetic field (B ~ 15nT) plasma sheet allowed the authors to conclude an association of these electrons with the neutral sheet and no major contribution from the ionosphere. A Fermi-type acceleration mechanism is implied, as the events tend to occur after Earthward high-speed ion flows.

Plasma flow and magnetic field shears proceeding a depleted flux tube [Pontius and Wolf, 1990] convecting Earthward in the plasma sheet [Sergeev et al., 1996] provide another example of situations where field-aligned current generation should occur. Flow bursts in the plasma sheet that are associated with small auroral expansions have been studied with the Geotail spacecraft [Nakamura et al., 2001]. The observation of flow bursts associated with strong flow shears were noted tailward of 15 R_E.

Expressions for the field-aligned current density in a magnetized plasma in relation to the twist or shear of the magnetic field were derived by Southwood and Kivelson [1991]. These authors have continued and simplified work by Hasegawa [1979].

A background field **B**, which need not be uniform, carries a current, **j**, described by:

$$\nabla \times \mathbf{B} = \mu_0 \mathbf{j} \tag{4.1}$$

Taking the current as parallel and perpendicular components:

$$\mathbf{j} = \mathbf{j}_\perp + \mathbf{j}_\parallel \tag{4.2}$$

where $\mathbf{j}_\perp = j_\perp \hat{\mathbf{e}}_\perp$ and $\mathbf{j}_\parallel = j_\parallel \hat{\mathbf{e}}_\parallel$ are along appropriate unit vectors, allows the study of how the individual components of a magnetic field perturbation, **b**, affect the currents in the system. By initially taking the scalar product of Equation 4.1 with the unit magnetic field $\hat{\mathbf{B}}$ stipulating that there is no initial parallel currents gives:

$$(\nabla \times \mathbf{B}) \cdot \hat{\mathbf{B}} = \mu_0 \mathbf{j}_\perp \cdot \hat{\mathbf{B}} = 0 \tag{4.3}$$

If we now allow a small perturbation magnetic field, **b**, which may in general be associated with a FAC we can describe this parallel current using:

$$\mu_0 j_\parallel = (\nabla \times \mathbf{b}) \cdot \hat{\mathbf{B}} \neq 0 \tag{4.4}$$

Compressional and transverse components of the field perturbation can be extracted using:

$$\mathbf{b} = \mathbf{b}_\perp + \mathbf{b}_\parallel \tag{4.5}$$

where $\mathbf{b}_\perp = b_\perp \hat{\mathbf{e}}_\perp$ and $\mathbf{b}_\parallel = b_\parallel \hat{\mathbf{e}}_\parallel$, leads to:

$$\nabla \times (\mathbf{b}_\perp + \mathbf{b}_\parallel) \cdot \hat{\mathbf{B}} = (\nabla \times \mathbf{b}_\perp) \cdot \hat{\mathbf{B}} + (\nabla \times \mathbf{b}_\parallel) \cdot \hat{\mathbf{B}} \tag{4.6}$$

Applying Equation 4.3 and the identity:

$$\nabla \cdot (\mathbf{A} \times \mathbf{B}) = \mathbf{B} \cdot (\nabla \times \mathbf{A}) - \mathbf{A} \cdot (\nabla \times \mathbf{B})$$

Equation 4.6 is reduced to show that only variations in the perpendicular component of a magnetic field perturbation affect the parallel current, i.e.:

$$\mu_0 j_{\parallel} = (\nabla \times \mathbf{b}_{\perp}) \cdot \hat{\mathbf{B}} \tag{4.7}$$

From the frozen-in condition:

$$\mathbf{E} = -\mathbf{v} \times \mathbf{B} \tag{4.8}$$

and

$$\nabla \times \mathbf{E} = \frac{\partial \mathbf{B}}{\partial t} \tag{4.9}$$

it can be shown that:

$$\mathbf{b} = \nabla \times (\xi \times \mathbf{B}) \tag{4.10}$$

where

$$\mathbf{u} = \frac{\partial \xi}{\partial t} \tag{4.11}$$

is the velocity representing the rate of change of the magnetic field displacement from the unperturbed location. Substituting Equation 4.10 in to Equation 4.7 gives:

$$\mu_0 j_{\parallel} = (\nabla \times \nabla \times (\xi \times \mathbf{B})) \cdot \hat{\mathbf{B}}$$

and with application of the following identity:

$$\nabla \times (\mathbf{A} \times \mathbf{B}) = \mathbf{A}(\nabla \cdot \mathbf{B}) - \mathbf{B}(\nabla \cdot \mathbf{A}) + (\mathbf{B} \cdot \nabla)\mathbf{A} - (\mathbf{A} \cdot \nabla)\mathbf{B}$$

leads to:

$$\mu_0 j_{\parallel} = \mathbf{B} \cdot \nabla\left(\hat{\mathbf{B}} \cdot (\nabla \times \xi)\right) \tag{4.12}$$

Applying Equation 4.11 to Equation 4.12 gives the parallel current in terms of the parallel component of vorticity, $\Omega_{\parallel}$:

$$\mu_0 j_{\parallel} = \int_0^t dt \mathbf{B} \cdot \nabla\left[\mathbf{B} \cdot \frac{(\nabla \times \mathbf{u})}{B}\right] = \int_0^t dt \mathbf{B} \cdot \nabla \boldsymbol{\Omega}_{\parallel} \tag{4.13}$$

The gradient of the parallel component of vorticity indicates that the stronger the vortex the stronger the FAC will be. The time integral also implies that a FAC becomes stronger if the vortex lasts for an extended period of time. The significances of the vorticity and time integral parts of Equation 4.13 are shown in Figure 4-2 where a force acts on a flux tube generating a curl of the magnetic field which will become more wound up with time.

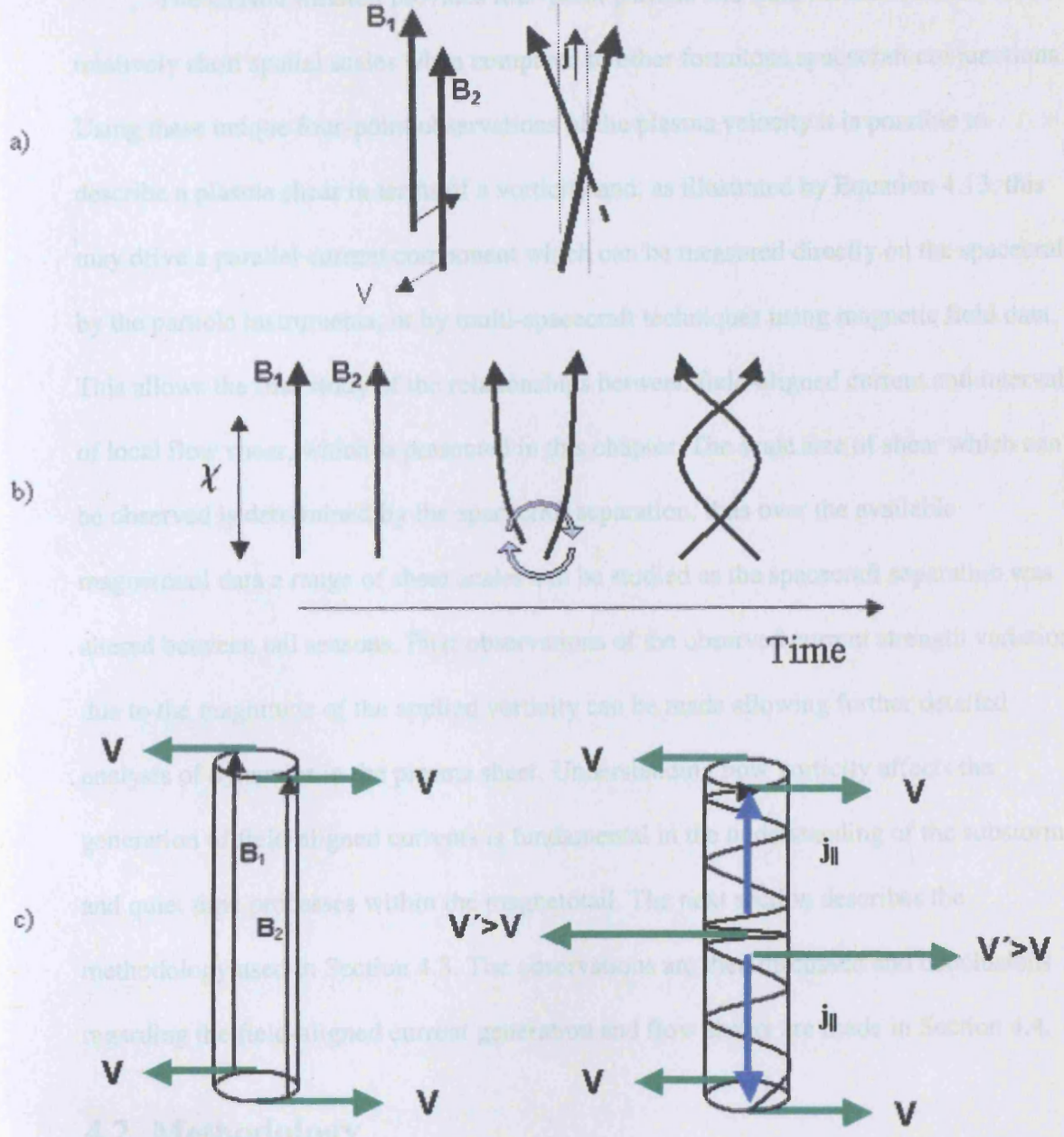

Figure 4-2 FAC generation on twisted flux-tube
a) Two magnetic field lines, B_1 and B_2, are subject to oppositely directed forces (shown as a velocity field) at one end of the field-lines. The field lines are sheared and a parallel current density, $j_{||}$, results. b) If the field-lines are subjected to a continuous shear then a twisted pair of field lines is produced. c) If the same shearing device is applied evenly along the field lines then no current density is produced: a gradient in the shear is required to produce the twisted field lines that produce the current density.

The Cluster mission provides four-point particle and field measurements over relatively short spatial scales when compared to other fortuitous spacecraft conjunctions. Using these unique four-point observations of the plasma velocity it is possible to describe a plasma shear in terms of a vorticity and, as illustrated by Equation 4.13, this may drive a parallel current component which can be measured directly on the spacecraft by the particle instruments, or by multi-spacecraft techniques using magnetic field data. This allows the first study of the relationships between field-aligned current and intervals of local flow shear, which is presented in this chapter. The scale size of shear which can be observed is determined by the spacecraft separation, thus over the available magnetotail data a range of shear scales can be studied as the spacecraft separation was altered between tail seasons. First observations of the observed current strength variations due to the magnitude of the applied vorticity can be made allowing further detailed analysis of dynamics in the plasma sheet. Understanding how vorticity affects the generation of field-aligned currents is fundamental in the understanding of the substorm and quiet time processes within the magnetotail. The next section describes the methodology used in Section 4.3. The observations are then discussed and conclusions regarding the field-aligned current generation and flow shears are made in Section 4.4.

4.2 Methodology

A survey of the Cluster burst mode dataset from 2001 and 2002 was performed to identify intervals in which electron and ion flow shears existed across the spacecraft quartet. The survey was restricted to the burst mode dataset, of which there is more during 2002, to ensure the fullest electron distributions were obtained and the electron moments could be calculated using ground calibration techniques in which photoelectron

and spacecraft potential effects could be removed. The importance of using the most complete electron dataset is due to there being no 4 spacecraft ion measurements due to the failure of one of the CIS instruments. A flow shear was identified if a maximum flow difference of at least 100 kms^{-1} over the spacecraft tetrahedron was identified in that interval. For each event selected, a detailed analysis of the location of the spacecraft in relation to the plasma sheet boundary layer was performed. Events for study were only selected if the flow shear occurred when the spacecraft were located purely in the plasma sheet to avoid fast field-aligned flow along the PSBL from any reconnection site down tail interfering with our analysis [e.g. Eastman et al., 1984].

Three intervals were selected for detailed study: 18:00 – 18:15 UT 18th August 2002, 17:55 – 18:15 UT 25th August 2002 and 18:50 –19:00 UT 13th September 2002. For each interval the location of each spacecraft within the plasma sheet / lobe plasma regimes were identified in terms of the plasma beta. The central plasma sheet (CPS) is identified at $\beta > 0.5$ [e.g. Schödel et al., 2001]. The calculation of the plasma vorticity within the CPS was made to predict where enhancements of the field-aligned currents might be expected according to Equation 4.13. We then search for corresponding field-aligned flows in both pitch-angle distributions and by moment calculation. Comparison with the average parallel current density across the spacecraft tetrahedron was then made using the magnetic field curlometer technique [Dunlop, 2002, and references therein].

In the curlometer technique, Ampere's law is used to estimate the average current density through the tetrahedron formed by the spacecraft. The current density passing through each face of the tetrahedron as shown in Figure 4-3 (i.e. that of formed by spacecraft [1, *i*, *j*] in the following notation, where index *i* and *j* are indexes of other

spacecraft) is calculated:

$$\mu_0 \mathbf{J} \cdot (\Delta \mathbf{r}_i \times \Delta \mathbf{r}_j) = \Delta \mathbf{B}_i \cdot \Delta \mathbf{r}_j - \Delta \mathbf{B}_j \cdot \Delta \mathbf{r}_i \quad (4.14)$$

where

$$\Delta \mathbf{r}_i \equiv \mathbf{r}_i - \mathbf{r}_1 \text{ and } \Delta \mathbf{r}_j \equiv \mathbf{r}_j - \mathbf{r}_1 \quad (4.15)$$

$$\Delta \mathbf{B}_i \equiv \mathbf{B}_i - \mathbf{B}_1 \text{ and } \Delta \mathbf{B}_j \equiv \mathbf{B}_j - \mathbf{B}_1 \quad (4.16)$$

With knowledge of the tetrahedron configuration, the normal to each face is known and hence the current densities can then be rotated into a geophysical coordinate system. By summing the vectors produced through 3 sides (the fourth being redundant but suitable for verification purposes) the average current density can be calculated and converted into geophysical co-ordinates.

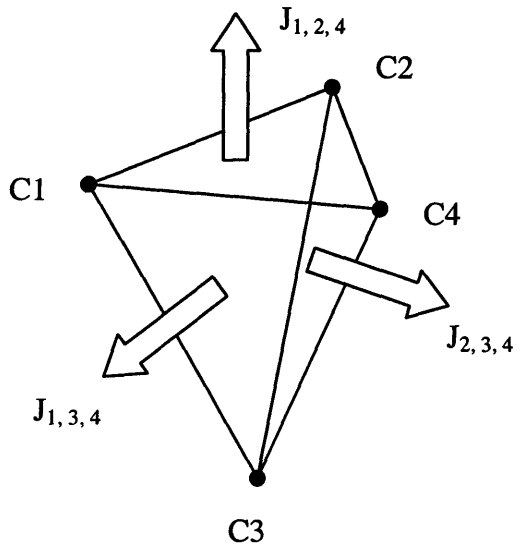

Figure 4-3 Current components through each face of the Cluster tetrahedron
Through each face, labelled as [1, *i*, *j*] where *i* and *j* are indices of the other spacecraft, a current density normal to this plane can be calculated. Knowledge of the spacecraft positions allows the total current passing through the tetrahedron to be calculated in geophysical co-ordinates. The fourth side (not labelled) is redundant and can be used a consistency check.

The principle assumption in this technique is that the magnetic field varies linearly over the spacecraft tetrahedron so that $\boldsymbol{J}$ is constant over the volume. This is valid if the spacecraft separation is much less than the length scales of the variation of the current density. However, it is noted by Dunlop et al. [2002] that even if this assumption is not valid and the estimation of the current density is inaccurate, it may still reflect real effects within the volume. An estimate of div B can also be obtained from this technique and is a useful measure of the validity of the approximation of Curl B, as it is dependent on the errors incurred from the difference approximation and also from the errors associated with the measurement.

In this chapter, we adopt a similar technique in order to assess the curl of the electron velocity field. Where possible, the electron convective flow is checked with available ion measurements and with $\mathbf{E}\times\mathbf{B}$ drift calculations. From Equation 4.8 only the shear in the convective motion $\mathbf{u}_\perp$ gives a component of $\boldsymbol{\Omega}_{\|}$, and since we expect both ions and electrons to remain frozen-in in this regime, $\mathbf{u}_{\perp e}$ should be identical to $\mathbf{u}_\perp = \mathbf{E}\times\mathbf{B}$. Specifically we use the function form:

$$\boldsymbol{\Omega} = \Delta\mathbf{u}_i \cdot \Delta\mathbf{r}_j - \Delta\mathbf{u}_j \cdot \Delta\mathbf{r}_i \qquad (4.17)$$

where

$$\Delta\mathbf{r}_i \equiv \mathbf{r}_i - \mathbf{r}_1 \text{ and } \Delta\mathbf{r}_j \equiv \mathbf{r}_j - \mathbf{r}_1 \qquad (4.18)$$

$$\Delta\mathbf{u}_i \equiv \mathbf{u}_i - \mathbf{u}_1 \text{ and } \Delta\mathbf{u}_j \equiv \mathbf{u}_j - \mathbf{u}_1$$

and the vorticity is calculated in the same way as the curl of the magnetic field in the curlometer technique.

4.3 Application of Methodology

For each event an overview of the electron data from PEACE and magnetic field data from FGM will be presented. In addition to this data, the plasma beta calculated for both the electron and ion data will be presented to aid the identification of the central plasma sheet. It is important to ensure that flow shears are correctly identified within the central plasma sheet, as fast flows on the plasma sheet boundary layer associated with reconnection could complicate and misguide the data interpretation.

Following each overview, details of the electron and ion flows perpendicular to the magnetic field are presented to identify flow shears of interest to this study. As mentioned in Chapter 2, there is a V_Z offset due to calibration issues of the anode response from the spin-axis sections of the sensor. As this work requires the computation of the full electron velocity, it is necessary to correct for any offsets that exists in the data to allow meaningful conclusions to be drawn. The calibration issue remains open and complex, and may vary for each detecting anode and energy range. This may also be complicated by degradation of the sensors with time. To date, no routine method for optimal calibration has been derived and each event is taken on a case-by-case basis. For each event a simple estimation of the associated V_Z offset for the PEACE data was made. This was performed by taking three 10 minute intervals around the interval of study where no significant flows are observed. The velocity data was then averaged and then the average V_Z measurement over the three intervals was subtracted off the study interval. In Table 4-1, the V_Z offsets for each spacecraft over the study intervals are shown. All PEACE velocity data presented in this chapter have had these offsets applied to them.

Interval	Cluster 1	Cluster 2	Cluster 3	Cluster 4
18th August 2002	140	-79	277	410
25th August 2002	52	-136	165	219
13th September 2002	199	2	503	499

Table 4-1 V_Z offsets (km s^{-1}) for each of the Cluster spacecraft.

To verify the usage of these moments for subsequent analysis a comparison is made to the perpendicular component of the $\mathbf{E}\times\mathbf{B}$ velocity. Agreement in the $V_{\perp Z}$ between the electrons and the other data sets is the key factor in deciding if the moments are suitable for vorticity calculations. Once a fully calibrated and corrected dataset is available, multi-point techniques may be used without this concern. The electric field used has taken the electric field from the spin plane and has incorporated the assumption that $E \cdot B = 0$ to produce the electric field vector along the spin axis. This assumption may not hold and the Principle Investigator team has removed data in cases where this assumption may not be valid. In a more detailed study the validity of the electric field data should be checked as it may not produce a valid benchmark dataset for comparison with PEACE data after it has been combined with the magnetic field data. In the examples presented in this thesis, the electric field data has assumed to be suitable for the comparisons attempted and no validation of its suitability has been performed. Intervals where this assumption may not hold are identified and the data should be re-evaluated to ensure its accuracy. This type of work is on-going between the investigating teams to aid each other in calibration issues.

After the identification of the periods of perpendicular flow shears, an assessment of the parallel component of vorticity using the 4-spacecraft technique described above is made using the magnetic field at the barycentre of the tetrahedron. This is compared to the parallel components of the currents observed at each spacecraft and also to the parallel component of the current through the tetrahedron as provided from the magnetic field curlometer technique.

To summarise the presented data, correlation plots are then presented to indicate to what level flow shears are associated with field-aligned currents.

4.3.1 18:00 – 18:15 UT 18th August 2002

During the interval 18:00 – 18:15 UT 18th August 2002 the Cluster quartet was located at (-18.0, -5.2, 2.3) $R_{E\,GSM}$. The spacecraft configuration was as shown in Figure 4-4. Cluster 2 is located furthest north followed by Clusters 4 and 1. Cluster 1 is separated in GSM-X from the other spacecraft by ~3000 km. Cluster 2 is separated from Cluster 1 and 4 in GSM-Y also. The AE index for the 18th August 2002 is shown in Figure 4-5. During the interval of interest the AE was ~100 nT with no proximity to a substorm onset or intensification implying that we would not expect to observe any substorm related currents in the magnetotail, however, flow shears may be present and quiet-time currents may exist.

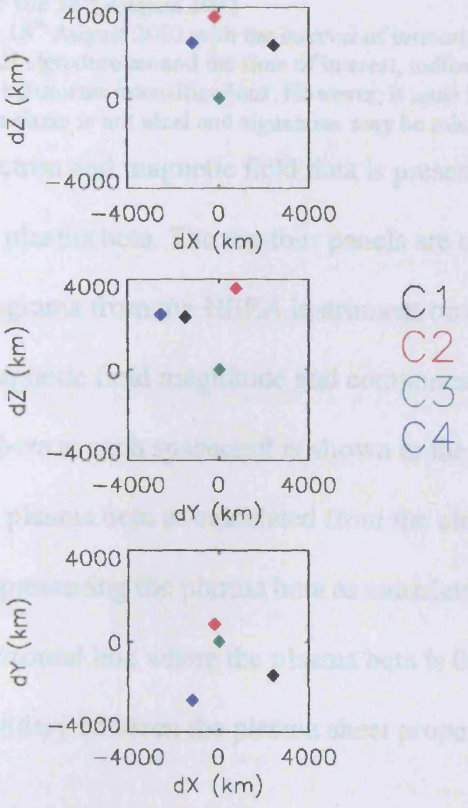

Figure 4-4 Cluster configuration on 18th August 2002
The spacecraft tetrahedron configuration is presented. The Cluster spacecraft are represented in their standard colours.

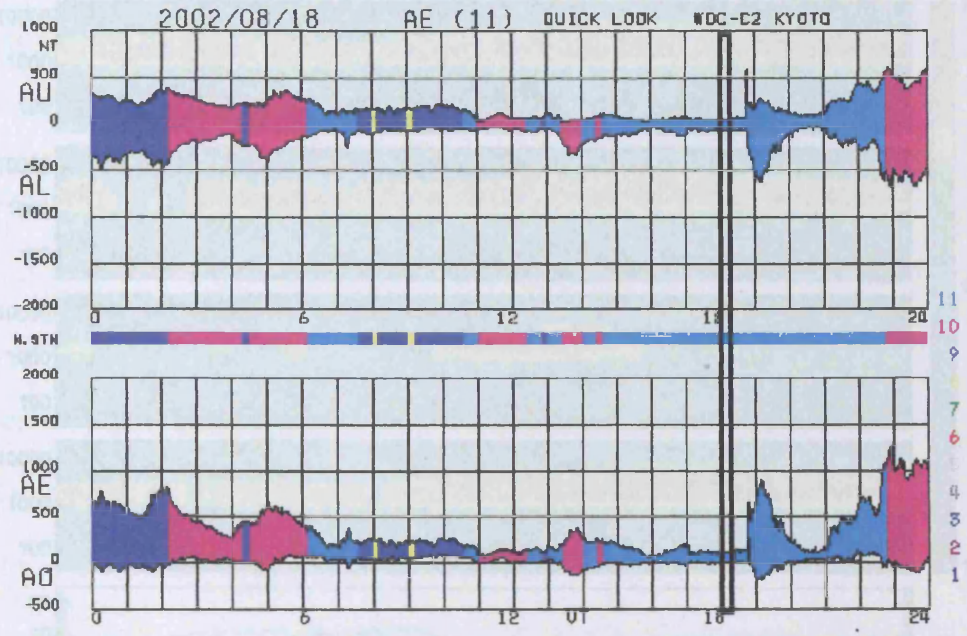

Figure 4-5 The AE index for the 18th August 2002
The AE index is show for the 18th August 2002 with the interval of interest marked. The lack of any sharp increase in the AE signature around the time of interest, indicated by the black box, implies that there are no substorms intensifications. However, it must be noted that the coverage of the magnetometer chain is not ideal and signatures may be missed.

An overview of the electron and magnetic field data is presented in Figure 4-6 together with a measure of the plasma beta. The top four panels are omni-directional differential energy flux spectrograms from the HEEA instrument on each spacecraft. The next four panels contain the magnetic field magnitude and components in the GSM coordinate frame. The plasma beta at each spacecraft is shown in the bottom panel with the solid lines representing the plasma beta as calculated from the electron number density and the dashed lines representing the plasma beta as calculated from the proton density where available. A horizontal line where the plasma beta is 0.5 is marked on the last panel as a guide to the boundary between the plasma sheet proper and the plasma sheet boundary layer.

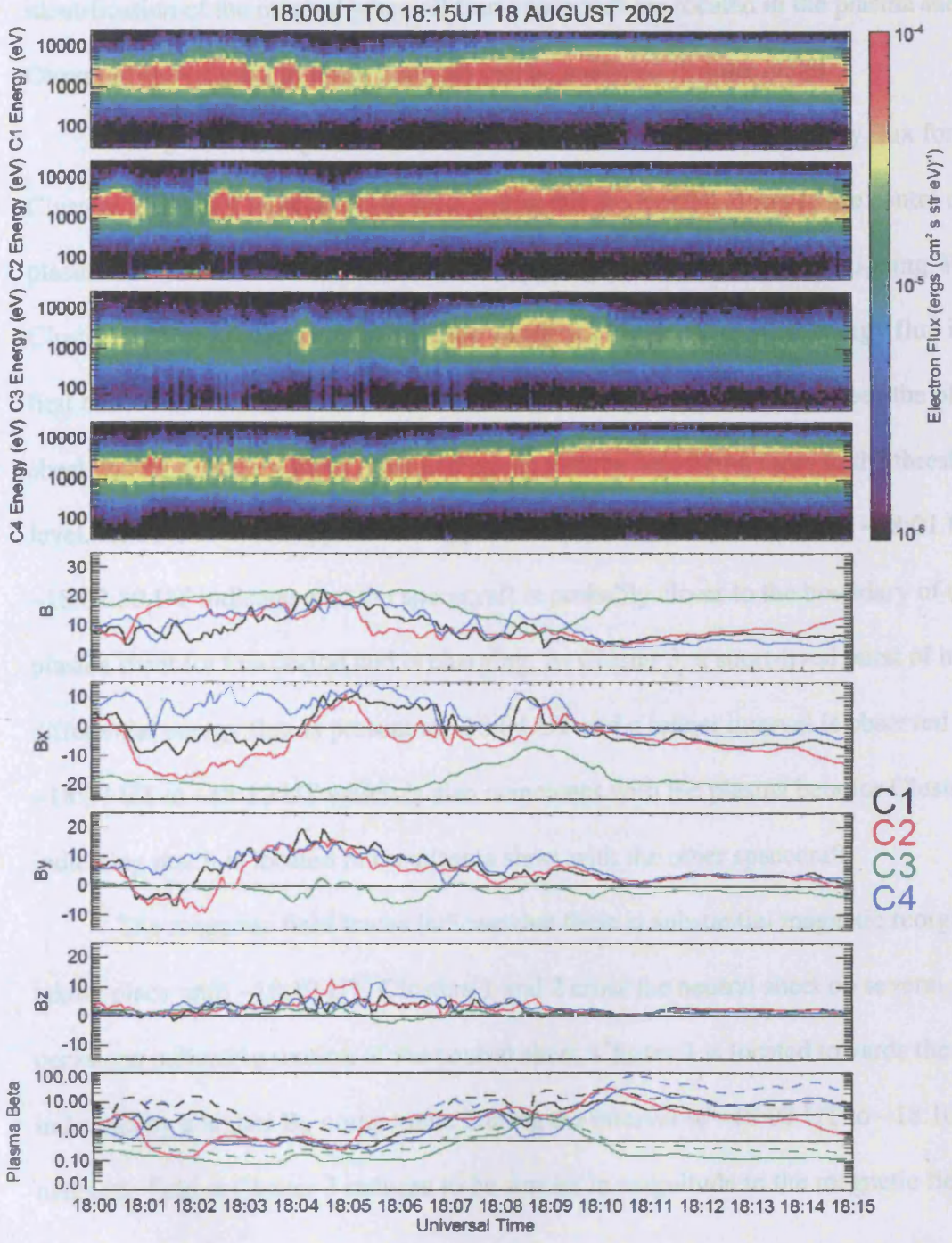

Figure 4-6 PEACE and FGM data for 18th August 2002
Omni-direction electron differential energy flux spectrograms are shown for each spacecraft together with the magnetic field magnitude and components in the GSM co-ordinate frame. The plasma beta is shown (solid for electrons and dashed for protons) with the 0.5 plasma sheet cut-off marked.

A description of the electron and magnetic field data follows to allow the identification of the interval when all four spacecraft are located in the plasma sheet. Observed flow shears in those intervals can be analysed in more detail.

The generally higher omni-directional electron differential energy flux for Clusters 1, 2 and 4 indicates that these spacecraft are located closer to the centre of the plasma sheet than Cluster 3, which is consistent with the spacecraft positioning. For Clusters 1, 2 and 4 there are small scale variations in the differential energy flux in the first half of the data shown and this is associated with the crossing between the plasma sheet and its boundary layer indicated by the plasma beta being close to the threshold level. At Cluster 2, the appearance of photoelectrons in the plot between ~18:01 UT and ~18:02:30 UT indicates that the spacecraft is probably closer to the boundary of the plasma sheet for this period and is charging. At Cluster 3, a short-lived burst of higher differential energy flux is present at ~18:04 UT and a longer interval is observed from ~18:07 UT to ~18:10 UT which is also coincident with the plasma beta for Cluster 3 indicating that it is located in the plasma sheet with the other spacecraft.

The magnetic field traces indicate that there is substantial magnetic reorganisation taking place until ~18:10 UT. Clusters 1 and 2 cross the neutral sheet on several occasions indicating motion of the neutral sheet. Cluster 3 is located towards the lobes as indicated by a higher B_X component. During the interval of ~18:07 UT to ~18:10 UT the magnetic field at Cluster 3 reduces to be similar in magnitude to the magnetic field at the other spacecraft.

From this data description the interval of interest for multi-spacecraft analysis of the flow shears within the plasma sheet is ~18:07:30 UT and ~18:10 UT. The

perpendicular flows at each spacecraft are shown in Figure 4-7 in magnitude and components in the GSM co-ordinate frame.

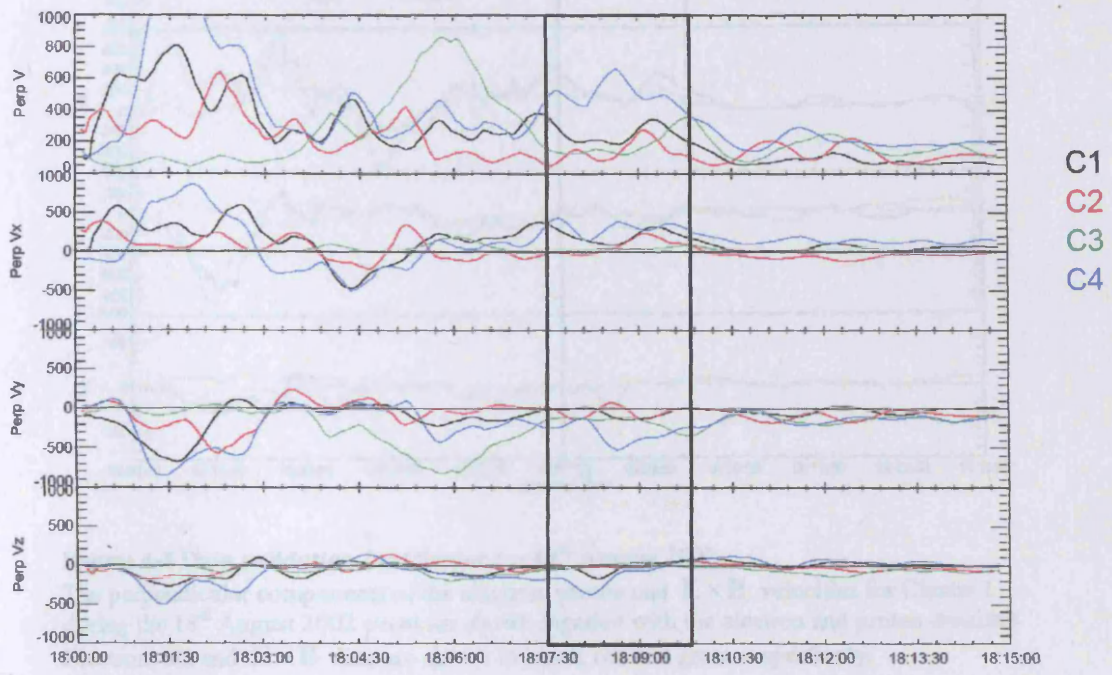

Figure 4-7 Perp electron velocity to indicate flow shears – 18th August 2002
The perpendicular velocity and GSM components are shown for each Cluster spacecraft to illustrate the flow shears that are observed during this interval.

The velocity data for this event is verified to check its suitability for multi-spacecraft analysis after the correction of the PEACE data for the V_Z offset. Comparison is made between the perpendicular components of the electron velocity, the CIS/CODIF proton velocity (when available) and the $\mathbf{E}\times\mathbf{B}$ velocity and is shown in Figure 4-8 - Figure 4-11. The number density of electrons and protons are also shown for comparison. Electron, ion and $\mathbf{E}\times\mathbf{B}$ data are shown in black, red and green respectively. The interval of interest between ~18:07:30 and ~18:10:00 UT is marked by a black box.

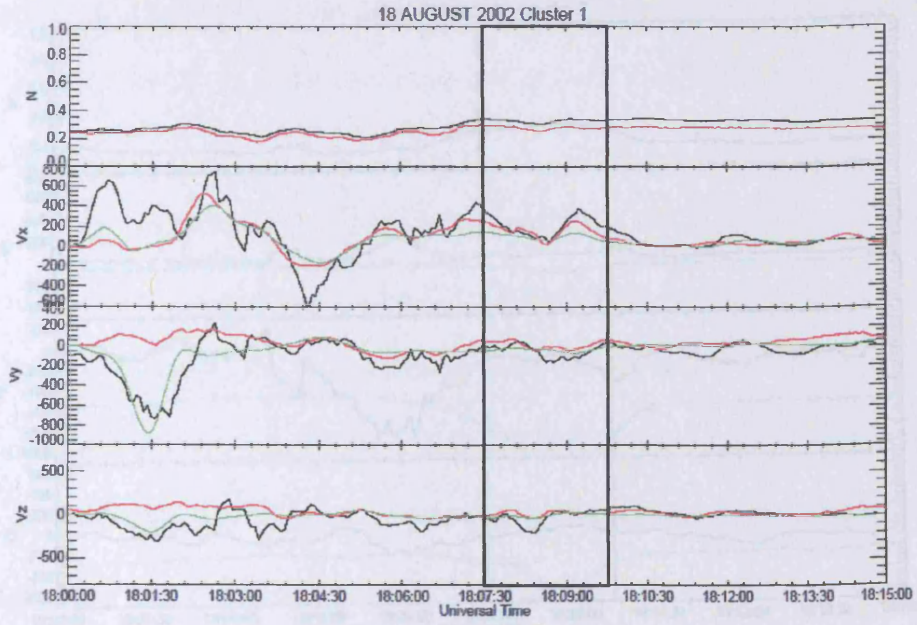

Figure 4-8 Data validation for Cluster 1 – 18th August 2002
The perpendicular components of the electron, proton and $\mathbf{E}\times\mathbf{B}$ velocities for Cluster 1 during the 18th August 2002 event are shown together with the electron and proton densities. Electron, ion and $\mathbf{E}\times\mathbf{B}$ data are shown in black, red and green respectively.

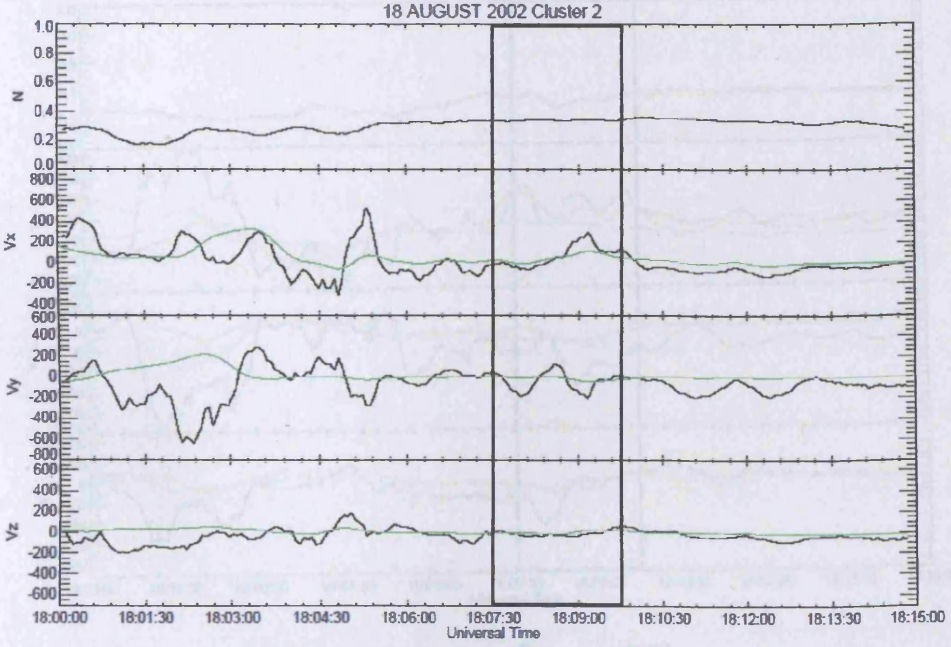

Figure 4-9 Data validation for Cluster 2 – 18th August 2002

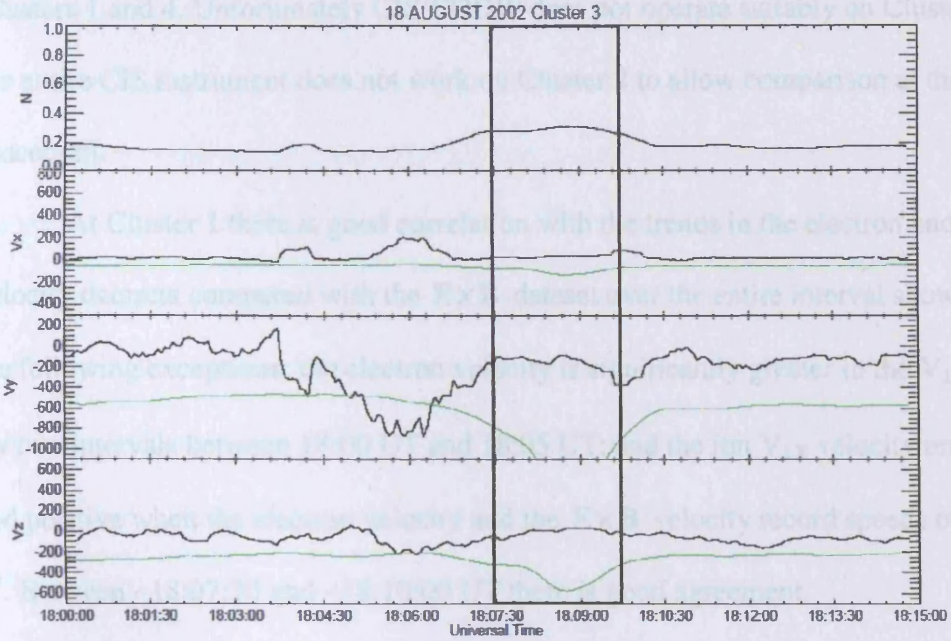

Figure 4-10 Data validation for Cluster 3 – 18th August 2002
The perpendicular components of the electron and $\mathbf{E}\times\mathbf{B}$ velocities for Cluster 3 during the 18th August 2002 event are shown together with the electron density. Electron and $\mathbf{E}\times\mathbf{B}$ data are shown in black and green respectively.

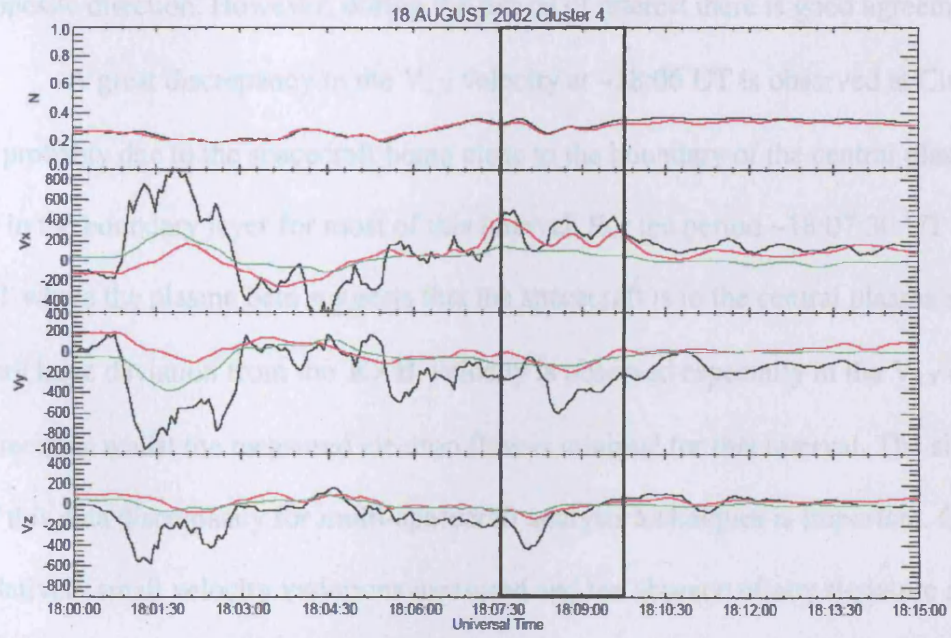

Figure 4-11 Data validation for Cluster 4 – 18th August 2002

There is good correlation in the electron and proton number densities measured by Clusters 1 and 4. Unfortunately CIS/CODIF does not operate suitably on Cluster 3 and the entire CIS instrument does not work on Cluster 2 to allow comparison at these spacecraft.

At Cluster 1 there is good correlation with the trends in the electron and ion velocity datasets compared with the $\mathbf{E}\times\mathbf{B}$ dataset over the entire interval shown noting the following exceptions: the electron velocity is significantly greater in the $V_{\perp X}$ direction for two intervals between 18:00 UT and 18:05 UT; and the ion $V_{\perp Y}$ velocity remains slow and positive when the electron velocity and the $\mathbf{E}\times\mathbf{B}$ velocity record speeds of ~700 km s^{-1}. Between ~18:07:30 and ~18:10:00 UT there is good agreement.

Similar disagreements occurs at Cluster 2 in the $V_{\perp Y}$ velocity as shown in Figure 4-9, this time the electron data is ~4 times the magnitude of the $\mathbf{E}\times\mathbf{B}$ velocity and in the opposite direction. However, during the period of interest there is good agreement.

A great discrepancy in the $V_{\perp Y}$ velocity at ~18:06 UT is observed at Cluster 3 and is probably due to the spacecraft being close to the boundary of the central plasma sheet or in the boundary layer for most of this interval. For the period ~18:07:30 UT to ~18:10 UT where the plasma beta suggests that the spacecraft is in the central plasma sheet, a very large deviation from the $\mathbf{E}\times\mathbf{B}$ velocity is observed especially in the $V_{\perp Y}$ and $V_{\perp Z}$ directions whilst the measured electron flow is minimal for this interval. The significance of this data discrepancy for multi-spacecraft analysis techniques is important. Given the relatively small velocity variations measured and the absence of any signature associated with a large change in flow speed or direction the data will result in an over-estimate or

under-estimate of the vorticity magnitude, but the sense direction of the vorticity should remain significant.

At Cluster 4 there is a set of large electron velocity differences early on in the interval shown and the passage of the moving neutral sheet may be the cause of the large differences observed during this interval. During the interval ~18:07:30 UT to ~18:10:00 UT there is good similarity between the ion and electron motion in the V_X direction, whilst in V_Y and V_Z directions the measured ion velocity are similar to the $\mathbf{E}\times\mathbf{B}$ velocity where the electrons deviate in magnitude but follow the same direction.

When all 4 spacecraft are located within the central plasma sheet there are differences to the electron and ion velocities, but, apart from spacecraft 3, the velocity components appear realistic for further analysis. As mentioned, the difference at Cluster 3 during the period of interest would result in an under- or over-estimate in a calculated vorticity as the measured velocity components are small. The magnitude of the vorticity should therefore be read with caution, however, variations in the direction of the vorticity and magnitude may be physically meaningful.

A further test to examine the suitability of the data is to compare the parallel component of the curl of the electron velocity and parallel component of the curl of the velocity as calculated from the electric and magnetic fields.

A strong correlation would indicate that these two datasets are comparable and that the velocity moments are suitable for multi-spacecraft analysis techniques. A low correlation would indicate that further investigation into the dataset would need to be carried out to assess the suitability of the data with physical phenomena and data calibration issues being considered. In the case of poor correlation, the PEACE moments

may still be valid with the discrepancy being associated with the assumptions used in the calculation of the spin-axis component of the electric field.

For this event, a correlation coefficient of -0.74 is found indicating a strong anti-correlation. This suggests that the datasets are not comparable. The discrepancy of the observed velocity data from PEACE and that of from $\mathbf{E}\times\mathbf{B}$ on Cluster 3 is likely to be the cause. If the perpendicular component of the vorticity from the electron data and from $\mathbf{E}\times\mathbf{B}$ are compared then a strong correlation is found. This could be associated with a breakdown of the assumptions used to calculate the electric field vector parallel to the spin axis.

Although the data is unlikely to be suitable for detailed analysis, the methodology will be continued. Some interesting features maybe found although without the supporting evidence that the vorticity calculated from the PEACE data is representative these observations should be taken with caution.

Application of both the curlometer and vorticity techniques to the magnetic field and electron velocity data was performed and the results are shown in Figure 4-12.

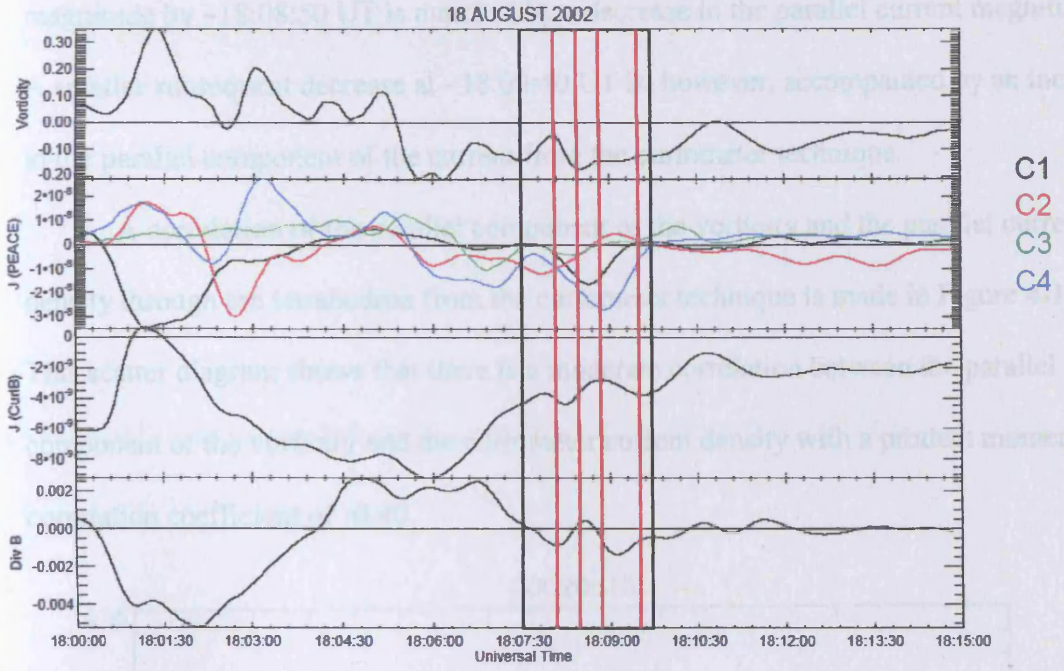

Figure 4-12 Vorticity and curlometer results – 18th August 2002
The parallel electron vorticity about the spacecraft tetrahedron, the parallel component of the electron current at each spacecraft and the parallel component of the current density passing through the spacecraft tetrahedron are shown. A measure of the accuracy of the curl of B is given by the divergence of B. The interval where all four spacecraft are located within the plasma sheet is marked in black. Key times that are referred to are market in red.

During the interval ~18:07:30 UT to ~18:10:00 UT there is no change in direction of the vorticity or the parallel current density from the curlometer technique. During this interval however, Clusters 1 and 3 do observe parallel electron flows changing direction albeit at small magnitude.

From 18:07:30 UT to ~18:08:10 UT the parallel component of vorticity steadily decreases its lowest value during this interval. The corresponding change in the magnitude of the parallel component of the current from the curlometer technique decreases and then increases throughout this change.

An increase in the magnitude of the vorticity then takes place until a maximum is reached at ~18:08:20 UT. This change is accompanied with an increase and then decrease

in the parallel current from the curlometer technique. A small decrease in the vorticity magnitude by ~18:08:50 UT is matched by a decrease in the parallel current magnitude. A smaller subsequent decrease at ~18:09:40 UT is, however, accompanied by an increase in the parallel component of the current from the curlometer technique.

A correlation of the parallel component of the vorticity and the parallel current density through the tetrahedron from the curlometer technique is made in Figure 4-13. This scatter diagram shows that there is a moderate correlation between the parallel component of the vorticity and the curlometer current density with a product moment correlation coefficient of -0.40.

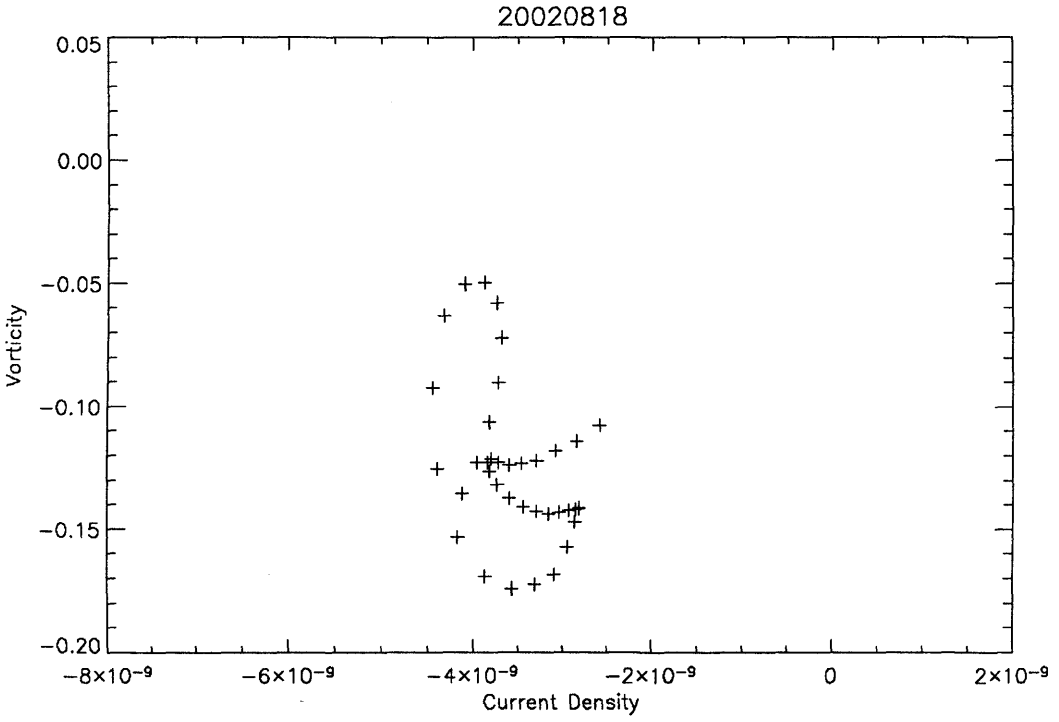

Figure 4-13 Current density dependence on vorticity – 18th August 2002
A vorticity vs. current density from the curlometer technique scatter diagram. There is a moderate negative correlation between the two with a Pearson's product moment correlation coefficient of -0.40.

4.3.2 17:55 – 18:15 UT 25th August 2002

Between 17:55 and 18:15 UT 25th August 2002 the Cluster quartet were located at (-17.4, -3.0, 3.8) $R_{E\,GSM}$ and the configuration of the spacecraft was as shown in Figure 4-14. As in the previous case study there is a large separation in GSM-X between Clusters 1 and 4 with these spacecraft separated from Cluster 2 in GSM-Y. As in the previous example, the AE index was low ~50 nT for the entire interval with no proximity to a substorm onset or intensification. The AE index for the entire day is shown in Figure 4-15 with the period of interest marked in black.

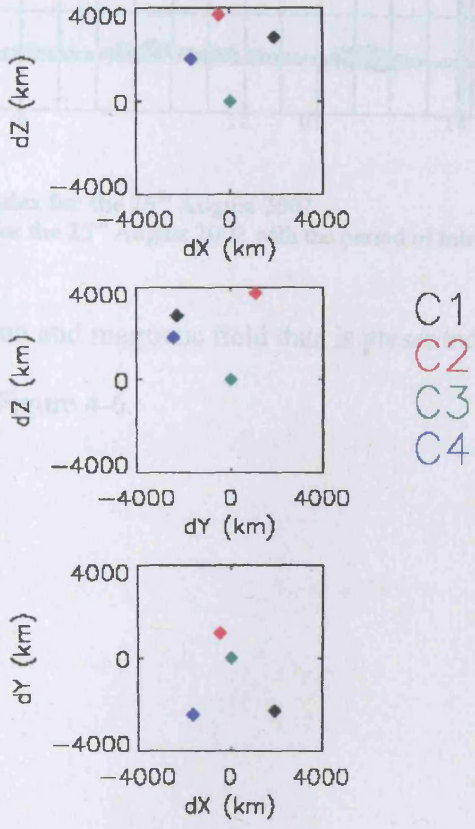

Figure 4-14 Cluster configuration on 25th August 2002
The spacecraft tetrahedron configuration is presented. The Cluster spacecraft are represented in their standard colours.

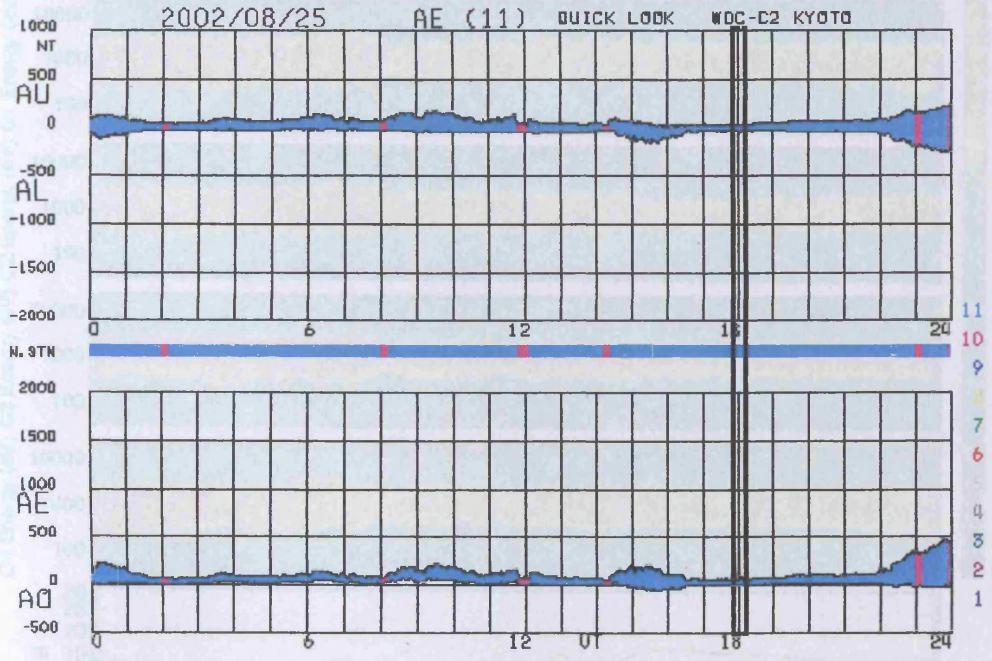

Figure 4-15 The AE index for the 25th August 2002
The AE index is show for the 25th August 2002 with the period of interest marked.

An overview of the electron and magnetic field data is presented in Figure 4-16 in the same style and format as Figure 4-6.

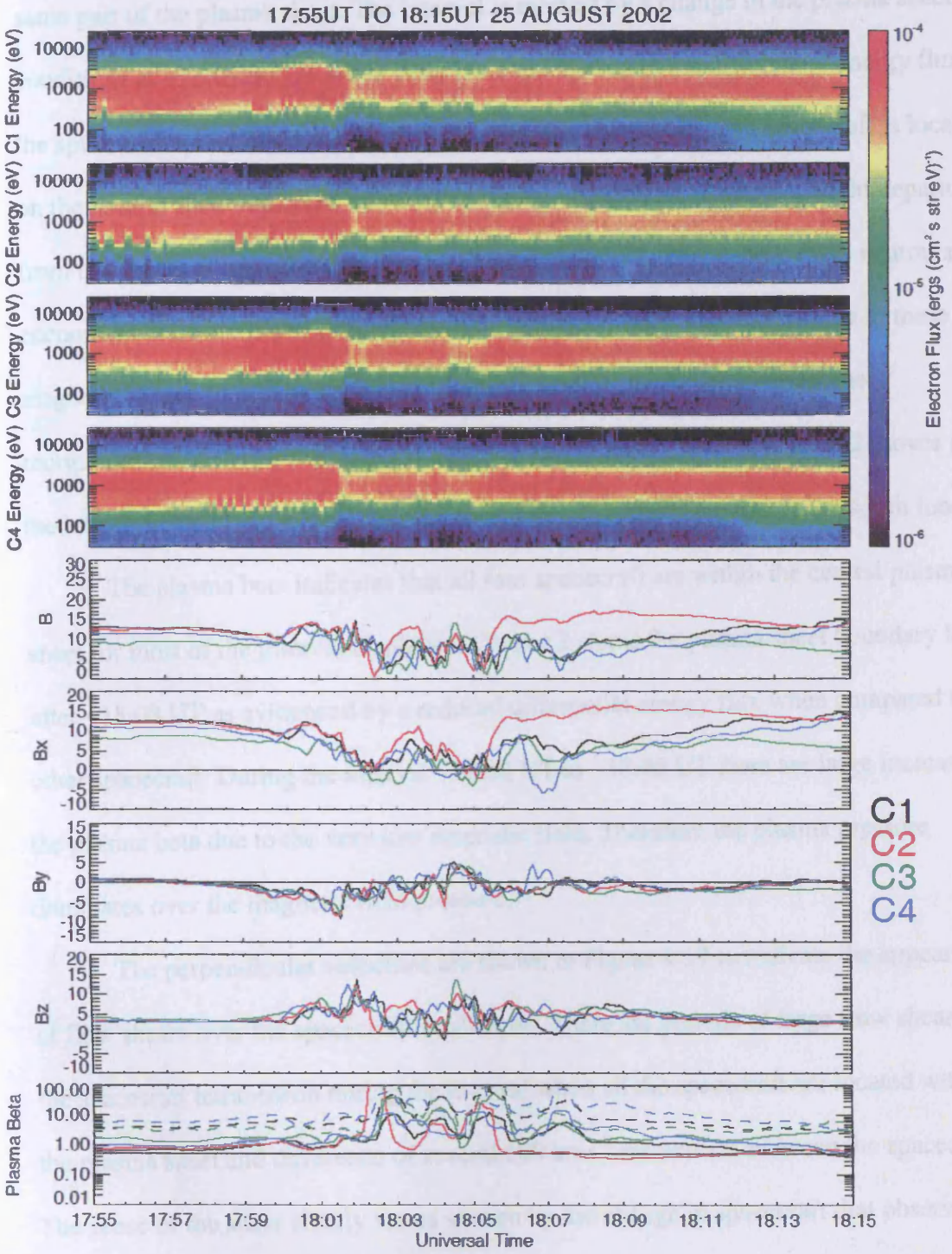

Figure 4-16 PEACE and FGM data for 25th August 2002
Omni-direction electron differential energy flux spectrograms are shown for each spacecraft together with the magnetic field magnitude and components in the GSM co-ordinate frame. The plasma beta is shown (solid for electrons and dashed for protons) with the plasma beta 0.5 plasma sheet cut-off marked.

Unlike the 18th August 2002 event, each spacecraft observed approximately the same part of the plasma sheet. The interval is marked by a change in the plasma sheet conditions at ~18:01:30 UT when there is a sudden drop in the differential energy flux as the spacecraft move into a colder plasma sheet. By ~18:02 UT each spacecraft is located on the neutral sheet indicated by ~0 nT in the B_X component. There is a slight departure from the centre of the neutral sheet at ~18:04 – 18:05 UT. Throughout these neutral sheet encounters there are noted differences in the magnetic field and currents due to these magnetic shears should be detected. After this neutral sheet encounter another reorganisation of the neutral sheet is detected and is clearly seen as Cluster 2 moves into the lobe indicated by the large B_X component with Cluster 3 moving to the south lobe.

The plasma beta indicates that all four spacecraft are within the central plasma sheet for most of the interval displayed. Cluster 2 skims the plasma sheet boundary layer after ~18:08 UT as evidenced by a reduced differential energy flux when compared to the other spacecraft. During the interval ~18:02 UT to ~18:06 UT there are large increases in the plasma beta due to the very low magnetic field. Therefore the plasma pressure dominates over the magnetic field pressure.

The perpendicular velocities are shown in Figure 4-17 to indicate the appearance of flow shears over the spacecraft tetrahedron. There are periods of large flow shears over the spacecraft tetrahedron during the interval when all the spacecraft are located within the plasma sheet and difference of several 100 kms^{-1} are evident between the spacecraft. The sense of the shear clearly varies as seen by the change in spacecraft that observes the greatest flow.

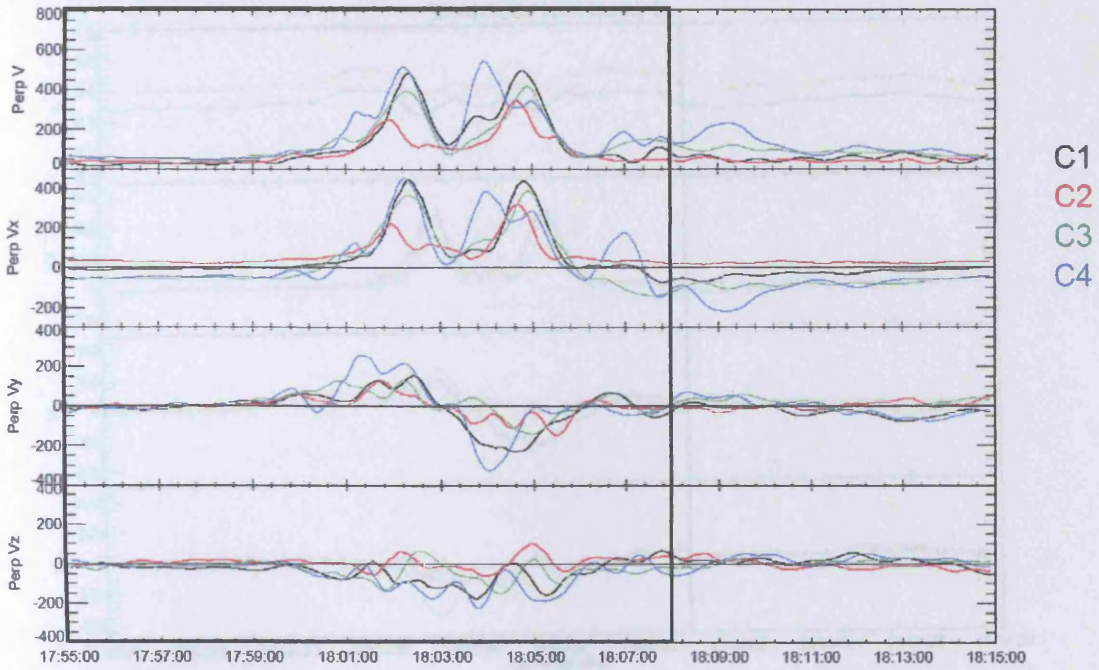

Figure 4-17 Perp electron velocity to indicate flow shears – 25th August 2002
The perpendicular electron velocities (km s^{-1}) for each spacecraft showing both magnitude and components in GSM.

As in the previous example, a correction of the PEACE data for the V_Z offset is applied and the velocity data for this event is verified for suitability for multi-spacecraft analysis after the correction of the PEACE data for the V_Z offset. Using the same format as Figure 4-8 - Figure 4-11, the perpendicular components of the electron velocity, the CIS/CODIF proton velocity (when available) and the $\mathbf{E}\times\mathbf{B}$ velocity are shown in Figure 4-18 - Figure 4-21.

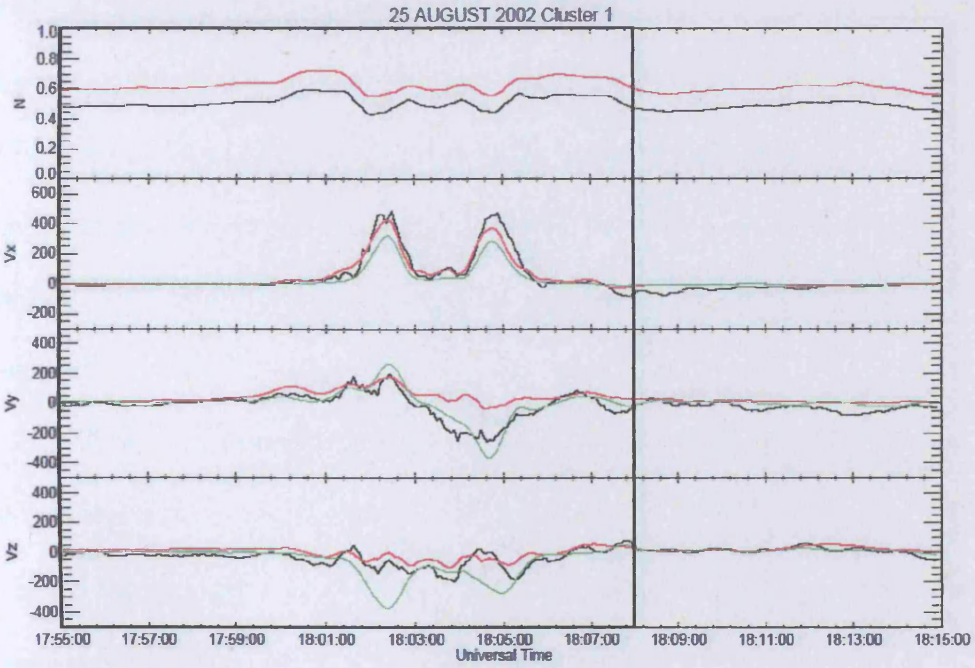

Figure 4-18 Data validation for Cluster 1 – 25th August 2002
The perpendicular components of the electron, proton and $\mathbf{E}\times\mathbf{B}$ velocities for Cluster 1 during the 25th August 2002 event are shown together with the electron and proton densities. Electron, ion and $\mathbf{E}\times\mathbf{B}$ data are shown in black, red and green respectively.

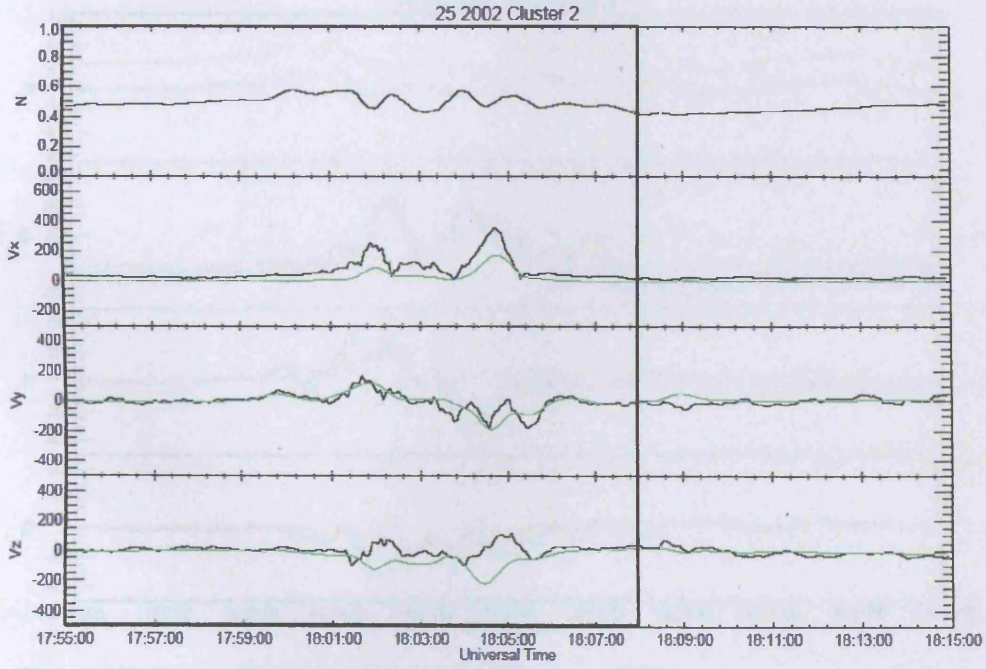

Figure 4-19 Data validation for Cluster 2 – 25th August

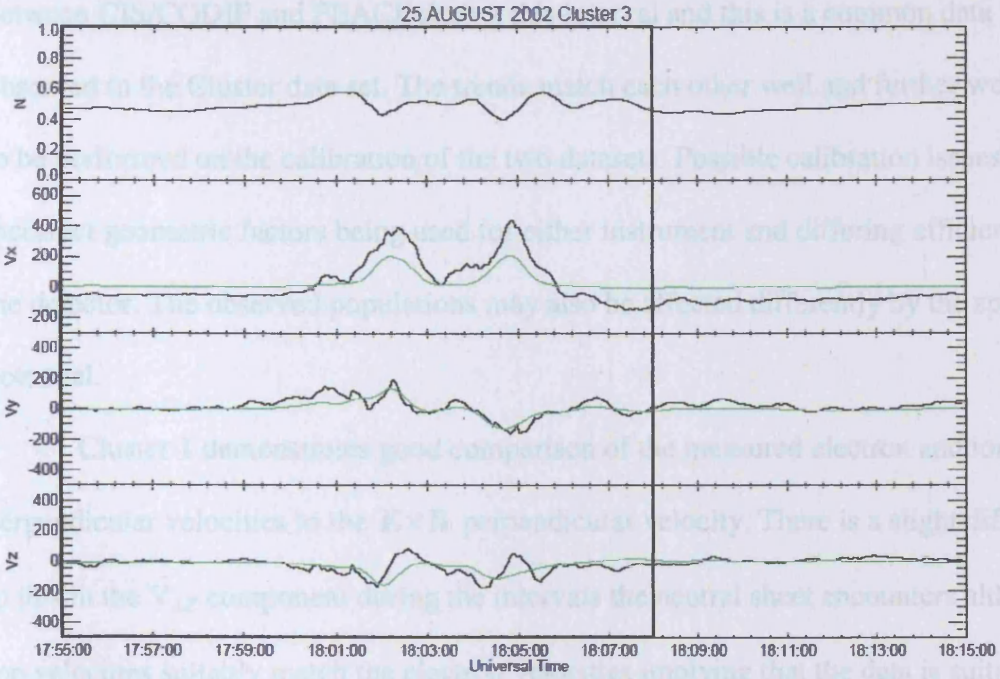

Figure 4-20 Data validation for Cluster 3 – 25th August 2002
The perpendicular components of the electron and $\mathbf{E}\times\mathbf{B}$ velocities for Cluster 3 during the 25th August 2002 event are shown together with the electron density. Electron and $\mathbf{E}\times\mathbf{B}$ data are shown in black and green respectively.

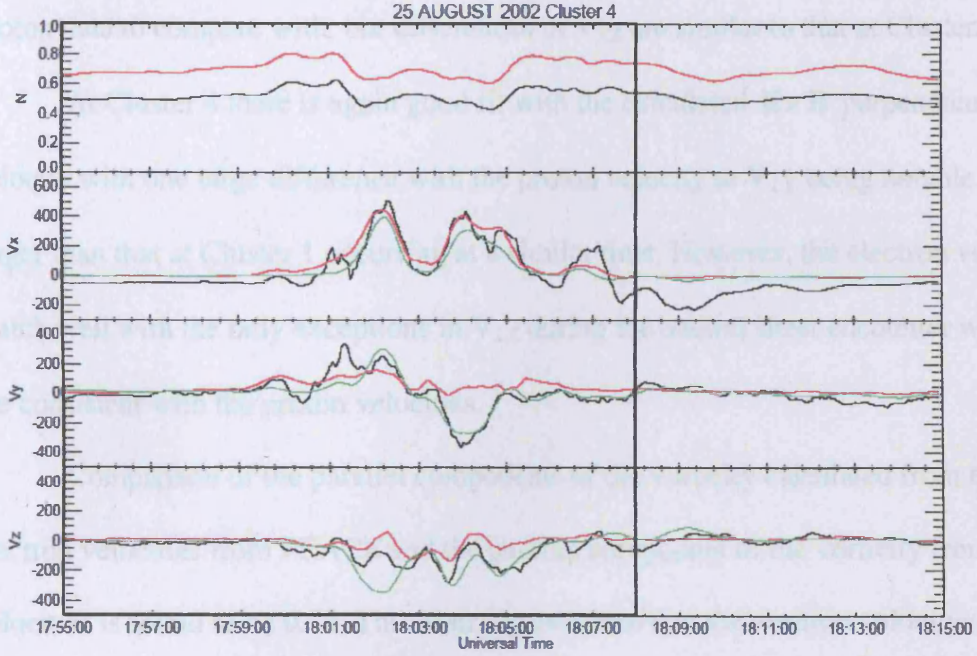

Figure 4-21 Data validation for Cluster 4 – 25th August 2002

Where proton density is available it is clear there is a constant offset difference between CIS/CODIF and PEACE during this interval and this is a common data feature observed in the Cluster data set. The trends match each other well and further work needs to be performed on the calibration of the two datasets. Possible calibration issues include incorrect geometric factors being used for either instrument and differing efficiencies of the detector. The observed populations may also be affected differently by the spacecraft potential.

Cluster 1 demonstrates good comparison of the measured electron and ion perpendicular velocities to the $\mathbf{E}\times\mathbf{B}$ perpendicular velocity. There is a slight difference to this in the $V_{\perp Z}$ component during the intervals the neutral sheet encounters although ion velocities suitably match the electron velocities implying that the data is suitable for further analysis.

Similar observations are made at Clusters 2 and 3. Unfortunately there is no proton data to compare with, but differences in $V_{\perp Z}$ are similar to that at Cluster 1.

At Cluster 4 there is again good fit with the calculated $\mathbf{E}\times\mathbf{B}$ perpendicular velocity with one large difference with the proton velocity in $V_{\perp Y}$ being notable which is larger than that at Cluster 1 occurring at a similar time. However, the electron velocities match well with the only exceptions in $V_{\perp Z}$ during the neutral sheet encounter where they are consistent with the proton velocities.

Comparison of the parallel components of the vorticity calculated from the electron velocities from PEACE and the parallel component of the vorticity from $\mathbf{E}\times\mathbf{B}$ velocities is found to be 0.77. This is strong evidence that the electron velocity data is suitable for further analysis.

The corrected electron moments are suitable for multi-spacecraft analysis and the application of both the curlometer and vorticity techniques to the magnetic field and electron velocity data are shown in Figure 4-22. The variations of the electron velocity over the spacecraft are the result of real shears.

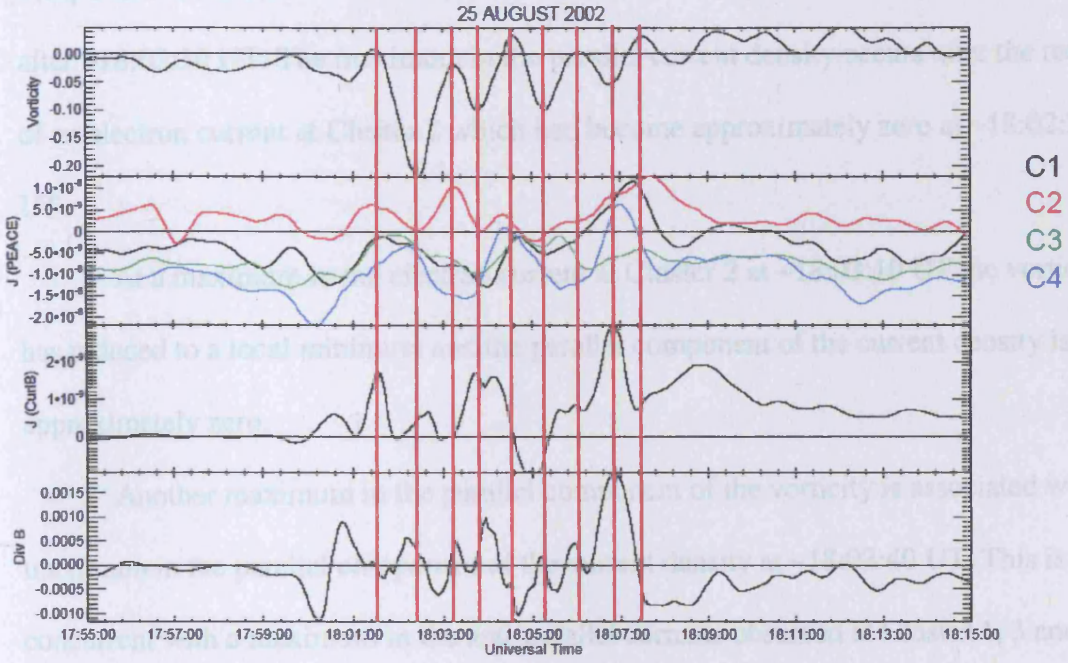

Figure 4-22 Vorticity and curlometer results – 25th August 2002
The parallel electron vorticity around the spacecraft tetrahedron, the parallel component of the electron current at each spacecraft and the parallel component of the current density passing through the spacecraft are shown. A measure of the accuracy of the curl of B is given by the divergence of B.

The parallel component of the vorticity changes direction frequently during this interval as does the parallel current density through the tetrahedron determined from the curlometer technique. There are interesting intervals to note where a vorticity change does not result in the expected current density change. A description of the observations at the key times marked by red vertical lines on Figure 4-22 is given below.

At ~18:01:30 UT there is a peak in the parallel current density marked by a minimum in the parallel component of the vorticity. This takes place during an interval of decreasing electron currents observed by the PEACE instrument.

A large increase in magnitude of the parallel component of vorticity follows ~18:01:30 UT reaching a maximum at ~18:02:30 UT. During this change the parallel component of the current returns to zero before increasing again to its maximum shortly after ~18:02:30 UT. The maximum in the parallel current density occurs after the return of an electron current at Cluster 2 which had become approximately zero at ~18:02:30 UT.

At a maximum in the electron current at Cluster 2 at ~18:03:10 UT the vorticity has reduced to a local minimum and the parallel component of the current density is approximately zero.

Another maximum in the parallel component of the vorticity is associated with a maximum in the parallel component of the current density at ~18:03:40 UT. This is concurrent with a maximum in the anti-parallel currents observed at Cluster 1, 3 and 4 and approximately no current at Cluster 2.

A change in direction of the parallel component of vorticity occurs between ~18:04:20 UT and ~18:04:50 UT with a maximum at ~18:04:40 UT. At the maximum parallel component of vorticity there is no parallel component of the current density through the tetrahedron, however, the current density does change direction at this time. The current density changes back to its original direction shortly after another maximum in the parallel component of vorticity is achieved at ~18:05:20 UT.

The parallel component of the current density remains steady during a minimum in the parallel component of vorticity at ~18:06:00 UT shortly before reaching a maximum at ~18:06:40 UT concurrently with a maximum of the parallel component of vorticity.

Another change in direction of the parallel component of vorticity occurs with a maximum being achieved at ~18:07:20 UT which is closely associated with a minima in the parallel component of the current density although there has not been an expected change of sign of the parallel current direction.

A detailed analysis of the vorticity compared to the current density during the interval 18:01 UT to 18:06 UT is shown in the scatter diagram in Figure 4-23. A product moment correlation coefficient of 0.06 indicates that there is no correlation between the parallel component of the vorticity and the parallel component of the current density through the tetrahedron. However, key features in the description of the data do indicate a connection which is also indicated by the absence of randomly distributed data in the scatter diagram. A more complex explanation of the dataset observations is required to fully interpret the correlation coefficient of this data.

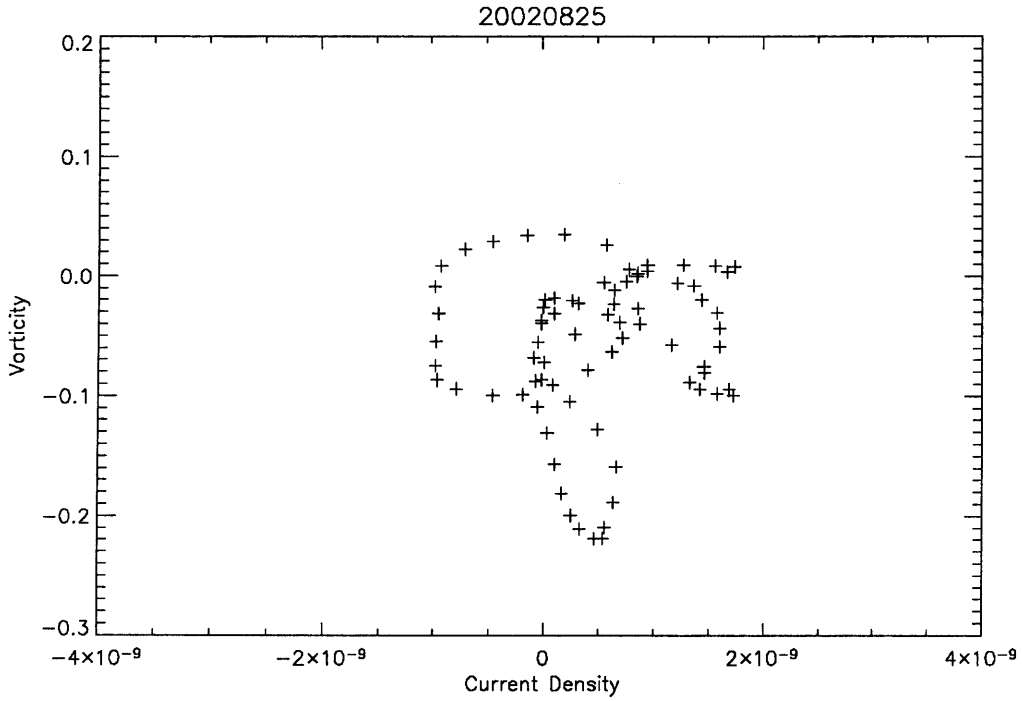

Figure 4-23 Current density dependence on vorticity – 25th August 2002
A parallel vorticity vs. parallel component of the current density from the curlometer technique scatter diagram. There is a trend for departure from the zero vorticity to be associated with a change in the current density, however, the sense of the increase of the current density varies therefore implying a more complicated description of the current generation to be found. The Pearson's product moment correlation coefficient is 0.06 for this event.

4.3.3 18:50 – 19:00 UT 13th September 2002

The Cluster quartet was located at (-17.8, 2.5, 1.9) $R_{E\,GSM}$ during 18:50 – 19:00 UT 13th September 2002 and the configuration of the spacecraft during this interval is as shown in Figure 4-24. The AE index was decreasing from ~300 nT to ~200 nT during this interval and was recovering from a substorm with an onset at ~18:15 UT with an AE index of ~500 nT. The AE index for the entire day is shown in Figure 4-25.

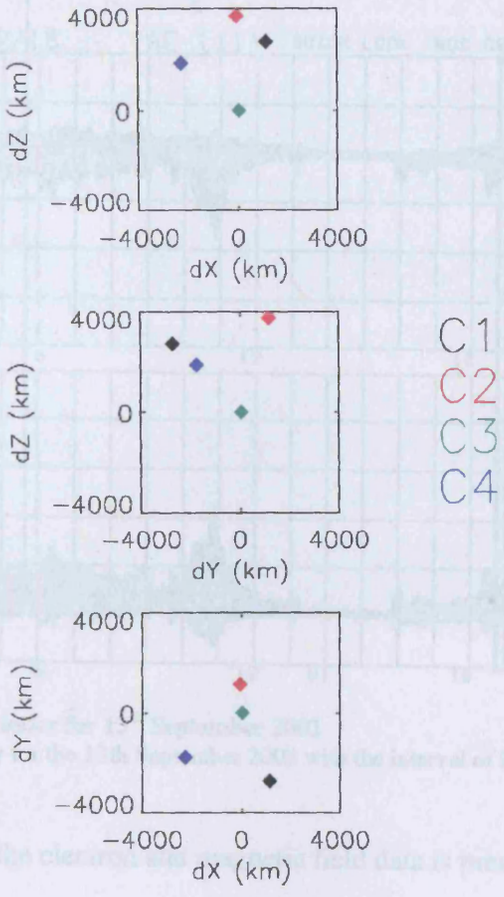

Figure 4-24 Cluster configuration on 13th September 2002
The spacecraft tetrahedron configuration is presented. The Cluster spacecraft are represented in their standard colours.

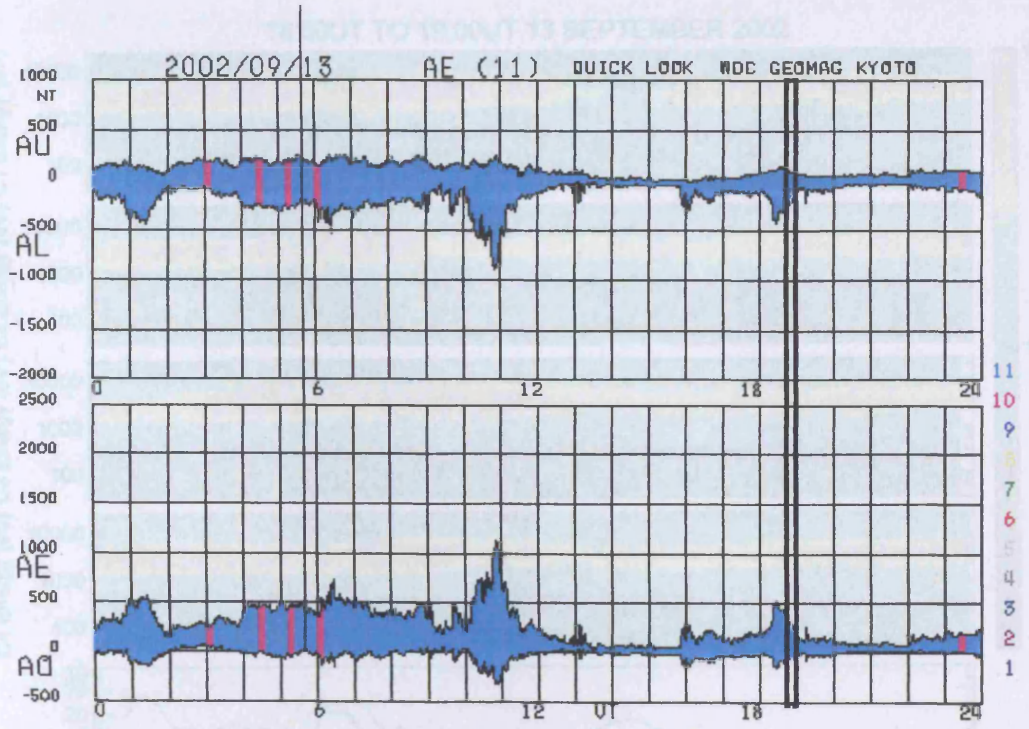

Figure 4-25 The AE index for 13th September 2002
The AE index is show for the 13th September 2002 with the interval of interest marked.

An overview of the electron and magnetic field data is presented in Figure 4-26 in the same style and format as Figure 4-6.

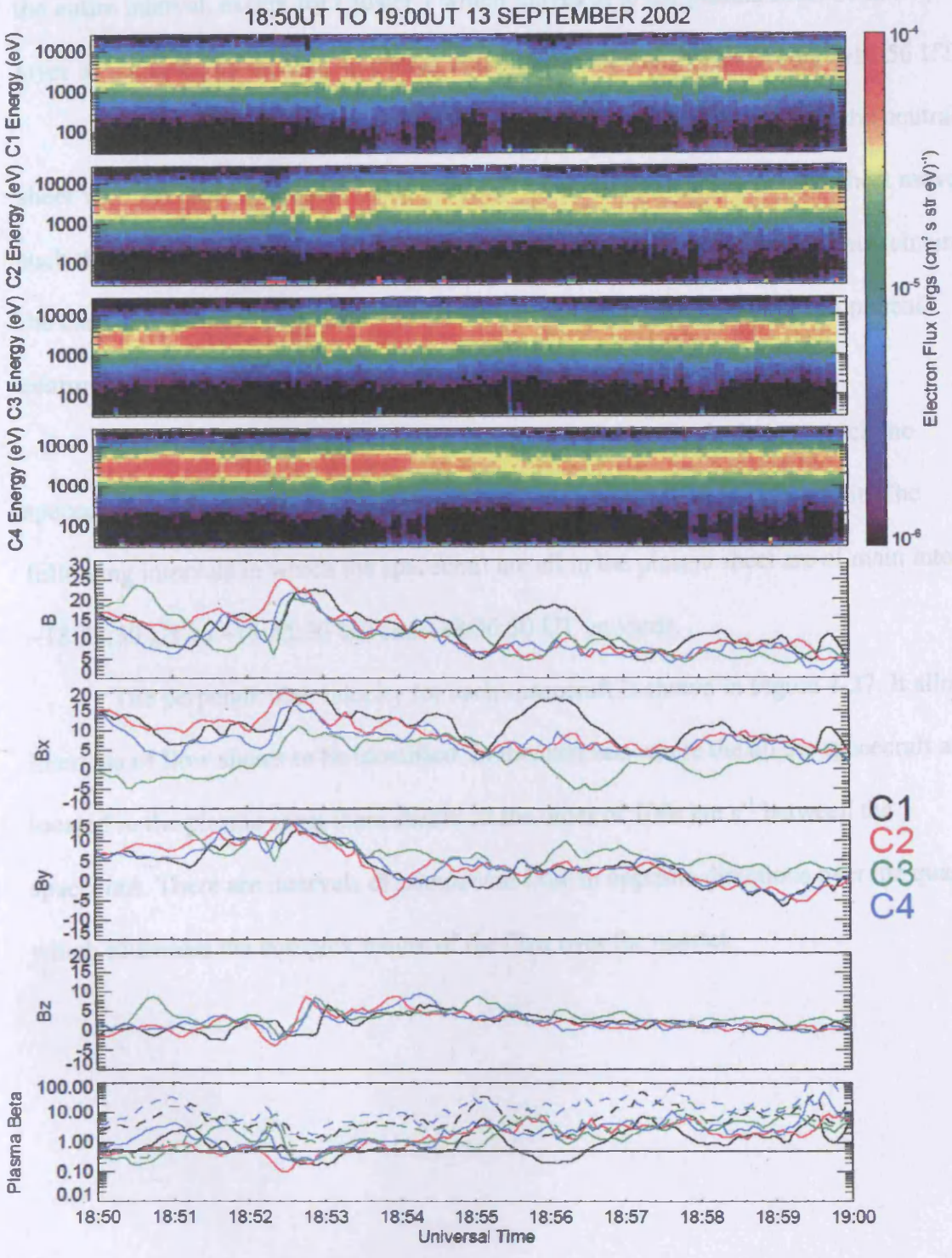

Figure 4-26 PEACE and FGM data for 13th September 2002
Omni-direction electron differential energy flux spectrograms are shown for each spacecraft together with the magnetic field magnitude and components in the GSM co-ordinate frame. The plasma beta is shown (solid for electrons and dashed for protons) with the plasma beta equal to 0.5 plasma sheet cut-off marked.

The four spacecraft are located in a roughly constant temperature plasma sheet for the entire interval, except for Cluster 1 which moves in to the plasma sheet boundary layer as indicated by the drop in energy and differential energy flux around ~18:56 UT.

Initially, Cluster 3 is located on the neutral sheet or slightly south of the neutral sheet with the other spacecraft being north of the neutral sheet. The neutral sheet moves such that by ~18:52 UT all the spacecraft observe similar magnetic fields. This remains the case until Cluster 1 and then Cluster 3 observe deflections in the B_X component centred on ~18:56 UT and ~18:56:30 UT respectively.

As indicated by the plasma beta, there are a few intervals during which the spacecraft are either in the plasma sheet boundary layer fully or are close to it. The following intervals in which the spacecraft are all in the plasma sheet are of main interest: ~18:53:30 UT to ~18:55:30 UT and ~18:56:30 UT onwards.

The perpendicular velocity for each spacecraft is shown in Figure 4-27. It allows intervals of flow shears to be identified. In the intervals where the all the spacecraft are located in the plasma sheet there shears on the order of 100s km s^{-1} between the spacecraft. There are intervals of component flow in opposite directions over the quartet which illustrates the complex nature of the flow over the quartet.

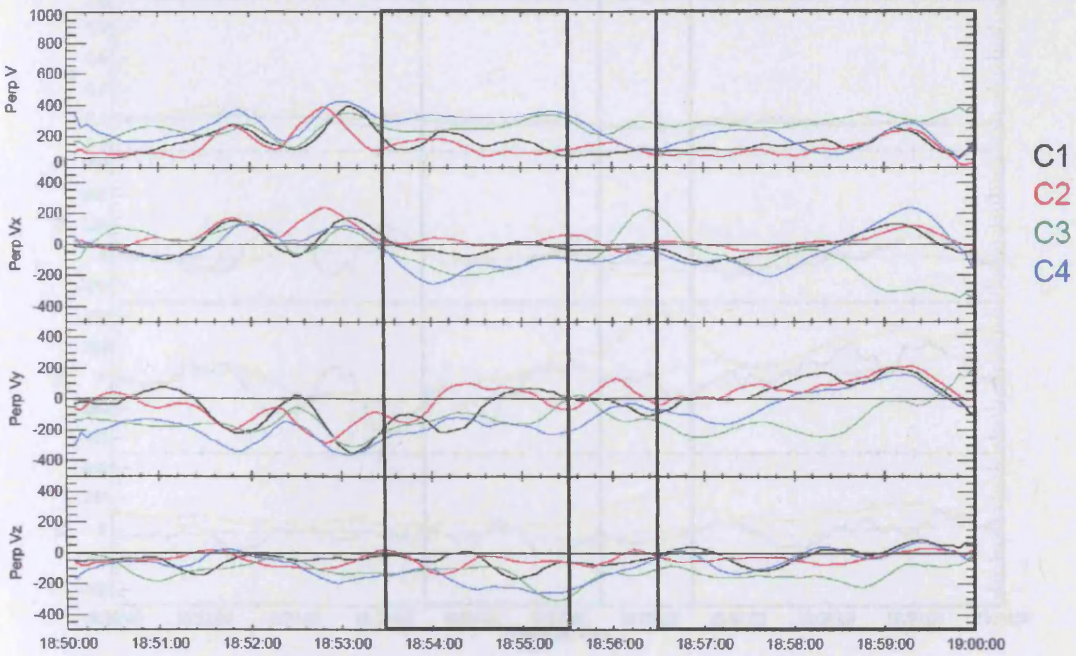

Figure 4-27 Perp electron velocity to indicate flow shears – 13th Sept 2002
The perpendicular velocities (km s^{-1}) for each of the Cluster spacecraft during this interval. The components are in GSM co-ordinates.

The validation of the electron moments is shown in Figure 4-28 - Figure 4-31.

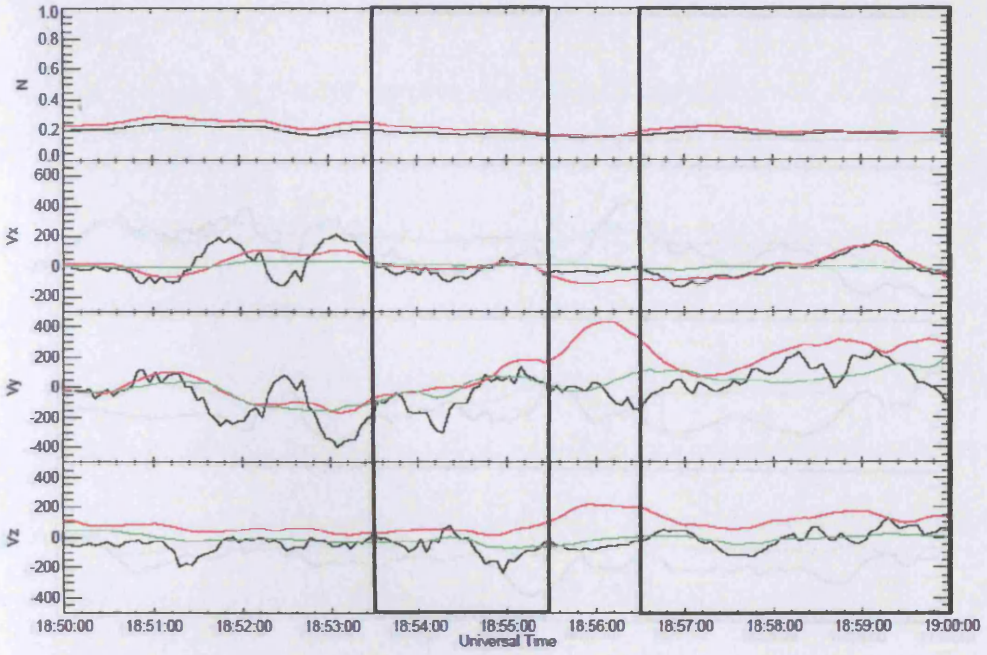

Figure 4-28 Data validation for Cluster 1 – 13th September 2002
The perpendicular components of the electron, proton and $\mathbf{E}\times\mathbf{B}$ velocities for Cluster 1 during the 13th September 2002 event are shown together with the electron and proton densities. Electron, ion and $\mathbf{E}\times\mathbf{B}$ data are shown in black, red and green respectively.

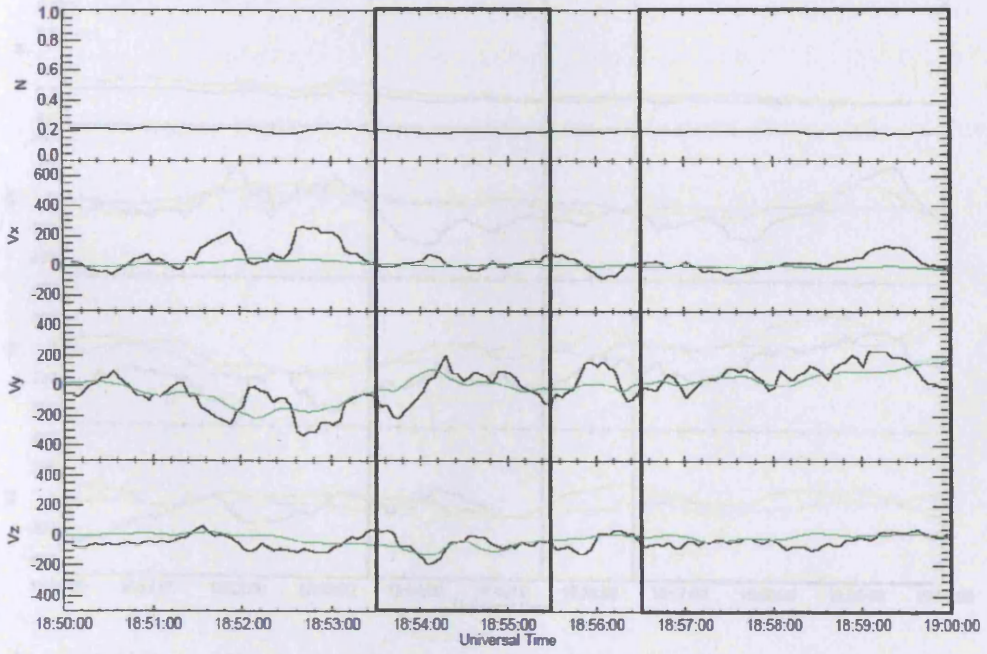

Figure 4-29 Data validation for Cluster 2 – 13th September 2002

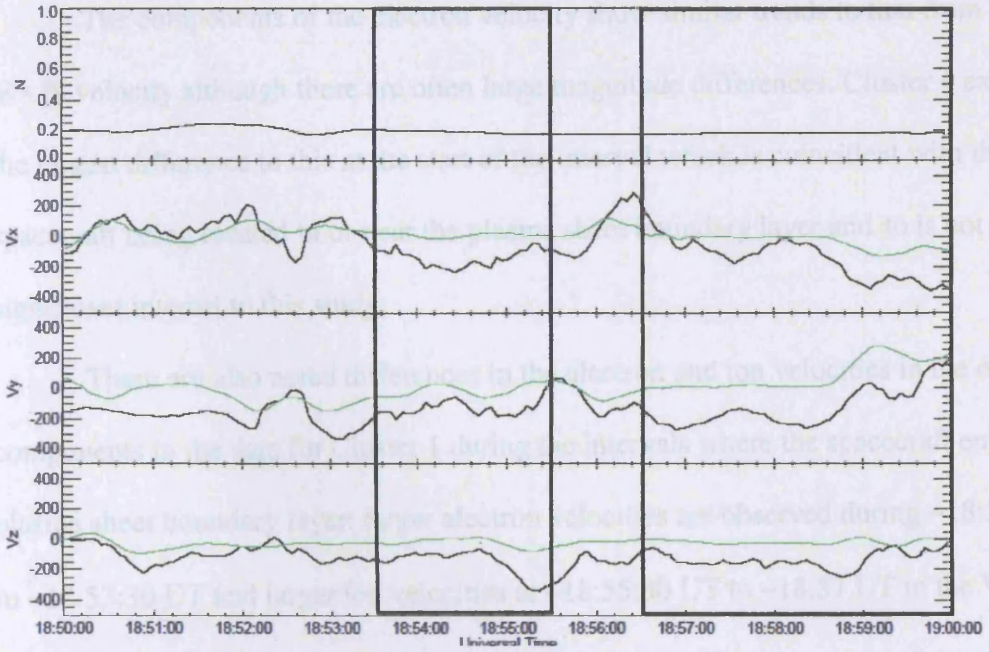

Figure 4-30 Data validation for Cluster 3 – 13th September 2002
The perpendicular components of the electron and $\mathbf{E}\times\mathbf{B}$ velocities for Cluster 3 during the 13th September 2002 event are shown together with the electron density. Electron and $\mathbf{E}\times\mathbf{B}$ data are shown in black and green respectively.

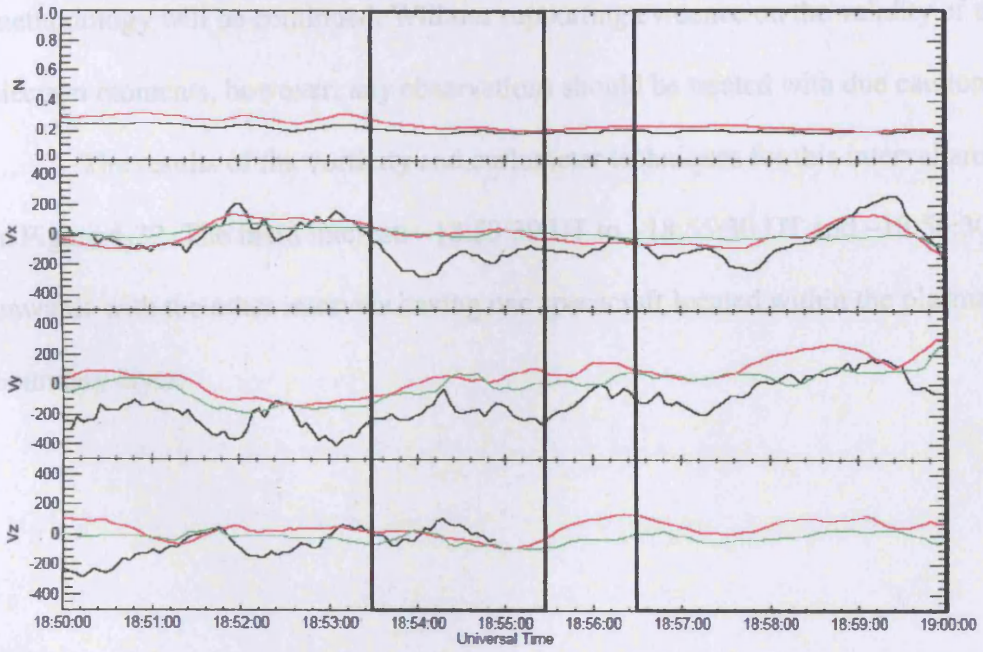

Figure 4-31 Data validation for Cluster 4 – 13th September 2002

The components of the electron velocity show similar trends to that from the $\mathbf{E}\times\mathbf{B}$ velocity although there are often large magnitude differences. Cluster 4 exhibits the largest difference to this at the start of the interval which is coincident with the spacecraft being located in or near the plasma sheet boundary layer and so is not of significant interest to this study.

There are also noted differences in the electron and ion velocities in the other components in the data for Cluster 1 during the intervals where the spacecraft enters the plasma sheet boundary layer: larger electron velocities are observed during ~18:51:30 UT to ~18:53:30 UT and larger ion velocities at ~18:55:30 UT to ~18:57 UT in the $V_{\perp Y}$.

A correlation coefficient of 0.18 between the parallel component of the vorticity calculated from PEACE velocity data and that calculated from $\mathbf{E}\times\mathbf{B}$ indicates that the data may not be suitable for further detailed analysis. As with the first example, the methodology will be continued. Without supporting evidence on the validity of the electron moments, however, any observations should be treated with due caution.

The results of the vorticity and curlometer techniques for this interval are shown in Figure 4-32. The main interest: ~18:53:30 UT to ~18:55:30 UT and ~18:56:30 UT onwards with the other intervals having one spacecraft located within the plasma sheet boundary layer.

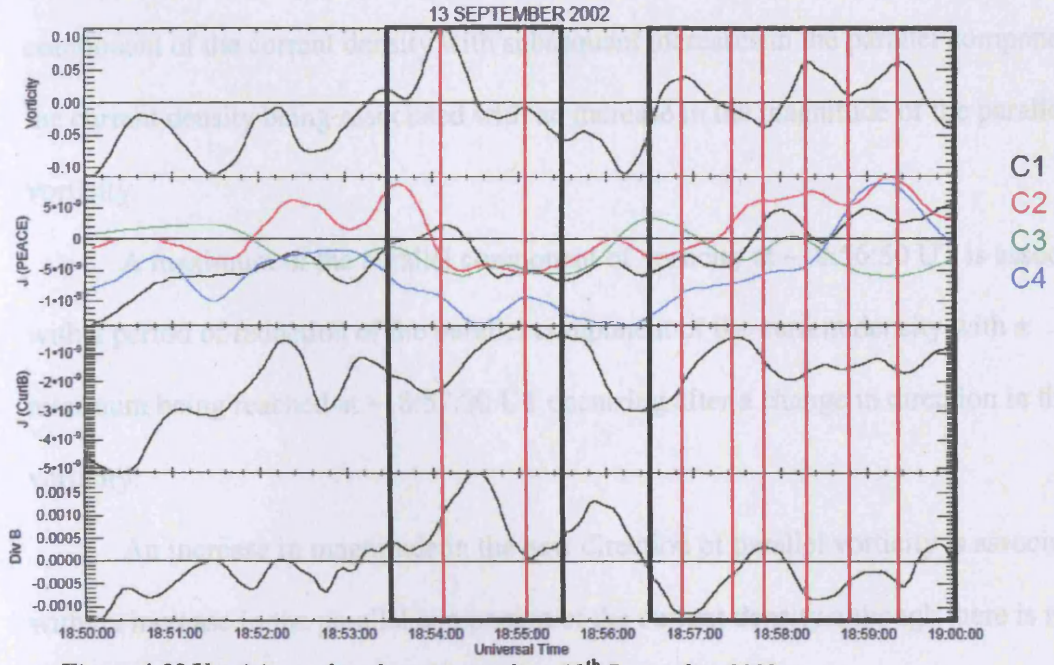

Figure 4-32 Vorticity and curlometer results – 13th September 2002
The electron vorticity around the spacecraft tetrahedron, the electron component of the current at each space and the total current density passing through the spacecraft are shown. A measure of the accuracy of the curl of B is given by the divergence.

Throughout the intervals when all four spacecraft are located within the plasma sheet there are several changes in both the magnitude and the direction of the parallel component of vorticity. Of key interest is that changes in direction are not associated with changes in the direction sense of the parallel component of the current density through the spacecraft tetrahedron. A description of key events, at intervals marked by vertical red lines in Figure 4-32, is presented.

The parallel component of vorticity initially increases from near-zero to a maximum at ~18:54:10 UT. This is associated with an increase in magnitude of the parallel component of the current density and is associated with larger currents observed at Clusters 2, 3 and 4.

The subsequent reduction, including a brief change in direction, in the parallel component of the vorticity to nearly zero at ~18:55:05 UT is associated with no parallel component of the current density with subsequent increases in the parallel component of the current density being associated with an increase in the magnitude of the parallel vorticity.

A maximum of the parallel component of vorticity at ~18:56:50 UT is associated with a period of reduction of the parallel component of the current density with a minimum being reached at ~18:57:30 UT occurring after a change in direction in the vorticity.

An increase in magnitude in the new direction of parallel vorticity is associated with an increase in the parallel component of the current density although there is no change in direction sense as would be expected. This increase stops and a reduction of the current density magnitude takes places as the vorticity changes sign and reaches a maximum at ~18:58:40 UT.

There is little variation in the parallel component of the current density although the vorticity reaches a minima at ~18:58:50 UT and a maxima later at ~18:59:20 UT.

The individual electron current traces at each spacecraft also repeat the previous case observation of oppositely directed currents being observed at different spacecraft. With intervals like ~18:58:30 UT to 19:00 UT showing clearly that during an interval of large vorticity over the quartet can be associated with oppositely directed currents.

To examine the correlation between the vorticity and the current density calculated from the curlometer technique the data for the plasma sheet intervals is plotted

in scatter diagram form in Figure 4-33. An increase in vorticity produces an increase in the magnitude of the parallel component of the current density with a correlation of -0.39.

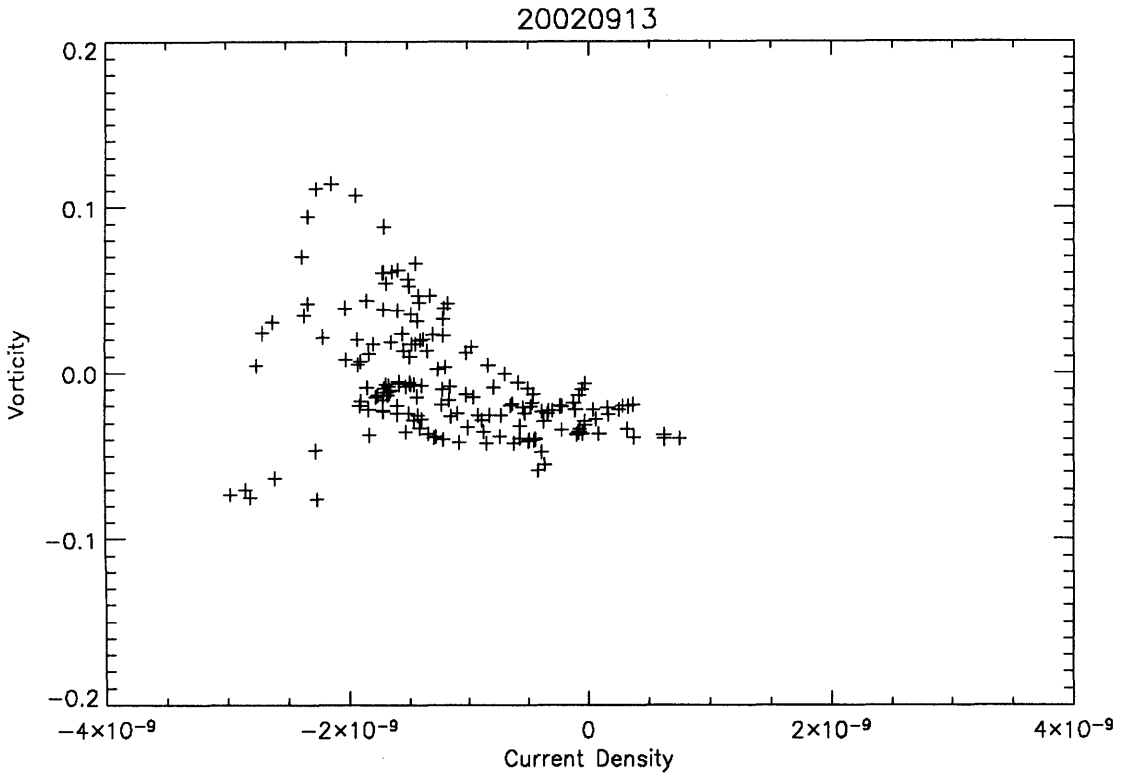

Figure 4-33 Current density dependence on vorticity – 13th September 2002
A vorticity vs. current density from the curlometer technique scatter diagram. An increase in vorticity produces an increase in the current density magnitude; however the direction sense is different. The data is correlated with a Pearson's product moment of -0.39.

4.4 Summary and Conclusion

By selecting the periods of enhanced flow activity when the 4 Cluster spacecraft can be shown to lie within the plasma sheet, the correlation between flow shears and field aligned current generation has been studied.

Three periods of enhanced flow shears have been studied with care taken to identify any interval where the spacecraft are in the plasma sheet boundary layer as a spacecraft on a magnetic field-line associated with the PSBL may observe field-aligned flow from a reconnection site that will complicate the analysis.

During each of the three examples presented above there are periods when a clear flow shear exists in the component of the flow perpendicular to the magnetic field over the spacecraft tetrahedron. The nature of this flow shear is catagorized by calculating the parallel component of the vorticity. The calculated current density from the curl of the magnetic field and the observed parallel electron motion at each spacecraft have been studied with relation to the vorticity.

The 18th August 2002 case study indicates that there is a moderate correlation (correlation coefficient of -0.40) between the parallel vorticity component and the parallel current density through the tetrahedron. The correlation shown in Figure 4-12 is complex indicating elements where an increase in vorticity is associated with increased parallel current flow in the anti-parallel direction and others where an increase in the vorticity magnitude has no effect on the parallel current density.

A low correlation coefficient of 0.06 between the parallel vorticity and current density implies little association between the two in the 25th August 2002 case. However, Figure 4-22 is clearly composed of several trends with changes in vorticity direction and magnitudes are associated with a particular set of changes in the parallel component of the current density. This is indicative of there being a change within the system so that a change in vorticity direction does not imply a change in direction of the current generated.

The 13th September 2002 event illustrates that there is a connection between the vorticity and the parallel component of the current density calculated from the curlometer technique. An increase in the magnitude of the vorticity is associated with an increase in the magnitude of the anti-parallel component of the current density.

The examples of oppositely directed parallel electron motion at one spacecraft compared to the others provide an explanation as to the observed current density direction. A gradient in the flow-shear, a vorticity, is required in Equation 4.13 for the generation of a shear in the magnetic field that results in a current. The main aspect, however, is that the vorticity along the flux tube must also vary, i.e. $\nabla\Omega$ is fundamental to field-aligned current generation. If the gradient of the vorticity along the flux tube changes magnitude, or indeed direction, then the flow of field-aligned currents will change in magnitude and indeed may change in direction.

The observations presented are not inconsistent with the generation of field-aligned current by flow-shear if it is possible that the location of greatest shear has moved to within the spacecraft tetrahedron. This situation is illustrated in Figure 4-34, where two possible locations of the greatest flow shear of a flux tube is located entirely outside of the spacecraft tetrahedron and another where it falls within the tetrahedron. In the first situation, all spacecraft will see similar electron distributions, however, in the second situation, it is expected that one spacecraft will observe a different distribution.

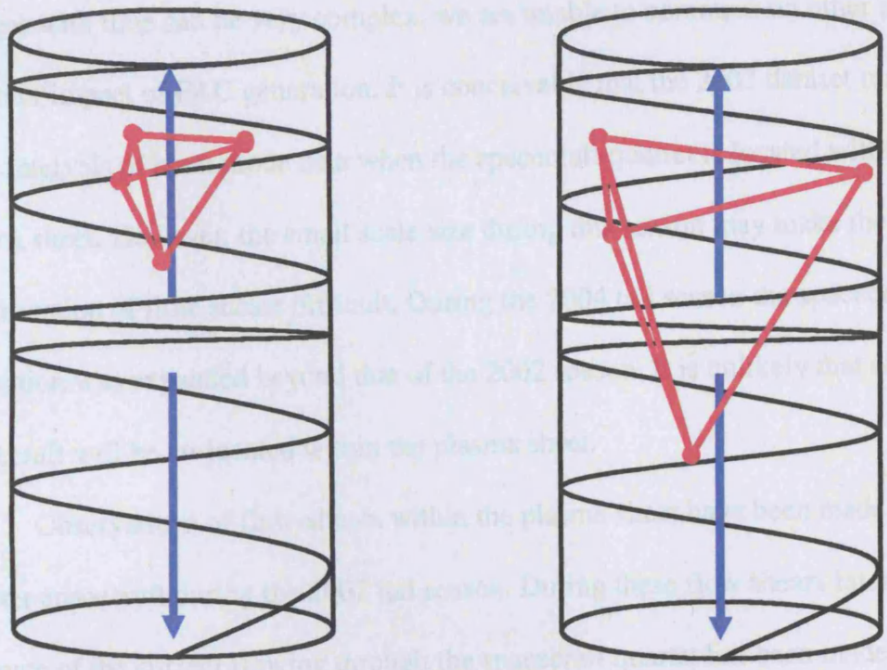

Figure 4-34 Possible model to explain results
A cartoon illustration of the generation of field-aligned currents by flow shears on magnetic flux-ropes. One the left a flow shear whose greatest shear is located away from the spacecraft tetrahedron produces a current system and the quartet observes the same direction for the current. However, if the location of the greatest flow-shear falls within the spacecraft tetrahedron then one spacecraft will observe an oppositely directed flow.

Given that Cluster 3 leads the quartet in its orbit and is typically of a few thousand kilometres further south than Cluster 1, 2 and 4, it would be expected that the Cluster 3 observes the opposite electron distribution. Given that Cluster 2 observes the opposite electron distribution suggests the location of greatest flow shear along the flux tube is not confined to the GSM-XY plane and can move.

The observations studied took place during 2002. The lack of suitable events in 2001 is due to the less frequent use of burst mode operations. In both years many burst mode datasets were not useful for this study as they contained entirely PSBL or PSBL and magnetic lobe data. Unfortunately, this has resulted in only one spacecraft tetrahedron scale size being considered. Whilst providing evidence that flow shears on

that spatial scale can be associated with FACs and illustrating that the way the shear changes with time can be very complex, we are unable to comment on other scale sizes and their impact of FAC generation. It is conceivable that the 2003 dataset may contain more intervals of burst mode data when the spacecraft quartet is located within the plasma sheet. However, the small scale size during this season may make the identification of flow shears difficult. During the 2004 tail season the spacecraft separation was expanded beyond that of the 2002 season. It is unlikely that all the spacecraft will be co-located within the plasma sheet.

Observations of flow-shears within the plasma sheet have been made by the Cluster spacecraft during the 2002 tail season. During these flow shears intervals, an estimate of the current flowing through the spacecraft quartet has been made from the curl of the magnetic field and this has been compared to the sense of the vorticity. There are specific intervals where the vorticity and current density follow similar trends, however exceptions exist that imply a more complicated situation. By investigating the electron flow at each spacecraft in more detail it is clear that the direction of the field-aligned flows can vary across the tetrahedron. This implies, if the source of the flow is the same as that seen at the other spacecraft and is related to the observed shear, then the location of greatest shear has moved to within the spacecraft quartet, and an estimate of the current density, averaged over the whole quartet, will not provide the predicted observation of the flows at specific spacecraft.

If the observations are generated by the location of the greatest flow shear moving within the spacecraft tetrahedron then this implies that a gradient of flow shears along a

section of a flux tube on the same length scale as the inter-spacecraft separation is enough to generate observed field-aligned currents.

Performing differencing of velocities using electron data is made difficult due to their thermal speeds and the natural variability of the electron motion. Choosing events with large inter-spacecraft difference, whilst there may be quantitative errors, produces qualitative results that allow meaningful interpretation to be made. This is the first such study of field-aligned current generation with direct measurement of plasma vorticity. Further studies of this system are best addressed with more satellites located along the flux tube so that the change of vorticity can be determined and accounted for. Whilst a large number of dedicated spacecraft flying in formation may provide this insight, there is the possibility of a suitable mission conjunction occurring that with Cluster providing that extra data point required for multiple vorticity determinations to be made.

5 Flux Rope Associated Travelling Compression Regions

5.1 Introduction

Two phenomena found in the magnetotail that are particularly well suited for study by the Cluster mission are magnetic flux ropes and the possibly related phenomenon of travelling compression regions (TCRs). A description of each of these structures is presented and the science questions that are only resolvable with a multi-spacecraft mission like Cluster are stated.

During magnetic reconnection in the magnetotail, loop magnetic field structures, known as plasmoids, are formed in the plasma sheet [e.g. Hones et al., 1984]. An illustration of the formation of a plasmoid is shown in Figure 5-1a where the onset of magnetic reconnection at a near-Earth neutral line (NENL) produces a closed magnetic structure between it and the distant neutral line (DNL). Bipolar B_Z signatures in magnetic field data can be used to identify these plasmoids as they propagate tailward during the final stages of the substorm. In Figure 5-1b a simplified schematic of the plasmoid is shown at the time of formation.

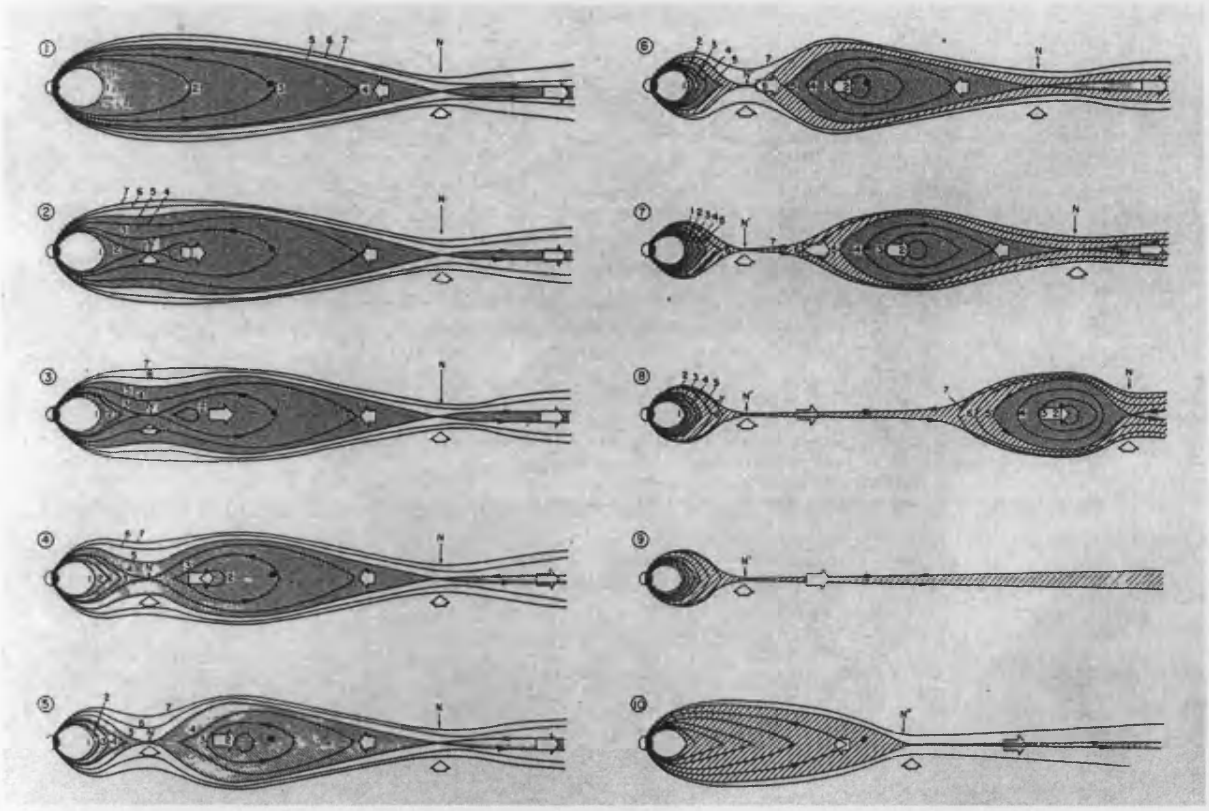

Figure 5-1 The magnetotail during a substorm
A) A schematic of the magnetotail during a substorm is shown. Panel 1 shows the steady-state situation where reconnection occurs at the DNL at the same rate as dayside reconnection. In panel 2, excess magnetic field is stored in the magnetotail as the reconnection rate at the DNL is now less than at the magnetopause. A breakdown of ideal MHD has allowed magnetic reconnection to occur at the NENL and a plasmoid is created as closed magnetic field lines are reconnected. Reconnection continues and eventually open magnetic field lines are reconnected as in panel 6. At this point the plasmoid has start to propagate tailward and leaves a thin plasma sheet behind it. The plasmoid exits the magnetotail and the plasma sheet recovers as the substorm finishes [From Hones, 1984].

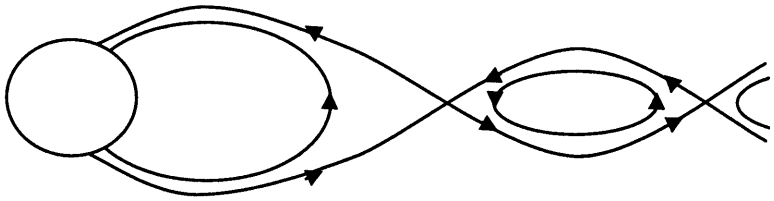

Figure 5-1 The magnetic topology of the magnetotail at plasmoid generation
B) The magnetic field topology of the magnetotail at plasmoid generation. The sense of the magnetic field within the plasmoid is shown for reference.

A spacecraft located in the magnetotail would observe the tailward passage of a plasmoid as high tailward plasma flows associated with a magnetic field signature as illustrated in Figure 5-2. The average speed of the associated plasma flows is ~ 490 km s^{-1} [Moldwin and Hughes, 1992].

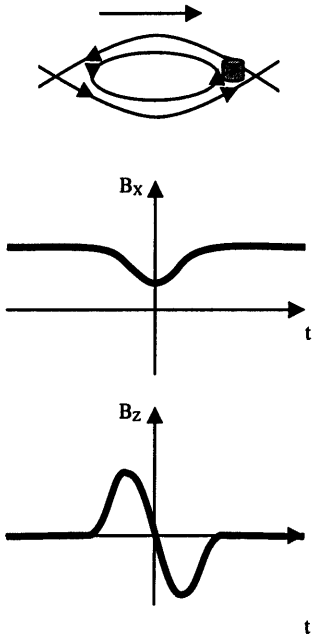

Figure 5-2 Magnetic field signature of tailward propagating plasmoid
The magnetic field signature associated with a tailward propagating plasmoid produced in a substorm. A plasmoid moves over a spacecraft and the magnetic field is seen to be directed first in the positive B_Z direction and then in the negative B_Z direction. The magnetic field within the plasmoid has less field strength in the B_X direction due to being now separated from the stretched magnetic field lines of the magnetotail.

Many plasmoids have a helical magnetic structure as they are formed by slightly non-antiparallel magnetic field lines at reconnection and are frequently referred to as flux-ropes [e.g. Hughes and Sibeck, 1987; Slavin et al., 1989; Lepping et al., 1995]. The helical field topography of a flux-rope can give the structure a significant axial field, nominally B_Y in the canonical tail picture. An illustration of the magnetic field topology of an ideal force-free flux-rope is provided in Figure 5-3.

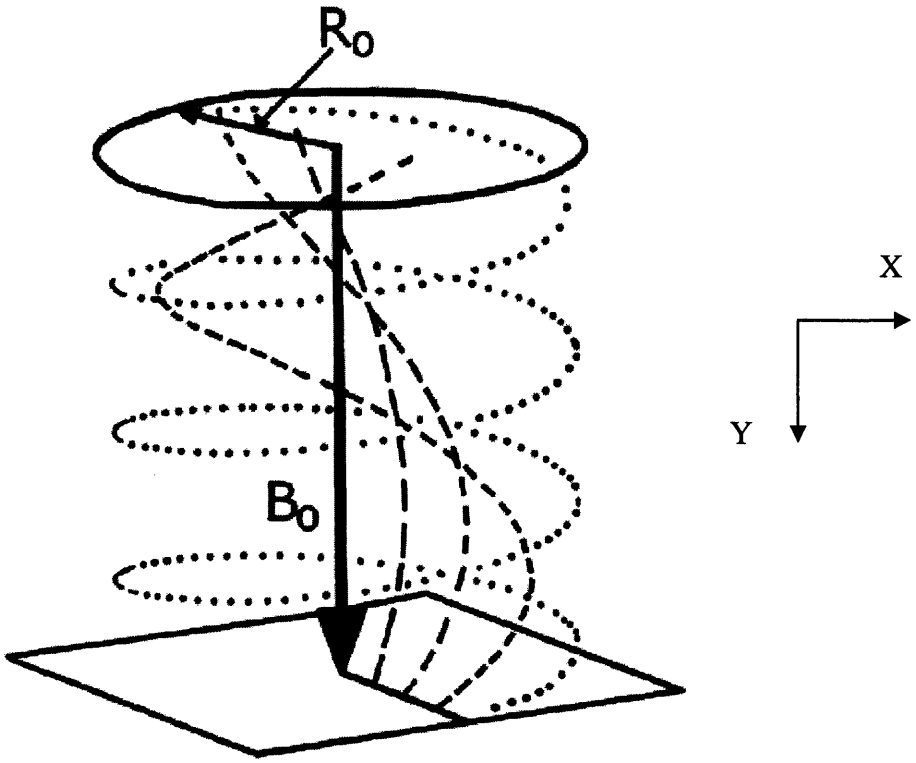

Figure 5-3 Magnetic field configuration of a flux-rope
The magnetic field configuration of a magnetic flux-rope is shown. The radius of the flux-rope is given by R_0 and the core magnetic field strength is B_0. The pitch-angle of the magnetic field to the axial field increases with increasing distance from the centre of the flux-rope [From Slavin et al., 2003].

A spacecraft passing through a plasmoid with a flux-rope core (i.e. a magnetic field structure that has an element with an axial component and another without a significant axial component) in a similar situation as in Figure 5-2 or through an isolated flux-rope would observe the magnetic variations as shown in Figure 5-4.

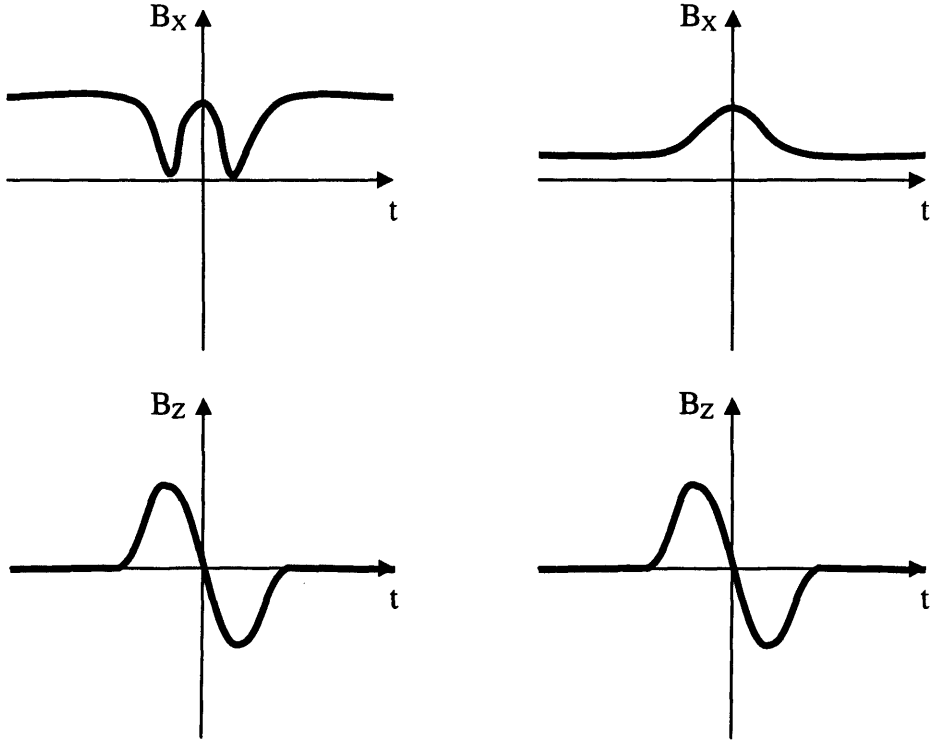

Figure 5-4 Flux-rope core inside a plasmoid and an isolated flux-rope
The magnetic field variations observed by a spacecraft passing through a tailward propagating plasmoid with a flux-rope core (left) and an isolated flux-rope (right). An isolated flux-rope has a significant B_Y variation.

The direction of travel of a plasmoid or flux-rope results in differences in the bipolar B_Z signature and is demonstrated in Figure 5-5. The direction of the flux-rope's propagation with respect to the spacecraft can be determined by identifying the sense of the B_Z signatures, i.e. North-South implies tailward propagation and South-North implies Earthward propagation. Earthward propagating flux ropes were first identified by Moldwin and Hughes [1992] in ISEE 3 data. Recent Cluster observations have used four

spacecraft timing methods to confirm the identification of Earthward and tailward flux-ropes made by bipolar magnetic field analysis [Slavin et al., 2003].

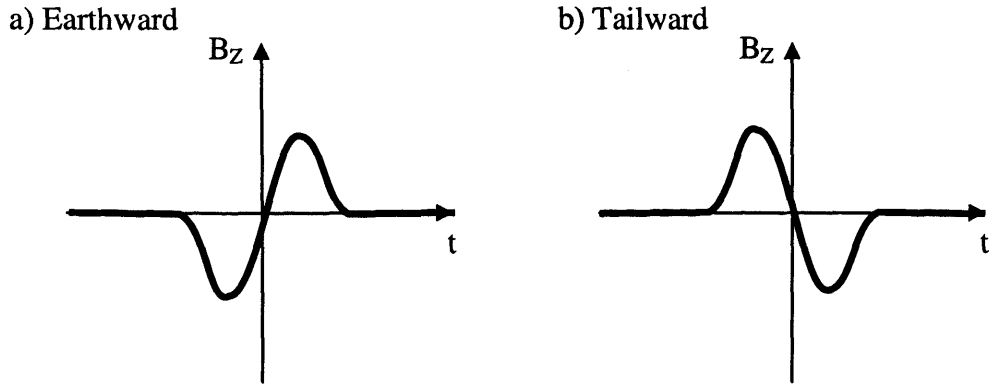

Figure 5-5 Earthward and tailward propagating plasmoid signatures
The formation of a plasmoid with the topology as shown in Figure 5.1b moves a) Earthward over a spacecraft and b) tailward over a spacecraft. In both cases the spacecraft observes the same B_X signature as illustrated in Figures 5.2 and 5.3. However, the polarity of the bipolar signature in the B_Z component of the magnetic field is different. In the Earthward case the signature is South-then-North (SN) and in the tailward case the signature is North-the-South (NS).

Works on identifying the internal magnetic configuration of a flux-rope in the distant tail have been performed [e.g. Slavin et al., 1989] and evidence points to the magnetic field signature approximating to a 'force-free' helical structure in which $\mathbf{J} \times \mathbf{B} \approx 0$. Flux-ropes are often associated with the fast plasma flows [e.g. Machida et al., 1994] and isotropic electron distributions [Scholer et al., 1984].

The observed signatures of the flux-rope propagating in the plasma sheet varies with the distance from the neutral sheet [e.g. Owen and Slavin, 1992]. An illustration of signatures of the passage of a flux-rope by observers at different distances from the neutral sheet is shown in Figure 5-6. In this figure, a spacecraft with trajectory AA′ observes a compression in the lobe magnetic field strength with a North-South B_Z perturbation. This perturbation is known as a travelling compression region (TCR) [Slavin et al., 1992]. A trajectory along BB′ would observe plasma associated with the

plasma sheet and TCR signature as in the AA´ case. If a spacecraft were to transit the flux-rope itself along a trajectory CC´ then plasma sheet-type plasma should be identified and the magnetic structure obeying the dipolar B_Z characteristic, but also illustrating a helical field should be observed.

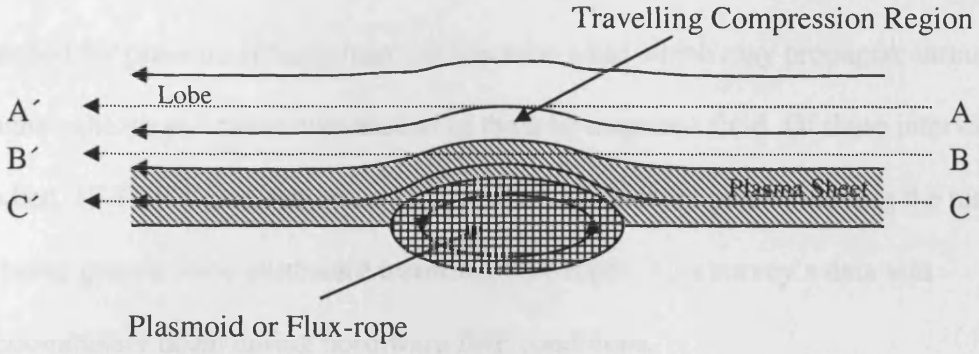

Figure 5-6 Plasmoid / flux-rope associated disturances
A plasmoid or flux-rope in the plasma sheet will cause a disturbance in the plasma sheet to exist and a compression of the magnetic field. As the plasmoid or flux-rope propagates along the tail, this plasma sheet bulge and the compressed magnetic field in the lobes will also propagate. A spacecraft on trajectory AA´ will just detect the travelling compression region whereas a spacecraft on trajectory BB´ will also observe the plasma sheet bulge as it propagates. A spacecraft would detect the magnetic field signatures of the plasmoid/flux-rope itself if it were traversing CC´ [Adapted from Owen and Slavin, 1992].

There have been many observations of TCRs that are believed to be associated with the dynamics of magnetic flux ropes or plasmoids in the plasma sheet [e.g. Slavin et al., 1993; Slavin et al., 1999; Sauvaud et al., 1996]. These signatures are identified by an increase in the total magnitude of the magnetic field strength with a bipolar B_Z signature that is consistent with a magnetic object travelling past the observation point generating the disturbance (N-S indicating tailward motion and S-N being Earthward). Usually these events are associated with substorm activity, but observations of plasmoid-like structures have been made during quiet-time intervals [Kawano et al., 1996]. To date no direct

observation of TCRs associated with a flux rope has been made, allowing for other possible generation methods. For example, the TCR signatures could be generated by wave activity within the magnetotail causing large scale motion of the plasma sheet, or compression of the lobe magnetic field could also be made by high pressure regions in the magnetosheath constricting the magnetotail on a large scale [Slavin et al., 1994]. In a study by Moldwin et al. [2001], 21 S-N TCR signatures observed by IMP 8 were cross-matched for pressure enhancements in the solar wind which may propagate through the magnetosheath and cause constriction of the lobe magnetic field. Of these intervals studied, 17 TCR signatures could be explained by pressure pulses, leaving the rest open to being generated by earthward travelling flux-ropes. This survey's data was predominately taken during northward IMF conditions.

Using the Cluster quartet, we are for the first time able to probe into the plasma sheet with multiple spacecraft whilst also having an observation point outside of the plasma sheet. It may thus be possible to observe TCR signatures simultaneously with flux rope signatures. A representation of a flux-rope passing over some of the Cluster spacecraft whilst one observes the lobe magnetic field is shown in Figure 5-7.

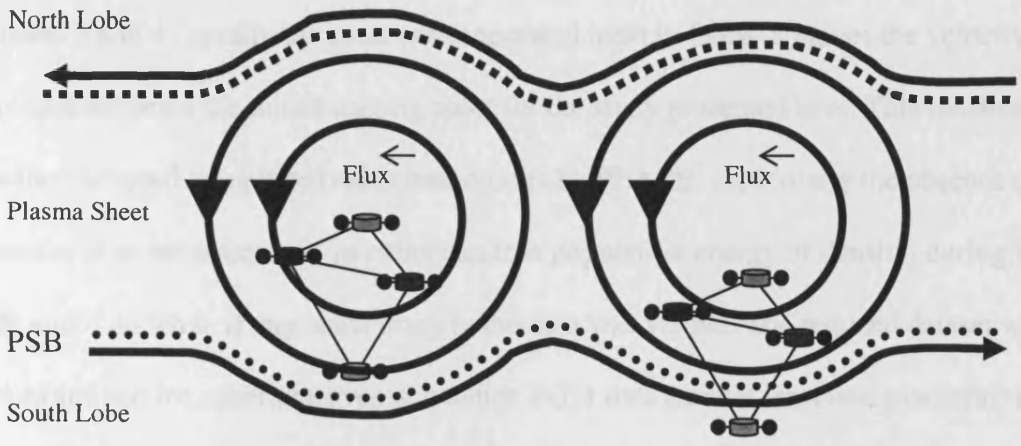

Figure 5-7 Possible flux-rope and TCR encounters with Cluster
The four Cluster spacecraft represented in two possible situations when a TCR is observed. On the left hand side, 3 spacecraft observe a flux-rope whilst the fourth skims this flux-rope and may observe a draping field or compression in the magnetic field whilst still located in the plasma sheet. On the right hand side, 3 spacecraft observe a flux-rope whilst the fourth remains in the lobe entirely and only detects the TCR.

A description of the travelling compression region dataset and an illustration of how Cluster may be used to identify TCR and flux ropes simultaneously are described in the next section. In Section 5.3, a force-free flux-rope model is described. Three candidate events from the 2001 magnetotail season and one from 2002 are described and analyzed in Section 5.4. We particularly concentrate on the observed plasma conditions observed during these candidate events. These results and conclusions are summarized in Section 5.5.

5.2 TCR Dataset and Methodology

A catalogue of 148 TCRs has been compiled by Slavin [Unpublished document, 2004]. Data from the FGM instrument were analyzed for 2001 and 2002 tail seasons and TCR events were identified together with the nature of bipolar B_Z signature. Propagation speeds of the TCRs have been calculated taking a simple approximation that the TCR

propagates purely in the GSM-X direction, and therefore the time taken to pass between Clusters 1 and 4 (usually the spacecraft separated most in GSM-X) gives the velocity. This dataset forms the initial starting point for the study presented here. This database was then adapted to include basic observations by PEACE, particularly the absence or presence of an enhancement, in either electron population energy or density, during the TCR and if so what, if any, anisotropy in the data was visible. The reduced dataset was then examined for candidate events in which FGM data from at least one spacecraft in the plasma sheet could be successfully fitted to the force-free flux-rope model to determine if any of these TCR signatures observed by the spacecraft remaining in the lobes could be unambiguously associated with plasma sheet flux-ropes.

Initially, at least one spacecraft was required to remain in the magnetic lobe where there is no significant electron population to act as a monitor for TCR signatures. This resulted in three events being identified which will be discussed in detail below. The low number of candidate events is explainable by the scale size of the spacecraft tetrahedron with respect to the size of the flux-rope and thickness of the overlying plasma sheet. If a relatively large spacecraft separation was in use then we would expect to observe more intervals with a spacecraft located in the sparsely populated lobe while at least one other was located in the plasma sheet. If, however, the relative spacecraft separation is too small, we would expect the plasma signatures to be more often identical across the quartet, making the observation of two spatially separated plasma populations less likely. Thus we expect more events to be identified as the Cluster separation increased during its extended mission. The magnetic field observed at the spacecraft in the plasma sheet was then used to attempt a fit to the force-free flux-rope model. Thus we are potentially able

to identify if the lobe TCR signatures observed are directly associated with flux-ropes in the plasma sheet.

After this analysis the condition that one spacecraft be located in a sparsely populated magnetic lobe was relaxed so that the PSBL may be included, but at least one spacecraft had to observe a compression in the magnetic field whilst another had to observe a significant reduction in B_X (to less than 10nT) to ensure closer proximity to the neutral sheet. This was performed to allow a greater chance of observing a flux-rope and not simply the associated draping field. One event was identified for analysis matching this condition. The flux-rope model was then tested against this data.

5.3 Force-Free Flux Rope Model

A successful model of flux-rope structure is that of the force-free rope, where the current density within the rope structure is proportional to the magnetic field [Goldstein, 1983]. This is the simplest model and defines the minimum energy state for helical field structures. The force-free condition is described by the α-parameter in the equation:

$$\nabla \times \mathbf{B} = \mu_0 \mathbf{J} = \alpha \mathbf{B} \tag{5.1}$$

The α-parameter was shown to be approximately constant in a solar wind magnetic cloud structure, a large scale flux-rope with both ends connected to the Sun, by Burlaga [1988]. This approximation allows, by vector identity, the following differential equation to be formulated:

$$\nabla \times (\nabla \times \mathbf{B}) = \alpha(\nabla \times \mathbf{B}) = \alpha^2 \mathbf{B} \tag{5.2}$$

$$\nabla^2 \mathbf{B} = -\alpha^2 \mathbf{B} \tag{5.3}$$

In cylindrical polar co-ordinates, the natural coordinate system for a flux-rope, the solutions to this differential equation, the axial, tangential and radial component, were found by Lundquist [1950] and use the zeroth- and first-order Bessel functions, J_0 and J_1:

$$B_A = B_0 J_0(\alpha r) \tag{5.4}$$

$$B_T = B_0 H J_1(\alpha r) \tag{5.5}$$

$$B_R = 0 \tag{5.6}$$

where: r is the distance from the axis of the flux rope; B_0 is the core magnetic field along the axis of the flux rope (i.e. where r=0); H=±1 and is the helicity of magnetic field with respect to the direction of the core magnetic field. The radius of the flux-rope is R_0 and a useful quantity is Y_0/R_0. This is known as the impact parameter, where Y_0 defines the

distance to the centre of the flux-rope at closest approach of a chord (e.g. a spacecraft trajectory) passing through the flux-rope. The schematic of a spacecraft traversal of a flux-rope is illustrated in Figure 5-8.

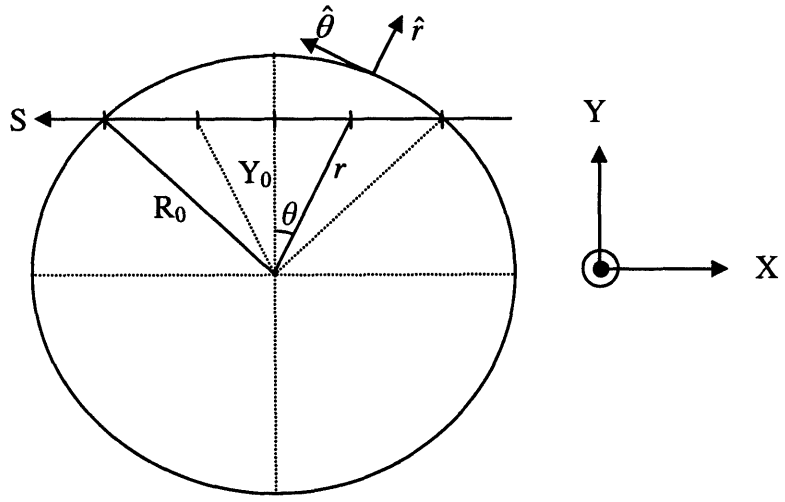

Figure 5-8 Geometry of a trajectory through a flux-rope
The geometry of a spacecraft trajectory, S, passing through a flux-rope as viewed down the axis of the flux-rope. The component of the trajectory along the axis of the flux rope has no effect on the calculation of the model magnetic field as this is purely dependant on the distance to the axis. R_0 is the radius of the flux-rope and is initially taken to be 1. Y_0 is the distance of closest approach of the spacecraft to the centre of the flux-rope.

To complete the description of the passage of a spacecraft through the magnetic flux rope being modelled, the following parameters are required: the latitude and longitude of the axis of the flux rope in relation to the chosen coordinate frame; and, the time when closest approach was achieved, t_0. Note however that these parameters are not needed in the basic assessment of the structure of the magnetic field as a force-free flux-rope.

This is the fundamental flux-rope model used by Lepping et al. [1990] for the successful fitting of interplanetary magnetic clouds, and is used in this work to identify magnetic field structures within the plasma sheet as being those of a flux-rope [Slavin,

2003]. Other flux-rope models exist [e.g. Priest, 1990] and may ultimately prove more suitable for the magnetic structures identified. However, for the prime objective here, to directly determine if TCR signatures in the lobe are associated with flux-rope type signatures, this basic model is adequate. The application of this model with Cluster FGM data is explained below following the methodology of Lepping et al. [1990].

The method of testing the force-free flux-rope model with the observed data will be explained in two parts. Firstly, the raw data is prepared for the comparison. Secondly, the calculation of the expected field from the model is obtained. Once these two datasets are generated, an appropriate 'goodness-of-fit' test can be applied. It is worth noting that the model fitting is performed to unit magnetic field vectors, in order to emphasize the change in direction of the magnetic field within the structure of the flux-rope. Scaling of the model result can then be made, if desired, to also fit to the observed data's magnitude.

The initial step in fitting to this model is the definition of the axes of the coordinate system to be used. The principle axis of the flux-rope is given as the Z-axis with the X- and Y- axis being perpendicular to this forming a right-handed set. Minimum Variance Analysis (MVA), also known as principal component analysis, is used to find an approximation to the axes directions. The initial 'guess' for the X-, Y- and Z-axes are that they are along the minimum, maximum and intermediate axes from MVA respectively, since this is what is recovered from analysis of the force-free flux-rope model field. MVA is therefore applied to the normalized observed dataset which is then rotated into the MVA co-ordinate system to provide the correctly aligned field (B^O) for fitting. To obtain the best result possible, the sample of observed data that was taken for MVA was varied in size and start position over the period of interest to obtain the best fit.

The rotation angles of the original GSE magnetic field data into the MVA co-ordinate system thus provide an estimate for the flux-rope orientation within the magnetosphere. However, the actual axes may differ depending on the value of the impact parameter. Lepping et al. [1990] found this correction to the orientation to be: 3.1° for an impact parameter of 0.3 increasing to 17.8° when the impact parameter was 0.9.

The model field is calculated by first computing the distance of the spacecraft to the central axis from when it first enters the flux-rope to when it exits the flux-rope (refer to Figure 5.8). Initially a unit radius flux-rope is used and the core field is taken to be unity. The number of data points to be computed is taken to match the number of observed data points to which we are trying to fit. The distance to the flux-rope axis, reduces to the problem of working out the distance of a point along a chord of a circle for the n data points evenly spread along that chord.

The variations of B_A and B_T, the axial and tangential magnetic fields, are determined purely from this distance and are rotationally symmetric about the axis. The Cartesian components are taken as:

$$B_X = -B_T \sin(\theta) \tag{5.7}$$

$$B_Y = B_T \cos(\theta) \tag{5.8}$$

$$B_Z = B_A \tag{5.9}$$

and are rotated into their appropriate MVA coordinate system (B^M).

The model fitting procedure operates as shown in the flow chart in Figure 5-9 testing a range of impact and helicity flux-rope parameters. A Chi-Squared statistic is produced and this allows for the determination of the best model fit. The formulization of the Chi-Square statistic is given as:

$$\chi^2 = \sum \left(\left(B_X^O - B_X^M\right)^2 + \left(B_Y^O - B_Y^M\right)^2 + \left(B_Z^O - B_Z^M\right)^2 \right) / N \qquad (5.10)$$

In the adaptation of this method by Slavin et al. [2003] a 'reduced Chi-Squared' test is performed accepting the model as a 'good fit' if:

$$\sqrt{\chi_R^2} < 0.04 \qquad (5.11)$$

where: $\chi_R^2 = \chi/(3N - n)$ with N being then number of data points used in the fit and n=5 is the number of parameters fit in the model. The results of the fitting are ignored if the inequality in Equation 5.11 is not true. A null result implies that the data does not model a force-free flux-rope and quantities such as the impact parameter are meaningless. In the case of a null result, further analysis, out of the scope of this thesis, could be performed to compare other flux-rope models and also draping field models allowing a more detailed picture to be identified.

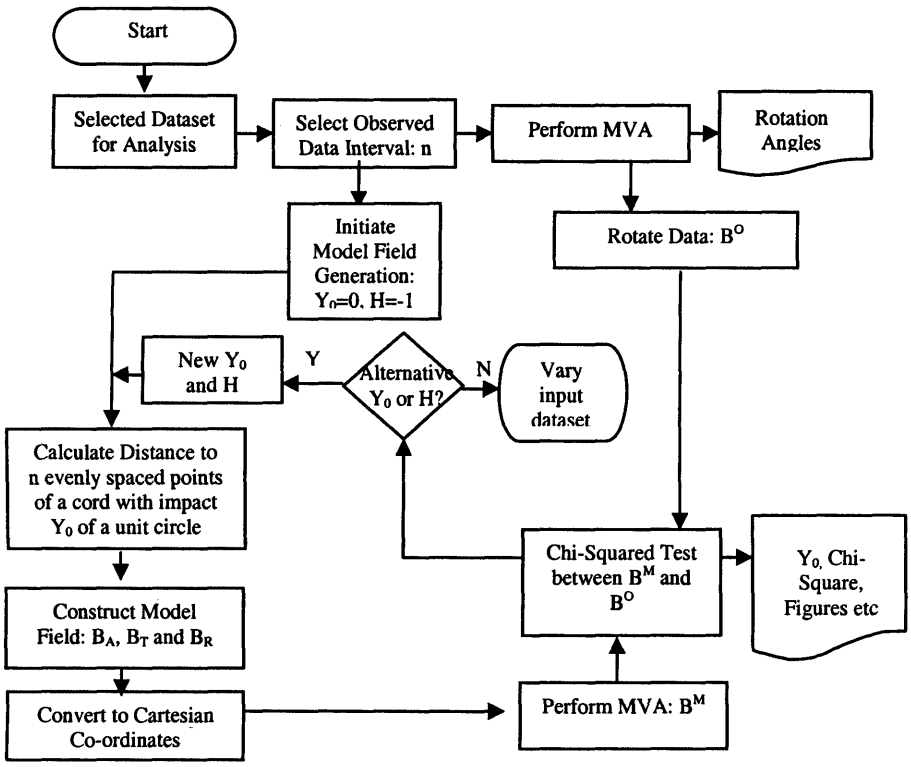

Figure 5-9 Fitting routine
A flow chart illustrating the force-free fitting routine used to establish if the magnetic field observed during the selected intervals is associated with the magnetic field of a flux-rope.

A more detailed fit can be implemented if required by rotating the observed data set by an angle determined with knowledge of the impact parameter. An iterative process can be performed to repeat the determination of the impact parameter and application of the appropriate correction factor. This rotation is not performed in our presented analysis as the pinning down of the direction of the flux-rope principal axis is not our primary interest.

Once the impact parameter has been obtained, the flux-rope radius is obtained by considering the distance covered by the plasma during the interval observed, taking the ion velocity as the speed of the flux-rope, and applying Pythagoras' theorem with the radius of the flux-rope and the impact parameter.

Application of the Lepping et al. [1990] force-free flux rope fitting procedure was first used to replicate the results obtained by Slavin et al. [2003] for a flux rope observed by Cluster on 22nd August 2001. Data from the PEACE and FGM instruments is shown in Figure 5-10 for all the Cluster spacecraft (N.B. PEACE on Cluster 3 returned bit-shifted data which is currently not recoverable and is therefore not shown). In the figure the electron differential energy fluxes parallel, perpendicular and anti-parallel to the magnetic field are shown for Cluster 1, 2 and 4 together with the magnetic field magnitude and components for all spacecraft.

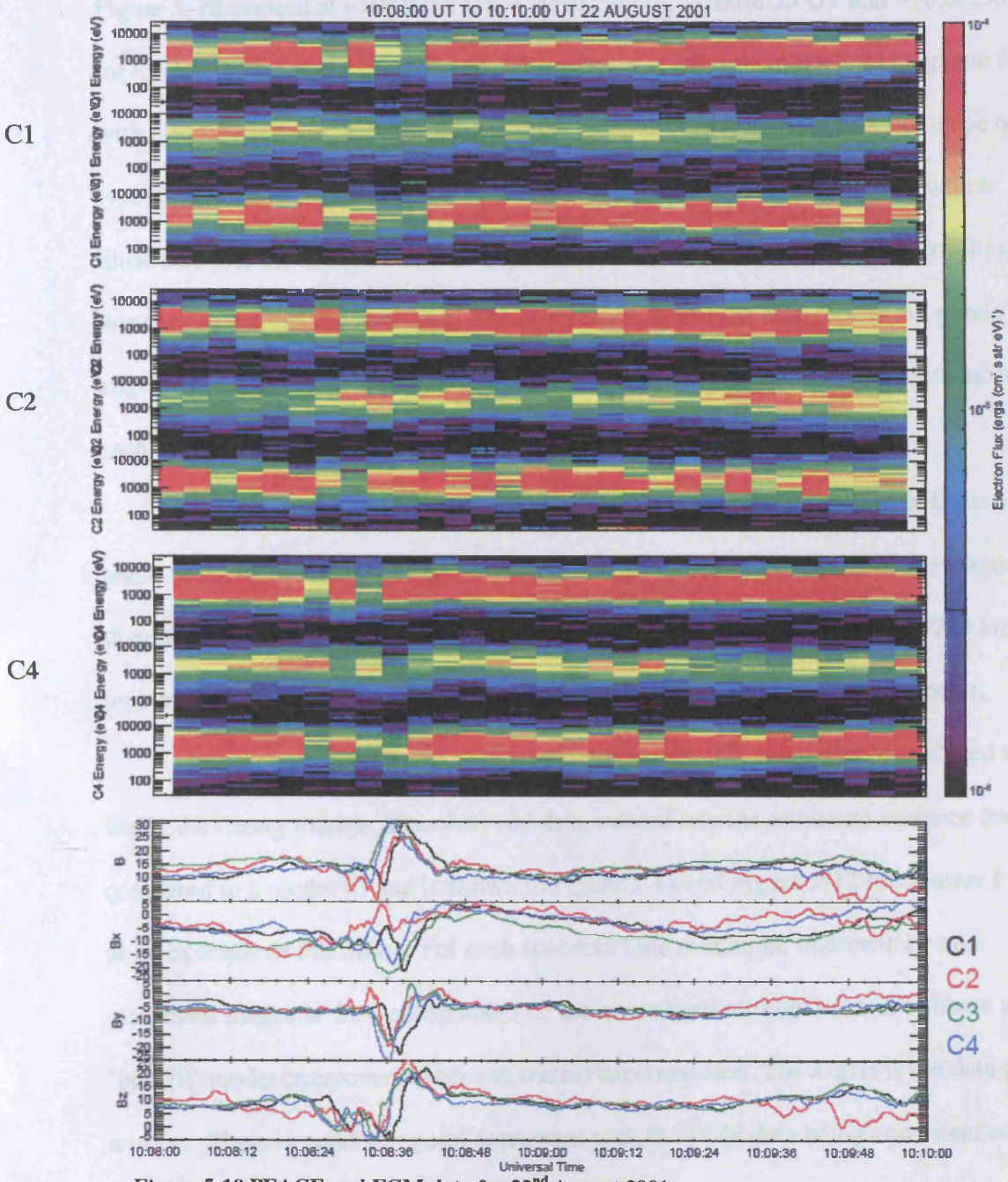

Figure 5-10 PEACE and FGM data for 22nd August 2001

The first 9 panels show the electron differential energy flux spectrograms for field-aligned, perpendicular and anti-parallel electrons for Clusters 1, 2 and 4 respectively (Cluster 3 returned bit-shifted data for this interval and is not shown). The final 4 panels show the magnitude of the magnetic field and the B_X, B_Y and B_Z components from FGM in the GSM coordinate system for each spacecraft.

Clear bipolar signatures are observed in the B_z component of the magnetic field in Figure 5-10 centred at ~10:08:38 UT, ~10:08:36 UT, ~10:08:35 UT and ~10:08:36 UT for Cluster 1, 2, 3 and 4 respectively. These occur at maxima in the total magnetic field, with clear maxima in B_Y indicating that the signatures maybe those of a flux-rope of the type illustrated in Figure 5-4. There are, however, significant B_X signatures which illustrates that the GSM co-ordinate system is not the most appropriate one for illustrating this data as a magnetic flux-rope. The implication is that the flux-rope is not purely aligned with the GSM-Y axis at this point in space. The magnetic field disturbances at each spacecraft are approximately 9 to 12 seconds long.

A basic timing analysis [Slavin et al., 2003] taking the separation of Clusters 1 and 4 (0.22 R_E in X) and noting the ~2 second difference in the timing of the magnetic disturbance at these spacecraft give an approximate Earthward velocity of ~700 kms^{-1} and the duration of the event therefore implies the structure is ~1 R_E in diameter.

For each spacecraft, the magnetic field data for this event was re-analyzed to verify the fitting routine. The observed data, rotated into the minimum variance frame is compared to a model fit and is shown in Figure 5-11 and Figure 5-12 for Cluster 1 and 4 as an example of the fitting. For each spacecraft the minimum, intermediate and maximum magnetic field components of the normalised observed data are shown with the 'best fit' model components (smooth traces) superimposed. The x-axis is the data-point number. There is generally good agreement with the FGM data being consistent with that expected for a force-free magnetic flux-rope. The impact parameter for Clusters 1 and 4 were found to be 0.42 and 0.51 respectively and agree with the range provided in Slavin et al. [2003] of 0.41 to 0.66. This flux-rope has a positive helicity.

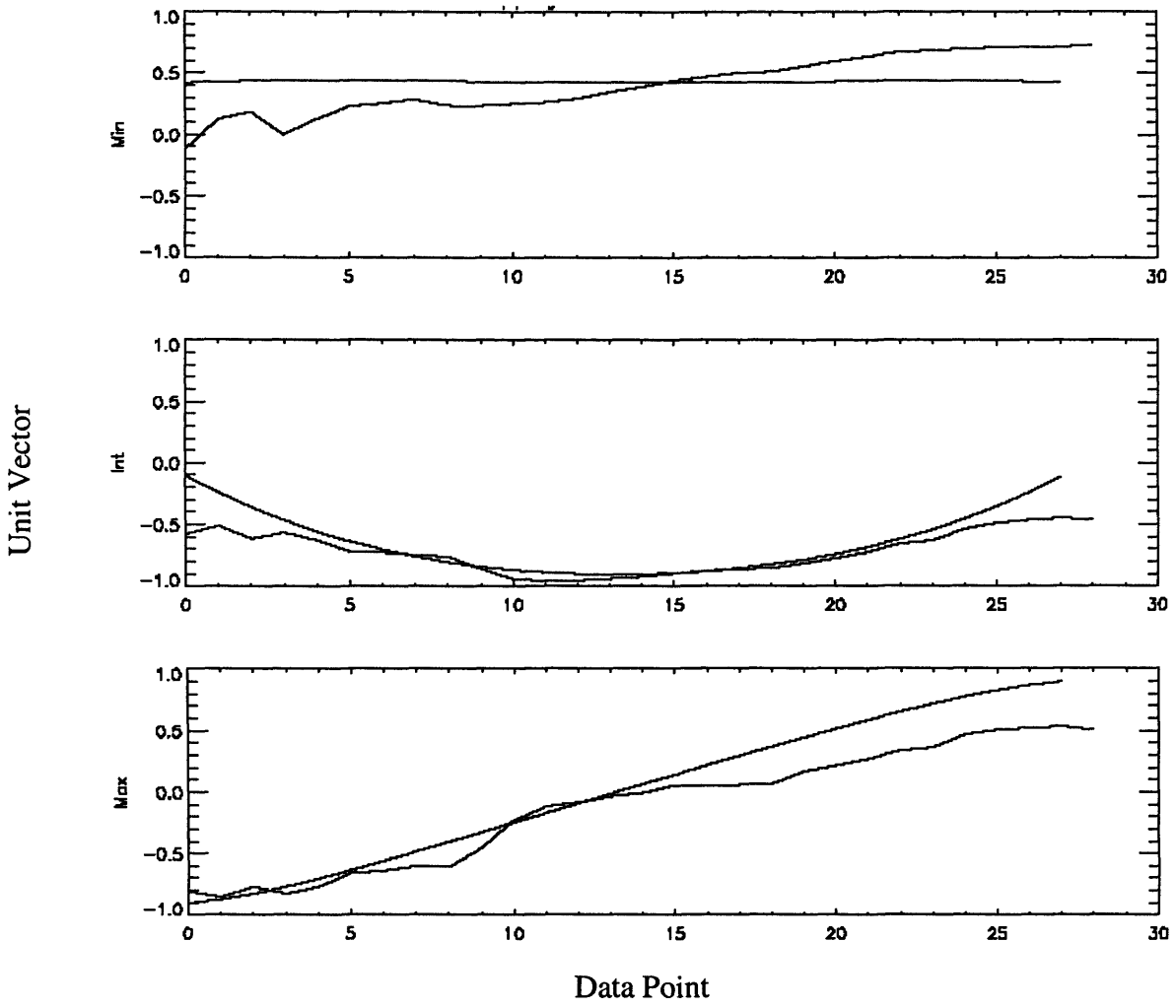

Figure 5-11 Force-free flux-rope fit for Cluster 1 – 22nd August 2001
The force-free flux-rope fitting results compared to the observed data for the 22nd August 2001 event for Cluster 1. The smooth line is that of the Lepping et al. [1990] model with an impact parameter of 0.42. The other line shows the observed unit-vector data. The reduced chi-squared for this fitting is 0.04 indicating a suitable fit.

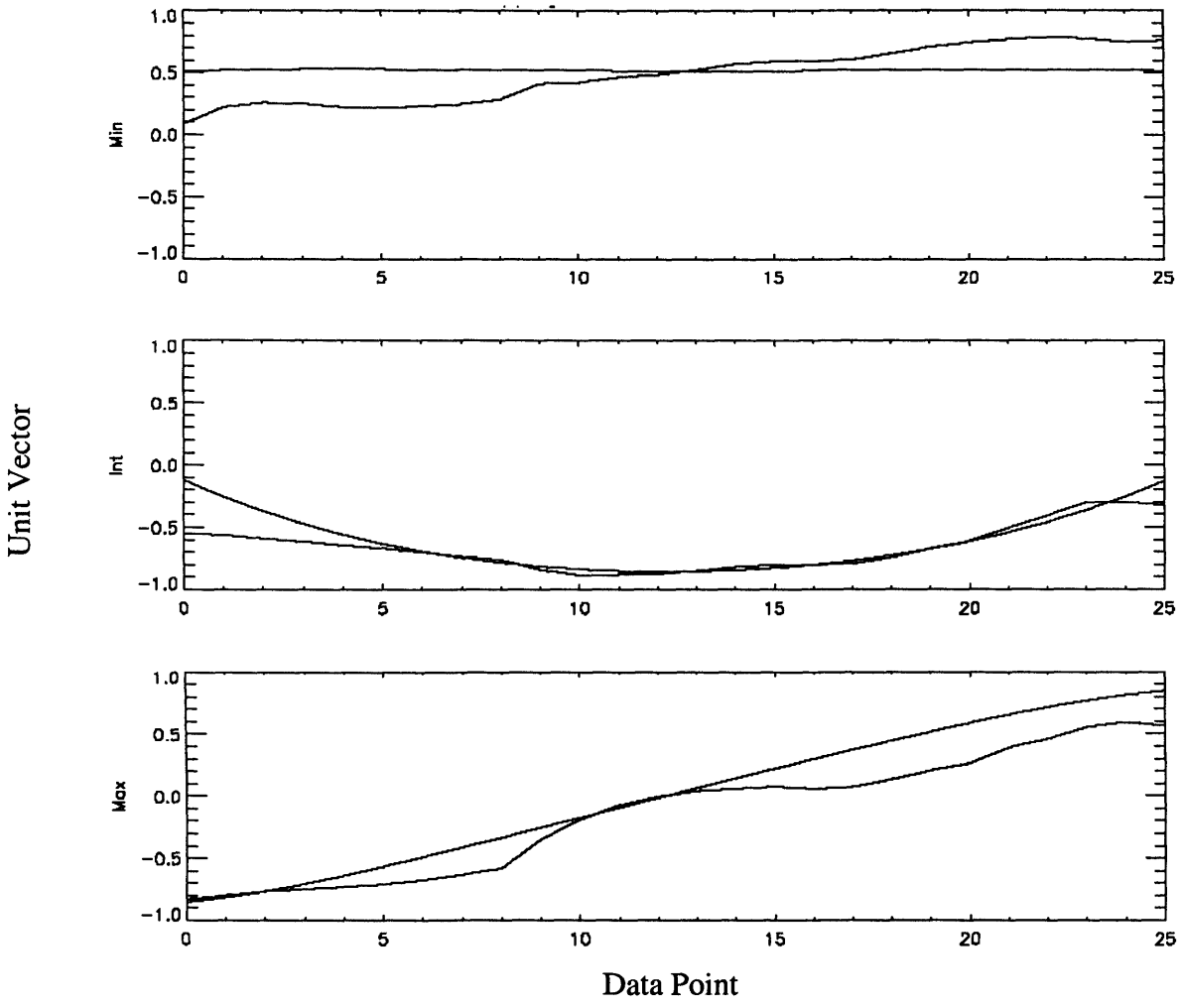

Figure 5-12 Force-free flux-rope fit for Cluster 4 – 22nd August 2001
The force-free flux-rope fitting results compared to the observed data for the 22nd August 2001 event for Cluster 4. The Lepping et al. [1990] model with an impact parameter of 0.51 is shown with the observed data. The reduced chi squared for this fitting is 0.03 indicating a good fit.

The period which best fits the data at each spacecraft is 7 seconds and 6.25 seconds respectively for Cluster 1 and 4. The ion velocity during this interval is 500-750 kms^{-1} (not shown), and leads to the diameter of the flux rope to be between 0.61 and 0.90 R_E. This is shorter than the results obtained by Slavin et al. [2003] who find the average duration to be ~9 seconds at each spacecraft leading to a flux-rope of diameter of 0.96 to 1.08 R_E. This difference is due to only a first level fit being performed on to the data as

further rotations of the dataset due to an initial impact parameter of 0.42 – 0.51 have not been performed and are not necessary to confirm that the magnetic field signatures of this event are modelled by a basic force-free flux-rope model.

In reproducing the Slavin et al. [2003] results, it was noted that artefacts in the data often reduced the size of the interval that could be used for the fitting, often resulting in poor counting statistics. Whilst the FGM data can be provided in higher resolution than the 4 vectors per second used here, the extra complexity revealed causes practical limitations when performing the fit. Given the simplicity of the model, too much detail in the data detracts from the basic aim of identifying if the magnetic structure is that of a flux-rope or not.

No detailed analysis of the PEACE electron data was provided by Slavin et al., [2003] for this event. Unfortunately, Cluster 3 was returning bit-shifted data for the PEACE instrument and the correct data is not obtainable from the telemetered data at this time. The 3 other spacecraft provided an insight into the plasma properties within this flux-rope.

The PEACE data for Clusters 1 and 2, shown in Figure 5-10, show slightly conflicting pitch-angle distributions for the interval of the flux-rope and the surrounding data. Cluster 1 indicated that the total differential energy flux of the flux-rope decreases slightly, whereas Cluster 2 observed an increase in the differential energy flux particularly at perpendicular pitch-angles. At Cluster 4, which is further away from the axis of the flux rope than Cluster 1 by impact parameter, a decrease in the differential energy flux is observed starting slightly before the flux-rope, returning to its original level before the flux-rope has entirely passed. Unlike Scholer et al. [1984], the data does

not indicate an entirely isotropic electron distribution. However, these observations show the limited conclusions that can be made from short time scale observations during normal mode operations, as only a few spacecraft spins' worth of data are available. Due to the rapid motion of the structure it is also possible that there is an aliasing of the electron distributions.

5.4 Study Events

Three events containing travelling compression region signatures observed by at least one spacecraft whilst the remainder see plasma sheet plasma are presented. Potentially, one spacecraft may observe the magnetic field and associated plasma for a flux rope within the plasma sheet and this would be direct evidence for the association of TCR signatures with such structures passing along the plasma sheet. A further example, where all four spacecraft are located within the plasma sheet, but one still observes an increase in the magnetic field strength is also presented. The events presented are: 07:44 to 07:47 UT 17th September 2001; 21:08 to 21:10 UT 19th September 2001; 21:22 to 21:25 UT 19th September 2001; and, 21:28 to 21:32 UT 25th August 2002.

For each event, the spacecraft configuration, magnetic field in GSM coordinates and electron data are presented and discussed. The PEACE data shown are omni-directional spectrograms in differential energy flux. The energy range shown is 34 eV to 26.4 keV. The description of the fitting procedure for each spacecraft located within the plasma sheet for each event is then discussed and the results, if a flux rope is identified, are described. Where a force-free flux rope model has been successfully fitted, basic details of the flux-rope are provided. A more in-depth analysis of the flux-rope parameters, extra data rotations due to the value of the impact parameter etc., is required

to obtain the exact model results and this should be explored with varying magnetic field data resolutions to test the robustness of the model.

5.4.1 17th September 2001 07:44-07:47 UT

The spacecraft configuration for this interval is shown in Figure 5-13 constructed of three panels showing the GSM-ZX, -ZY, and –YZ separations. Cluster 2 is furthest north during this interval followed by Cluster 1 and 4 with Cluster 3 located furthest south of the tetrahedron as is typical for the mid-tail season. Cluster 4 is located away from the other spacecraft in GSM-X.

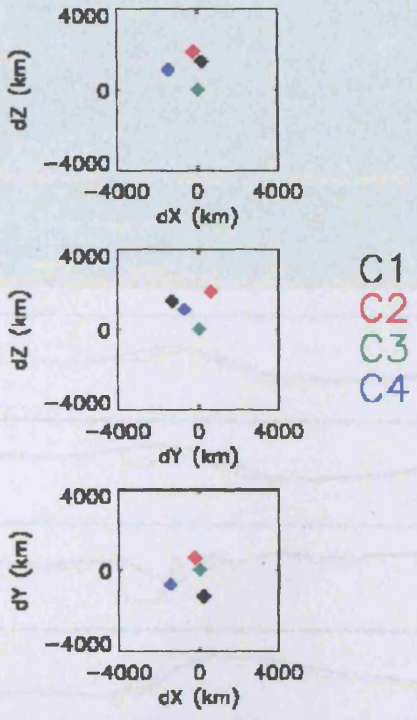

Figure 5-13 Cluster configuration on 17th September 2001
The spacecraft configuration for the 17th of September 2001 event in the GSM co-ordinate system. The Cluster spacecraft are shown in their standard colours of black, red, green and blue for Cluster 1, 2, 3 and 4 respectively.

The PEACE directional differential energy flux spectrograms for each spacecraft and the FGM magnetic field components in GSM, shown in the standard spacecraft colours, are presented in Figure 5-14 and Figure 5-15.

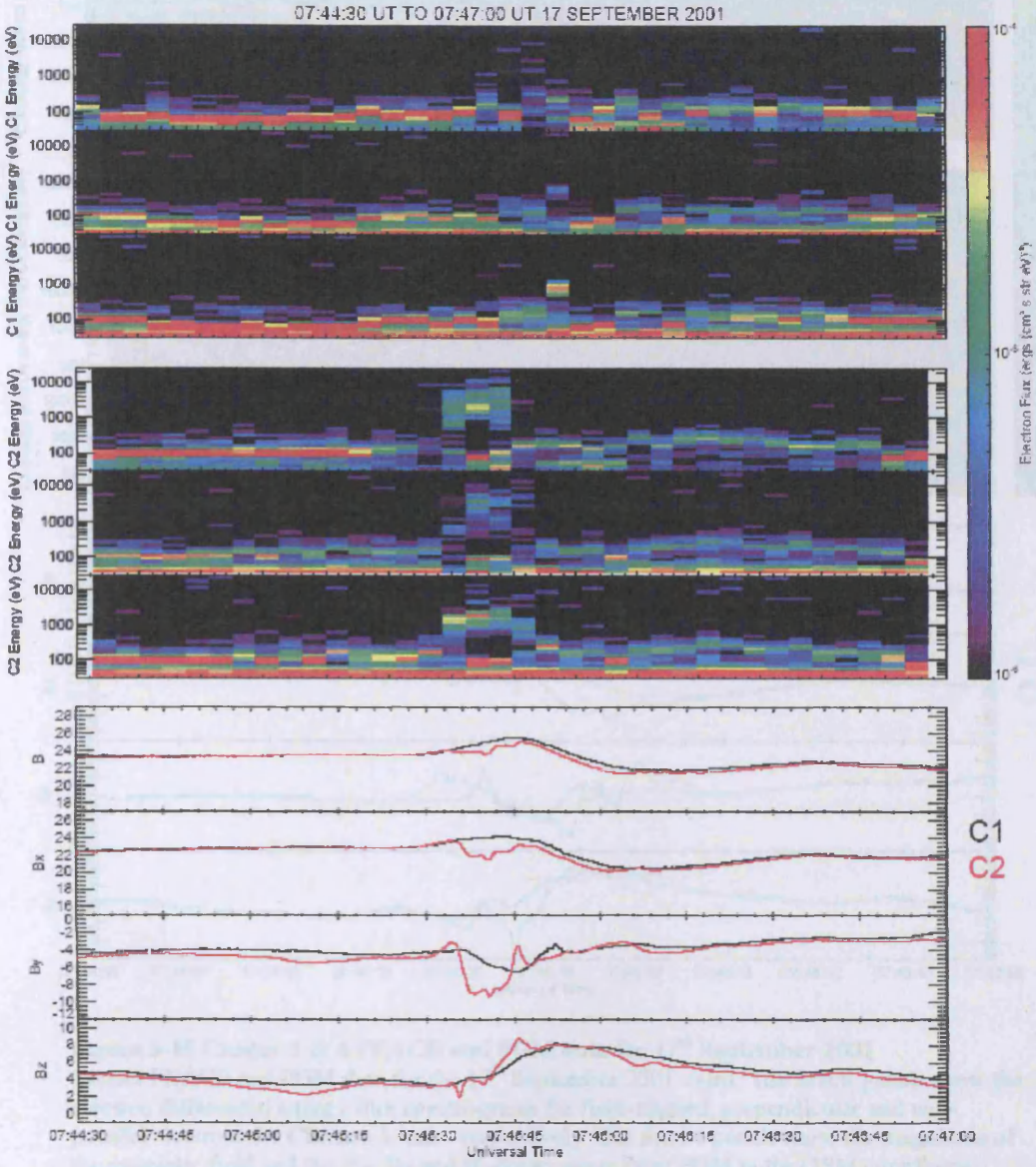

Figure 5-14 Cluster 1 & 2 PEACE and FGM data for 17th September 2001
Cluster PEACE and FGM data for 17th September 2001 event. The first 6 panels show the electron differential energy flux spectrograms for field-aligned, perpendicular and anti-parallel electrons for Clusters 1 and 2 respectively. The final 4 panels show the magnitude of the magnetic field and the B_X, B_Y and B_Z components from FGM in the GSM coordinate system.

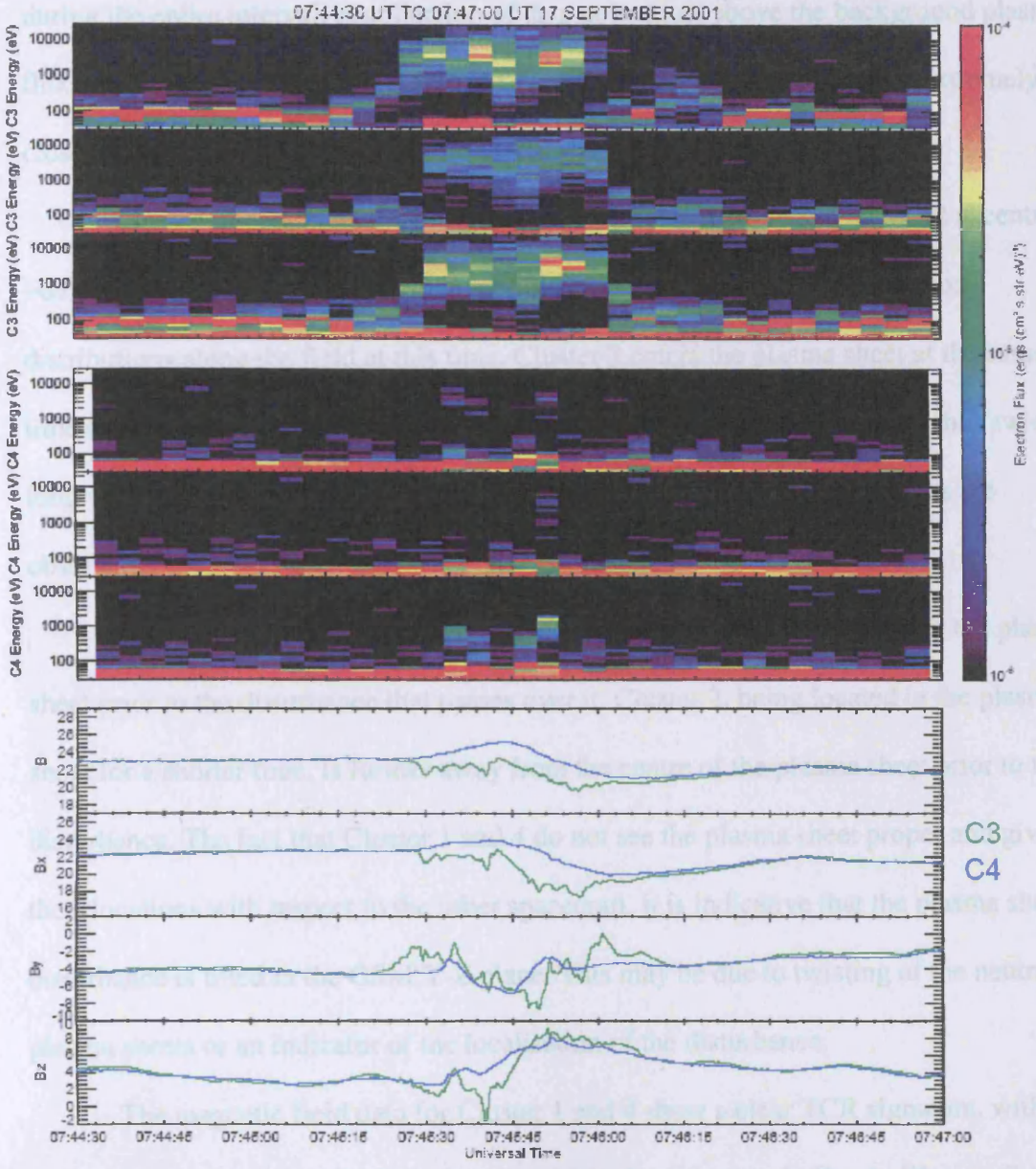

Figure 5-15 Cluster 3 & 4 PEACE and FGM data for 17th September 2001
Cluster PEACE and FGM data for the 17th September 2001 event. The first 6 panels show the electron differential energy flux spectrograms for field-aligned, perpendicular and anti-parallel electrons for Clusters 3 and 4 respectively. The final 4 panels show the magnitude of the magnetic field and the B_X, B_Y and B_Z components from FGM in the GSM coordinate system.

At Cluster 1 and 4, the PEACE data indicated the spacecraft remain in the lobes during the entire interval. A collection of data points just above the background plasma fluxes around the interval ~07:45:36 UT to ~07:45:51 UT may indicate an extremely close encounter to the plasma sheet boundary layer.

Cluster 2 encounters the plasma sheet for approximately 3 spins, ~ 12 s, centred at ~07:45:40 UT. Pitch angle data indicates bi-direction streaming of the electron distributions along the field at this time. Cluster 3 enters the plasma sheet at the same time as Cluster 2. However, Cluster 3 remains in the plasma sheet for more than twice as long. Again, throughout the interval, bi-directional field-aligned distributions are observed.

These observations suggest that Cluster 3 is the closest to the edge of the plasma sheet prior to the disturbance that passes over it. Cluster 2, being located in the plasma sheet for a shorter time, is further away from the centre of the plasma sheet prior to the disturbance. The fact that Cluster 1 and 4 do not see the plasma sheet proper and given their locations with respect to the other spacecraft, it is indicative that the plasma sheet disturbance is tilted in the GSM Y-Z plane. This may be due to twisting of the neutral and plasma sheets or an indicator of the localisation of the disturbance.

The magnetic field data for Cluster 1 and 4 show a clear TCR signature, with an increase in the total magnitude and a smooth bipolar signature in B_Z. At Clusters 2 and 3, which enter the plasma sheet, there is a divergence from TCR signatures observed at the other two spacecraft. Both Clusters 2 and 3 are located slightly closer to the neutral sheet than Clusters 1 and 4 until approximately 07:45:45 UT when the B_X component shows the neutral sheet is now closer to Cluster 3 and Cluster 2 is now located back in the lobes.

From the Slavin [2004] database the TCR has a duration of ~17 s and moves Earthward at ~750 kms^{-1}.

Attempts to fit the force-free flux-rope model to the Cluster 2 data was unsuccessful and therefore this data does not appear to be associated with the spacecraft encountering a force-free flux-rope. An explanation of what this data may represent follows the description of the fitting for Cluster 3.

The magnetic field from 07:45:40 UT until 07:46:00 UT at Cluster 3, with 5 vectors per second, is successfully modelled by a force-free flux-rope with an impact parameter of 0.88. This is a significant fit with a reduced chi-squared value of 0.019. The magnetic field data and the model data in MVA coordinates are shown in Figure 5-16. Given an ion velocity of ~400 km s^{-1} this leads to a flux-rope radius of ~ 1.32 R_E. The eigenvectors from the MVA analysis provide an intermediate direction, i.e. approximate flux rope axis, of $(0.26, 0.89, 0.37)_{GSE}$ which indicates that this flux-rope is roughly in the GSE-XY plane.

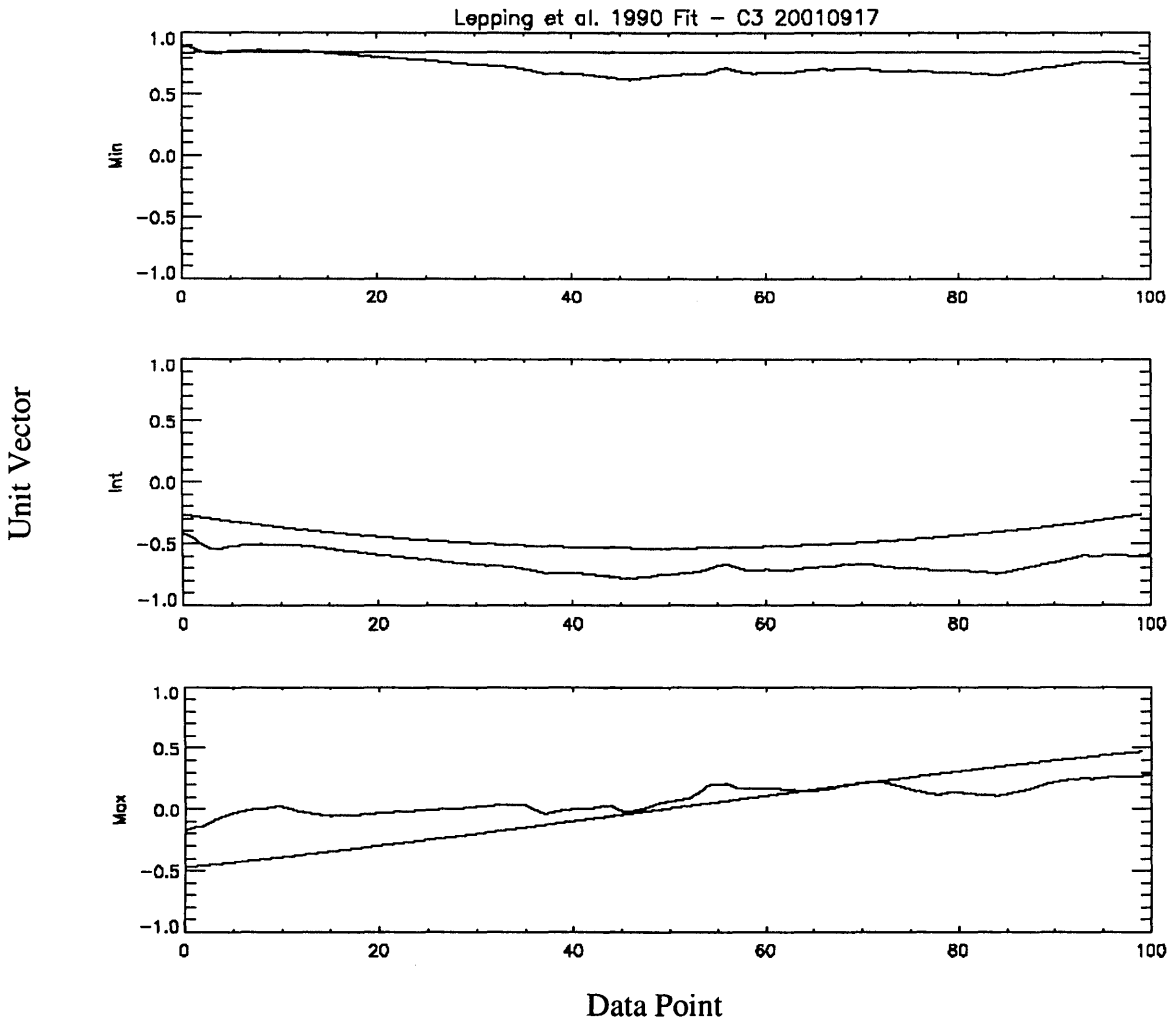

Figure 5-16 Force-free flux rope fit for Cluster 3 – 17th September 2001
The magnetic field from Cluster 3 for the interval 07:45:40 UT to 07:46:00 UT 17th September 2001 event is shown in MVA coordinates. Superimposed are the components, again in MVA, of a force-free flux-rope model with an impact parameter of 0.88. This fit has a reduced chi-squared test statistic of 0.019 making this a significant fit.

An alternative model result is also possible for this data. If the period of interest is restricted to the time interval when Cluster 2 also observes plasma sheet plasma, such that we assume that the plasma bulge caused by a flux-rope is preceded by plasma sheet type plasma, a less significant fit with an impact parameter of 0.91 can be fit for the data between 07:45:43 UT and 07:45:52 UT with a reduced chi-squared test statistic of 0.035. Using the same ion velocity, this result implies a flux-rope radius of ~ 0.94 R_E.

The plasma that is observed at Cluster 2 may well be part of the plasma sheet boundary layer that has been pushed up by the flux-rope passing underneath it or it may be plasma sheet plasma itself that is on a draped magnetic field generated by the passage of the flux rope.

5.4.2 19th September 2001 21:08-21:10 UT

The events of 19th September 2001 have been described in detail [Slavin et al., 2003; Owen et al. 2005; Boralv et al., Submitted]. The interval of interest covers several encounters with the plasma sheet, sometimes for extended periods, with TCR signatures observed in the magnetic field data. Clusters 1, 2 and 4 penetrate deeper into the plasma sheet than Cluster 3. Slavin et al. [2003] identify TCR signatures at the Cluster quartet and note the observation of plasma at Cluster 1, 2, and 4. These authors calculate the average speed of 6 TCRs to be 413 km s^{-1}. The association of TCRs with bulges in the north-south thickness of the plasma sheet is taken as evidence of flux-ropes generate TCRs. Owen et al. [2005] examine the currents that flow in observed plasma sheet bulges as they propagate, identifying that cases where Earthward movement is associated with tailward streaming of electrons may be associated with the closure of Hall current systems. These authors also identify evidence for the onset of multiple X-lines. A more global aspect of this substorm event is given by Boralv et al. [Submitted]. Here, analysis of the intervals where a TCR is observed at one spacecraft and the plasma sheet is observed at the others is performed to discover if there are indeed encounters with a force-free flux rope.

Using the same description as in Figure 3, the spacecraft configuration for this event in the south lobe is shown in Figure 5-17. Cluster 2 remains the most north spacecraft followed by Cluster 4 and then Cluster 1.

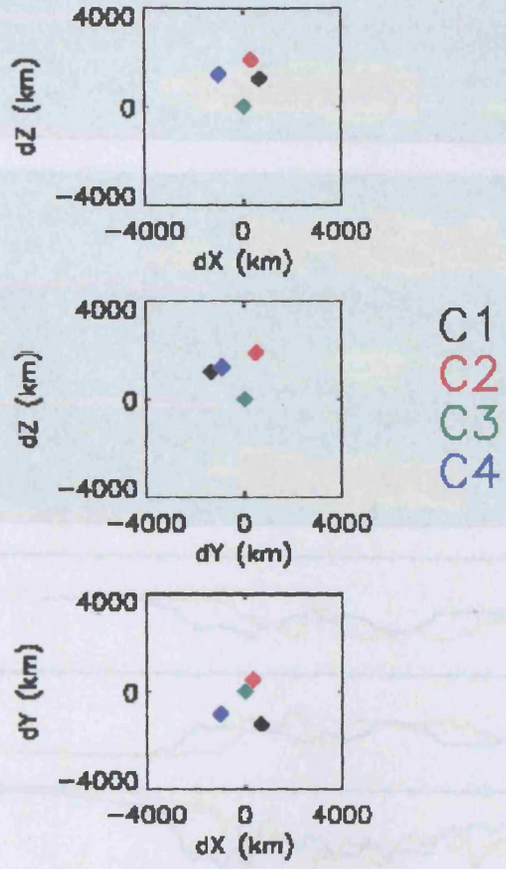

Figure 5-17 Cluster configuration on 19th September 2001
The spacecraft configuration for the 19th of September 2001 events in the GSM co-ordinate system. The Cluster spacecraft are shown in their standard colours of black, red, green and blue for Cluster 1, 2, 3 and 4 respectively.

The PEACE directional differential energy flux spectrograms for each spacecraft and the FGM magnetic field components in GSM are presented in Figure 5-18 and Figure 5-19.

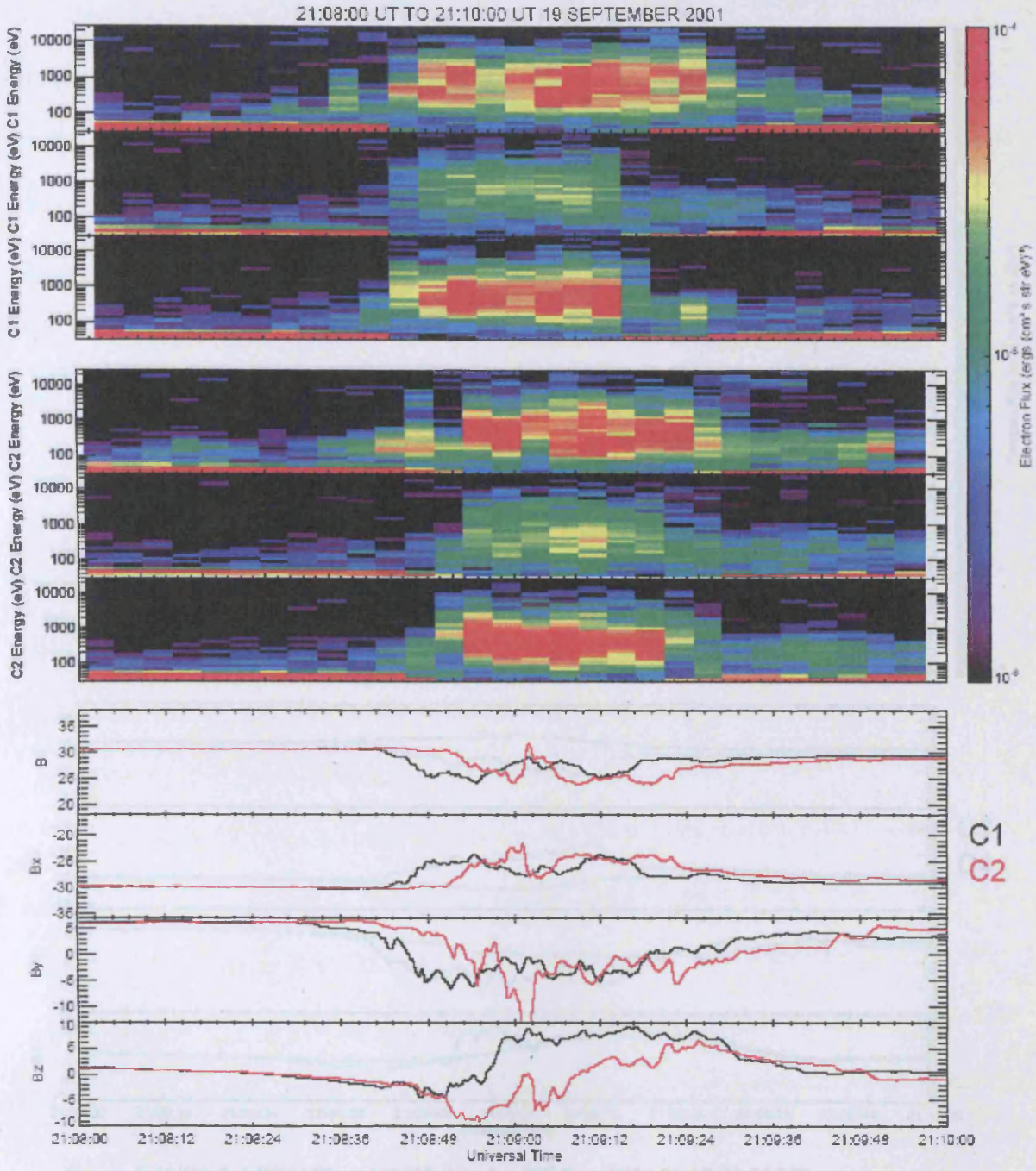

Figure 5-18 C1 & 2 PEACE and FGM data for 19th Sept 2001 21:08-21:20 UT
Cluster PEACE and FGM data for the 19th September 2001 21:08-21:10 UT event. The first 6 panels show the electron differential energy flux spectrograms for field-aligned, perpendicular and anti-parallel electrons for Clusters 1 and 2 respectively. The final 4 panels show the magnitude of the magnetic field and the B_X, B_Y and B_Z components from FGM in the GSM coordinate system.

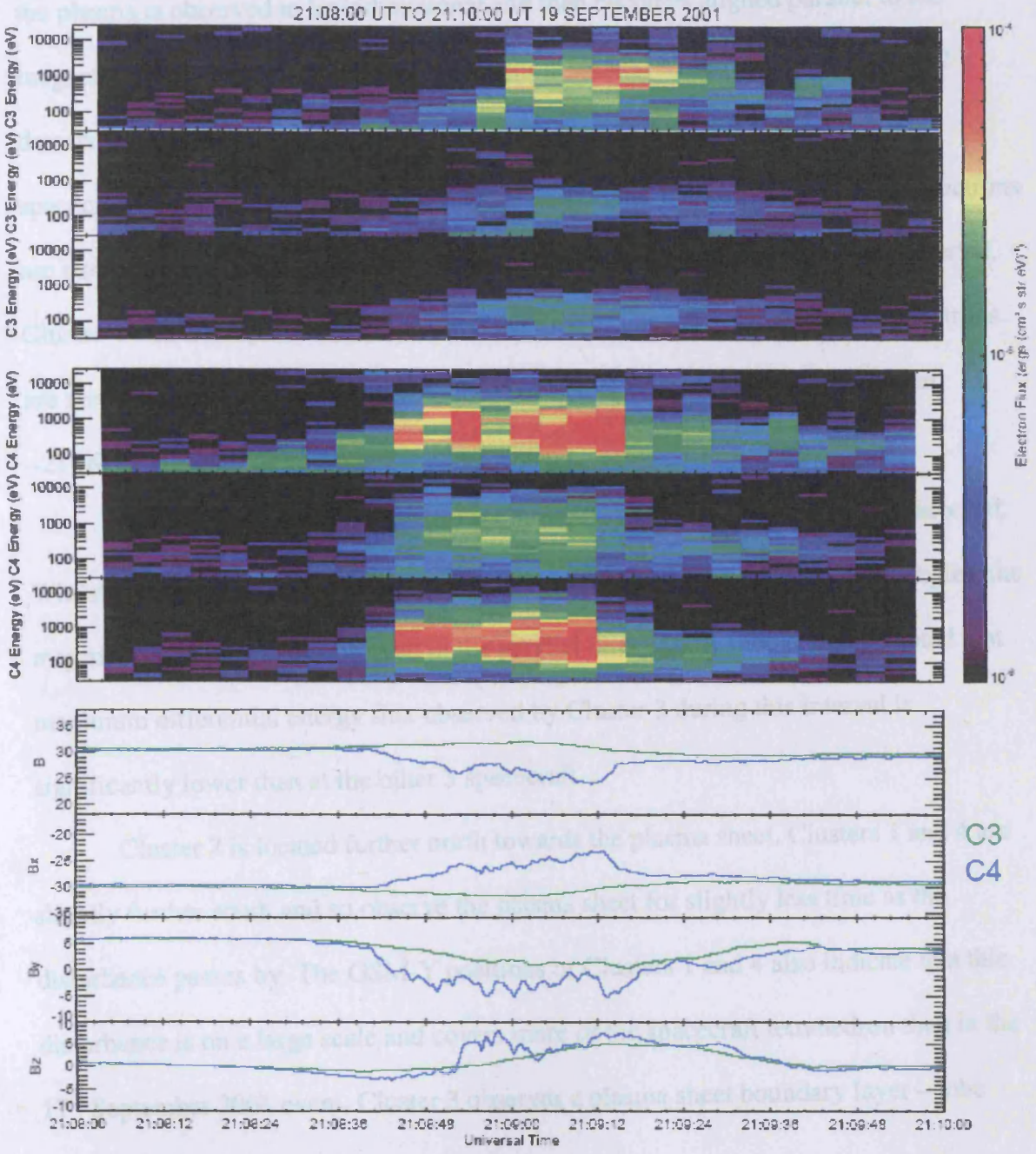

Figure 5-19 C3 & 4 PEACE and FGM data for 19th Sept 2001 21:08-21:20 UT
Cluster PEACE and FGM data for the 19th September 2001 21:08-21:10 UT event. The first 6 panels show the electron differential energy flux spectrograms for field-aligned, perpendicular and anti-parallel electrons for Clusters 3 and 4 respectively. The final 4 panels show the magnitude of the magnetic field and the B_X, B_Y and B_Z components from FGM in the GSM coordinate system.

At ~21:08:44 UT Cluster 1 is engulfed by the plasma sheet. Until ~21:09:18 UT the plasma is observed to be bidirectional and then becomes aligned parallel to the magnetic field. At 21:09:32 UT the spacecraft is located within the lobes. Cluster 2 detects the plasma sheet approximately 4 seconds after it is seen at Cluster 1. The spacecraft then returns to the lobe at ~ 21:09:32 UT, but unlike at Cluster 1, the electrons are streaming along the magnetic field in both directions throughout the entire interval. Cluster 4 enters the plasma sheet at the same time as Cluster 1. Bi-directional electrons are seen throughout the interval, with the differential energy flux decreasing after ~21:09:20 UT until re-entering the lobe proper.

The plasma signature observed at Cluster 3 is different to the other 3 spacecraft. Whilst there is some plasma observed at anti-parallel and perpendicular pitch angles, the majority of the plasma is observed in the parallel direction. It should also be noted that maximum differential energy flux observed by Cluster 3 during this interval is significantly lower than at the other 3 spacecraft.

Cluster 2 is located further north towards the plasma sheet. Clusters 1 and 4 are slightly further south and so observe the plasma sheet for slightly less time as the disturbance passes by. The GSM-Y positions of Clusters 1 and 4 also indicate that this disturbance is on a large scale and covers more of the spacecraft tetrahedron than in the 17th September 2001 event. Cluster 3 observes a plasma sheet boundary layer – lobe population.

The magnetic field at Cluster 3 is consistent with a TCR passing the spacecraft. Whilst Cluster 3 observes an increase in the magnetic field strength, the other spacecraft observe a reduction as they enter the plasma sheet. From the size of the B_X components

of the magnetic field, it appears that Cluster 2 is located closest to the neutral sheet followed by Cluster 4.

Results from the flux-rope fitting routine indicate that the magnetic field data from Cluster 1 can be modelled as a flux-rope with an impact parameter of 0.98 with a significant chi-squared value of 0.021 for the interval 21:09:01 UT to 21:09:19 UT. With an ion velocity of ~150 km s^{-1} this indicates a flux-rope with a radius of 1.06 R_E. Similar results are found at Clusters 2 and 4. Due to the nature of the impact parameter being so close to the radius of the flux-rope a more detailed analysis of this data should be performed with other flux-rope models and also with draping field models to ensure that this result is indicative of a force-free flux-rope. It should be assessed whether the simple force-free flux-rope model is reliable at the boundary of a flux-rope.

5.4.3 19th September 2001 21:21-21:25 UT

The spacecraft configuration remains approximately the same for this event as above, and the reader is directed to Figure 5-15 for details. The PEACE directional differential energy flux spectrograms for each spacecraft and the FGM magnetic field components in GSM are presented in Figure 5-20 and Figure 5-21.

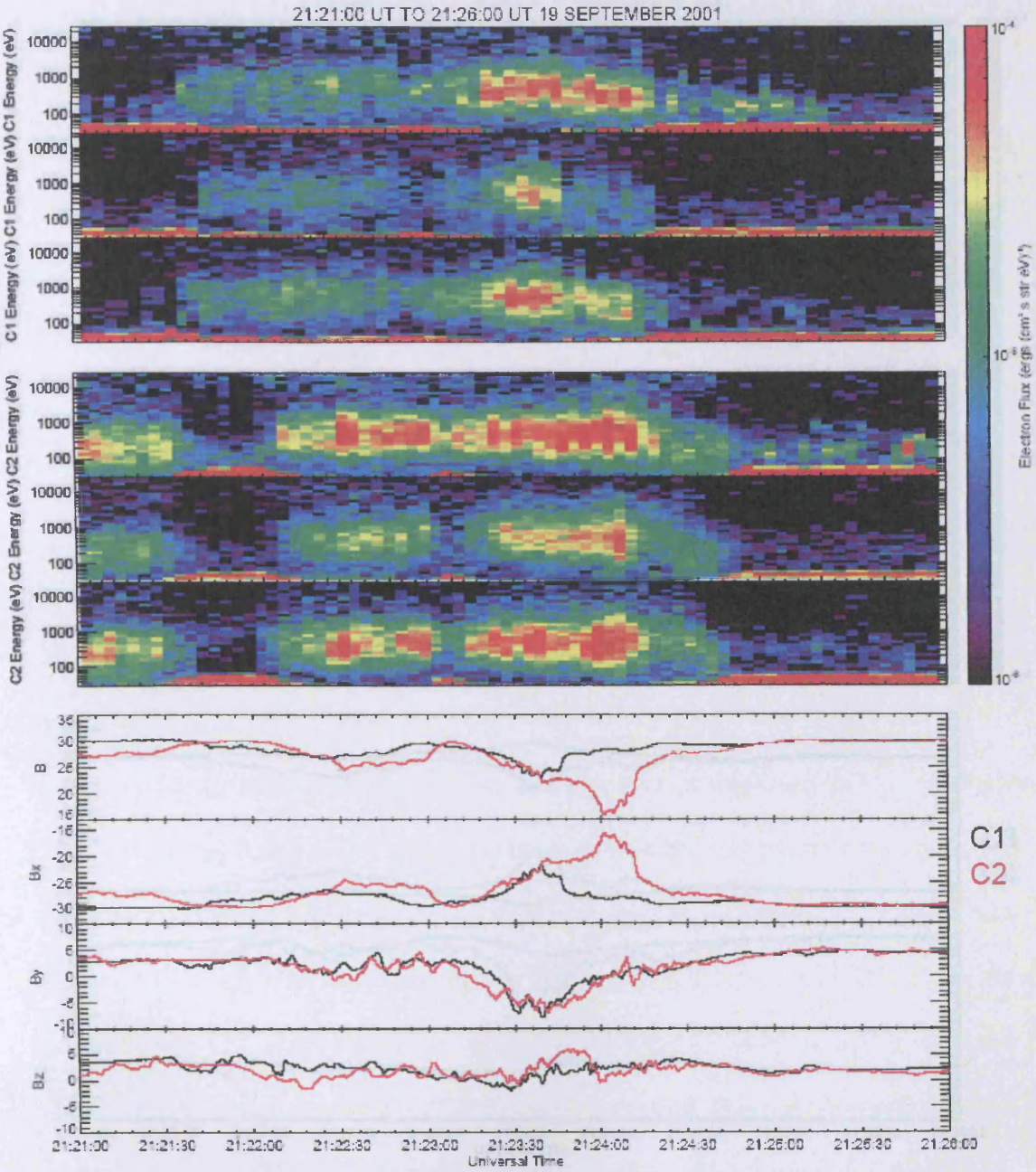

Figure 5-20 C1 & 2 PEACE and FGM data for 19th Sept 2001 21:21-21:25 UT
Cluster PEACE and FGM data for the 19th September 2001 21:21-21:25 UT event. The first 6 panels show the electron differential energy flux spectrograms for field-aligned, perpendicular and anti-parallel electrons for Clusters 1 and 2 respectively. The final 4 panels show the magnitude of the magnetic field and the B_X, B_Y and B_Z components from FGM in the GSM coordinate system.

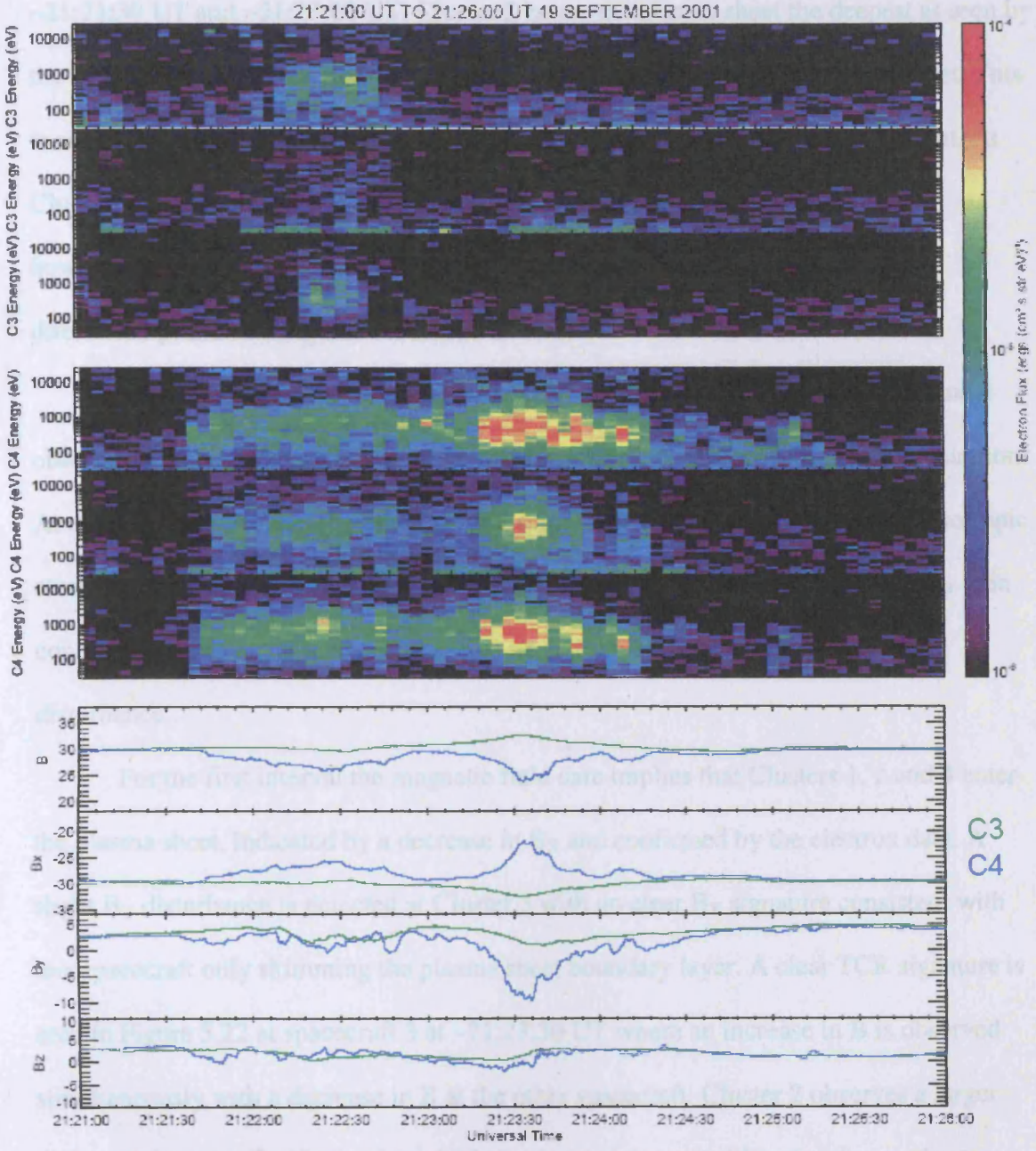

Figure 5-21 C3 & 4 PEACE and FGM data for 19th Sept 2001 21:08-21:20 UT
Cluster PEACE and FGM data for the 19th September 2001 21:21-21:25 UT event. The first 6 panels show the electron differential energy flux spectrograms for field-aligned, perpendicular and anti-parallel electrons for Clusters 3 and 4 respectively. The final 4 panels show the magnitude of the magnetic field and the B_X, B_Y and B_Z components from FGM in the GSM coordinate system.

This event shows all 4 Cluster spacecraft encountering the plasma sheet between ~21:21:30 UT and ~21:23:00 UT. Cluster 2 enters the plasma sheet the deepest as seen by the largest differential energy flux observed, ~21:22:30 UT over the Cluster quartet. This is consistent with the spacecraft being located furthest north in the south lobe event. At Clusters 1 and 4, the spacecraft observe plasma sheet plasma for a longer interval, however the differential energy flux is lower. Cluster 3 observes low-density bi-directional plasma during this first interval.

During the later interval of ~21:23:00 UT to ~21:24:30 UT, Clusters 1, 2 and 4 observe a higher differential energy flux with Cluster 2 observing it for a longer duration. At each of these spacecraft there is several spins' worth of data that shows more isotropic electron distributions, indicating that we pass further into the plasma sheet. Cluster 3, in contrast, remains in the lobe and observes no activity associated with this second disturbance.

For the first interval the magnetic field data implies that Clusters 1, 2 and 4 enter the plasma sheet, indicated by a decrease in B_X and confirmed by the electron data. A slight B_Y disturbance is detected at Cluster 3 with no clear B_X signature consistent with this spacecraft only skimming the plasma sheet boundary layer. A clear TCR signature is seen in Figure 5.22 at spacecraft 3 at ~21:23:30 UT where an increase in B is observed simultaneously with a decrease in B at the other spacecraft. Cluster 2 observes a larger differential energy flux indicative of it being located deeper within the plasma sheet. Cluster 2 is deepest in the plasma sheet at ~21:24 UT at a time when Clusters 1 and 4 are observing less differential energy flux than when they were deepest in the plasma sheet.

The model fitting routine at Cluster 1 and 4 indicates that the data does not describe a force-free magnetic flux rope with no reduced chi-square test statistic being significant. However, for Cluster 2 the magnetic field data from 21:24:02 UT until 21:24:22 UT with 5 vectors per second is modelled by a force-free flux-rope with an impact parameter of 0.98 with a significant reduced chi-squared test statistic of 0.02. This implies a flux-rope radius of 1.18 R_E taking an ion velocity of ~150 km s^{-1} (not shown). The observed and model data in MVA coordinates are shown in Figure Figure 5-22.

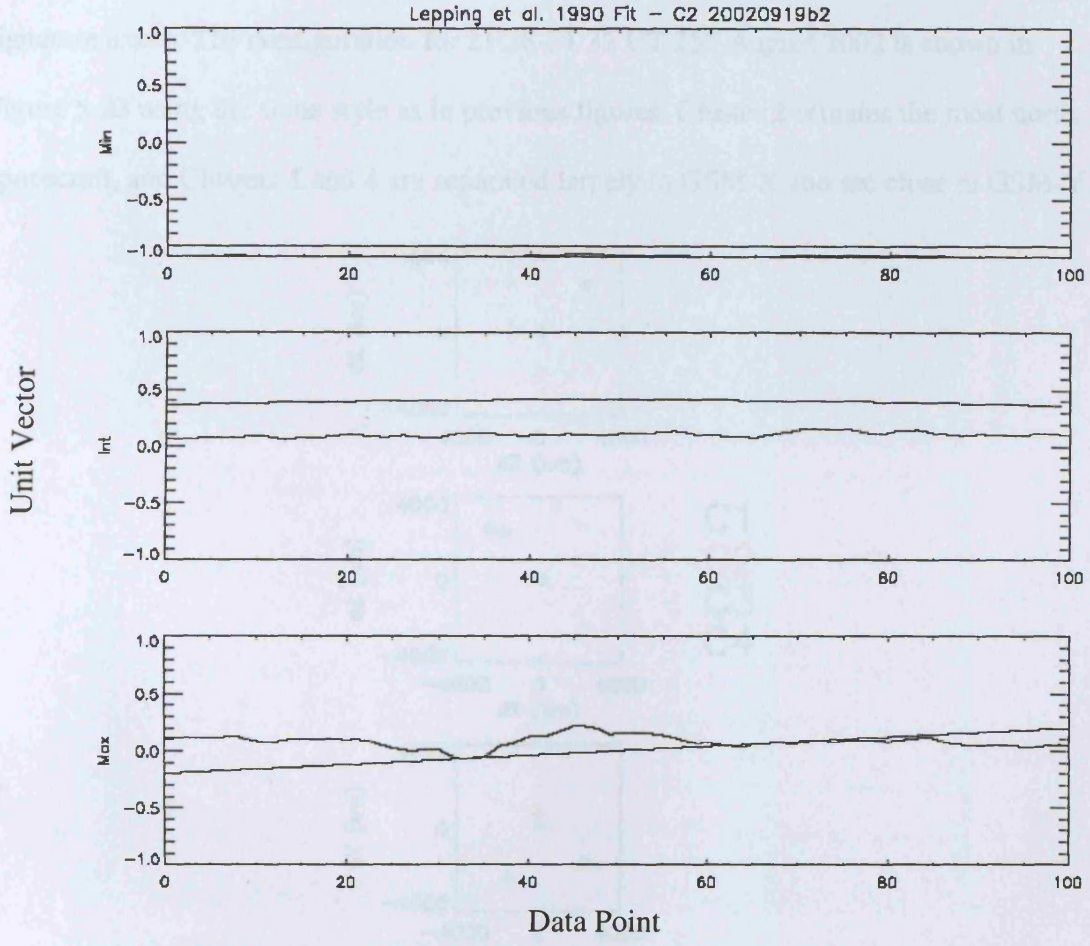

Figure 5-22 Force-free flux-rope fit for Cluster 2 – 19th September 2001
The magnetic field from Cluster 2 for the interval 21:24:02 UT to 21:24:22 UT 19th September 2001 event is shown in MVA coordinates. Superimposed are the components, again in MVA, of a force-free flux-rope model with an impact parameter of 0.98. This fit has a reduced chi-squared test statistic of 0.02 making this a significant fit.

5.4.4 25th August 2002 21:28-21:32 UT

In the 2002 tail season the separation scales of the Cluster spacecraft were larger than in 2001 and thus, in principle, offer a better dataset for this study. The greater separation will reduce the number of events were the spacecraft observe similar features, therefore if one spacecraft detects a clear flux-rope signature it is more unlikely that the others will also observe the flux-rope and therefore are less likely to see if a TCR signature exists. The configuration for 21:28-21:32 UT 25th August 2002 is shown in Figure 5-23 using the same style as in previous figures. Cluster 2 remains the most north spacecraft, and Clusters 1 and 4 are separated largely in GSM-X and are close in GSM-Y.

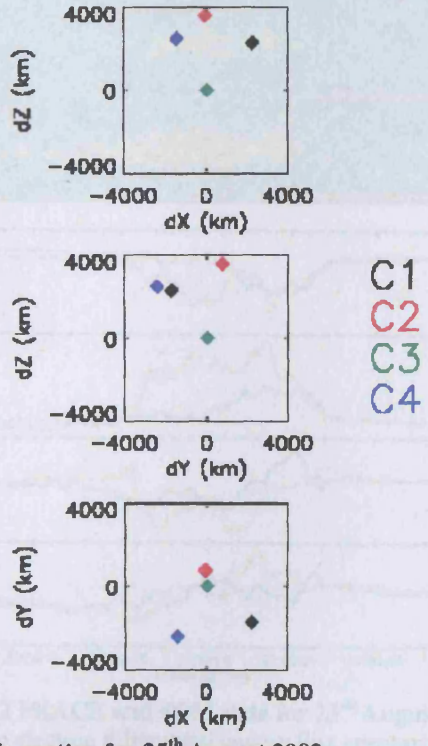

Figure 5-23 Cluster configuration for 25th August 2002
The spacecraft configuration for the 25th of August 2002 event in the GSM co-ordinate system. The Cluster spacecraft are shown in their standard colours of black, red, green and blue for Cluster 1, 2, 3 and 4 respectively.

The PEACE omni-directional differential energy flux spectrograms for each spacecraft and the FGM magnetic field components in GSM are presented in Figure 5-24 and Figure 5-25.

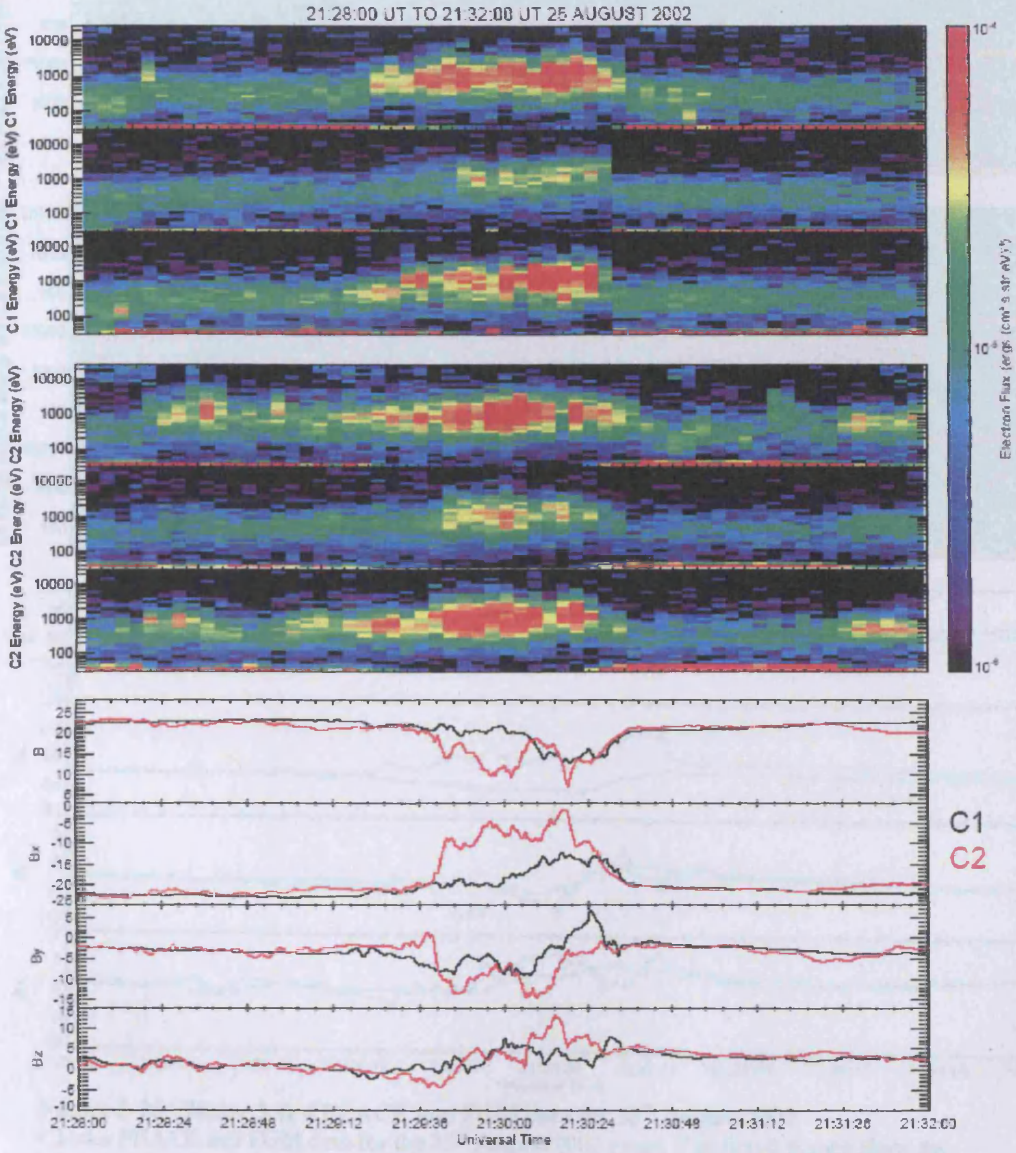

Figure 5-24 Cluster 1 & 2 PEACE and FGM data for 25th August 2002
The first 6 panels show the electron differential energy flux spectrograms for field-aligned, perpendicular and anti-parallel electrons for Clusters 1 and 2 respectively. The final 4 panels show the magnitude of the magnetic field and the B_X, B_Y and B_Z components from FGM in the GSM coordinate system.

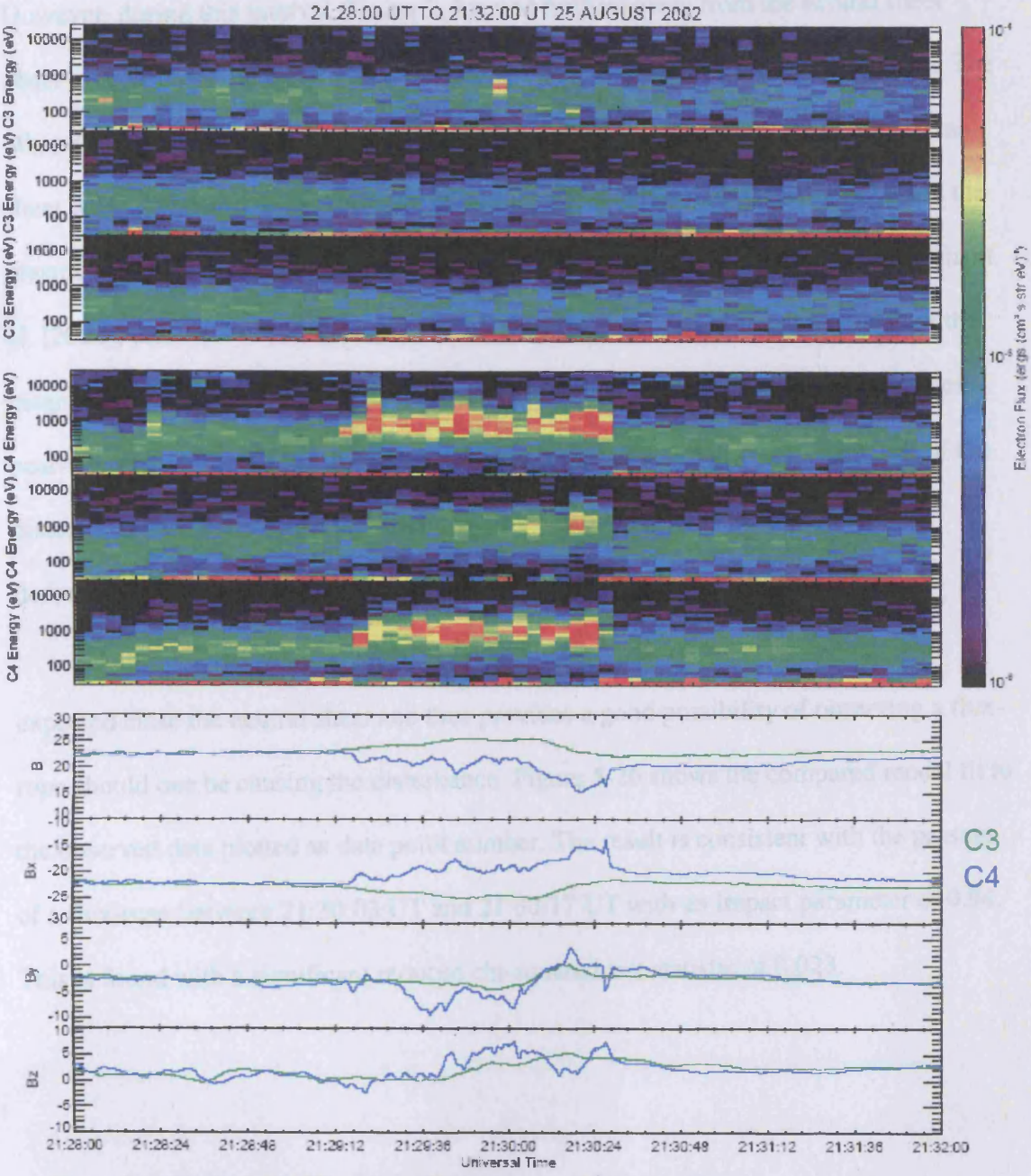

Figure 5-25 Cluster 3 & 4 PEACE and FGM data for 25th August 2002
Cluster PEACE and FGM data for the 25th August 2002 event. The first 6 panels show the electron differential energy flux spectrograms for field-aligned, perpendicular and anti-parallel electrons for Clusters 3 and 4 respectively. The final 4 panels show the magnitude of the magnetic field and the B_X, B_Y and B_Z components from FGM in the GSM coordinate system.

Unlike the previous events, the four spacecraft are located in plasma sheet plasma. However, during this interval Cluster 3, located furthest away from the neutral sheet observes compression in the magnetic field, noted particularly in the B_X component. The other 3 spacecraft observe a large increase in the differential energy flux of the plasma sheet when compared to the background plasma sheet either side of this interval and the plasma has several hundred electron-volts more energy. Unlike the example by Slavin et al. [2003], there is a noted difference in the plasma conditions inside and outside of the magnetic field disturbance. The Cluster 2 electron data in Figure 5-24 has intervals of near-isotropy at ~21:30 UT. However, at Clusters 1 and 4 and throughout the rest of the disturbance at Cluster 2, the distributions are not isotropic and are similar to the description of the electron data in Section 5.3 for the Slavin et al. [2003] event.

Cluster 2 observes the greatest change in B_X, with values approaching those expected close the neutral sheet and thus provides a good possibility of observing a flux-rope should one be causing the disturbance. Figure 5-26 shows the compared model fit to the observed data plotted as data point number. The result is consistent with the passage of a flux-rope between 21:30:03 UT and 21:30:17 UT with an impact parameter of 0.94. This is found with a significant reduced chi-squared test statistic of 0.023.

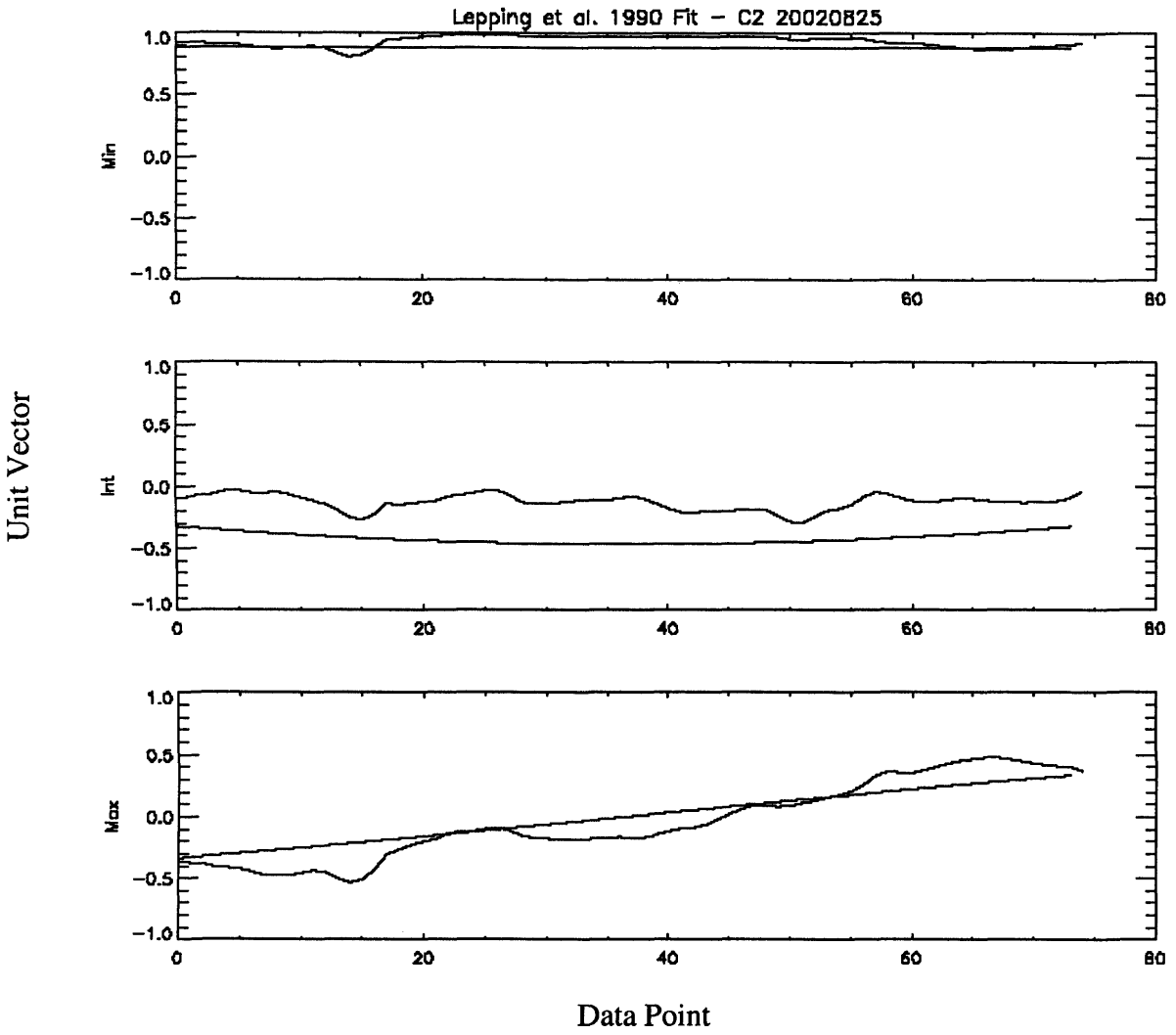

Figure 5-26 Force-free flux-rope fit for Cluster 3 on 25th August 2002
The magnetic field from Cluster 3 for the interval 21:30:03 UT to 21:30:17 UT 25th August 2002 event is shown in MVA coordinates. Superimposed are the components, again in MVA, of a force-free flux-rope model with an impact parameter of 0.94. This fit has a reduced chi-squared test statistic of 0.023 making this a significant fit.

With an ion velocity of approximately 200 km s^{-1} (not shown) the modelled flux-rope has a radius of 0.64 R_E. The MVA analysis indicates that the flux-rope axis is approximately aligned along $(-0.73, 0.64, 0.22)_{GSE}$.

5.5 Summary and Conclusions

The first three events presented here with observations at one of the Cluster spacecraft showing a travelling compression region in the lobe whilst some of the others have a short passage through the plasma sheet were examined for evidence of a force-free flux-rope. This would be the first direct evidence of lobe TCRs being the associated with flux-ropes in the plasma sheet.

Details of the fitting of the force-free flux-rope model for the 17th September 2001 event suggest that Cluster 3 passed through the outer part of a 0.94-1.32 R_E flux rope with an impact parameter of 0.88 to 0.91. Plasma was also simultaneously observed at Cluster 2 although the magnetic field is not successfully modelled by a force-free flux rope and is probably plasma associated with a draping field or the plasma sheet boundary layer. Subsequent analysis of the plasma and magnetic field is required to assess its association with the events observed at Cluster 3.

The substorm events of the 19th September 2001 consisted of several opportunities to observe TCRs with flux-rope signatures. The first subset suggests that Cluster 1, 2 and 4 passed through the very outer edge of a flux-rope with an impact parameter of 0.98. However, whilst these fits were statistically significant, further assessment of the robustness of the model is required and an exploration of the external magnetic field of a flux-rope should be considered to verify this as a meaningful result.

Later on the 19th September 2001 two intervals where the Cluster quartet encountered plasma sheet plasma were observed in close succession. The interval is similar to that described in Figure 5.7. Fitting of the data indicates that only Cluster 2 detects magnetic field that could be associated with a force-free flux rope. This occurs

when Cluster 2 is the closest to the neutral sheet. However, the fitting is associated with an impact parameter of 0.98 which should be analysed in more detail to assess its accuracy.

The 25th August 2002 shows a clear example where the Cluster quartet observe both a TCR and a flux-rope with Cluster 2 passing sufficiently into the flux-rope to detect strong magnetic field signatures with an impact parameter of 0.94. Clusters 1 and 4 see similar plasma conditions to that at Cluster 2 and therefore may be observing disturbances associated with the flux-rope. Cluster 3 during this interval has observed no change in the electron environment during this interval, monitoring only the TCR in the magnetic field.

These are the first clear observation of travelling compression regions accompanied by a flux-rope deeper in the plasma sheet. However none of the spacecraft penetrate deeply into the flux-rope. A detailed study of the solar wind and magnetosheath conditions would also need to take place to determine if this TCR could not also be associated with other generation mechanisms.

The spacecraft separation distances during 2001 and 2002 may be too small for an ideal study of TCRs associated with flux-ropes within the plasma sheet. The spacecraft separation is smaller for 2003 and therefore is not expected to provide a significant contribution to this question, although it may provide prime examples of flux-rope encounters. During the 2004 tail season the spacecraft separation is suitably large so that spacecraft may be distributed throughout the entire plasma sheet with one spacecraft remaining in the lobes as an external monitor. Later tail seasons may provide even larger separations.

Slavin et al. [2002] using Geotail data found that the average flux-rope radius associated with bursty-bulk flows was of the order 1.4 R_E. The observations provided here are smaller than this and indicate that the flux-rope structures are small compared to the possible extent of the plasma sheet (as discussed in Chapter 3 regarding the substorm thinning and expansion). With a larger spacecraft separation distance there will be an improved probability of observing such a small structure within the plasma sheet than can be achieved with the 2001 and 2002 datasets.

It should also be re-iterated that the model used in this chapter is the simplest flux-rope model and therefore may be insufficient for flux-ropes found in the magnetotail. Whilst it is possible that the force-free model is not appropriate, subtle variations of the focre-free flux-rope model associated with different plasma-beta conditions [Kivelson and Khurana, 1995] may be more realistic and should be considered.

6 Conclusions

This thesis has presented novel research in to magnetotail processes utilising the unique four-point measurement dataset provided by the Cluster spacecraft during the 2001 and 2002 magnetotail passes. The dynamics of the magnetotail are fundamental in the understanding of substorm dynamics and energy flow throughout the magnetosphere. The Cluster mission has allowed a detailed analysis of large scale motion within the magnetotail utilising multi-point analysis techniques as well as providing an improved spatial sampling frequency which has limited previous single, dual or fortuitous satellite conjunction studies.

The development of a technique to determine the motion of the substorm plasma sheet as it thins and expands during a substorm allowed the first comprehensive study of boundary motion between the plasma sheet and the magnetic lobes [Dewhurst et al., 2004] and is presented in Chapter 3.

Expansion of the plasma sheet was found to be directed mainly in the GSM-Z direction appropriate for the hemisphere in which the observations were made. Exceptions to this provide further evidence for the existence of complex neutral sheet topology and twisting due to external factors. An apparent asymmetry between the expansion directions in the GSM-Y direction on either side of the neutral sheet were identified, although explained by a lack of observations in the dusk sector. Further examples of anomalous expansion were identified which are in line with severe tilting of the neutral sheet. The explosive nature of the plasma sheet expansion was also found with velocities of ~ 61±37 km s^{-1} being observed, an increase by 20 km s^{-1} to other cited results.

A significant contribution to the knowledge of substorm associated thinning was also made. The results indicate a larger variation in the thinning direction which indicates that the processes involved are complex and that the magnetotail configuration may play a significant role in the way the plasma sheet thins.

During substorms, magnetotail currents play an important role in transferring energy from the magnetotail to and from the ionosphere. The use of another multi-spacecraft analysis technique, the curlometer, was used to measure the field-aligned currents flowing through the spacecraft tetrahedron. These were compared to a similar technique for the electron velocity data resulting in vorticity measurement. A survey of flow shears within the plasma sheet was performed to identify intervals where the vorticity and the current density could be compared. This situation is expected to occur during the diversion of reconnected flux-tubes away from the midnight sector as they propagate Earthward and encounter the dipolar part of the terrestrial magnetic field.

Three flow shear intervals were studied and the complex association between the parallel component of vorticity and the parallel current density was identified. What is clearly evident is that changes are not linear and some change of the physical configuration of the flow shear region must be taking place to explain the results.

The results are explained if the gradient of the vorticity which drives the currents changes or the location of the greatest vorticity moves within the volume bound by the spacecraft tetrahedron. This implies that flow shears may have an important vertical extent scale of the order of the spacecraft separation. This is the first time such observations has been made.

The production of plasmoids and flux-ropes is also a key substorm process which has been an issue in the debate between the mechanisms that trigger a substorm. These flux-ropes have been conjectured to cause travelling compression regions (TCRs) within the magnetotail lobes, yet the lack of observations of both phenomena by fortuitous spacecraft conjunctions has not provided any evidence to directly support this theory.

Using the multiple-point measurements of Cluster, a study of events identified as being TCRs and also being associated with one or more spacecraft observing a plasma enhancement has been made. Modelling of the magnetic field to identify if the magnetic structures are consistent with a force-free flux rope model has been performed.

Successful application of this has been made and encounters with the outer part of a flux-rope by one or more spacecraft has been made simultaneously with observations of a compression region by another spacecraft. During one event a spacecraft went as deep as 12 % of the flux-rope radius. However most encounters were within the outer 2 % of the flux-rope identified and more research into other flux-rope models and possible draping field models are required to securely identify these observations as direct flux-rope – TCR associations.

The data used in this thesis was taken from the 2001 and 2002 datasets. An initial point of call for future work is to perform this identical research on the 2003 and 2004 datasets. During 2003 the spacecraft separation was reduced to the order of 100s km whilst in 2004 it was expanded beyond that of 2002.

For the substorm plasma sheet expansion study richer detail may be obtained from the 2004 dataset although the large separation scale will reduce the sensitivity if the assumptions of planarity and constant velocity of the plasma sheet – lobe interface can

not be taken for granted. The 2004 dataset will provide an excellent opportunity for the detection of flux-ropes with associated TCRs as there will be a larger probability of making an observation of a flux-rope if the spacecraft within the plasma sheet are separated more.

Details of the scale sizes of the flow shears required to generate field-aligned currents should be obtained from the 2003 dataset. It is accepted that there may be little difference in the flows during most situations due to the small separation, but the likelihood of all four spacecraft being located in the plasma sheet during burst mode intervals will be increased. As well as analysis of the other separation scale sizes the work presented in this thesis could be extended by the multiple spacecraft missions, with more than 4 spacecraft performing formation flying in locations where flow shears are expected to be at largest.

7 Glossary of Terms

7.1 The Auroral Electrojet (AE) Index

The AE index is a measure of the magnetic disturbance in the auroral regions. It is derived from the variations in the horizontal component of the magnetic field observed at 10-13 magnetometer sites distributed (unevenly) around the auroral oval in the northern hemisphere.

For a given time a value of the maximum and minimum deviations for the baseline of no activity from the entire magnetometer chain are chosen to be the Auroral Upper and Auroral Lower indices. Over time these values provide an envelope of the largest and smallest magnitudes of the magnetic disturbances.

The values of AU and AL are used to derive to more indices: those of AO and AE representing the mean and difference of AU and AL respectively. The AE index represents the overall activity the electrojets and the AO index provides a measure of the equivalent zonal current.

Many temporal resolutions of the AU and AL derived indices are available from the World Data Centers. However, the complex process of identification and removal of spikes from the datasets that feed into the indices has resulted in a back log of data to be processed. In this case, numerical data at 1 minute resolution is only available for early years. Pictorial data is available for other years; however, this does add complications with regard to subsequent data analysis.

The AE index is often used to identify the onset of a substorm which is observed as a sharp increase in. Intensifications of a substorm are identified by similar increases.

Unfortunately, there is the possibility for substorms to not be identified by the AE index as the magnetometer chain that feeds the AE index is not uniformly distributed in local time with large gaps identified, for example, in the Russian sector. Therefore, the absence of a magnetic signature in the AE index does not imply there was no substorm activity and other data sets, such as auroral precipitation cameras, should be studied.

More detailed information of the AE index can be found in Davis and Sugiura [1966].

7.2 Geocentric Solar Ecliptic and Magnetospheric Coordinates

The two most common co-ordinate systems used in magnetotail physics are those of the geocentric solar ecliptic (GSE) and geocentric solar magnetospheric (GSM) systems.

Both the GSE and GSM systems have a common X-axis which is the Sun-Earth line. In the GSE system the Z-axis is aligned with the ecliptic North pole, whereas in the GSM system the Z-axis is defined as the projection of the Earth's magnetic field dipole axis on to the GSE-YZ plane. The Y-axis is set to make the right-hand set in both cases.

Other co-ordinate systems can be used and are often more appropriate for particular studies. A detailed presentation of geophysical co-ordinate systems and the transformation matrices from one system to another is present by Hapgood [1992].

7.3 Pearson's Product Moment Correlation Coefficient

The correlation of one data set to another is a useful tool in mathematics. There are a variety of statistical process that can be adapted, however, the most frequently encountered is that of least-squares fitting. This technique is also known as Pearson's correlation technique with the result, a number between -1 and 1 each representing perfect anti-correlation and correlation respectively and 0 representing no correlation, often referred to as the product moment correlation coefficient.

For a detailed mathematical derivation of the this technique the reader is directed to Weisstein [viewed 2005] for further details.

8 References

Akasofu, S. –I., and S. Chapman, The ring current, geomagnetic disturbances and the Van Allen radiation belts, J. Geophys. Res., 66, 1231, 1961

Akasofu, S. -I., The development of the auroral substorm, Planet. Space Sci., 12, 273, 1964

Akasofu, S. –I., Polar and Magnetospheric Substorms, D. Reidel, Norwell, Mass., 1968

Akasofu, S. –I. and C. –I Meng, Effects of the IMF on the Plasma Sheet, Planet. Space Sci., 34, 683, 1986

Angelopoulos, V., F. V. Coroniti, C. F. Kennel, M. G. Kivelson, R. J. Walker, C. T. Russell, R. L. McPherron, E. Sanchez, C. –I. Meng, W. Baumjohann, G. D. Reeves, R. D. Belian, N. Sato, E. Friis-Christensen, P. R. Sutcliffe, K Yumoto, T. Harris, Multipoint analysis of a bursty bulk flow event on April 11, 1985, J. Geophys. Res., A101, 4967, 1996

Arnoldy, R. L. and T. E. Moore, Longitudinal structure of substorm injections at synchronous orbit, J. Geophys. Res., 88, 6213, 1983

Atkinson, G., An approximate flow equation for geomagnetic flux tubes and its application to polar substorms, J. Geophys. Res., 72, 5373-5382, 1967

Aubry, M. P. and R. L. McPherron, Magnetotail changes in relation to the solar wind magnetic field and magnetospheric substorms, J. Geophys. Res., 76, 4381, 1971

Axford, W. I. and C. O. Hines, A unifying theory of high-latitude geophysical phenomena and geomagnetic storms, Canadian J. Phys., 39, 1433-1464, 1961

Axford, W. I., The interaction between the solar wind and the earth's magnetosphere, J. Geophys. Res., 67, 3791, 1962

Axford, W. I., H. E. Petschek and G. L. Siscoe, Tail of the magnetosphere, JGE, 70, 1231, 1965

Baker, D. N., S. J. Bame, R. D. Bian, W. C. Fledman, J. T. Gosling, P. R. Higbie, E. W. Hones Jr., D. J. McComas, and R. D. Zwicl, Correlated dynamical changes in the near-Earth and distant magnetotail regions: ISEE 3, J. Geophys. Res., 89, 3855-3864, 1984

Baker, D. N., V. Angelopoulos, W. Baunjohann, R. L. McPherron and T. I. Pulkkinen, The neutral line model of substorms: Past results and present view, J. Geophys. Res., 101, 12975, 1996

Balogh, A., M. W. Dunlop, S. W. H. Cowley, D. J. Southward, J. G. Thomlinson, K. H. Glassmeier, G. Musmann, H. Lühr, S. Buchert, M. H. Acuña, D. H. Fairfield, J. A. Slavin, W. Riedler, K. Schwingenschuh, M. G. Kivelson, The Cluster Magnetic Field Investigation, Space Sci. Rev., 79, 65, 1997

Bame, S. J., J. R. Asbridge, H. E. Felthauser, E. W. Hones Jr. and I. B. Strong, Characteristics of the plasma sheet in the Earth's magnetotail, J. Geophys. Res., 72, 113, 1967

Baumjohann, W., G. Paschmann, and C. A. Cattell, Average plasma properties in the central plasma sheet, J. Geophys. Res., 94, 1989

Baumjohann, W., G. Paschmann, T. Nagai and H. Lühr, Superposed Epoch Analysis of the Substorm Plasma Sheet, J. Geophys. Res., 96, 11065, 1991

Baumjohann, W., G. Paschmann and T. Nagai, Thinning and Expansion of the Substorm Plasma Sheet, J. Geophys. Res., 97, 17173, 1992

Baumjohann, W., M. Hesse, S. Kokubun, T. Mukai, T. Nagai, A. A. Petrukovich, Substorm dipolarization and recovery, J. Geophys. Res., A104, 24995, 1999

Berdichevsky, D., G. Thejappa, R. J. Fitzenreiter, R. P. Lepping, T. Yamamoto, S. Kokubun, R. W. McEntire, D. J. Williams, and R. P. Lin, Widely spaced wave-particle observations during GEOTAIL and Wind magnetic conjunctions in the Earth's ion foreshock with near-radial interplanetary magnetic field, J. Geophys. Res., Vol. 104, No. A1, 463-482, 1999

Biermann, L., Kometschweife und solare Korpuskularstrahlung, Z. Astrophys., 29, 274, 1951.

Birn, J., M. Hesse, and K Schindler, MHD simulations of magnetotail dynamics, J. Geophys. Res., 101, 12939, 1996

Birn, J., M. Hesse, G. Haerendel, W. Baumjohann and K. Shiokawa, Flow braking and the substorm current wedge, J. Geophys. Res., A104, 19895, 1999

Bonnevier, B. R. and G. Rostoker, A three-dimensional model current system for polar magnetic substorms, J. Geophys. Res., 75, 107, 1970

Burlaga, L. F., Magnetic clouds: Constant alpha force-free configurations, J. Geophys. Res., 93, 7217, 1988

Cairns, I.H., and J.G. Lyon, MHD simulations of Earth's bow shock at low mach numbers: Standoff distances, J. Geophys. Res., 100, 17,173, 1995

Carlson, C. W., Adv. Space. Res., 2, 67, 1983

Chapman, S., and V. C. A. Ferraro, A new theory of magnetic storms, Part 1, The initial phase, Terrest. Magnetism and Atmospheric Elec., 37, 147-156, 1932

Cheng, C. Z., A. T. Y. Lui, kinetic ballooning instability for substorm onset and current distruption observed by APMTE/CC, Geophys. Res. Lett., 25, 4091, 1998

Clauer, C. R., and Y. Kamide, DP 1 and DP 2 current systems for the March 22, 1979 substorms, J. Geophys. Res., 90, 1343-1354, 1985

Coates, A. J., Bowles, J. A., Gowen, R. A., Hancock, B. K., Johnstone A. D., and Kellock ,S. J., The AMPTE UKS Three-Dimensional Ion Experiment, IEEE Trans. Geoscience and Remote Sensing, GE-23, 3, 287, 1985

Coroniti, F. V., and C. F. Kennel, Changes in the magnetospheric configuration during substorm growth phase, J. Geophys. Res., 77, 3361, 1972

Cowley, S. W. H., The causes of convection in the Earth's magnetosphere: A review of developments during the IMS, Rev. Geophys., 20, 531-565, 1982

Credland, J., G. Mecke, and J. Ellwood, The Cluster mission: ESA's spacefleet to the magnetosphere, Space Sci. Rev., 79, 33, 1997

Crooker, N. U., G. L. Siscoe, C. T. Russell, and E. J. Smith, Factors controlling degree of correlation between ISEE 1 and ISEE 3 interplanetary magnetic field measurements, J. Geophys. Res., 87, 2224, 1982

Cummings, W. D., J. N. Barfield, and P. J.Colemanm Magnetospheric substorms observed at synchronous orbit, J. Geophys. Res., 73, 6687, 1968

Daglis, I. A., S. Livi, E. T. Sarris, and B. Wilken, Energy density of ionospheric and solar wind origin ion the near-Earth magnetotail during substorms, J. Geophys. Res., 99, 5691-5703, 1994

Dandouras, J., H. Rème, A. Saint-Marc and J. A. Sauvaud, A Statistical Study of Plasma Sheet Dynamics Using ISSE 1 and 2 Energetic Particle Flux Data, J. Geophys. Res., 91, 6861, 1986

Dandouras, J., On the average shape and position of the geomagnetic neutral sheet and its influence on plasma sheet statistical studies, J. Geophys. Res., 93, 7345, 1988

Davis, T. N., and M. Sugiura, Auroral electrojet activity index AE and its universal time variations, J. Geophys. Res., 71, 785, 1966

Dewhurst, J. P., C. J. Owen, A. N. Fazakerley, and A. Balogh, Thinning and expansion of the substorm plasma sheet: Cluster PEACE timing analysis, Ann. Geophys., 1432-0576/ag/2004-22-1, 2004

Dungey, J. W., Interplanetary magnetic field and the auroral zones, Phys. Rev. Lett, 6, 47, 1961

Dunlop, M. W., and T. I. Woodward, Analysis of thick, non-planar boundaries using the discontinuity analyser, Ann. Geophysicae, 17, 984, 1999

Dunlop, M. W., A. Balogh, K.-H. Glassmeier, and P. Robert, Four-point Cluster applications of magnetic field analysis tools: The Curlometer, J. Geophys. Res., 107, 1384, doi:10.1029/2001JA0055088, 2002

Eastman, T. E., L. A. Frank, W. K. Peterson, and W. Lennartsson, The plasma sheet boundary layer, J. Geophys. Res., 89, 1553-1572, 1984

Eastman, T. E., L. A. Frank, and C. Y. Huand, The boundary layers as the primary transport regions of the Earth's magnetotail, J. Geophys. Res., 90, 9541, 1985

El-Alaoui, M., Current disruption during November 24, 1996, substorm, J. Geophys. Res., 106, 4, 6229, 2001

Elphic, R. C., Multipoint observations of the magnetopause: Results from ISEE and AMPTE, Adv. Space Res., 8, 9-10, 223-238, 1988

Escoubet, C. P., M. Fehringer, and M. Goldstein, The Cluster Mission, Ann. Geophys., 19, 1197, 2001

Fairfield, D. H., and N. F. Ness, Magnetic field measurements with the IMP 2 satellite, J. Geophys. Res., 72, 2379, 1967

Fairfield, D. H. and N. F. Ness, Configuration of the geomagnetic tail during substorms, J. Geophys. Res., 75, 7032, 1970

Fairfield, D. H., and J. D. Scudder, Polar rain - Solar coronal electrons in the earth's magnetosphere, J. Geophys. Res., 90, 4055, 1987

Fairfield, D. H., Magnetotail energy storage and the variability of the magnetotail current sheet, in Magnetic Reconnection in Space and Laboratory, Geophys. Monogr. Ser., 30 edited by E. W. Hones Jr., 168-177, AGU, Washington D. C., 1984

Formisano, V., Orientation and shape of the earth's bow shock in three dimensions, Planet. Space Sci., 27, 1151-1161, 1979

Frank, L. A., J. B. Sigwarth, W. R. Paterson and S. Kokubun, Two encounters of the substorm onset region with the Geotail spacecraft, J. Geophys. Res., 106, 5811, 2001

Frank, L. A., W. R. Paterson, J. B. Sigwarth and T. Mukai, Observations of plasma sheet dynamics Earthward of the onset region with the Geotail spacecraft, J. Geophys. Res., 106, 18823, 2001

Gabriel AH, Bely-Dubau F, Lemaire P, The contribution of polar plumes to the fast solar wind, Astro. J., 589 (1), 623, Part 1, 2003, Geophys. Res., 86, 11265, 1981

Goertz, C. K. and R. A. Smith, Thermal catastrophe model of substorms, J. Geophys. Res., 94, 6561, 1989

Goldstein, H., On the field configuration in magnetic clouds, Solar Wind Fivem NASA Conf. Publ., 2280, 731, 1983

Gustafsson, G., R. Boström, B. Holback, G. Holmgren, A. Lundgren, K. Stasiewicz, L. Åhlén, F. S. Mozer, D. Pamkow, P. Harvey, P. Berg, R. Ulrich, A. Pedersen, R. Schmidt, A. Butler, A. W. C. Fransen, D. Klinge, M. Thomsen, C.-G. Fälthammar, P.-A. Lindqvist, S. Christenson, J. Holtet, B. Lybekk, T. A. Sten, P. Tanskanen, K. Lappalainen and J. Wygant, The Electric Field and Wave Experiment for the Cluster Mission, Space Sci. Rev., 79, 137, 1997

Haaland, S., B. U. O Sonnerup, M. W. Dunlop, A. Balogh, E. Georgescu, H. Hasegawa, B. Klecker, G. Paschmann, P. Puhl-Quinn, H. Reme, H. Vaith, A. Vaivads, Magnetopause orientation, motion, and thickness from Cluster: Comparison of multi-spacecraft and single-spacecraft techniques, Spatio-Temporal Analysis and Multipoint Measurements in Space, Orléans, France, 12th – 16th May 2003, Submitted to Ann. Geophys.

Hapgood, M. A., Space physics coordinate transformations: a user guide, Planet. Space Sci., 40, 5, 711-717, 1992

Hapgood, M. A., T. G. Dimbylow, D.C. Sutcliffe, P. A. Chaizy, P. S. Ferron, P. M. Hill and X. Tiratay, The Joint Science Operations Centre, Space Sci. Rev., 79, 487, 1997

Harvey, C. C., Spatial Gradients and the Volumetric Tensor, in Analysis Methods for Multi-Spacecraft Data, edited by G Paschmann and P. Daly, International Space Science Institute and ESA Publications Division, http://www.issi.unibe.ch, 2000

Hasagawa, A., Generation of Field Aligned Currents During Substorms, Dynamics of the Magnetosphere, 529, S.-I. Akasofu (ed), D. Reidel Publishing, 1979

Heelis, R. A., The effects of interplanetary magnetic field orientation on the dayside high-latitude ionospheric convection, J. Geophys. Res., 89, 2873-2880, 1984

Heppner, J. P., N. F. Ness, C. S. Scearce, and T. L. Skillman, Explorer 10 magnetic field measurements, J. Geophys. Res., 68, 1, 1963

Hollweg J. V. and P. A. Isenberg, Generation of the fast solar wind: A review with emphasis on the resonant cyclotron interaction, J. Geophys. Res., 107, 1147, 2002

Hones, E. W., Jr., J. R. Asbridge, S. J. Bame and I. B. Strong, Outward Flow of Plasma in the Magnetotail Following Geomagnetic Bays, J. Geophys. Res., 72, 5879, 1967

Hones, E. W., Jr., S. –I. Akasofu, P. Perreault, S. J. Bame and S. Singer, Poleward expansion of the auroral oval and associated phenomena in the magnetotail during auroral substorms, J. Geophys. Res., 75, 7060, 1970

Hones, E. W., Jr., S. Singer, L.J. Lanzerotti, J. D. Pierson and T. J. Rosenberg, The magnetospheric substorm of August 25-26, 1967, J. Geophys. Res., 76, 2977, 1971a

Hones, E. W., Jr., Plasma flow in the plasma sheet and its relation to substorms, Radio Sci., 8, 879, 1973

Hones, E. W., Jr., I. D. Palmer, and P. R. Higbi, Energetic Protons of magnetospheric origin in plasma sheet associated with substorms, J. Geophys. Res., 81, 3866-3874, 1975

Hones, E. W., Jr., D. N. Baker, S. J. Bame W. C. Feldman, J. T. Gosling, D. J. McComas, R. D. Zwickl, J. A. Slavin, E. J. Smith, and B. T. Tsurutani, Structure of the magnetotail at 220 Re, Geophys. Res. Lett., 11, 5-7, 1984

Hones, E. W., Jr., T. Pytte and H. I. West Jr., Associations of Geomagnetic Activity With Plasma Sheet Thinning and Expansion: A Statistical Study, J. Geophys. Res., 89, 5471, 1984

Horbury, T. S., P. J. Cargil, E. A. Lucek, A. Balogh, M. W. Dunlop, T. M. Oddy, C. Carr, P. Brown, A. Szabo, and K. H. Fornacon, Cluster magnetic field observations of the bowshock: Orientation, motion and structure, Ann. Geophys., 19, 10-12, 1399-1409, 2001

Hughes, W. J., and D. G. Sibeck, On the 3-dimentional structure of plasmoids, GRL, 14, 636, 1987

Hurrican, O. A., B. H. Fong, S. C. Cowley, F. V. Coroniti, C. F. Kennel, R. Pellat, Substorm detonation, J. Geophys. Res., A104, 10221, 1999

Ieda A, D. H. Fairfield, T. Mukai , Y. Saito, S. Kokubun, K. Liou, C. I. Meng, G. K. Parks, M. J. Brittnacher, Plasmoid ejection and auroral brightenings, J. Geophys. Res., 106, 3845, 2001

Jacquey, C., J. Sauvaud and J. Dandouras, Location and propagation of the magnetotail current disruption during substorm expansion: Analysis and simulation of an ISEE multi-onset event, Geophys. Res. Lett.,18, 389, 1991

Johnstone, A. D., C. Alsop, S. Burdge, P. J. Carter, A. J Coates, A. J. Coker, A. N. Fazakerley, M. Grande, R. A. Gowen, C. Gurgiolo, B. K. Hancock, B. Narheim, A. Preece, P. H. Sheather, J. D. Winningham, R. D. Woodliffe, PEACE: A Plasma Electron and Current Experiment, Space Sci. Rev., 79, 351, 1997

Kan, J. R., A global magnetosphere-ionosphere model of substorms, J. Geophys. Res., 93, 5624, 1988

Kauffman, R. L., Substorm currents: Growth phase and onset, J. Geophys. Res., 92, 7471, 1987

Kawano H, Nishida A, Fujimoto M, Mukai T, Kokubun S, Yamamoto T, Terasawa T, Hirahara M, Saito Y, Machida S, Yumoto K, Matsumoto H, Murata T, A quasi-stagnant plasmoid observed with geotail on October 15, 1993, J. Geomag and Geolelec., 48, 525, 1996

Kellogg, P. J., Flow of plasma around the earth, J. Geophys. Res., 67, 3805, 1962

Kivelson, M. G., and K. K. Khurana, Models Of Flux Ropes Embedded In A Harris Neutral Sheet - Force-Free Solutions In Low And High-Beta Plasmas, J. Geophys. Res., 100, 23637-23645, 1995

Kokubun, S., and R. L. McPherron, Substorm signatures at synchronous altitude, J. Geophys. Res., 86, 11265, 1981

Krimigis, S. M., G. Haerendel, R.W. McEntire, G. Paschmann, and D.A. Bryant, The Active Magnetospheric Particle Tracer Explorers (AMPTE) program, EOS, 63, 843-850, 1982

Lepping, R. P., J. A. Jones, and L. F. Burlaga, Magnetic Field Structure of Interplanetary Magnetic Clouds at 1AU, J. Geophys. Res, 95, 11957, 1990

Lepping, R. P., et al., Cross-tail magnetic flux ropes as observed by the Geotail spacecraft, GRL, 22, 1193, 1995

Liou, K., C. I. Meng, T. Y. Lui, P. T. Newell, M. Brittnacher, G. Parks, G. D. Reeves, R. R. Anderson, and K. Yumoto, On the relative timing of substorm onset signatures, J. Geophys. Res., 104, 22807, 1999

Liou, K, C. –I. Meng, A. T. Lui, P. T. Newell and S. Wing, Magnetic dipolarization with substorm expansion onset, J. Geophys. Res., 107, 10.1029/2001JA000179, 2002

Lopez, R. E., The position of the magnetotail neutral sheet in the near-earth region, Geophys. Res. Lett., 17, 1617, 1990

Lopez, R. E., D. G. Sibeck, A. T. Y. Lui, K. Takahashi, R. W. McEntire, T. A. Potemra, and D. Klumper, Substorm variations in the magnitude of the magnetic field, J. Geophys. Res., 103, 14444, 1998

Lui, A. T. Y., Current disruption in the Earth's magnetosphere: observations and models, J. Geophys. Res., A101, 13067, 1996

Lui, A. T. Y., K. Liou, P. T. Newell, C. –I. Meng, S. –I. Ohtani, T. Ogino, S. Kokubun, Brittnacher, G. K. Parks, Plasma and magnetic flux transport associated with auroral breakups, Geophys. Res. Lett., 25, 4095, 1998

Lui, A. T. Y, K. Liou, M. Nose, S. Ohtani, D. J. Williams, T. Mukai, K. Tsurda, S. Kokubun, Near-Earth dipolarization: evidence for a non-MHD process, Geophys. Res. Lett., 26, 2905, 1999

Lyons, L. R., and T. W. Speiser, Evidence for current sheet acceleration in the geomagnetic tail, J. Geophys. Res., 87, 2276, 1982

Lyons, L. R., A new theory for magnetospheric substorms, J. Geophys. Res., 100, 19065, 1995

Machida, S., et al., Geotail low energy particle and magnetic field observations of a plasmoid at X=142 RE, GRL, 21, 2295, 1994

Machida, S., Y. Miyashita, A. Ieda, A. Nishida, T. Mukai, Y. Saito and S. Kokubun, Geotail observations of flow velocity and north-south magnetic field variations in the near and mid-distanct tail associated with substorm onset, Geophys. Res. Lett., 26, 635, 1999

Maezawa, K., Magnetotail boundary motion associated with geomagnetic substorms, J. Geophys. Res., 80, 3543-3548, 1975

McPherron, R. L., Growth phase of magnetospheric substorms, J. Geophys. Res., 75, 5592, 1970

McPherron, R. L., C. T. Russell and M. P. Aubry, Satellite studies of the magnetospheric substorm on August 16, 1968, 9, Phenomenological model of substorms, J. Geophys. Res., 78, 3131, 1973

Miyashita, Y., S. Machida, T. Mukai, Y. Saito, K. Tsuruda, H. Hayakawa and P. R. Sutcliffe, A statistical study of variations in the near and middistant magnetotail associated with substrom onsets: GEOTAIL observations, J. Geophys. Res., 105, 15913, 2000

Moldwin, M. B., and W. J. Hughes, On the formation and evolution of plasmoids: A survey of ISEE 3 geotail data, J. Geophys. Res., 97, 19259, 1992

Moldwin, M. B and W. J. Hughes, Observations Of Earthward And Tailward Propagating Flux Rope Plasmoids - Expanding The Plasmoid Model Of Geomagnetic Substorms, J. Geophys. Res., 99, 183, 1994

Moldwin, M. B., M. R. Collier, J. A. Slavin, and A. Szabo, On the origin of reverse polarity TCRs, Geophys. Res. Lett., 28, 10, 1925, 2001

Mukai, T., S. Machida, Y. Saito, M. Hirahara, T. Terasawa, N. Kaya, T. Obara, M. Ejiri, and A. Nishida, The low energy particle (LEP) experiment onboard the Geotail satellite, J. Geomag. Geoelectr., 46, 669-692, 1994

Nagai, T., Observed magnetic substorm signatures at synchronous altitude, J. Geophys. Res., 4405, 1982

Nagai, T., and S. Machida, Magnetic Reconnection in the Near-Earth Magnetotail, in New Perspectives on the Earth's Magnetotail, ed. A. Nishida, D. N. Baker, and S. W. H. Cowley,American Geophysical Union, Washington, D. C., 1998

Nagai, T., M. Fujimoto, R. Nakamura, Y. Saito, T. Mukai, T. Yamamoto, A. Nishida, S. Kokubun, G. D. Reeves, and R. P. Lepping, Geotail observations of a fast tailward flow at XGSE = -15 RE, J. Geophys. Res., 103 ,23543, 1998

Nagai, T., M. Fujimoto, Y. Saito, S. Machida, T. Terasawa, R. Nakamura, T. Yamamoto, T. Mukai, A. Nishida, and S. Kokubun, Structure and dynamics of magnetotail reconnection for substorm onsets with Geotail observations, J. Geophys. Res., 103, 4419, 1998

Nagia, T., H. J. Singer, T. Mukai, T. Yamamoto, and S. Kokubun, Development of substorms in the near-Earth tail, Adv. Space Res., 25, 1651, 2000

Nakamura, R., W. Baumjohannm R, Schödel, M. Brittnacher, V. A. Sergeev, M. Kubyshkina, T. Mukai, and K. Liou, Earthward flow bursts, auroral streamers, and small expansions, J. Geophys. Res., 106, 10791, 2001

Ness, N. F., The earth's magnetotail, J. Geophys. Res., 70, 2989, 1965

Neugebauer, M. and C. W. Snyder, Solar-Wind Measurements near Venus, J. Geophys. Res. 70, 1587, 1965

Nishida, A. and K. Fujii, Thinning of the Near-Earth (10 ~ 15 RE) Plasma Sheet Preceding the Substorm Expansion Phase, Planet. Space Sci., 24, 849, 1976

Ohmi T., M. Kojima, M. Tokumaru, K. Fujiki, K. Hakamada, Origin of the slow solar wind, Adv. Space Res., 33, 689, 2004

Ohtani, S., S. Kokubun and C. T. Russell, Radial expansion of the tail current disruption during substorms: A new approach to the substorm onset region, J. Geophys. Res., 97, 3129, 1992

Olsen, R. C., The Hidden Ion Population of the Magnetosphere, J. Geophys. Res., 87, 3481, 1982

Owen, C. J., and J. A. Slavin, Energetic Ion Events Associated with Travelling Compression Regions, Proceedings of the International Conference on Substorms, Kiruna, Sweden, ESA SP-335, 1992

Owen, C.J., J.A. Slavin, I.G. Richardson, N. Murphy and R.J. Hynds, Average Motion, Structure and Orientation of the Distant Magnetotail Determined from Remote Sensing the Edge of the Plasma Sheet Boundary Layer with E > 35 keV Ions, J. Geophys. Res., 100, 185, 1995

Owen, C. J., J. A. Slavin, A. N. Fazakerley, M. W. Dunlop, A. Balogh, Cluster electron observations of the separatrix layer during traveling compression regions, J. Geophys. Res., 32, L03104, 2005

Parker, E. N., Extension of the solar corona into interplanetary space, J. Geophys. Res., 64, 1675, 1959

Parker, E. N., The solar flare phenomenon and the theory of reconnection and annihilation of magnetic fields, Astrophys J. Suppl., 177, 1963

Parks, G., C. S. Lin, K. A. Amderson, R. P. Lin, and H. Reme, ISEE 1 and 2 particle observations of the outer plasma sheet boundary layer, J. Geophys. Res., 84, 6471, 1979

Paschmann, G., F. Melzner, R. Frenzel, H. Vaith, P. Parigger, U. Pagel, O. H. Bauer, G. Haerendel, W. Baumjohann, N. Scopke, R. B. Torbert, B. Biggs, J. Chan, K. Lynch, K. Morey, J. M. Quinn, D. Simpson, C. Young, C. E. McIlwain, W. Fillius, S. S. Kerr, R. Mahieu, and E. C. Whipple, The Electron Drift Instruement for Cluster, Space Sci. Rev., 79, 233, 1997

Pontius, D. H., Jr., and R. A. Wolf, Transient Flux Tubes in the Terrestrial Magnetosphere, Geophys. Res. Lett., 17, 49, 1990

Priest, E. R., The Equilibrium of Magnetic Flux Ropes (Tutorial Lecture), Geophys. Mono. 58, 1, 1990

Pytte, T., R. L. McPherron, M. G. Kivelson, H. I. West, Jr. and E. W Hones Jr., Multiple-satellite studies of magnetospheric substorms: Plasma sheet recovery and the poleward leap of auroral zone activity, J. Geophys. Res., 83, 5256, 1978

Reiff, P. H. and J. L. Burch, IMF By-dependent plasma flow and Birkeland currents in the dayside magnetosphere - 2. A global model for northward and southward IMF, J. Geophys. Res., 90, 1595-1609, 1985.

Remé, H., J. M. Bosqued, J. A. Sauvaud, A. Cros, J. Dandouras, C. Aoustinm, J. Bouyssou, C. d'Uston, E. Möbius, K. Crocker, M. Granoff, L. M. Kistler, M. Popecki, D. Hovestadt, B. Klecker, G. Paschmann, M., Scholer, C. W. Carlson, D. W. Curtis, R. P. Lin, J. O. McFadden, V. Formisano, E. Amata, M. B. Bavassano-Cattaneo, P. Baldetti, G. Belluci, R. Bruno, G. Chionchio, A. Di Lellis, E. G. Shelley, G. Ghielmetti, W. Lennartsson, A. Korth, H. Rosenbauer, R. Lundin, S. Orsen, G. K. Parks, M McCarthy and H. Balsiger, The Cluster Ion Spectrometry (CIS) Experiment, Space Sci. Rev., 79, 303, 1997

Riedler, W., T. Torkar, F. Rüdenauer, M, Fehrringer, A. Pedersenm R, Schmidt, R. J. Grard, H. Arends, B. T. Narheim, J. Troim, R. Torbert, R. C. Olsen, E. Whipple, R. Goldstein, N., Valavanoglou, and Hua Zhao, Active Spacecraft Potential Control, Space Sci. Rev., 79, 271, 1997

Rostoker, G. D., Current flow in the magnetosphere during magnetospheric substorms, J. Geophys. Res., 79, 1994, 1974

Rostoker, G., S. –I. Akasofu, J. Fosters, R. A. Greenwald, Y. Kamide, K. Kawasaki, A. T. Y. Lui, R. L. PcPherron and C. T. Russell, Magnetospheric substorms – Definitions and signatures, J. Geophys. Res., 85, 1663, 1980

Rostoker, G., Phenomenology and physics of magnetospheric substorms, J. Geophys. Res., 101, 12995, 1996

Roux, A., S. Perraut, P. Robert, A. Morane, A. Pedersen, A. Korth, G. Kremser, B. Aparicio, D. Rogers, R. Pellinen, Plasma sheet instabilities related to the westward travelling surge, J. Geophys. Res., A96, 17697, 1991

Russell, C. T., and R. L. McPherron, The magnetotail and substorms, Space Sci. Rev., 15, 205, 1973

Russell, C. T., G. L. Siscoe, and E. J. Smith, Comparison of ISEE-1 and -3 interplanetary magnetic field observations, Geophys. Res. Lett., 7, 381-384, 1980

Sablik, M. J., J. R. Scherrer, J. D. Winningham, R. A. Frahm, and T. Schrader, TFAS (A Tophat For All Species) - Design And Computer Optimization Of A New Electrostatic Analyzer, IEEE Trans. Geosci. Rem. Sense., 28, 1034, 1990

Salem C, Hoang S, Issautier K, et al., Wind-ulysses in-situ thermal noise measurements of solar wind electron density and core temperature at solar maximum and minimum, Adv. Space. Res., 32, 491, 2003

Sauvaud JA, Jacquey C, Beutier T, Owen C, Lepping RP, Russell CT, Belian RJ, Large scale dynamics of the magnetospheric tail induced by substorms: A multisatellite study, J. Geomag. and Geoelec., 48, 675, 1996

Schindler, K., A theory of the substorm mechanism, J. Geophys. Res., 79, 2803-2810, 1974

Schödel, R., W. Baumjohann, R. Nakamura, V. A. Sergeev, and T. Mukia, Rapid flux transport in the central plasma sheet, J. Geophys. Res., 106, 301, 2001

Scholer, M., et al., Characters of plasmoid-like structures in the distant magnetotail, JGR, 89, 8872, 1984

Scime, E. E., How to really measure low energy electrons in space, Measurement Techniques in Space Plasmas: Field, AGU, Geophysical Monograph, 103, 229, 1998

Sergeev, V. A., V. Angelopoulos, J. T. Gosling, C. A. Cattell, and C. T. Russell, Detection of localized, plasma-depleted flux tubes or bubbles in the midtail plasma sheet, J. Geophys. Res., 101, 10917, 1996

Sergeev, V. A., J. –A. Sauvaud, D. Popescu, R. A. Kovrazhkin, K. Lios, P. T. Newell, M. Brittnacher, G. Parks, R. Nakamura, T. Mukai, G. D. Reeves, Multiple-spacecraft observations of a narrow transient plasma jet in the Earth's plasma sheet, Geophys. Res. Lett., 27, 851, 2000

Sergeev, V., A. Runov, W. Baumjohann, R. Nakamura, T. L. Zhang, M. Volwerk, A. Balogh, H. Rème, J. A. Sauvaud, M. André, and B. Klecker, Current sheet flapping motion and structure observed by Cluster, GRL, 30, 1327, doi:10.1029/2002GL016500, 2003

Shiokawa, K., W. Baumjohann, G. Haerendel, G. Paschmann, J. F. Fennell, E. Friis-Christensen, H. Luhr, G. D. Reeves, C. T. Russell, P. R. Sutcliffe, and K.

Takahashi, High-speed ion flow, substorm current wedge, and multiple Pi 2 pulsations, J. Geophys. Res., 103, 4491, 1998

Shiokawa, K., W. Baumjohann, and G. Paschmann, Bi-directional electrons in the near-Earth plasma sheet, Ann. Geophys, 21, 1497, 2003

Sibeck, D. G., R. E. Lopez, and E. C. Roelof, Solar wind control of the magnetopause shape, location, and motion, J. Geophys. Res., 96, 5489-5495, 1991

Sibeck, D. G., and J. T. Gosling, Magnetosheath density fluctuations and magnetopause motion, J. Geophys. Res., 101, 31-40, 1996

Sigsbee, K., C. A. Cattell, R. L. Lysak, C. W. Carlson, R. E. Ergun, J. P. McFadden, F. Mozer, R. C. Elphic, R. J. Strangeway, K. Tsuruda, T. Yamamoto, S. Kokubun, D. Fairfield, R. Pfaff, G. Parks, M. Brittnacher, FAST - Geotail correlative studies of magnetosphere - ionosphere coupling in the nightside magnetosphere, GRL, 1997/1998

Slavin, J. A., et al., Substorm associated traveling compression regions in the distant tail: ISEE-3 geotail observations, GRL, 11, 657, 1984

Slavin, J. A., et al., CDAW 8 observations of plasmoids in the Geotail: An assessment, JGR, 94, 15153, 1989

Slavin, J. A., M. F. Smith, E. L. Mazur, D. N. Baker, E. W. Hones, Jr., T. Iyemori, and E. W. Greenstadt, ISEE 3 Observations of Travelling Compression Regions in the Earth's Magnetotail, J. Geophys. Res., 98, 15425, 1993

Slavin, J. A., Smith MF, Mazur EL, Baker DN, Hones EW, Iyemori T, Greenstadt EW, ISEE-3 Observations of Traveling Compression Regions in the Earths Magnetotail, JGR, 98, 15425, 1993

Slavin, J. A., et al., Evolution of the plasmoid-lobe interaction with downtail distance, Geophys. Res. Lett., 21, 2765, 1994

Slavin, J. A., Hesse M, Owen CJ, Taguchi S, Fairfield DH, Lepping RP, Kokuban S, Mukai T, Lui ATY, Anderson RR, Matsumoto H, Sutcliffe PR, Dual spacecraft observations of lobe magnetic field perturbations before, during and after plasmoid release, GRL, 26, 2897, 1999

Slavin, J. A., D. H. Fairfield, R. P. Lepping, M. Hesse, A. Ieda, E. Tanskanen, N. Ostgaard, T.Mukai, T. Nagai, H. J. Singer, P. R. Sutcliffe, Simultaneous

observations of earthward flow bursts and plasmoid ejection during magnetospheric substorms, J. Geophys. Res., 107, 1106, 2002

Slavin, J. A., C. J. Owen, M. W. Dunlop, E. Boralv, M. B. Modlwin, D. G. Sibeck, E. Tanskanen, M. L. Goldstein, A. Fazakerley, A. Balogh, E. Luceh, I Richter, H. Reme, J. M. Bosquet, Cluster four spacecraft measurements of small traveling compression regions in the near-tail, Geo. Phys. Lett., 30 (23), 2208, 2003

Slavin et al., Geotail observations of magnetic flux ropes in the plasma sheet, J. Geophys. Res., 108, 1015, doi:10.1029.2002JA009557, 2003

Smith, E. J., R. E. Holtzer, and C. T. Russell, Magnetic emissions in the magnetosheath at frequencies near 100 Hz, J. Geophys. Res., 74, 3027, 1969

Song, P., R. C. Elphic, and C. T. Russell Multi-spacecraft observations of magnetopause surface waves: ISEE 1 and 2 determinations of amplitude, wavelength and period, Adv. Space Res., 8, 9-10, 245-248, 1988

Southwood, D. J., and M. G. Kivelson, An Approximate Description of Field-Aligned Currents in a Planetary Magnetic Field, J. Geophys. Res., 96, 67, 1991

Szita, S., A. N. Fazakerley, P. J. Carter, A. M James, P. Trávníček, G. Watson, M. André, A. Eriksson, and K. Torkar, Cluster PEACE observations of electrons of spacecraft origin, Ann. Geo., 19, 1721-1730, 2001

Treumann, R. A., and W. Baumjohann, Advanced Space Plasma Physics, 1997, Imperial College Press, London, England, ISBN 1-86094-026-9

Troshichev, O. A., Plasma pressure and the field-aligned currents in the magnetosphere, Adv. Space. Res., 33, 729, 2004

Van Allen, J. A., G. H. Ludwig, E. C. Ray, and C. E. McIlwain, Observations of high intensity radiation by satellites 1958 Alpha and Gamma, Jet Propul., 28, 588-592, 1958

Van Allen, J. A., and L. A. Frank, Radiation around the Earth to a radial distance of 107,400 km, Nature, 183, 430, 1959

Vasyliunas, V. M., Theoretical models of magnetic field line merging, Rev. Geophys. Space Phys., 13, 303, 1975

Voronkov, I., R. Rankin, P. Frycz, V. T. Tikhonchuk, and J. C. Samson, Coupling of shear flow and pressure gradient instabilities, J. Geophys. Res., 102, 9629, 1997

Weisstein, E. W, Correlation Coefficient, Mathworld – A Wolfram Web Resource, http://mathworld.wolfram.com/CorrelationCoefficient.html, 2005

Wilken, B., W. I. Axford, I. Daglis, P. Daly, W. Güttler, W. H. Ip, A. korth, G. Kremser, S. Livi, V. M. Vasyliunas, J. Woch, D. Baker, R. D. Belian, J. B. Blake, J. F. Fennell, L. R. Lyons, H. Borg, T. A. Fritz, F. Gliem, R. Rathje, M. Grande, D. Hall, K. Kecsueméty, S. McKenna-Lawlor, K. Mursula, P. Tanskanen, Z. Pu, I. Sandahl, E. T. Sarris, M. Scholer, M. Sculz, F. Sørass and S. Ullaland, RAPID: The Imaging Energetic Particle Spectrometer on Cluster, Space Sci, Rev., 79, 399, 1997

Williams, D. J., Energetic ion beams at the edge of the plasma sheet: ISEE 1 observations plus a simple explanatory model, J. Geophys. Res., 86, 5507, 1981

Wilson, R. J, Private Communication, 2004

Yamomoto, T., A. Matsuoka, K. Tsuruda, H. Hayakawa, and A. Nishida, Dense plasmas in the distant magnetotail as observed by Geotail, Geophys. Res. Lett., 21, 2875, 1994

Zelenyi, L. M., P. Triska, and A. A. Petrukovich, INTERBALL—Dual probe and dual mission, Adv. Space Res., 20,4-5 ,549-557, 1997

Zhang, T. L., W. Baumjohann, and R. Nakamura, A wavy twisted neutral sheet observed by CLUSTER, Geophys. Res. Lett., 29, 1899, doi:10.1029/2002GL015544, 2002

Zwickl, R. D., D. N. Baker, S. J. Bame, W. C. Feldman, J. T. Gosling, E. W. Hones, Jr., D. J. McComas, B. T. Tsurutani, and J. A. Slavin, Evolution of the earth's distant magnetotail – ISEE 3 electron plasma results, J. Geophys. Res., 89, 1007, 1984